

Inverse force problems for the wave equation

Shilan Othman Hussein

Submitted in accordance with the requirements for the degree of
Doctor of Philosophy

The University of Leeds
Department of Applied Mathematics

April 2016

The candidate confirms that the work submitted is her own, except where work which has formed part of jointly authored publications has been included and that appropriate credit has been given where reference has been made to the work of others.

This copy has been supplied on the understanding that it is copyright material and that no quotation from the thesis may be published without proper acknowledgement.

© 2016 The University of Leeds and Shilan Othman Hussein

Jointly Authored Publications

The candidate confirms that the work submitted is her own, except where work which has formed part of jointly authored publications has been included. The contribution of the candidate and the other authors to this work has been explicitly indicated below. The candidate confirms that appropriate credit has been given within the thesis where reference has been made to the work of others.

Almost all of the work presented in Chapters 2-5 has already been refereed and published, as follows:

- Hussein, S.O. and Lesnic, D. Determination of a space-dependent source function in the one-dimensional wave equation, *Electronic Journal of Boundary Elements*, **12**, 1-26, 2014.
- Hussein, S.O. and Lesnic, D. Determination of forcing functions in the wave equation. Part I: the space-dependent case, *Journal of Engineering Mathematics*, **96**, 115-133, 2016.
- Hussein, S.O. and Lesnic, D. Determination of forcing functions in the wave equation. Part II: the time-dependent case, *Journal of Engineering Mathematics*, **96**, 135-153, 2016.
- Lesnic, D., Hussein, S.O. and Johansson, B.T. Inverse space-dependent force problem for the wave equation, *Journal of Computational and Applied Mathematics*, (accepted).

Also, almost all of the work in Chapter 6 has been submitted and is under review, as follows:

- Hussein, S.O., Lesnic, D. and Yamamoto, M. Reconstruction of space-dependent potential and/or damping coefficients in the wave equation, (submitted).

It is likely that after receiving the referee reports this paper will be considerably rewritten. One also notes that some theoretical results obtained by the joint authors of the above papers have not been included in the present thesis and emphasis was rather made on the main original computational work performed and the numerically results obtained by the candidate.

To my parents

Othman Hussein and Galawezh Ali

Acknowledgements

First of all, appreciation is due to Allah whose guidance and powers have granted me with the health, knowledge and patience to finish this work.

I would like to extend my great thanks to my supervisor Professor Daniel Lesnic for his guidance, support, helpful conversations and advice throughout the research of my PhD, sharing knowledge and expertise. Indeed, words cannot express my deep gratitude, appreciation and thanks for all the support, guidance and time he had provided during my stay in Leeds.

My deepest appreciation to all staff in the School of Mathematics, with special thanks to the Inverse Problems Group and to Tim Hainsworth, who has always been very friendly and helpful.

My special thanks are due to my parents, I always say I wish to put their names on my thesis, for always going out of their way to make sure that I received a good education and for their constant encouragement, for their patience while I have been away. I will be forever indebted.

I would also like to thank, from this position, all my colleagues and friends in Leeds for all their support.

I express special gratitude to my family for their prayers and continuous support for me. Special thanks for my sister Devan, she always encourages me and takes care for me, and my oldest brother Mohammed, he has on my behalf while I am here. I would also like to thank my brother Rahel for his kindness, and to my lovely youngest brother Ahmad, for his patience while I have been away, and my thanks to both my brothers Rebin and Rebaz.

My gratitude extend to Professor Dlawer Ala'Aldeen for his program the Human Capacity Development Programme (HCDP) in Kurdistan and Ass.Professor Adil Kadir Jabbar for his valuable advice to encourage my studies in the UK.

Abstract

Inverse problems have become more and more important in various fields of science and technology, and have certainly been one of the fastest growing areas in applied mathematics over the last three decades. However, as inverse problems typically lead to mathematical models which are ill-posed, their solutions are unstable under data perturbations and classical numerical techniques fail to provide accurate and stable solutions.

The work in this thesis focuses on inverse force problems for the wave equation which consists of determining an unknown space/time-dependent force function acting on a vibrating structure from Cauchy boundary, final time displacement or integral data. The novel contribution of this thesis involves the development of efficient numerical algorithms for these inverse but ill-posed problems. We have used the boundary element method (BEM) to discretise the wave equation with a constant wave speed, and the finite difference method (FDM) for non-constant wave speed and/or inhomogeneous wave propagating medium.

Imposing the available boundary and additional conditions, upon discretisation the inverse and ill-posed problem is recast into one of solving an ill-conditioned system of equations.

The accuracy and convergence of the numerical results are investigated for various test force functions. The stability of the numerical solutions is investigated by introducing random noise into the input data which yields unstable results if no regularisation is used. The Tikhonov regularization method is employed in order to reduce the influence of the measurement errors on the numerical results. The choice of the regularization parameter is based on trial and error or on the L-curve criterion. Iterative regularizing methods such as the Landweber and conjugate gradient methods are also employed in one chapter. The inverse numerical solutions are compared with their known analytical solutions, where available, and with the corresponding direct numerical solutions otherwise.

Contents

1	Introduction	1
1.1	Motivation and outline of thesis	1
1.2	Direct problems	2
1.3	Inverse problems	3
1.4	Numerical methods for discretising partial differential equations	4
1.4.1	Boundary Element Method (BEM)	4
1.4.2	Finite Difference Method (FDM)	5
1.4.3	Finite Element Method (FEM)	5
1.4.4	Error estimates and order of convergence	6
1.5	Regularization methods	7
1.6	Outline of the thesis	9
2	Determination of a space-dependent force function from Cauchy data	11
2.1	Introduction	11
2.2	Mathematical formulation	12
2.3	The boundary element method (BEM) for solving the direct problem (2.9)-(2.13)	14
2.4	Method for solving the inverse problem (2.14)-(2.18)	21
2.5	Numerical results and discussion	23
2.5.1	Exact data	25
2.5.2	Noisy data	28
2.6	Alternative control	32
2.6.1	Exact data	34
2.6.2	Noisy data	35

2.7	Conclusions	36
3	Determination of forcing functions in the wave equation. Part I: the space-dependent case	38
3.1	Introduction	38
3.2	Mathematical formulation	39
3.2.1	Mathematical analysis	41
3.3	Numerical solution of the direct problem	43
3.4	Numerical solution of the inverse problem	44
3.5	Numerical results and discussion	47
3.5.1	Example 1 ($h(x, t) = 1$)	47
3.5.2	Example 2 ($h(x, t) = 1 + t$)	53
3.5.3	Example 3 ($h(x, t) = 1 + x + t$)	60
3.5.4	Example 4 ($h(x, t) = t^2$)	62
3.6	Extension to multiple sources	65
3.6.1	Example 5	67
3.7	Conclusions	68
4	Determination of forcing functions in the wave equation. Part II: the time-dependent case	70
4.1	Introduction	70
4.2	Mathematical formulation	71
4.3	Numerical solution of the direct problem	73
4.4	Numerical solution of the inverse problem	74
4.5	Numerical results and discussion	76
4.5.1	Example 1	76
4.5.2	Example 2	87
4.5.3	Example 3	95
4.6	Conclusions	106
5	Inverse space-dependent force problem for the wave equation	108
5.1	Introduction	108
5.2	Problem formulation	109
5.2.1	Inverse problem	110

5.3	Variational formulation of the inverse problems	112
5.4	An iterative procedure for the inverse problem	114
5.5	Numerical results and discussion	115
5.5.1	Example 1	116
5.5.2	Example 2	122
5.5.3	Example 3	128
5.5.4	Example 4	135
5.5.5	Example 5	142
5.6	Two-dimensions	147
5.6.1	Example 6	148
5.7	Conclusions	155
6	Reconstruction of space-dependent potential and/or damping coefficients in the wave equation	157
6.1	Introduction	157
6.2	Mathematical formulation	158
6.3	Numerical solutions of the direct and inverse problems	159
6.3.1	Direct problem	159
6.3.2	Inverse problems	161
6.4	Numerical results and discussion	161
6.4.1	Example 1 (determination of $Q_0(x)$ when $Q_1(x)$ is known)	161
6.4.2	Example 2 (determination of $Q_1(x)$ when $Q_0(x)$ is known)	168
6.4.3	Example 3 (determination of $Q_0(x)$ and $Q_1(x)$)	172
6.5	Conclusions	176
7	General conclusions and future work	178
7.1	Conclusions	178
7.2	Future work	184
8	Appendix A	185
	References	195

List of Figures

2.1	The numerical results for $v_x(0, t)$ obtained using the BEM with $M = N \in \{20, 40, 80\}$	24
2.2	Normalised singular values $sv(k)/sv(1)$ for $k = \overline{1, K}$, for $N = 80$ and $K = 20$	25
2.3	The numerical solution (...) for $(b_k)_{k=\overline{1, K}}$ for $K = 20$, $N = 80$, obtained with no regularization, i.e. $\lambda = 0$, for exact data, in comparison with the exact solution (2.73) (—).	27
2.4	The exact solution (2.65) for $f(x)$ in comparison with the numerical solution (2.54) for various $K \in \{5, 10, 20\}$, no regularization, for exact data.	27
2.5	The numerical solution (— — —) for $u(x, t)$ obtained with various $K \in \{5, 10, 20\}$, no regularization, for exact data, in comparison with the exact solution (2.64) (—).	28
2.6	The exact solution (2.65) for $f(x)$ in comparison with the numerical solution (2.54) for various $K \in \{5, 10, 20\}$, no regularization, for $p\% = 1\%$ noisy data.	30
2.7	The numerical solution (— — —) for $u(x, t)$ obtained with various $K \in \{5, 10, 20\}$, no regularization, for $p\% = 1\%$ noisy data, in comparison with the exact solution (2.64) (—).	30
2.8	The accuracy error $\ f_{numerical} - f_{exact}\ $, as a function of λ , for $K = 20$ and $p\% = 1\%$ noise.	31
2.9	The L-curve for the Tikhonov regularization (2.62), for $K = 20$ and $p\% = 1\%$ noise.	31

LIST OF FIGURES

2.10	The exact solution (2.65) for $f(x)$ in comparison with the numerical solution (2.54), for $K = 20$, $p\% = 1\%$ noise, and regularization parameters $\lambda \in \{10^{-2}, 10^{-1}, 10^0\}$	32
2.11	The numerical results for $v(0, t)$ obtained using the BEM with $M = N \in \{20, 40, 80\}$	33
2.12	The numerical solution (...) for $(b_k)_{k=\overline{1, K}}$ for $K = 20$, $N = 80$, obtained with no regularization, i.e. $\lambda = 0$, for exact data, in comparison with the exact solution (2.81) (—).	34
2.13	The exact solution (2.65) for $f(x)$ in comparison with the numerical solution (2.77) for various $K \in \{5, 10, 20\}$, no regularization, for exact data.	35
2.14	The exact solution (2.65) for $f(x)$ in comparison with the numerical solution (2.77) for $K = 20$, $p\% = 1\%$ noise, and regularization parameters $\lambda \in \{10^{-4}, 10^{-3}, 10^{-2}\}$	36
3.1	Normalised singular values σ_k/σ_1 for $k = \overline{1, (M-1)}$, for (a) Example 1, (b) Example 2, (c) Example 3, and (d) Example 4. . . .	46
3.2	Exact and numerical solutions for the displacement $u(x, t)$ and the absolute error between them for the direct problem, obtained with $N = M = 80$, for Example 1.	48
3.3	The exact (—) solution (2.65) for the force $f(x)$ in comparison with the numerical solution (···) for various $N = M =$ (a) 10, (b) 20, (c) 40, and (d) 80, and no regularization, for exact data, for the inverse problem of Example 1.	49
3.4	The absolute errors between the exact and numerical displacement $u(x, t)$ obtained with $N = M \in \{10, 20, 40, 80\}$ and no regularization, for exact data, for the inverse problem of Example 1.	50
3.5	The exact solution (2.65) for the force $f(x)$ in comparison with the numerical solution (—●—) for $N = M = 80$, with no regularization, for $p = 1\%$ noisy data, for the inverse problem of Example 1. . . .	51
3.6	The accuracy error $\ \underline{f}_{\text{num}} - \underline{f}_{\text{exact}}\ $, as a function of λ , for $N = M = 80$ and $p = 1\%$ noise, for the inverse problem of Example 1.	52

LIST OF FIGURES

3.7	The L-curve for the Tikhonov regularization, for $N = M = 80$ and $p = 1\%$ noise, for the inverse problem of Example 1.	53
3.8	The exact solution (2.65) for the force $f(x)$ in comparison with the numerical solution (3.31), for $N = M = 80$, $p = 1\%$ noise, and regularization parameters $\lambda \in \{10^{-7}, 10^{-6}, 10^{-5}\}$, for the inverse problem of Example 1.	53
3.9	Numerical solutions for the displacement $u(x, t)$ obtained using the direct problem with various $N = M \in \{10, 20, 40, 80\}$ in (a)-(d), respectively, for Example 2.	55
3.10	Numerical solution for the flux tension at $x = 0$, for various $N = M \in \{5, 10, 20, 80\}$, for the direct problem of Example 2.	56
3.11	The accuracy error $\ \underline{f}_{\text{num}} - \underline{f}_{\text{exact}}\ $, as a function of λ , for $M = N = 80$, $p \in \{1, 3, 5\}\%$ noise, obtained using (a) zeroth, (b) first, and (c) second-order regularization, for the inverse problem of Example 2.	58
3.12	The L-curve for the zeroth-order Tikhonov regularization, for $N = M = 80$ and $p \in \{1, 3, 5\}\%$ noise, for the inverse problem of Example 2.	59
3.13	The exact solution (3.34) for the force $f(x)$ in comparison with the numerical regularized solution (3.35), for $N = M = 80$, $p \in \{1, 3, 5\}\%$ noise, and various order regularization methods, for the inverse problem of Example 2.	60
3.14	The exact solution (3.34) for the force $f(x)$ in comparison with the regularized numerical solution (3.35), for $N = M = 80$, $p \in \{1, 3, 5\}\%$ noise, and various order regularization methods, for the inverse problem of Example 3.	61
3.15	Numerical solution for the flux tension at $x = 0$, for various $N = M \in \{5, 10, 20, 80\}$, for the direct problem of Example 4.	63
3.16	The exact solution (3.34) for the force $f(x)$ in comparison with the regularized numerical solution (3.35), for $N = M = 80$ and $p \in \{1, 3, 5\}\%$ noise, and various order regularization methods, for the inverse problem of Example 4.	64

LIST OF FIGURES

3.17	The exact (—) solutions (3.47) for the force components $f(x)$ and $g(x)$ in comparison with the numerical solutions for various $N = M \in \{10, 20, 40, 80\}$, and no regularization, for exact data, for the inverse problem of Example 5.	68
3.18	The exact (—) solutions (3.47) for the force components $f(x)$ and $g(x)$ in comparison with the numerical solutions, for $N = M = 80$, $p = 1\%$ noise and various order regularization methods, for the inverse problem of Example 5.	68
4.1	Normalised singular values σ_k/σ_1 for $k = \overline{1, M}$, for Examples 1-3.	76
4.2	The absolute errors between the exact (4.24) and numerical displacement $u(x, t)$ obtained by solving the direct problem with $N = M =$ (a) 10, (b) 20, (c) 40, and (d) 80, for Example 1.	78
4.3	The absolute error between the exact (4.26) and numerical $\Lambda(t)$ obtained by solving the direct problem with $N = M \in \{10, 20, 40, 80\}$, for Example 1.	79
4.4	The exact (—) solution for $h(t)$ in comparison with the numerical solution (— Δ —) for various $N = M =$ (a) 10, (b) 20, (c) 40, and (d) 80, and no regularization, for exact data, for the inverse problem of Example 1.	80
4.5	The log-log plot of the ℓ^2 -errors between the analytical and numerical (a) $h(t)$ and (b) $u(x, t)$, as functions of N , for Example 1.	81
4.6	The absolute errors between the exact (4.24) and numerical displacement $u(x, t)$ obtained with $N = M =$ (a) 10, (b) 20, (c) 40, and (d) 80, and no regularization, for exact data, for the inverse problem of Example 1.	82
4.7	The exact (—) solution for $h(t)$ in comparison with the numerical solution (— Δ —) for $N = M = 80$, $p = 1\%$ noise, and no regularization, for the inverse problem of Example 1.	83

LIST OF FIGURES

4.8	The accuracy error $\ \underline{h}_{\text{num}} - \underline{h}_{\text{exact}}\ $, as a function of λ , for $M = N = 80$, $p \in \{1, 3, 5\}\%$ noise, obtained using (a) zeroth, (b) first, and (c) second-order regularization, for the inverse problem of Example 1.	84
4.9	The L-curves for $N = M = 80$, $p \in \{1, 3, 5\}\%$ noise, and (a) zeroth, (b) first and (c) second-order regularizations, for the inverse problem of Example 1.	85
4.10	The exact (—) solution for $h(t)$ in comparison with the regularized numerical solution (4.27), for $N = M = 80$, $p \in \{1, 3, 5\}\%$ noise, for the inverse problem of Example 1.	86
4.11	Numerical solutions for the displacement $u(x, t)$ obtained by solving the direct problem with various $N = M =$ (a) 10, (b) 20, (c) 40, and (d) 80, for Example 2.	88
4.12	Numerical solution for the integral (4.3), obtained by solving the direct problem with various $N = M \in \{5, 10, 20, 40, 80\}$, for Example 2.	89
4.13	The exact (—) solution (4.30) for $h(t)$ in comparison with the numerical solution (— Δ —) for various $N = M =$ (a) 10, (b) 20, (c) 40, and (d) 80, and no regularization, for exact data, for the inverse problem of Example 2.	90
4.14	The accuracy error $\ \underline{h}_{\text{num}} - \underline{h}_{\text{exact}}\ $, as a function of λ , for $M = N = 80$, $p \in \{1, 3, 5\}\%$ noise, obtained using (a) zeroth, (b) first, and (c) second-order regularization, for the inverse problem of Example 2.	92
4.15	The L-curves for $N = M = 80$, $p \in \{1, 3, 5\}\%$ noise, and (a) zeroth, (b) first and (c) second-order regularization, for the inverse problem of Example 2.	93
4.16	The exact solution (4.30) for $h(t)$ in comparison with the regularized numerical solution (4.27), for $N = M = 80$, $p \in \{1, 3, 5\}\%$ noise, for the inverse problem of Example 2.	94
4.17	The absolute errors between the exact (4.35) and numerical displacement $u(x, t)$ obtained by solving the direct problem with $N = M =$ (a) 10, (b) 20, (c) 40, and (d) 80, for Example 3.	97

LIST OF FIGURES

4.18	The absolute error between the exact (4.36) and numerical $\Lambda(t)$ obtained by solving the direct problem with $N = M \in \{10, 20, 40, 80\}$, for Example 3.	98
4.19	The exact (—) solution (4.34) for $h(t)$ in comparison with the numerical solution (— Δ —) for various $N = M =$ (a) 10, (b) 20, (c) 40, and (d) 80, no regularization, for exact data, for the inverse problem of Example 3.	99
4.20	The log-log plot of the ℓ^2 -errors between the analytical and numerical (a) $h(t)$ and (b) $u(x, t)$, as functions of N , for Example 3.	100
4.21	The absolute errors between the exact (4.35) and numerical displacement $u(x, t)$ obtained with $N = M =$ (a) 10, (b) 20, (c) 40, and (d) 80, and no regularization, for exact data, for the inverse problem of Example 3.	101
4.22	The accuracy error $\ \underline{h}_{\text{num}} - \underline{h}_{\text{exact}}\ $, as a function of λ , for $M = N = 80$, $p \in \{1, 3, 5\}\%$ noise, obtained using (a) zeroth, (b) first, and (c) second-order regularization, for the inverse problem of Example 3.	103
4.23	The L-curves for $N = M = 80$, $p \in \{1, 3, 5\}\%$ noise, and (a) zeroth, (b) first and (c) second-order regularizations, for the inverse problem of Example 3.	104
4.24	The exact solution (4.34) for $h(t)$ in comparison with the numerical regularized solution (4.27), for $N = M = 80$, $p \in \{1, 3, 5\}\%$ noise, for the inverse problem of Example 3.	105
5.1	The absolute errors between exact and numerical solutions for (a) $u_T(x)$ and (b) $U_T(x)$, for $N = M \in \{10, 20, 40, 80\}$ for the direct problem of Example 1.	118
5.2	(a) The objective function $\tilde{J}(f_k)$ and (b) the accuracy error $E(f_k)$, versus the number of iterations $k = \overline{1, 5000}$, no noise for the inverse problem of Example 1.	119

LIST OF FIGURES

5.3 The numerical solution f_k at various iteration numbers k , in comparison with the exact solution (5.39), no noise for the inverse problem of Example 1. 120

5.4 (a) The objective function $\tilde{J}(f_k)$ and (b) the accuracy error $E(f_k)$, versus the number of iterations $k = \overline{1, 500}$, for $p = 10\%$ (—), $p = 30\%$ (- - -) and $p = 50\%$ (⋯) noise for the inverse problem of Example 1. The horizontal lines in (a) represent the threshold $\tau^2\epsilon^2/2$ with $\tau = 1.15$ 121

5.5 The exact solution f in comparison with the numerical solution f_k for (a) $k_{opt} \in \{373, 276, 232\}$ and (b) $k_{discr} \in \{300, 245, 205\}$, for $p \in \{10, 30, 50\}\%$ noise, for the inverse problem of Example 1. . . . 122

5.6 (a) The objective function $J(f_k)$ and (b) the corresponding accuracy error $E(f_k)$ for the inverse problem of Example 2 with the displacement measurement (5.55), and (c) the objective function $\tilde{J}(f_k)$ and (d) the corresponding accuracy error $E(f_k)$ for the inverse problem of Example 2 with the time-average displacement measurement (5.56). All curves are as functions of the number of iterations $k = \overline{1, 50}$, for no noise. 124

5.7 The numerical solution f_k at various iteration numbers k , in comparison with the exact solution (5.58), no noise for the inverse problem of Example 2 with (a) the displacement measurement (5.55), and (b) the time-average displacement measurement (5.56). 125

5.8 (a) The objective function $J(f_k)$ and (b) the corresponding accuracy error $E(f_k)$ for the inverse problem of Example 2 with the displacement measurement (5.55), and (c) the objective function $\tilde{J}(f_k)$ and (d) the corresponding accuracy error $E(f_k)$ for the inverse problem of Example 2 with the time-average displacement measurement (5.56). All curves are as functions of the number of iterations $k = \overline{1, 50}$, for $p = 1\%$ (—), $p = 3\%$ (- - -) and $p = 5\%$ (⋯) noise. The horizontal lines in (a) and (c) represent the threshold $\tau^2\epsilon^2/2$ with $\tau = 1.15$ and $\tau = 1.25$, respectively. 126

5.9 The numerical solution f_k at various iteration numbers k , in comparison with the exact solution (5.58), for $p \in \{1, 3, 5\}\%$ noise for the inverse problem of Example 2 with the displacement measurement (5.55) for (a) $k_{opt} \in \{7, 6, 6\}$, (b) $k_{discr} \in \{6, 5, 4\}$, and with the time-average displacement measurement (5.56) for (c) $k_{opt} \in \{36, 30, 27\}$, (d) $k_{discr} \in \{33, 27, 24\}$ 128

5.10 Numerical solution for (a) $u(x, 1)$ and (b) $\int_0^1 u(x, t)dt$, for various $N = M \in \{5, 10, 20, 80\}$, for the direct problem of Example 3. . . 130

5.11 (a) The objective functions $J(f_k)$, $\tilde{J}(f_k)$ and (b) the accuracy error $E(f_k)$, versus the number of iterations $k = \overline{1, 10^5}$, no noise for the inverse problem of Example 3 with the displacement measurement (5.2) (- - -) and with the time-average displacement measurement (5.14) (—). 131

5.12 The numerical solution f_k at various iteration numbers k , in comparison with the exact solution (5.61), no noise for the inverse problem of Example 3 with (a) the displacement measurement (5.2), and (b) the time-average displacement measurement (5.14). 131

5.13 (a) The objective function $J(f_k)$ and (b) the corresponding accuracy error $E(f_k)$ for the inverse problem of Example 3 with the displacement measurement from Figure 5.10(a) with $N = M = 80$, and (c) the objective function $\tilde{J}(f_k)$ and (d) the corresponding accuracy error $E(f_k)$ for the inverse problem of Example 3 with the time-average displace measurement of Figure 5.10(b) with $N = M = 80$. All curves are functions of the number of iterations $k = \overline{1, 10^5}$, for $p = 1\%$ (—), $p = 3\%$ (- - -) and $p = 5\%$ (\cdots) noise. The horizontal lines in (a) and (c) represent the threshold $\tau^2\epsilon^2/2$ with $\tau = 1.2$ and $\tau = 1.1$, respectively. 133

5.14 The numerical solution f_k at various iteration numbers k , in comparison with the exact solution (5.61), for $p \in \{1, 3, 5\}\%$ noise for the inverse problem of Example 3 with the displacement measurement from Figure 5.10(a) with $N = M = 80$ for (a) $k_{opt} \in \{34080, 20363, 15577\}$, (b) $k_{discr} \in \{17712, 7949, 7012\}$, and with the time-average displacement measurement from Figure 5.10(b) with $N = M = 80$ for (c) $k_{opt} \in \{95908, 49208, 26760\}$, (d) $k_{discr} \in \{64996, 35905, 14998\}$ 135

5.15 Numerical solution for $u(x, 1)$, for various $N = M \in \{5, 10, 20, 80\}$, for the direct problem of Example 4. 136

5.16 (a) The objective function $J(f_k)$ and (b) the accuracy error $E(f_k)$, versus the number of iterations $k = \overline{1, 10^5}$, obtained using the Landweber method (—) and the CGM (- - -), no noise for the inverse problem of Example 4. 138

5.17 Numerical solution f_k for various iteration numbers $k \in \{10^1, 10^3, 10^5\}$, in comparison with the exact solution (5.64), obtained using (a) the Landweber method and (b) the CGM, no noise for the inverse problem of Example 4. 138

5.18 (a) and (c) The objective function $J(f_k)$, and (b) and (d) the accuracy error $E(f_k)$, versus the number of iterations $k = \overline{1, 10^5}$, obtained using the Landweber method and the CGM, respectively, for $p = 1\%$ (—), $p = 3\%$ (- - -) and $p = 5\%$ ($\cdot \cdot \cdot$) noise for the inverse problem of Example 4. The horizontal lines represents the threshold $\tau^2 \frac{\epsilon^2}{2}$ with $\tau = 1.15$ 140

5.19 The exact solution f in comparison with numerical solution f_k for (a) and (c) $k_{opt} \in \{10171, 3429, 68\}$ and $k_{opt} \in \{2908, 295, 12\}$, and (b) and (d) $k_{discr} \in \{2995, 95, 70\}$ and $k_{discr} \in \{130, 21, 11\}$, obtained using the Landweber method and the CGM, respectively, for $p \in \{1, 3, 5\}\%$ noise for the inverse problem of Example 4. 142

5.20 Numerical solution for $\int_0^1 u(x, t) dt$, for various $N=M \in \{5, 10, 20, 80\}$, for the direct problem of Example 5. 143

LIST OF FIGURES

5.21 (a) The objective function $\tilde{J}(f_k)$ and (b) the accuracy error $E(f_k)$, versus the number of iterations $k = \overline{1, 10^5}$, for various $\gamma = 1$ (—), $\gamma = 5$ (- - -) and $\gamma = 15$ (- • -), no noise for the inverse problem of Example 5.	144
5.22 Numerical solution f_k for various iteration numbers $k \in \{10^1, 10^3, 10^5\}$, in comparison with the exact solution (5.70), for (a) $\gamma=1$, (b) $\gamma=5$ and (c) $\gamma=15$, no noise for the inverse problem of Example 5.	145
5.23 (a) The objective function $\tilde{J}(f_k)$ and (b) the accuracy error $E(f_k)$, versus the number of iterations $k = \overline{1, 10^5}$, for $p = 1\%$ (—), $p = 3\%$ (- - -) and $p = 5\%$ (⋯⋯) noise for the inverse problem of Example 5 obtained with $\gamma = 15$. The horizontal lines represents the threshold $\tau^2 \frac{\epsilon^2}{2}$ with $\tau = 1.1$	146
5.24 The exact solution (5.70) for f in comparison with the numerical solution f_k for (a) $k_{opt} \in \{14823, 2275, 1523\}$ and (b) $k_{discr} \in \{9599, 2000, 1000\}$, for $p \in \{1, 3, 5\}\%$ noise for the inverse problem of Example 5 obtained with $\gamma = 15$	147
5.25 The absolute errors between the exact (5.83) and numerical solutions (5.84) for $\int_0^1 u(x, y, t) dt$ for various $N = M \in \{10, 20, 40, 80\}$ and $K = 2N \in \{20, 40, 80, 160\}$ in (a)-(d), respectively, for the direct problem of Example 6.	150
5.26 (a) The objective function (5.85) and (b) the accuracy error (5.86), versus the number of iterations $k = \overline{1, 500}$, no noise for the inverse problem of Example 6.	151
5.27 The numerical solution f_k for $k \in \{5, 50, 500\}$, in comparison with the exact solution (5.81), no noise for the inverse problem of Example 6.	152
5.28 (a) The objective function (5.85) and (b) the accuracy error (5.86), versus the number of iterations $k = \overline{1, 1000}$, for $p = 1\%$ (—), $p = 3\%$ (- - -) and $p = 5\%$ (⋯⋯) noise for the inverse problem of Example 6. The horizontal lines represents the threshold $\tau^2 \frac{\epsilon^2}{2}$ with $\tau = 1.05$	153

LIST OF FIGURES

5.29	The exact solution (5.81) for f in comparison with the numerical solution f_k for $k_{discr} \in \{796, 599, 597\}$ for $p \in \{1, 3, 5\}\%$ noise, respectively, for the inverse problem of Example 6.	155
6.1	The exact solutions (a) $u(0, t) = 3e^t$, (b) $u(1, t) = e^t$ in comparison with the numerical solutions for various $N = M \in \{5, 10, 20\}$, for the direct problem of Example 1.	163
6.2	(a) The objective function (6.21), as a function of the number of iterations, and (b) the exact solution (6.20) for the coefficient $Q_0(x)$ in comparison with the numerical solutions, for various $N = M \in \{5, 10, 20\}$, no noise for the inverse problem of Example 1. Figures (c) and (d) represent the same quantities as (a) and (b), but obtained by minimizing the partial objective function (6.22) instead of (6.21).	165
6.3	The exact solution (6.20) for the coefficient $Q_0(x)$ in comparison with the numerical solutions obtained by minimizing (6.21) (- - -) or (6.22) ($\cdot \cdot \cdot$), with no regularization, for $p = 1\%$ noisy data for the inverse problem of Example 1.	166
6.4	The accuracy error E_0 , as a function of λ , for $p \in \{1, 3, 5\}\%$ noise, for the inverse problem of Example 1, obtained by minimizing: (a) the functional (6.24) and (b) the partial functional (6.25).	167
6.5	(a) The regularized objective function (6.24), as a function of the number of iterations, and (b) the exact solution (6.20) for the coefficient $Q_0(x)$ in comparison with the numerical solutions, for $p \in \{1, 3, 5\}\%$ noise and regularization parameters $\lambda \in \{0.05, 0.1\}$, for the inverse problem of Example 1. Figures (c) and (d) represent the same quantities as (a) and (b), but obtained by minimizing the partial regularized objective function (6.25) instead of (6.24).	168
6.6	(a) The objective function (6.29), as a function of the number of iterations, and (b) the exact solution (6.28) for the coefficient $Q_1(x)$ in comparison with the numerical solutions, for various $N = M \in \{5, 10, 20\}$, no noise for the inverse problem of Example 2.	170

LIST OF FIGURES

6.7	The exact solution (6.28) for the coefficient $Q_1(x)$ in comparison with the numerical solution (- - -), with no regularization, for $p = 1\%$ noisy data for the inverse problem of Example 2.	171
6.8	The accuracy error E_1 , as a function of λ , for $p \in \{1, 3, 5\}\%$ noise, for the inverse problem of Example 2.	172
6.9	(a) The regularized objective function (6.30), as a function of the number of iterations, and (b) the exact solution (6.28) for the coefficient $Q_1(x)$ in comparison with the numerical solutions, for $p \in \{1, 3, 5\}\%$ noise and regularization parameters $\lambda \in \{0.05, 0.1\}$, for the inverse problem of Example 2.	172
6.10	(a) The objective function (6.38), as a function of the number of iterations, (b) the exact solution (6.36) for $Q_0(x)$ and (c) the exact solution (6.37) for $Q_1(x)$ in comparison with the numerical solutions, for various $N = M \in \{10, 20, 40\}$, no noise for the inverse problem of Example 3.	174
6.11	The exact solutions given by (a) equation (6.36) and (b) equation (6.37) for the coefficients $Q_0(x)$ and $Q_1(x)$, respectively, in comparison with the numerical solutions, with no regularization, for $p = 1\%$ noisy data for the inverse problem of Example 3.	175
6.12	The exact solutions given by (a) equation (6.36) and (b) equation (6.37) for the coefficients $Q_0(x)$ and $Q_1(x)$, respectively, in comparison with the numerical solutions, with regularization, for $p = 1\%$ noisy data for the inverse problem of Example 3.	176

Chapter 1

Introduction

1.1 Motivation and outline of thesis

The wave equation governs many physical problems such as the vibrations of a spring or membrane, acoustic scattering, etc.

When it comes to mathematical modeling probably the most investigated are inverse acoustic scattering problems in which one aims to determine an unknown obstacle from the far field measurement of the scattered wave (at different directions and/or various frequencies), see ([Colton and Kress, 2013](#)).

Another inverse problem for the wave equation concerns the determination of the speed of propagation from lateral Cauchy boundary conditions, see ([Isakov, 1998](#), Sect. 8.1).

On the other hand, inverse force problems have been less investigated and in this thesis we consider the problem of force identification from measured data for the hyperbolic wave equation. This inverse formulation is significant to modelling several practical applications related to unknown force loads and control.

For example, external force identification of applied loadings from output measurements of system responses can be experienced in many engineering applications dealing with wave, wind, seismic, explosion, or noise excitations.

In ([Huang, 2001](#)), the determination of the time-dependent external forces in a non-linear damped vibration system from the knowledge of the measured displacement and velocity at different times has been investigated.

Another important application of this inverse problem is to distinguish between various types of seismic events such as implosion, explosion or earthquake, which generate waves that propagate through the Earth and can be recorded using seismometers. In (Sjogreen and Petersson, 2014) a seismic source modelled as a point moment tensor forcing in the elastic wave equation for the displacement was estimated by minimizing the gap between the time-dependent measured/recorded and computed wave forms, see (Tarantola, 1984).

A final application that is mentioned here is represented by inverse problems in ocean acoustics concerned with the identification of the acoustic parameters of the ocean, the elastic parameters of the seafloor or an acoustic source, see (Collins and Kuperman, 1994). In these inverse problems the acoustic pressure satisfying the wave equation is measured on an array of hydrophones and the time-dependent intensity and space location of a point force/source and/or the speed of sound in the ocean are to be determined from these measurements.

Because part of the cause of the physical phenomenon is unknown one has to compensate for this lack of information by measuring an appropriate part of the effect. What quantity to measure is the delicate choice/constraint when formulating inverse problems, but a proper formulation would be able to ensure that the unknown force can be uniquely retrieved from the proposed additional measurements. However, stability can in general not be restored.

1.2 Direct problems

To define various classes of inverse problems, we should first define a direct (forward) problem. Indeed, something "inverse" must be the opposite of something "direct". For example, consider problems of mathematical physics.

In mathematical physics, a direct problem is usually a problem of modelling some physical fields, processes, or phenomena (electromagnetic, acoustic, seismic, heat, etc.). The purpose of solving a direct problem is to find a function that describes a physical field or process at any point of a given domain at any instant of time (if the field is non-stationary). The formulation of a direct problem includes:

- the domain in which the process is studied;
- the equation that describes the process;
- the initial condition (if the process is non-stationary);
- the conditions on the boundary of the domain.

Direct problems are in general well-posed. According to (Hadamard, 1923), a problem is well-posed if it satisfies the following properties:

- The solution exists for all data.
- The solution is unique for all data.
- The solution depends continuously on the data (stability), i.e. small errors in the input data cause only small errors in the output solution.

If one or more of the above properties is violated this leads to an ill-posed problem.

Direct problems for the full wave equation in the time-domain of the reduced Helmholtz equation in the frequency-domain have been extensively studied in the literature, see for example (Niwa, Kobayashi and Kitahura, 1982). However, in many engineering problems certain quantities in the list above are not directly specified or measured and this leads to inverse problem formulations which are discussed in the next subsection.

1.3 Inverse problems

In our everyday life we are constantly dealing with inverse and ill-posed problems, e.g. inverse scattering for determining an obstacle from the knowledge of the far field pattern, electrocardiography for estimating epicardial potential distribution from that on the body surface, etc. Usually, the inverse problem implies identification of causes from known desirable or observable effects. This usually leads to an ill-posed problem which either has no solution in the desired class, or has many (two or more) solutions, or the solution procedure is unstable (i.e. arbitrarily small errors in the measurement data may lead to indefinitely large errors in the solutions). Most difficulties in solving ill-posed problems are caused

1.4 Numerical methods for discretising partial differential equations

by the solution instability. Therefore, the term "ill-posed problems" is often used for unstable problems.

Inverse problems of mathematical physics can be classified into groups depending on which functions are unknown and some other criteria, see (Kabanikhin, 2008),

1. The inverse problem is called a boundary/initial problem, if it is required to determine a boundary/initial condition.
2. The inverse problem is called a source/force problem, if it is required to determine the source/force.
3. The inverse problem is called a coefficient inverse problem (or medium problem), if it is required to reconstruct coefficients present in the governing equation or in the boundary conditions.

It should be noted that this classification is still incomplete. There are cases where both initial and boundary conditions are unknown, and cases where the domain (or a part of its boundary) is unknown.

The unknown conditions are to be determined with the assistance of an over specified condition. Noise becomes an important concern in the solution of most inverse problems, as the over specified condition is usually provided by using experimental field data.

1.4 Numerical methods for discretising partial differential equations

1.4.1 Boundary Element Method (BEM)

The boundary element method (BEM) attempts to use the given boundary conditions to fit boundary values into an integral equation, rather than values throughout the space defined by a partial differential equation. Once this is done, in the post-processing stage, the integral equation can then be used again to calculate numerically the solution directly at any desired point in the interior of the solution domain. The BEM has been applied in many areas of engineering and science

1.4 Numerical methods for discretising partial differential equations

including fluid mechanics, acoustics, electromagnetics and fracture mechanics, see (Wrobel, 2002) and (Aliabadi, 2002).

However, the BEM can only be applicable to problems for which the fundamental solution of the governing equation is available explicitly. These usually involve fields in linear homogeneous media. This places considerable restrictions on the range and generality of problems to which boundary elements can usefully be applied. Nonlinearities can be included in the formulation, although they will generally introduce volume integrals which then require the volume to be discretised before solution can be attempted, removing one of the most often cited advantages of BEM.

The theoretical treatment of the BEM in terms of order and convergence is rather sophisticated and it usually employs the Galerkin method of approximation, see e.g. (Schatz, Thomee and Wendland, 1990).

1.4.2 Finite Difference Method (FDM)

The FDM is a numerical method for approximating the solutions to differential equations using finite difference equations to approximate derivatives, see (Thomee, 2001). These derivative approximations are based on Taylor's series expansions hence their order of convergence can easily be obtained. One possible drawback of the FDM is that it cannot easily be applied on curved grids in irregular and arbitrary shaped domains.

1.4.3 Finite Element Method (FEM)

Nowadays, the FEM has become one of the most frequently used method for solving partial differential equations, see (Dhatt, Touzot and Lefrancois, 2012; Thomee, 2001). In the FEM, the solution domain is discretised by dividing it into non-overlapping elements of arbitrary shape and size. Within each element a certain number of nodes are defined at which the unknown nodal values are to be determined. These nodal values are used to approximate the exact solution by a finite linear combination of local basis functions.

Advantages: The computation is divided into discrete elements which may have complex shapes. Very flexible for complex geometries. Works well for even

1.4 Numerical methods for discretising partial differential equations

order differential equations. Has optimal order convergence for the wave equation, (Rauch, 1985).

Disadvantages: Programming is more complicated than the FDM.

1.4.4 Error estimates and order of convergence

Error estimates give a measure of the accuracy of a given numerical method by quantifying how fast the error between the numerical and exact solution decreases, in some norm $\|\cdot\|$, as we decrease the mesh size $h > 0$. They typically state that the accuracy error $\|u - u_h\|$ is of order $O(h^\alpha)$, i.e. $\|u - u_h\| \approx Ch^\alpha$, where $C > 0$ is some constant and $\alpha > 0$ is the order of convergence, or the convergence rate. From this estimate, one can obtain the rate $\alpha = \frac{\ln(\|u - u_{h_2}\|/\|u - u_{h_1}\|)}{\ln(h_2/h_1)}$ from two mesh sizes $h_1 > h_2$.

In the FDM, the order of convergence can easily be obtained from Taylor's series expansion and an example of such a derivation is provided in the Appendix A. Typically, forward and backward finite differences are of order 1, whilst central finite differences are of order 2.

In contrast to the FDM, the FEM (and BEM) uses a weak formulation based on integration rather than differentiation. Moreover, piecewise polynomial approximations of order $p \in \mathbb{N}$ are made for the unknown primary and secondary variables appearing in the resulting integrands. For elliptic operators, in general one has that the order of convergence of the FEM (and BEM) is $\alpha = p + 1$, see (Juhl, 1998; Wendland, 1983; Zinkiewicz, Taylor and Zhu, 2005). Thus, for example, for the Helmholtz equation, for a piecewise constant approximation one has that the order of the FEM (or BEM) is 1, whilst for a piecewise linear approximation the order is 2.

For the hyperbolic equations, a space-time FEM was introduced in (French, 1993) to solve the Dirichlet direct and well-posed problem for the wave equation and the main theoretical result obtained was that, for piecewise linear interpolants, the asymptotic rate of convergence of the error $\|u - u_h\|$ in the H^1 -norm consisting of space- and time-derivatives is $O(h^{1/2})$, i.e. the order is $1/2$.

As for as the BEM is concerned, for hyperbolic equations convergence results and error estimates are less known and various aspects are further discussed in

(Costabel, 2004; Ha-Duong, 2003).

1.5 Regularization methods

The solution of an inverse problem is usually recast as the minimization of an appropriate cost functional. However, inverse problems are in general ill-posed and this generates instability. Regularization methods are commonly used for restoring the stability of ill-posed problems. Some regularization methods are given by:

- A simple form of regularization, generally termed Tikhonov regularization after academician Andrey Nikolayevich Tikhonov, is essentially a trade-off between fitting the data and reducing a norm of the solution. For example, the Tikhonov regularised solution of the system of linear algebraic equations $A\underline{x} = \underline{b}$ is given by, see (Alifanov, Artyukhin and Rumyantsev, 1995),

$$\min_{\underline{x} \in \mathbb{R}^n} \{ \|\underline{A}\underline{x} - \underline{b}\|^2 + \lambda \|D_k \underline{x}\|^2 \}, \quad (1.1)$$

gives

$$\underline{x}_\lambda = (A^T A + \lambda D_k^T D_k)^{-1} A^T \underline{b}, \quad (1.2)$$

where D_k is the regularization derivative operator of order $k = 0, 1, 2, \dots$, and $\lambda > 0$ is the regularization parameter. The order k of the regularization matrix D_k is related to the C^k -smoothness of the solution which may (or may not) be *a priori* known or assumed, (Philips, 1962; Twomey, 1963). Thus, the order k penalises the k th-order derivative, i.e. continuity class C^0 (allows wiggles) for $k = 0$, first-order smoothness class C^1 (penalises gradient) for $k = 1$, second-order smoothness class C^2 (penalises curvature)

for $k = 2$, etc. In particular,

$$\begin{aligned}
 D_0 &= \begin{pmatrix} 1 & 0 & 0 & 0 & \dots & 0 \\ 0 & 1 & 0 & 0 & \dots & 0 \\ \dots & \dots & \dots & \dots & \dots & \dots \\ 0 & 0 & \dots & 0 & 0 & 1 \end{pmatrix}, \quad D_1 = \begin{pmatrix} 1 & -1 & 0 & 0 & \dots & 0 \\ 0 & 1 & -1 & 0 & \dots & 0 \\ \dots & \dots & \dots & \dots & \dots & \dots \\ 0 & 0 & \dots & 0 & 1 & -1 \end{pmatrix}, \\
 D_2 &= \begin{pmatrix} 1 & -2 & 1 & 0 & 0 & \dots & 0 \\ 0 & 1 & -2 & 1 & 0 & \dots & 0 \\ \dots & \dots & \dots & \dots & \dots & \dots & \dots \\ 0 & 0 & \dots & 0 & 1 & -2 & 1 \end{pmatrix}. \tag{1.3}
 \end{aligned}$$

In Chapters 2 and 3, we will use the Tikhonov regularization method of zeroth-, first- and second-order for solving linear inverse problems and in Chapter 6 for non-linear inverse problems.

- Truncated Singular value decomposition (TSVD) solution of the system of linear algebraic equations $A\underline{x} = \underline{b}$ is, see (Hansen and O’Leary, 1993),

$$\underline{x} = \sum_{i=1}^{n_t} \frac{u_i^T \underline{b}}{\sigma_i} v_i, \tag{1.4}$$

where the singular vectors \underline{u}_i and \underline{v}_i are orthonormal and the singular values σ_i are non-negative non-increasing numbers, i.e. $\sigma_1 \geq \sigma_2 \geq \dots \geq \sigma_n \geq 0$. Moreover, we have truncated the sum in (1.4) at a threshold level $n_t \leq n$, in order to avoid division with small singular values in (1.4) and thus prevent solution becoming unstable.

- Landweber and the conjugate gradient methods (CGM), see (Engl, Hanke and Neubauer, 2000), are iterative regularization methods which will be applied to solving the inverse force problem in Chapter 5.

All the above regularization methods require selecting proper regularization parameters for achieving accurate and stable numerical results. The choice of regularization parameters can be made according to certain criteria, e.g.,

- The discrepancy principle criterion, see (Alifanov, Artyukhin and Rumyantsev, 1995).

- The generalized cross-validation (GSV) criterion, see (Golub, Heath and Wahba, 1979).
- The L-curve criterion, see (Hansen, 2001). The L-curve is one of the most convenient tools for the analysis of discrete ill-posed problems and it will be used quite a lot in the thesis. The method is actually a plot for many positive regularization parameters of the norm $\|\underline{x}_\lambda\|$ of the regularised solution versus the corresponding residual norm $\|A\underline{x}_\lambda - b\|$. If such a curve has an L-shape then one can pick the regularization parameter at the corner of it (or more rigorously, at the point of maximum curvature). Generally speaking, the right of the curve corresponds to large values of λ which over-smooth the solution whilst the left of the curve corresponds to low values of λ which under-smooth the solution. Then, as a compromise, one can pick the value of λ at the corner where these two regions meet. It is also worth mentioning that there are counterexamples for which the L-curve fails to provide a clearly defined corner or no corner at all, see for more details (Hanke, 1996; Hansen, 2001; Vogel, 1996).

1.6 Outline of the thesis

The determination of an unknown spacewise dependent force function acting on a vibrating string from over-specified Cauchy boundary data is investigated numerically using the BEM combined with a regularized method of separating variables in Chapter 2.

Next, in Chapters 3 and 4 we consider inverse force problems for the wave equation which consists of determining the unknown space or time-dependent force function from additional data, respectively. In the spacewise dependent case the additional data is Cauchy boundary data, whilst in the time-dependent case the additional data is represented by a time-dependent measurement of an integral space average of the displacement. The problems are linear, but ill-posed. The solution may exist and is unique, but it does not depend continuously on the input measurement data which is subject to noise. Numerically, the FDM

combined with the Tikhonov regularization are employed in order to obtain a stable solution.

The FDM combined with iterative regularization is further applied in Chapter 5 to determine the displacement and the space-dependent force acting on a vibrating structure from measured final or time-average displacement in the wave equation. As in previous chapters, the problems are linear, but they are still ill-posed since small errors in the input data cause large errors in the output force. The stability is restored by stopping the iterations according to the discrepancy principle criterion once the residual becomes close to the amount of noise.

In Chapter 6, nonlinear inverse problems in which the unknown force depends on the displacement are investigated. They consist of nonlinear identifications of the space-dependent potential and/or damping coefficients in the wave equation from Cauchy boundary data. The FDM combined with the nonlinear Tikhonov regularization method is employed. The minimization is performed using the Matlab toolbox routine *lsqnonlin*.

Finally, in Chapter 7, general conclusions and suggestions for possible future work are given.

Chapter 2

Determination of a space-dependent force function from Cauchy data

2.1 Introduction

When it comes to mathematical modelling of wave phenomena probably the most investigated are the direct and inverse acoustic scattering problems, see e.g. (Colton and Kress, 2013).

On the other hand, inverse source/force problems for the wave equation have been less investigated. It is the objective of this chapter to investigate such an inverse force problem for the hyperbolic wave equation. The initial attempt is performed for the case of a one-dimensional vibrating string, but we have in mind extensions to higher dimensions in an immediate future work. The forcing function is assumed to depend only upon the single space variable in order to ensure uniqueness of the solution. The theoretical basis for our numerical investigation is given in (Cannon and Dunninger, 1970) where the uniqueness of solution of the inverse spacewise dependent force function for the one-dimensional wave equation has been established. In (Cannon and Dunninger, 1970) conditions to be satisfied by the force function in order to ensure continuous dependence upon the data were also given and furthermore, two methods based on linear programming and the least-squares method were proposed. However, no numerical results were presented and it is the main purpose of our study to develop an efficient numerical solution for this inverse linear, but ill-posed problem.

Because the wave speed is assumed constant, the most suitable numerical method for discretising the wave equation in this case is the boundary element method (BEM), see (Benmansour, Ouazar and Brebbia, 1988; Benmansour, 1993; Benmansour, Ouazar and Wrobel, 1997). Moreover, because an inhomogeneous source/force term is present in the governing equation, it is convenient to exploit the linearity of the problem by applying the principle of superposition. This recasts into splitting the original problem into a direct problem with no force, and an inverse problem with force, but with homogeneous boundary and initial conditions. This is explained in Section 2.2 where the mathematical formulation of the inverse problem under investigation is also given. Whilst the former problem requires a numerical solution such as the BEM, as described in Section 2.3, the latter problem is amenable to a separation of variables series solution with unknown coefficients. Upon truncating this series, the problem recasts as an ordinary linear least-squares problem which has to be regularized since the resulting system of linear equations is ill-conditioned, the original problem being ill-posed. The choice of the regularization parameter introduced by this technique is important for the stability of the numerical solution and in our study this is based on the L-curve criterion, (Hansen, 2001). All this latter analysis is described in detail in Section 2.4. Numerical results are illustrated and discussed in Sections 2.5 and 2.6 and conclusions are provided in Section 2.7.

2.2 Mathematical formulation

The governing equation for a vibrating string of length $L > 0$ acted upon by a space-dependent force $f(x)$ is given by the one-dimensional wave equation

$$u_{tt} = c^2 u_{xx} + f(x), \quad x \in (0, L) \times (0, \infty), \quad (2.1)$$

where u represents the displacement and $c > 0$ is the speed of sound.

Equation (2.1) has to be solved subject to the initial conditions

$$u(x, 0) = \varphi(x), \quad x \in [0, L], \quad (2.2)$$

$$u_t(x, 0) = \psi(x), \quad x \in [0, L], \quad (2.3)$$

2.2 Mathematical formulation

where φ and ψ represent the initial displacement and velocity, respectively, and to the Dirichlet boundary conditions

$$u(0, t) = P_0(t), \quad t \in [0, \infty), \quad (2.4)$$

$$\mu u(L, t) + (1 - \mu)u_x(L, t) = P_L(t), \quad t \in [0, \infty), \quad (2.5)$$

where $\mu \in \{0, 1\}$ with $\mu = 1$ for the Dirichlet boundary condition and $\mu = 0$ for the Neumann boundary condition. In (2.4) and (2.5), P_0 and P_L are given functions satisfying the compatibility conditions

$$P_0(0) = \varphi(0), \quad P_L(0) = \mu\varphi(L) + (1 - \mu)\varphi'(L). \quad (2.6)$$

If the force f is given, then equations (2.1)-(2.6) form a direct well-posed problem for the displacement $u(x, t)$ which can be solved using the BEM for example, (Benmansour, 1993). However, if the force function f is unknown then clearly the above equations are not sufficient to determine the pair solution $(u(x, t), f(x))$. Then, as suggested in (Cannon and Dunninger, 1970), we supply the above system of equations with the measurement of the flux tension of the string at the end $x = 0$, namely

$$u_x(0, t) = q_0(t), \quad t \in [0, T], \quad (2.7)$$

where q_0 is a given function over a time of interest $T > 0$. Then the inverse problem under investigation requires determining the pair solution $(u(x, t), f(x))$ satisfying equations (2.1)-(2.7). Remark that we have to restrict f to depend on x only since otherwise, if f depends on both x and t , we can always add to $u(x, t)$ any function of the form $t^2x^2(x-L)^2U(x, t)$ with arbitrary $U \in C^{2,1}([0, L] \times [0, \infty))$ and still obtain another solution satisfying (2.1)-(2.7). Note that the unknown force $f(x)$ depends on the space variable x , whilst the additional measurement (2.7) of the flux $q_0(t)$ depends on the time variable t . It is worth nothing that a corresponding inverse spacewise-dependent source identification problem given by equations (2.2), (2.4)-(2.7) also arises for the heat equation $u_t = u_{xx} + f(x)$, see (Cannon, 1968).

It has been shown in (Cannon and Dunninger, 1970) that the problem (2.1)-(2.7) has at most one solution, i.e. the uniqueness holds.

2.3 The boundary element method (BEM) for solving the direct problem (2.9)-(2.13)

Due to the linearity of the inverse problem (2.1)-(2.7) it is convenient to split it into the form, (Cannon and Dunninger, 1970),

$$u = v + w, \quad (2.8)$$

where v satisfies the well-posed direct problem

$$v_{tt} = c^2 v_{xx}, \quad (x, t) \in (0, L) \times (0, \infty), \quad (2.9)$$

$$v(x, 0) = \varphi(x), \quad x \in [0, L], \quad (2.10)$$

$$v_t(x, 0) = \psi(x), \quad x \in [0, L], \quad (2.11)$$

$$v(0, t) = P_0(t), \quad t \in [0, \infty), \quad (2.12)$$

$$\mu v(L, t) + (1 - \mu)v_x(L, t) = P_L(t), \quad t \in [0, \infty). \quad (2.13)$$

and (w, f) satisfies the ill-posed inverse problem

$$w_{tt} = c^2 w_{xx} + f(x), \quad (x, t) \in (0, L) \times (0, \infty), \quad (2.14)$$

$$w(x, 0) = w_t(x, 0) = 0, \quad x \in [0, L], \quad (2.15)$$

$$w(0, t) = 0, \quad t \in [0, \infty), \quad (2.16)$$

$$\mu w(L, t) + (1 - \mu)w_x(L, t) = 0, \quad t \in [0, \infty), \quad (2.17)$$

$$w_x(0, t) = q_0(t) - v_x(0, t), \quad t \in [0, T]. \quad (2.18)$$

Observe that we could also control the Dirichlet data (2.4) instead of the Neumann data (2.7) and this will also be addressed in Subsection 2.6. We remark that the solution of the direct and well-posed problem (2.9)-(2.13) has to be found numerically, say using the BEM, as described in the next section.

2.3 The boundary element method (BEM) for solving the direct problem (2.9)-(2.13)

The development of the BEM for the one-dimensional wave equation (2.9) is based on multiplying it with the fundamental solution, (Morse and Feshbach, 1953, p.893),

$$u^*(x, t; \xi, \tau) = -\frac{1}{2c}H(c(t - \tau) - |x - \xi|), \quad (2.19)$$

2.3 The boundary element method (BEM) for solving the direct problem (2.9)-(2.13)

where H is the Heaviside function and integrate the resulting equation over the solution domain. Afterwards, using integration by parts twice (with respect to both x and t) we transfer the space and time partial derivatives from the function u to the fundamental solution u^* . Finally, using that the fundamental solution (2.19) satisfies

$$u_{tt}^* - c^2 u_{xx}^* = -\delta(x - \xi)\delta(t - \tau), \quad (2.20)$$

and the properties of the Dirac delta function δ we obtain the boundary integral equation, (Benmansour, 1993, Sect. 3.4.2),

$$\begin{aligned} 2v(\xi, t) = & v(\xi - ct, 0) + v(\xi + ct, 0) + \frac{1}{c} \int_{\xi - ct}^{\xi + ct} v_t(x, 0) dx \\ & + v(L, t - (L - \xi)/c) + c \int_0^{t - (L - \xi)/c} v_x(L, \tau) d\tau + v(0, t - \xi/c) \\ & - c \int_0^{t - \xi/c} v_x(0, \tau) d\tau, \quad (\xi, t) \in (0, L) \times (0, \infty). \end{aligned} \quad (2.21)$$

Equation (2.21) is valid if

$$v(0, 0) = v(L, 0) = 0, \quad i.e. \quad \varphi(0) = \varphi(L) = 0. \quad (2.22)$$

Otherwise, if this condition is not satisfied then we can work with the modified function

$$\tilde{v}(x, t) = v(x, t) - \frac{\varphi(L) - \varphi(0)}{L} x - \varphi(0) \quad (2.23)$$

which satisfies the wave equation (2.9) and $\tilde{v}(0, 0) = \tilde{v}(L, 0) = 0$. Alternatively, if (2.22) is not satisfied, then equation (2.21) is only valid for $\xi - ct \neq 0$ and $\xi + ct \neq L$, as singularities will occur when the peak of the Dirac delta function coincides with one of the limits of the integrals involved, i.e. when $\xi = ct$ or $\xi = L - ct$. However, these singular integrals may be evaluated analytically as described in (Benmansour, 1993, Sect. 3.4.2).

It is very important to remark that in expression (2.21) the time and space coordinates must be within the domain $[0, L] \times [0, \infty)$ and the integrals must have their lower limit of integration smaller than the upper one. If any of these conditions are not satisfied the integrals are taken to be zero.

Equation (2.21) yields the interior solution $v(\xi, t)$ for $(\xi, t) \in (0, L) \times (0, \infty)$ of the wave equation (2.9) in terms of the initial and boundary data. In general,

2.3 The boundary element method (BEM) for solving the direct problem (2.9)-(2.13)

at a boundary point only one Dirichlet, Neumann or Robin boundary condition is imposed and the first step of the BEM methodology requires the evaluation of the missing (unspecified) boundary data. For this, we need first to evaluate the boundary integral equation (2.21) at the end points $\xi \in \{0, L\}$. A careful limiting process yields, (Benmansour, 1993),

$$\begin{aligned} v(0, t) &= v(ct, 0) + \frac{1}{c} \int_0^{ct} v_t(x, 0) dx + v(L, t - L/c) \\ &\quad + c \left[\int_0^{t-L/c} v_x(L, \tau) d\tau - \int_0^t v_x(0, \tau) d\tau \right], \quad t \in (0, \infty), \end{aligned} \quad (2.24)$$

$$\begin{aligned} v(L, t) &= v(0, t - L/c) + v(L - ct, 0) + \frac{1}{c} \int_{L-ct}^L v_t(x, 0) dx \\ &\quad + c \left[\int_0^t v_x(L, \tau) d\tau - \int_0^{t-L/c} v_x(0, \tau) d\tau \right], \quad t \in (0, \infty). \end{aligned} \quad (2.25)$$

These equations also hold under the assumption (2.22).

Since we want to calculate $v_x(0, t)$ only for $t \in [0, T]$, let us restrict the boundary integral equations (2.24) and (2.25) to the time interval $[0, T]$.

For the numerical discretisation of the boundary integral equations (2.24) and (2.25) we divide the time interval $[0, T]$ into a series of N small boundary elements $[t_{j-1}, t_j]$ for $j = \overline{1, N}$, where for a uniform discretisation $t_j = jT/N$ for $j = \overline{0, N}$. Similarly, we divide the space interval $[0, L]$ into a series of M small cells $[x_{i-1}, x_i]$ for $i = \overline{1, M}$, where for a uniform discretisation $x_i = iL/M$ for $i = \overline{0, M}$. We then approximate the boundary and initial values as

$$v(0, \tau) = \sum_{j=1}^N \phi^j(\tau) v_j^0, \quad v(L, \tau) = \sum_{j=1}^N \phi^j(\tau) v_j^L, \quad \tau \in [0, T], \quad (2.26)$$

$$v_x(0, \tau) = \sum_{j=1}^N \theta^j(\tau) v_j'^0, \quad v_x(L, \tau) = \sum_{j=1}^N \theta^j(\tau) v_j'^L, \quad \tau \in [0, T], \quad (2.27)$$

$$v(x, 0) = \sum_{i=1}^M \psi_i(x) u_0^i, \quad v_t(x, 0) = \sum_{i=1}^M \psi_i(x) v_0^i, \quad x \in [0, L], \quad (2.28)$$

where

$$v_j^0 := v(0, t_j), \quad v_j^L := v(L, t_j), \quad v_j'^0 := v_x(0, t_j), \quad v_j'^L := v_x(L, t_j), \quad j = \overline{1, N}, \quad (2.29)$$

$$u_0^i := v(x_i, 0), \quad v_0^i := v_t(x_i, 0), \quad i = \overline{1, M}. \quad (2.30)$$

2.3 The boundary element method (BEM) for solving the direct problem (2.9)-(2.13)

The functions ϕ^j , θ^j and ψ_i are interpolant, e.g. piecewise polynomial, functions chosen such that $\phi^j(t_n) = \theta^j(t_n) = \delta_{jn}$ for $j, n = \overline{1, N}$, $\psi_i(x_m) = \delta_{im}$ for $i, m = \overline{1, M}$, where δ_{jn} is the Kronecker delta symbol. For example, if $\theta^j(\tau)$ is a piecewise constant function then

$$\theta^j(\tau) = \chi_{(t_{j-1}, t_j]}(\tau) = \begin{cases} 1 & \text{if } t \in (t_{j-1}, t_j], \\ 0 & \text{otherwise,} \end{cases} \quad (2.31)$$

where $\chi_{(t_{j-1}, t_j]}$ represents the characteristic function of the interval $(t_{j-1}, t_j]$. Thus $v_x(0, \tau) = v_j^0$ for $\tau \in (t_{j-1}, t_j]$, etc. We also have that $\int_0^{t_n} \theta^j(\tau) d\tau = t_j - t_{j-1}$ for $j = \overline{1, n}$.

Observe that the above numerical BEM discretisation of the space-time boundary integral equations (2.24) and (2.25) is global in time, i.e. the solution is computed in one step for the entire time interval $(0, T]$. Various aspects of the BEM for time-dependent hyperbolic problems are further discussed in (Costabel, 2004). For the scalar wave equation in one or higher-dimension, where the boundary integrals are given in terms retarded potentials their analysis in terms of convergence and stability is based on variational methods, (Ha-Duong, 2003). However, for our particular numerical BEM described above (which is similar to the one developed in the PhD thesis of (Benmansour, 1993)) this sophisticated theoretical framework does not seem immediately applicable. As such, there are no theoretical estimates in terms of M and N yet available but, nevertheless, this investigation would be of interest to be addressed in a future work.

Using the approximations (2.26)-(2.30) into the equations (2.24) and (2.25) we obtain, for $n = \overline{1, N}$,

$$\begin{aligned} & v_n^0 + cv_n^0 \int_0^{t_n} \theta^n(\tau) d\tau - \phi^n(t_n - L/c)v_n^L - cv_n^L \int_0^{t_n - L/c} \theta^n(\tau) d\tau \\ &= \sum_{j=1}^{n-1} \phi^j(t_n - L/c)v_j^L + \sum_{i=1}^M \psi_i(ct_n)u_0^i + c \sum_{j=1}^{n-1} v_j^L \int_0^{t_n - L/c} \theta^j(\tau) d\tau \\ & - c \sum_{j=1}^{n-1} v_j^0 \int_0^{t_n} \theta^j(\tau) d\tau + \frac{1}{c} \sum_{i=1}^M v_0^i \int_0^{ct_n} \psi_i(x) dx =: F \end{aligned} \quad (2.32)$$

2.3 The boundary element method (BEM) for solving the direct problem (2.9)-(2.13)

and

$$\begin{aligned}
& v_n^L - cv_n'^L \int_0^{t_n} \theta^n(\tau) d\tau - \phi^n(t_n - L/c)v_n^0 + cv_n'^0 \int_0^{t_n - L/c} \theta^n(\tau) d\tau \\
&= \sum_{j=1}^{n-1} \phi^j(t_n - L/c)v_j^0 + \sum_{i=1}^M \psi_i(L - ct_n)u_0^i + c \sum_{j=1}^{n-1} v_j'^L \int_0^{t_n} \theta^j(\tau) d\tau \\
&- c \sum_{j=1}^{n-1} v_j'^0 \int_0^{t_n - L/c} \theta^j(\tau) d\tau + \frac{1}{c} \sum_{i=1}^M v_0^i \int_{L - ct_n}^L \psi_i(x) dx =: G. \tag{2.33}
\end{aligned}$$

Denoting

$$A = c \int_0^{t_n} \theta^n(\tau) d\tau, \quad B = \phi^n(t_n - L/c), \quad D = c \int_0^{t_n - L/c} \theta^n(\tau) d\tau, \tag{2.34}$$

equations (2.32) and (2.33) can be rewritten as

$$v_n^0 + Av_n'^0 - Bv_n^L - Dv_n'^L = F, \tag{2.35}$$

$$v_n^L - Av_n'^L - Bv_n^0 + Dv_n'^0 = G. \tag{2.36}$$

At each time t_n for $n = \overline{1, N}$, the system of equations (2.35) and (2.36) represents a time marching BEM technique in which the values of F and G are expressed in terms of the previous values of the solution at the times t_1, \dots, t_{n-1} . Note that upon the imposition of the initial conditions (2.10) and (2.11) we know

$$v_0^i = v(x_i, 0) = \varphi(x_i), \quad v_0^i = v_t(x_i, 0) = \psi(x_i), \quad i = \overline{1, M}. \tag{2.37}$$

The system of equations (2.35) and (2.36) contains 2 equations with 4 unknowns. Two more equations are known from the boundary conditions (2.12) and (2.13), namely

$$v_n^0 = v(0, t_n) = P_0(t_n) =: P_0^n, \quad n = \overline{1, N}, \tag{2.38}$$

$$\mu v_n^L + (1 - \mu)v_n'^L = \mu v(L, t_n) + (1 - \mu)v_x(L, t_n) = P_L(t_n) =: P_L^n, \quad n = \overline{1, N}. \tag{2.39}$$

The solution of the system of equations (2.35), (2.36), (2.38) and (2.39) can be expressed explicitly at each time step t_n for $n = \overline{1, N}$ and is given by:

(a) For $\mu = 1$, i.e. the Dirichlet problem (2.9)-(2.13) in which equation (2.13) is given by

$$v(L, t) = P_L(t), \quad t \in [0, \infty), \tag{2.40}$$

2.3 The boundary element method (BEM) for solving the direct problem (2.9)-(2.13)

and equation (2.39) yields

$$v_n^L = P_L^n, \quad n = \overline{1, N}, \quad (2.41)$$

the unspecified boundary values are the Neumann flux values. Introduction of (2.38) and (2.41) into (2.35) and (2.36) yields the simplified system of two equations with two unknowns given by

$$Av_n'^0 - Dv_n'^L = F - P_0^n + BP_L^n =: \tilde{F}, \quad (2.42)$$

$$Dv_n'^0 - Av_n'^L = G - P_L^n + BP_0^n =: \tilde{G}. \quad (2.43)$$

Application of Cramer's rule immediately yields the solution

$$v_n'^0 = \frac{D\tilde{G} - A\tilde{F}}{D^2 - A^2}, \quad v_n'^L = \frac{A\tilde{G} - D\tilde{F}}{D^2 - A^2}. \quad (2.44)$$

(b) For $\mu = 0$, i.e. the mixed problem (2.9)-(2.13) in which equation (2.13) is given by

$$v_x(L, t) = P_L, \quad t \in [0, \infty) \quad (2.45)$$

and equation (2.39) yields

$$v_n'^L = P_L^n, \quad n = \overline{1, N}, \quad (2.46)$$

the unspecified boundary values are the Neumann data at $x = 0$ and the Dirichlet data at $x = L$. Introduction of (2.38) and (2.46) into (2.35) and (2.36) yields

$$Av_n'^0 - Bv_n'^L = F - P_0^n + DP_L^n =: \tilde{F}, \quad (2.47)$$

$$Dv_n'^0 + v_n'^L = G + BP_0^n + AP_L^n =: \tilde{G}. \quad (2.48)$$

This yields the solution

$$v_n'^0 = \frac{\tilde{F} + B\tilde{G}}{A + DB}, \quad v_n'^L = \frac{A\tilde{G} - D\tilde{F}}{A + DB}. \quad (2.49)$$

Alternatively, instead of employing a time-marching BEM it is also possible to employ a global BEM by assembling (2.32) and (2.33) as a full system of $2N$

2.3 The boundary element method (BEM) for solving the direct problem (2.9)-(2.13)

linear equations with $4N$ unknown $v_j^0, v_j^L, v_j'^0, v_j'^L$ for $j = \overline{1, N}$, namely,

$$\begin{aligned} & \sum_{j=1}^n \left[cv_j'^0 \int_0^{t_n} \theta^j(\tau) d\tau - cv_j'^L \int_0^{t_n-L/c} \theta^j(\tau) d\tau - \phi^j(t_n - L/c) v_j^L \right] \\ &= \sum_{i=1}^M \left[\psi_i(ct_n) u_0^i + \frac{1}{c} v_0^i \int_0^{ct_n} \psi_i(x) dx \right] - v_n^0, \quad n = \overline{1, N}, \end{aligned} \quad (2.50)$$

and

$$\begin{aligned} & \sum_{j=1}^n \left[cv_j'^L \int_0^{t_n} \theta^j(\tau) d\tau - cv_j'^0 \int_0^{t_n-L/c} \theta^j(\tau) d\tau + \phi^j(t_n - L/c) v_j^0 \right] \\ &= - \sum_{i=1}^M \left[\psi_i(L - ct_n) u_0^i + \frac{1}{c} v_0^i \int_{L-ct_n}^L \psi_i(x) dx \right] + v_n^L \quad n = \overline{1, N}. \end{aligned} \quad (2.51)$$

The other $2N$ equations are given by (2.38) and (2.39). Introduction of (2.38) and (2.39) into (2.50) and (2.51) finally results in a linear system of $2N$ algebraic equations with $2N$ unknowns which can be solved using a Gaussian elimination procedure.

Once all the boundary values have been determined accurately, the interior solution can be obtained explicitly using equation (2.21). This gives

$$\begin{aligned} 2v(\xi, t_n) &= \sum_{j=1}^n \left[\phi^j(t_n - (L - \xi)/c) v_j^L + \phi^j(t_n - \xi/c) v_j^0 \right] \\ &+ c \sum_{j=1}^n \left[v_j'^L \int_0^{t_n-(L-\xi)/c} \theta^j(\tau) d\tau - v_j'^0 \int_0^{t_n-\xi/c} \theta^j(\tau) d\tau \right] + \sum_{i=1}^M \left[\psi_i(\xi - ct_n) \right. \\ &\left. + \psi_i(\xi + ct_n) \right] u_0^i + \frac{1}{c} \sum_{i=1}^M v_0^i \int_{\xi-ct_n}^{\xi+ct_n} \psi_i(x) dx, \quad n = \overline{1, N}, \quad \xi \in (0, 1). \end{aligned} \quad (2.52)$$

In (2.52), for the piecewise constant interpolation (2.31),

$$\begin{aligned} \int_0^{t_n-\xi/c} \theta^j(\tau) d\tau &= H(t_n - t_{j-1} - \xi/c)(t_j - t_{j-1}), \\ \int_0^{t_n-(L-\xi)/c} \theta^j(\tau) d\tau &= H(t_n - t_{j-1} - (L - \xi)/c)(t_j - t_{j-1}). \end{aligned}$$

The flux $v_x(0, t)$ obtained numerically using the BEM is then introduced into (2.18) and the inverse problem (2.14)-(2.18) for the pair solution $(w(x, t), f(x))$ is solved using the method described in the next section.

2.4 Method for solving the inverse problem (2.14)-(2.18)

Due to the simple form of equation (2.14) with constant c , inhomogeneous force term $f(x)$ independent of t , and homogeneous initial and boundary conditions (2.15)-(2.17), for solving the inverse problem (2.14)-(2.18) it is convenient to use the method of separation of variables, (Tikhonov and Samarskii, 1963, pp. 97-99), which yields an approximate solution explicitly given by, (Cannon and Dunninger, 1970),

$$w_K(x, t; \underline{b}) = \frac{\sqrt{2}}{c^2} \sum_{k=1}^K \frac{b_k}{\lambda_k^2} (1 - \cos(c\lambda_k t)) \sin(\lambda_k x), \quad (x, t) \in [0, L] \times [0, \infty), \quad (2.53)$$

$$f_K(x) = \sqrt{2} \sum_{k=1}^K b_k \sin(\lambda_k x), \quad x \in (0, L), \quad (2.54)$$

where K is a truncation number and

$$\lambda_k = \begin{cases} \frac{k\pi}{L} & \text{if } \mu = 1, \\ \frac{(k-\frac{1}{2})\pi}{L} & \text{if } \mu = 0. \end{cases} \quad (2.55)$$

The coefficients $\underline{b} = (b_k)_{k=1, \overline{K}}$ are to be determined by imposing the additional boundary condition (2.18). This results in

$$q_0(t) - v_x(0, t) =: g(t) = \frac{\partial w_k}{\partial x}(0, t; \underline{b}) = \frac{\sqrt{2}}{c^2} \sum_{k=1}^K \frac{b_k}{\lambda_k} (1 - \cos(c\lambda_k t)), \quad t \in [0, T]. \quad (2.56)$$

In practice, the additional observation (2.7) comes from measurement which is inherently contaminated with errors. We therefore model this by replacing the exact data $q_0(t)$ by the noisy data

$$q_0^\epsilon(t_n) = q_0(t_n) + \epsilon, \quad n = \overline{1, N}, \quad (2.57)$$

2.4 Method for solving the inverse problem (2.14)-(2.18)

where ϵ are N random noisy variables generated (using the Fortran NAG routine G05DDF) from a Gaussian normal distribution with mean zero and standard deviation σ given by

$$\sigma = p\% \times \max_{t \in [0, T]} |q_0(t)|, \quad (2.58)$$

where $p\%$ represents the percentage of noise. The noisy data (2.57) also induces noise in g as given by

$$g^\epsilon(t_n) = q_0^\epsilon(t_n) - v_x(0, t_n) = g(t_n) + \epsilon, \quad n = \overline{1, N}. \quad (2.59)$$

Then we apply the condition (2.56) with g replaced by g^ϵ in a least-squares penalised sense by minimizing the Tikhonov functional

$$\mathcal{J}(\underline{b}) := \sum_{n=1}^N \left[\frac{\sqrt{2}}{c^2} \sum_{k=1}^K \frac{b_k}{\lambda_k} (1 - \cos(c\lambda_k t_n)) - g^\epsilon(t_n) \right]^2 + \lambda \sum_{k=1}^K b_k^2, \quad (2.60)$$

where $\lambda \geq 0$ is a regularization parameter to be prescribed according to some criterion, e.g. the L-curve criterion, (Hansen, 2001).

Denoting

$$\underline{g}^\epsilon = (g^\epsilon(t_n))_{n=\overline{1, N}}, \quad Q_{nk} = \frac{\sqrt{2}(1 - \cos(c\lambda_k t_n))}{c^2 \lambda_k}, \quad n = \overline{1, N}, \quad k = \overline{1, K}, \quad (2.61)$$

we can recast (2.60) in a compact form as

$$\mathcal{J}(\underline{b}) = \| Q\underline{b} - \underline{g}^\epsilon \|^2 + \lambda \| \underline{b} \|^2. \quad (2.62)$$

In general, $N \geq K$ and the minimization of (2.62) then yields the zeroth-order Tikhonov regularization solution

$$\underline{b}_\lambda = (Q^{tr}Q + \lambda I)^{-1} Q^{tr} \underline{g}^\epsilon. \quad (2.63)$$

Once \underline{b} has been found, the spacewise dependent force function is obtained using (2.54). Also, the displacement solution $u(x, t)$ is obtained using (2.8) and (2.53).

2.5 Numerical results and discussion

In this section, we illustrate and discuss the numerical results obtained using the combined BEM+Tikhonov regularization described in Sections 2.3 and 2.4.

For simplicity, we take $c = L = T = \mu = 1$ and in the BEM we use constant time and space interpolation functions. We consider an analytical solution given by

$$u(x, t) = \sin(\pi x) + t + \frac{t^2}{2}, \quad (x, t) \in [0, 1] \times [0, \infty), \quad (2.64)$$

$$f(x) = 1 + \pi^2 \sin(\pi x) \quad x \in [0, 1]. \quad (2.65)$$

This generates the input data (2.2)-(2.5) and (2.7) given by

$$u(x, 0) = \varphi(x) = \sin(\pi x), \quad u_t(x, 0) = \psi(x) = 1, \quad x \in [0, 1], \quad (2.66)$$

$$u(0, t) = P_0(t) = t + \frac{t^2}{2}, \quad u(1, t) = P_L(t) = t + \frac{t^2}{2}, \quad t \in [0, \infty), \quad (2.67)$$

$$u_x(0, t) = q_0(t) = \pi, \quad t \in [0, 1]. \quad (2.68)$$

First we investigate the performance of the BEM described in Section 2.3 to solve the direct well-posed problem (2.9)-(2.13) for the function $v(x, t)$. Remark that condition (2.22) is satisfied by the initial displacement $\varphi(x)$ in (2.66) hence, there is no need to employ the modified function (2.23). Also note that the direct problem for $v(x, t)$ satisfying equation (2.9) (with $c = 1$) subject to the initial conditions (2.66) and the Dirichlet boundary conditions (2.67) does not have a closed form analytical solution available.

Figure 2.1 shows the numerical results for $v_x(0, t)$, as a function of t , obtained using the BEM with various $M = N \in \{20, 40, 80\}$. From this figure a convergent numerical solution, independent of the mesh, is apparently obtained with the ℓ^2 -error between subsequent discretisations (20 and 40) and (40 and 80) being very small and decreasing from 0.0986 to 0.0697, respectively.

The numerical solution for $v_x(0, t)$ obtained at the points $(t_n)_{n=\overline{1, N}}$ is then input into equation (2.56) to determine the values for $g(t_n)$ and its noisy counterpart $g^\epsilon(t_n)$ given by (2.59) for $n = \overline{1, N}$.

2.5 Numerical results and discussion

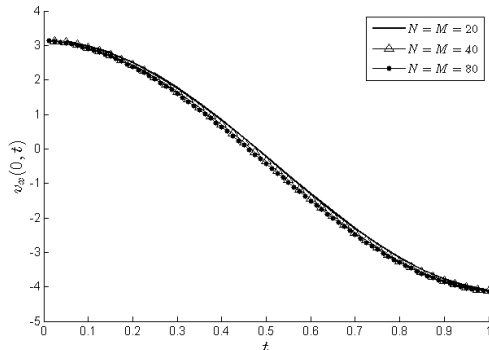


Figure 2.1: The numerical results for $v_x(0, t)$ obtained using the BEM with $M = N \in \{20, 40, 80\}$.

We turn now our attention to the pair solution (2.53) and (2.54) of the inverse problem (2.14)-(2.18). Since this problem is ill-posed we expect that the matrix Q in (2.61) having the entries

$$Q_{nk} = \frac{\sqrt{2}(1 - \cos(\frac{k\pi n}{N}))}{k\pi}, \quad n = \overline{1, N}, \quad k = \overline{1, K}, \quad (2.69)$$

will be ill-conditioned having singular values, i.e. the square roots of the eigenvalues of $Q^{tr}Q$, rapidly decaying to nearly zero. This behaviour is shown in Figure 2.2 which presents the normalised singular values $sv(k)/sv(1)$ for $k = \overline{1, K}$, for $N = 80$ and $K = 20$. The singular values have been calculated in MATLAB using the command `svd(Q)`. We can also calculate the condition number of the matrix Q defined as the ratio between the largest to the smallest singular values, using the MATLAB command `cond(Q) = sv(1)/sv(K)`. Table 2.1 shows the condition number of the matrix Q for various $N \in \{20, 40, 80\}$ and $K \in \{5, 10, 20\}$. We remark that the condition number is not affected by the increase in the number of measurements N , but it increases rapidly as the number K of basis functions increases.

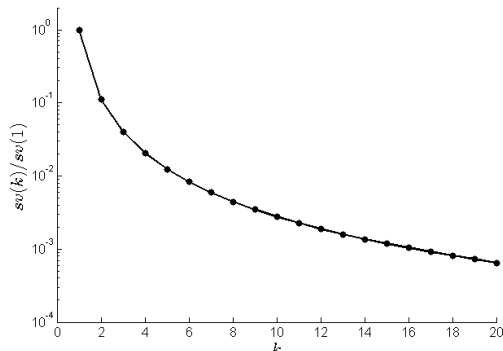


Figure 2.2: Normalised singular values $sv(k)/sv(1)$ for $k = \overline{1, K}$, for $N = 80$ and $K = 20$.

Table 2.1: Condition number of the matrix Q given by equation (2.69).

K	$N = 20$	$N = 40$	$N = 80$
5	82.62	82.25	82.28
10	371.6	367.0	365.7
20	$1.42E + 3$	$1.55E + 3$	$1.54E + 3$

Let us fix $N = 80$ and now proceed to solving the inverse problem (2.14)-(2.18) which based on the method of Section 2.4 has been reduced to solving the linear, but ill-conditioned system of equations

$$Q\underline{b} = \underline{g}^\epsilon. \tag{2.70}$$

Using the Tikhonov regularization method one obtains a stable solution given explicitly by equation (2.63) provided that the regularization parameter λ is suitably chosen.

2.5.1 Exact data

We first consider the case of exact data, i.e. $p = 0$ and hence $\epsilon = 0$ in (2.57) and (2.59). Then $\underline{g}^\epsilon = \underline{g}$ and the system of equations (2.70) becomes

$$Q\underline{b} = \underline{g}. \tag{2.71}$$

2.5 Numerical results and discussion

We remark that although we have no random noise added to the data q_0 , we still have some numerical noise in the data g in (2.56). This is given by the small discrepancy between the unavailable exact solution $v_x(0, t)$ of the direct problem and its numerical BEM solution obtained with $M = N = 80$ plotted in Figure 2.1. However, the rapid convergent behaviour shown in Figure 2.1 indicates that this numerical noise is small (at least in comparison with the large amount of random noise ϵ that we will be including in the data q_0 in Section 2.5.2).

Figure 2.3 shows the retrieved coefficient vector $\underline{b} = (b_k)_{k=1, \overline{K}}$ for $K = 20$ obtained using no regularization, i.e. $\lambda = 0$, in which case (2.63) produces the least-squares solution

$$\underline{b} = (Q^{tr} Q)^{-1} Q^{tr} \underline{g} \quad (2.72)$$

of the system of equations (2.70).

Note that the analytical values for the sine Fourier series coefficients are given by

$$b_k = \sqrt{2} \int_0^1 f(x) \sin(k\pi x) dx = \sqrt{2} \int_0^1 (1 + \pi^2 \sin(\pi x)) \sin(k\pi x) dx$$

which gives

$$b_k = \begin{cases} \frac{2\sqrt{2}}{\pi} + \frac{\pi^2}{\sqrt{2}} \simeq 7.8791 & \text{if } k = 1, \\ 0 & \text{if } k = \text{even}, \\ \frac{2\sqrt{2}}{k\pi} & \text{if } k = \text{odd} \geq 3. \end{cases} \quad (2.73)$$

By inspecting Figure 2.3 it appears that the leading term b_1 is the most significant in the series expansions (2.53) and (2.54). These expansions give the solutions $f(x)$ and $u(x, t)$ (via (2.8)) which are plotted in Figures 2.4 and 2.5, respectively. From these figures it can be seen that accurate numerical solutions are obtained.

2.5 Numerical results and discussion

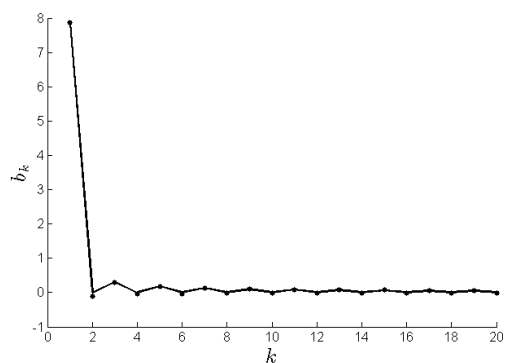


Figure 2.3: The numerical solution (...) for $(b_k)_{k=1, \overline{K}}$ for $K = 20$, $N = 80$, obtained with no regularization, i.e. $\lambda = 0$, for exact data, in comparison with the exact solution (2.73) (—).

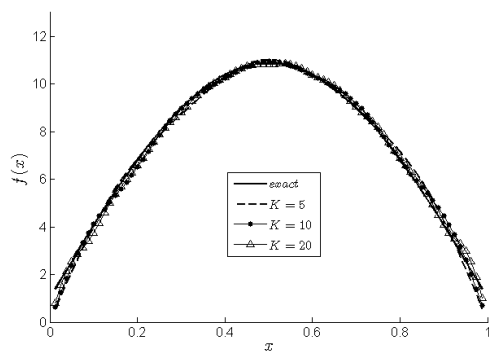


Figure 2.4: The exact solution (2.65) for $f(x)$ in comparison with the numerical solution (2.54) for various $K \in \{5, 10, 20\}$, no regularization, for exact data.

2.5 Numerical results and discussion

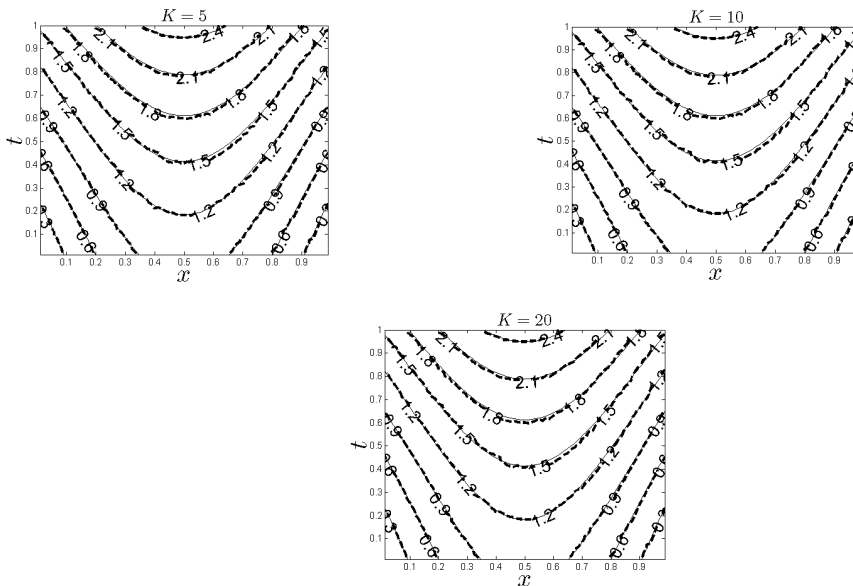


Figure 2.5: The numerical solution (---) for $u(x,t)$ obtained with various $K \in \{5, 10, 20\}$, no regularization, for exact data, in comparison with the exact solution (2.64) (—).

2.5.2 Noisy data

In order to investigate the stability of the numerical solution we include some ($p\% = 1\%$) noise into the input data (2.7), as given by equation (2.57). The numerical solutions for $f(x)$ and $u(x,t)$ obtained for various values of $K \in \{5, 10, 20\}$ and no regularization are plotted in Figures 2.6 and 2.7, respectively. First, by inspecting Figures 2.5 and 2.7 it can be observed that there is little difference between the results for $u(x,t)$ obtained with and without noise and that there is very good agreement with the exact solution (2.64). It also means that the numerical solution for the displacement $u(x,t)$ is stable with respect to noise added in the input data (2.7). In contrast, in Figure 2.6 the unregularized numerical solution for $f(x)$ manifests instabilities as K increases. For K (small) the numerically retrieved solution is quite stable showing that taking a small number of basis functions in the series expansion (2.54) has a regularization effect. However, as K increases to 10 or 20 it can be clearly seen that oscillations start to appear.

2.5 Numerical results and discussion

Eventually, these oscillations will become highly unbounded, as K increases even further. In order to deal with this instability we employ the Tikhonov regularization which yields the solution (2.63). We fix $K = 20$ and we wish to alleviate the instability of the numerical solution for $f(x)$ shown by $(-\Delta-)$ in Figure 2.6 obtained with no regularization, i.e. $\lambda = 0$, for $p\% = 1\%$ noisy data. Including regularization we obtain the solution (2.63) whose accuracy error, as a function of λ , is plotted in Figure 2.8. This error has been calculated as $\|f_{\text{numerical}} - f_{\text{exact}}\| = \sqrt{\sum_{n=1}^N (f_{\text{numerical}}(t_n) - f_{\text{exact}}(t_n))^2}$. From Figure 2.8 it can be seen that the minimum of the error occurs around $\lambda = 10^{-1}$. Clearly, this argument cannot be used as a suitable choice for the regularization parameter λ in the absence of an analytical (exact) solution (2.65) being available. However, one possible criterion for choosing λ is given by the L-curve method, (Hansen, 2001), which plots the residual norm $\|Q\mathbf{b}_\lambda - \mathbf{g}^\epsilon\|$ versus the solution norm $\|\mathbf{b}_\lambda\|$ for various values of λ . This is shown in Figure 2.9 for various values of

$$\lambda \in \{10^{-3}, 5 \times 10^{-2}, 10^{-2}, 8 \times 10^{-2}, 6 \times 10^{-2}, 4 \times 10^{-2}, 2 \times 10^{-2}, 10^{-1}, 0.2, 0.3, \dots, 1\}.$$

The portion to the right of the curve corresponds to large values of λ which make the solution oversmooth, whilst the portion to the left of the curve corresponds to small values of λ which make the solution undersmooth. The compromise is then achieved around the corner region of the L-curve where the aforementioned portions meet. Figure 2.9 shows that this corner region includes the values around $\lambda = 10^{-1}$ which was previously found to be optimal from Figure 2.8.

Finally, Figure 2.10 shows the regularized numerical solution for $f(x)$ obtained with various values of the regularization parameter $\lambda \in \{10^{-2}, 10^{-1}, 10^0\}$ for $p\% = 1\%$ noisy data. From this figure it can be seen that the value of the regularization parameter λ can also be chosen by trial and error. By plotting the numerical solution for various values of λ we can infer when the instability starts to kick off. For example, in Figure 2.10, the value of $\lambda = 10^0$ is too large and the solution is oversmooth, whilst the value of $\lambda = 10^{-2}$ is too small and the solution is unstable. We could therefore inspect the value of $\lambda = 10^{-1}$ and conclude that this is a reasonable choice of the regularization parameter which balances the smoothness with the instability of the solution.

2.5 Numerical results and discussion

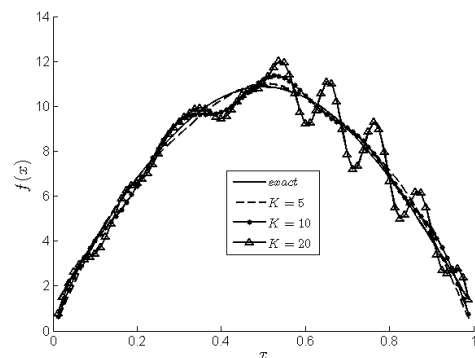


Figure 2.6: The exact solution (2.65) for $f(x)$ in comparison with the numerical solution (2.54) for various $K \in \{5, 10, 20\}$, no regularization, for $p\% = 1\%$ noisy data.

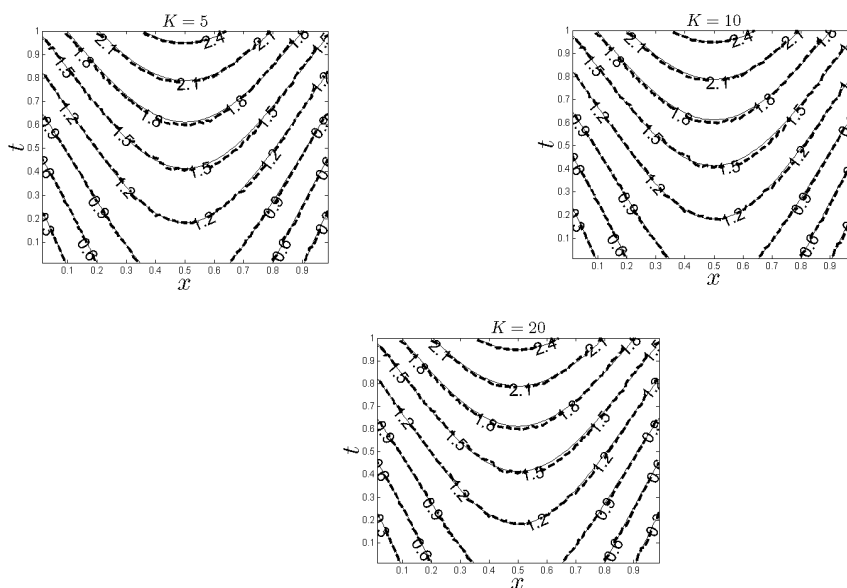


Figure 2.7: The numerical solution (---) for $u(x, t)$ obtained with various $K \in \{5, 10, 20\}$, no regularization, for $p\% = 1\%$ noisy data, in comparison with the exact solution (2.64) (—).

2.5 Numerical results and discussion

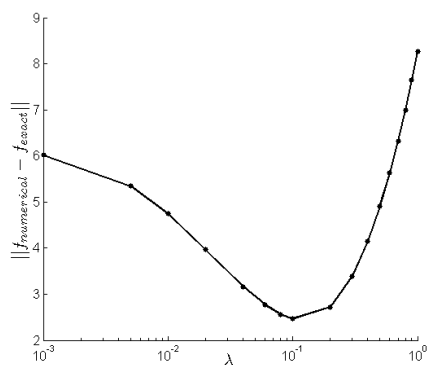


Figure 2.8: The accuracy error $\|f_{\text{numerical}} - f_{\text{exact}}\|$, as a function of λ , for $K = 20$ and $p\% = 1\%$ noise.

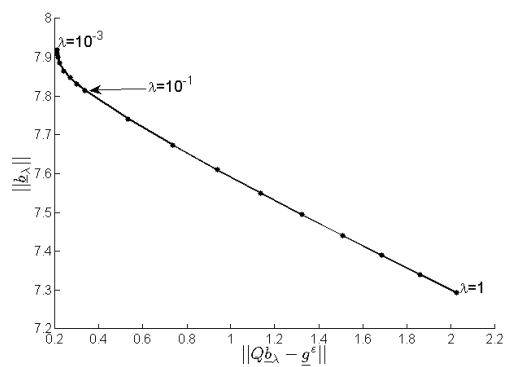


Figure 2.9: The L-curve for the Tikhonov regularization (2.62), for $K = 20$ and $p\% = 1\%$ noise.

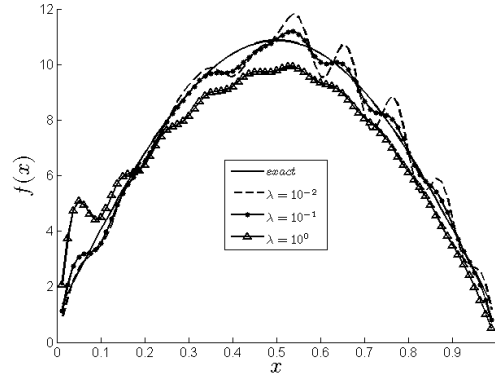


Figure 2.10: The exact solution (2.65) for $f(x)$ in comparison with the numerical solution (2.54), for $K = 20$, $p\% = 1\%$ noise, and regularization parameters $\lambda \in \{10^{-2}, 10^{-1}, 10^0\}$.

2.6 Alternative control

For completeness, we describe the previously remarked, after equation (2.18), alternative control namely, that we can replace equation (2.12) by

$$v_x(0, t) = q_0(t), \quad t \in [0, \infty) \quad (2.74)$$

and equation (2.18) by

$$w(0, t) = P_0(t) - v(0, t), \quad t \in [0, T]. \quad (2.75)$$

Then we can solve the well-posed direct problem (2.9)-(2.11), (2.13) and (2.74) to obtain first $v(0, t)$. For the same test example, as in the previous section, Figure 2.11 shows the numerical results for $v(0, t)$ obtained using the BEM with $M = N \in \{20, 40, 80\}$. From this figure a convergent numerical solution, independent of the mesh, is apparently achieved with the ℓ^2 -error between subsequent discretisations (20 and 40) and (40 and 80) being very small and decreasing from 0.0555 to 0.0388, respectively.

The value of $v(0, t)$ is then introduced into (2.75) to generate the Dirichlet data at $x = 0$ for the inverse problem given by equation (2.14)-(2.17) and (2.75). We solve this inverse problem, as described in Section 2.4, with the obvious

modifications to obtain the separation of variables solution

$$w_K(x, t; \underline{b}) = \frac{\sqrt{2}}{c^2} \sum_{k=1}^K \frac{b_k}{\lambda_k^2} (1 - \cos(c\lambda_k t)) \cos(\lambda_k x), \quad (x, t) \in [0, L] \times [0, \infty), \quad (2.76)$$

$$f_K(x) = \sqrt{2} \sum_{k=1}^K b_k \cos(\lambda_k x), \quad x \in (0, L), \quad (2.77)$$

where $\lambda_k = (k - \frac{1}{2})\pi/L$ for $k = \overline{1, K}$. The coefficient $\underline{b} = (b_k)_{k=\overline{1, K}}$ is determined by imposing the additional condition (2.75),

$$P_0(t) - v(0, t) =: h(t) = \frac{\sqrt{2}}{c^2} \sum_{k=1}^K \frac{b_k}{\lambda_k^2} (1 - \cos(c\lambda_k t)), \quad t \in [0, T], \quad (2.78)$$

in the Tikhonov regularized sense (2.60), namely, as minimizing the functional

$$\mathcal{J}(\underline{b}) := \sum_{n=1}^N \left[\frac{\sqrt{2}}{c^2} \sum_{k=1}^K \frac{b_k}{\lambda_k^2} (1 - \cos(c\lambda_k t_n)) - h^\epsilon(t_n) \right]^2 + \lambda \sum_{k=1}^K b_k^2. \quad (2.79)$$

Denoting

$$h^\epsilon = (h^\epsilon(t_n))_{n=\overline{1, N}}, \quad Q_{nk} = \frac{\sqrt{2}(1 - \cos(c\lambda_k t_n))}{c^2 \lambda_k^2}, \quad n = \overline{1, N}, \quad k = \overline{1, K}, \quad (2.80)$$

we can recast (2.79) in the compact form (2.61).

The condition numbers of the matrix Q , defined in equation (2.80), are given in Table 2.2 for various $N \in \{20, 40, 80\}$ and $K \in \{5, 10, 20\}$. From this table it can be seen that ill-conditioning increases significantly, as K increases.

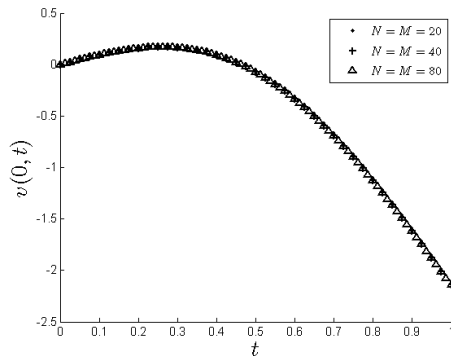


Figure 2.11: The numerical results for $v(0, t)$ obtained using the BEM with $M = N \in \{20, 40, 80\}$.

Table 2.2: Condition number of the matrix Q given by equation (2.80).

K	$N = 20$	$N = 40$	$N = 80$
5	$3.55E + 3$	$3.62E + 3$	$3.68E + 3$
10	$6.81E + 4$	$6.84E + 4$	$6.96E + 4$
20	$1.21E + 6$	$1.17E + 6$	$1.18E + 6$

2.6.1 Exact data

In the case of exact data, as in Section 2.5.1, Figure 2.12 shows the retrieved coefficients $(b_k)_{k=1, \overline{K}}$ for $K = 20$ obtained with no regularization, i.e. $\lambda = 0$, in comparison with the exact cosine Fourier series coefficients given by

$$b_k = \sqrt{2} \int_0^1 f(x) \cos \left(\left(k - \frac{1}{2} \right) \pi x \right) dx$$

which, for $f(x)$ given by (2.65), gives

$$b_k = \begin{cases} \frac{2\sqrt{2}(2\pi^2+3)}{3\pi} \simeq 6.8242 & \text{if } k = 1, \\ -\frac{2\sqrt{2}(2\pi^2(2k-1)+(-1)^k(4k^2-4k-3))}{\pi(8k^3-12k^2-2k+3)} & \text{if } k > 1. \end{cases} \quad (2.81)$$

Good agreement between the exact and numerical values can be observed. With these value of $\underline{b} = (b_k)_{k=1, \overline{K}}$, the solution (2.77) for the force function yields the numerical results illustrated in Figure 2.13. From this figure it can be seen that accurate numerical results are obtained.

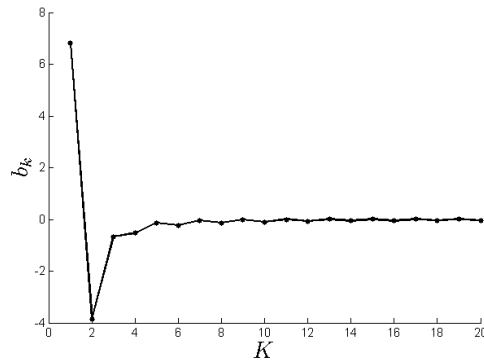


Figure 2.12: The numerical solution (...) for $(b_k)_{k=1, \overline{K}}$ for $K = 20$, $N = 80$, obtained with no regularization, i.e. $\lambda = 0$, for exact data, in comparison with the exact solution (2.81) (—).

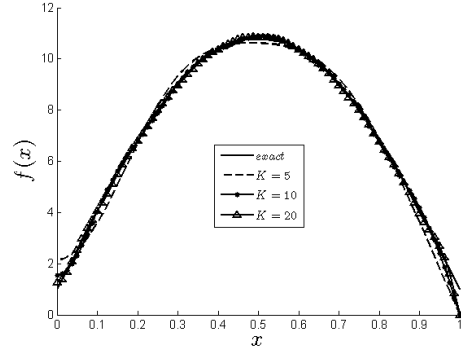


Figure 2.13: The exact solution (2.65) for $f(x)$ in comparison with the numerical solution (2.77) for various $K \in \{5, 10, 20\}$, no regularization, for exact data.

2.6.2 Noisy data

In the case of noisy data, as in Section 2.5.2, Figure 2.14 shows the regularized numerical solution for $f(x)$ obtained with various $\lambda \in \{10^{-4}, 10^{-3}, 10^{-2}\}$ for $p\% = 1\%$ noisy data added to $P_0(t)$ as

$$P_0^\epsilon(t_n) = P_0(t_n) + \epsilon, \quad n = \overline{1, N}, \quad (2.82)$$

where ϵ are N random noisy variables generated from a Gaussian normal distribution with mean zero and standard deviation σ given by

$$\sigma = p\% \times \max_{t \in [0, T]} |p_0(t)|. \quad (2.83)$$

From this figure it can be seen that the numerical results obtained with λ between 10^{-3} and 10^{-2} are reasonably stable and accurate.

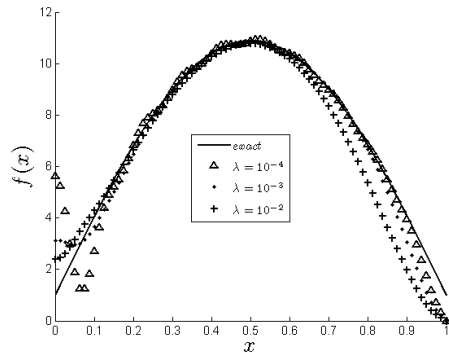


Figure 2.14: The exact solution (2.65) for $f(x)$ in comparison with the numerical solution (2.77) for $K = 20$, $p\% = 1\%$ noise, and regularization parameters $\lambda \in \{10^{-4}, 10^{-3}, 10^{-2}\}$.

2.7 Conclusions

An inverse force problem for the one-dimensional wave equation has been investigated. The unknown forcing term was assumed to depend on the space variable only and the additional measurement which ensures a unique retrieval was the flux at one end of the string. This inverse problem is uniquely solvable, but is still ill-posed since small errors in the input flux cause large errors in the output force. The problem was split into a direct well-posed problem for the linear wave equation, which is solved numerically using the BEM, and an inverse ill-posed problem whose unstable solution was expressed as a separation of variables truncated series. In order to stabilise the solution, the Tikhonov regularization method has been employed. The choice of the regularization parameter was based on the L-curve criterion. Numerical results show that accurate and stable solutions are obtained.

Of course, these techniques are well-known in the inverse problems literature but they have never been applied in this form for solving the inverse force problem for the wave equation of this chapter. One finds more literature on the corresponding inverse problem of determining a space-dependent heat source in the parabolic heat equation from Cauchy data, both theoretically (Cannon, 1968; Engl, Scherzer and Yamamoto, 1994; Hao, Chapter 4.3.1, 1998; Trong, Quan and

(Dinh Alain, 2006; Yamamoto, 1993) as well as numerically see (Ewing and Lin, 1989), who used hyperbolic regularization, (Coles and Murio, 2001), who used mollification, and (Hasanov, 2011), who used iterative regularization. Nevertheless, the techniques employed in this chapter are easily applicable to this inverse heat source problem as well.

In the inverse formulation of this chapter, boundary data is used to infer a domain quantity. In situations where this is not feasible it might be more practical to measure the displacement $u(x, t)$ for x in the space domain at a specified time $t = T$, as will be described in Chapter 5.

Chapter 3

Determination of forcing functions in the wave equation. Part I: the space-dependent case

3.1 Introduction

In the previous chapter we have used the BEM to numerically discretise the wave equation with a constant wave speed based on the available fundamental solution (2.19). Furthermore, by assuming that the force function $f(x)$ appears as a free term in the wave equation, the method of separating variables was applicable and regularization was used to stabilise the resulting system of linear algebraic equations. However, if the wave speed is not constant or, if the force appears in a non-free term as $f(x)h(x, t)$, the above methods are not applicable. Therefore, in order to extend this range of applicability, from now on in this chapter and, in fact, in the remaining of the thesis, the numerical method employed for discretising the wave equation is the finite difference method (FDM). The resulting system of linear equations is ill-conditioned, the original problem being ill-posed. Consequently, we apply the Tikhonov regularization for its solution. The choice of the regularization parameter introduced by this technique is important for the stability of the numerical solution and in this chapter this is based on the L-curve criterion, (Hansen, 2001).

The structure of the chapter is as follows. In Section 3.2, we briefly describe inverse force problems for the hyperbolic wave equation recalling the uniqueness theorems of (Engl, Scherzer and Yamamoto, 1994; Klibanov, 1992; Yamamoto, 1995). In Sections 3.3 and 3.4, we introduce the FDM, as applied to direct and inverse problems, respectively. Numerical results are illustrated and discussed in Sections 3.5 and an extension of the study is presented in Section 3.6. Conclusions are provided in Section 3.7.

3.2 Mathematical formulation

The governing equation for a vibrating bounded structure $\Omega \subset \mathbb{R}^n$, $n = 1, 2, 3$, acted upon by a force $F(\underline{x}, t)$ is given by the wave equation

$$u_{tt}(\underline{x}, t) = c^2 \nabla^2 u(\underline{x}, t) + F(\underline{x}, t), \quad (\underline{x}, t) \in \Omega \times (0, T), \quad (3.1)$$

where $T > 0$ is a given time, $u(\underline{x}, t)$ represents the displacement and $c > 0$ is the wave speed of propagation. For simplicity, we have assumed that c is a constant, but we can also let c be a function depending on the space variable \underline{x} . For example, in $n = 1$ -dimension, where Ω represents the interval $(0, L)$, $L > 0$, occupied by a vibrating inhomogeneous string, its small transversal vibrations are governed by the wave equation

$$\omega(x)u_{tt}(x, t) = u_{xx}(x, t) + F(x, t), \quad (x, t) \in (0, L) \times (0, T), \quad (3.2)$$

where $\omega(x) = c^{-2}(x)$ represents the mass density of the string, which is stretched by a force.

Equation (3.1) has to be solved subject to the initial conditions

$$u(\underline{x}, 0) = \varphi(\underline{x}), \quad \underline{x} \in \Omega, \quad (3.3)$$

$$u_t(\underline{x}, 0) = \psi(\underline{x}), \quad \underline{x} \in \Omega, \quad (3.4)$$

where φ and ψ represent the initial displacement and velocity, respectively. On the boundary of the structure $\partial\Omega$ we can prescribe Dirichlet, Neumann, Robin or mixed boundary conditions. In one-dimension, the physical interpretation of these boundary conditions for the transverse vibrations of a string on the interval

$(0, L)$ can be briefly summarised, as follows, see e.g. (Tikhonov and Samarskii, 1963). The Dirichlet value $u(0, t)$ represents the transverse position of the string at $x = 0$ and, if homogeneous, i.e. $u(0, t) = 0$, it means that the end $x = 0$ of the string is fixed or clamped. The Neumann value $u_x(0, t)$ represents the vertical component of the tension and, if homogeneous, i.e. $u_x(0, t) = 0$, it means that no external transverse force acts on the end $x = 0$. Finally, the homogeneous Robin boundary condition $-u_x(0, t) + \sigma_0 u(0, t) = 0$ with $\sigma_0 \geq 0$, comes from Newton's law modelling that a linearly transverse force is applied at the end $x = 0$ of the string.

Let us consider, for the sake of simplicity, Dirichlet boundary conditions being prescribed, namely,

$$u(\underline{x}, t) = P(\underline{x}, t), \quad (\underline{x}, t) \in \partial\Omega \times (0, T), \quad (3.5)$$

where P is a prescribed boundary displacement.

If the force $F(\underline{x}, t)$ is given, then equations (3.1), (3.3)-(3.5) form a direct well-posed problem. However, if the force function $F(\underline{x}, t)$ cannot be directly observed it hence becomes unknown and then clearly, the above set of equations is not sufficient to determine uniquely the pair solution $(u(\underline{x}, t), F(\underline{x}, t))$. Then, we consider the additional measurement of the flux tension of the structure on a (positive measure) portion $\Gamma \subset \partial\Omega$, namely,

$$\frac{\partial u}{\partial \nu}(\underline{x}, t) = q(\underline{x}, t), \quad (\underline{x}, t) \in \Gamma \times (0, T), \quad (3.6)$$

where $\underline{\nu}$ is the outward unit normal to $\partial\Omega$ and q is a given function. Other additional information, such as the 'upper-base' final displacement measurement $u(\underline{x}, T)$ for $\underline{x} \in \Omega$, will be investigated in Chapter 5.

Also, note that if instead of the Dirichlet boundary condition (3.5) we would have supplied a Neumann boundary condition then, the quantities u and $\partial u / \partial \nu$ would have had to be reversed in (3.5) and (3.6). In order to ensure a unique solution we further assume that

$$F(\underline{x}, t) = f(\underline{x})h(\underline{x}, t), \quad (\underline{x}, t) \in \Omega \times (0, T), \quad (3.7)$$

where $h(\underline{x}, t)$ is a known function and $f(\underline{x})$ represents the unknown space-dependent forcing function to be determined. This restriction is necessary because otherwise,

we can always add to $u(\underline{x}, t)$ any function of the form $t^2U(\underline{x})$ with $U \in C^2(\overline{\Omega})$ arbitrary with compact support in Ω , and still obtain another solution satisfying (3.1), (3.3)-(3.6). Physically, the choice (3.7) is useful in applications where the transient intensity of the force is known and it is only its spatial location/distribution that is unknown and has to be determined from the overprescribed boundary data (3.5) and (3.6).

Note that the unknown force $f(\underline{x})$ is an interior quantity and it depends on the space variable $\underline{x} \in \Omega \subset \mathbb{R}^n$, whilst the additional measurement (3.6) of the flux $q(\underline{x}, t)$ is a boundary quantity and it depends on $(\underline{x}, t) \in \Gamma \times (0, T)$. It is worth noting that a corresponding inverse spacewise-dependent source identification problem given by equations (3.3), (3.5)-(3.7) also arises for the heat equation $u_t = \nabla^2 u + f(\underline{x})h(\underline{x}, t)$, see (Engl, Scherzer and Yamamoto, 1994).

In the next subsection, we analyse more closely the uniqueness of solution of the inverse problem which requires finding the pair solution $(u(\underline{x}, t), f(\underline{x}))$ satisfying equations (3.1), (3.3)-(3.7).

3.2.1 Mathematical analysis

To start with, from (3.7), and taking for simplicity $c = 1$, equation (3.1) recasts as

$$u_{tt}(\underline{x}, t) = \nabla^2 u(\underline{x}, t) + f(\underline{x})h(\underline{x}, t), \quad (\underline{x}, t) \in \Omega \times (0, T). \quad (3.8)$$

We note that in the one-dimensional case, $n = 1$, and for $c = h = 1$ and other compatibility conditions satisfied by the data (3.3)-(3.6), (Cannon and Dunninger, 1970), based on the method of Fourier series, established the uniqueness of a classical solution of the inverse problem. We also have the following more general uniqueness result, see Theorem 9 of (Engl, Scherzer and Yamamoto, 1994).

Theorem 1. *Assume that $\Omega \subset \mathbb{R}^n$ is a bounded star-shaped domain with sufficiently smooth boundary such that $T > \text{diam}(\Omega)$. Let $h \in H^2(0, T; L^\infty(\Omega))$ be such that $h(\cdot, 0) \in L^\infty(\Omega)$, $h_t(\cdot, 0) \in L^\infty(\Omega)$ and*

$$H := \frac{\|h_{tt}\|_{L^2(0, T; L^\infty(\Omega))}}{\inf_{\underline{x} \in \Omega} |h(\underline{x}, 0)|} \quad \text{is sufficiently small.} \quad (3.9)$$

3.2 Mathematical formulation

If $\Gamma = \partial\Omega$, then the inverse problem (3.3)-(3.6) and (3.8) has at most one solution $(u(\underline{x}, t), f(\underline{x}))$ in the class of functions

$$u \in L^2(0, T; H^1(\Omega)), \quad u_t \in L^2(0, T; L^2(\Omega)), \quad u_{tt} \in L^2(0, T; (H^1(\Omega))'),$$

$$f \in L^2(\Omega), \quad (3.10)$$

where $(H^1(\Omega))'$ is the dual space of $H^1(\Omega)$, defined as the space of continuous linear functionals on $H^1(\Omega)$.

The function spaces involved in this theorem are given by, see (Lions, 1971), $L^2(\Omega) =$ space of functions square integrable in $\Omega = \{u; \int_{\Omega} |u|^2 d\underline{x} < \infty\}$, $L^\infty(\Omega) = \{u; \sup_{\underline{x} \in \Omega} |u| < \infty\}$, $H^1(\Omega) = \{u; u \in L^2(\Omega), \nabla u \in (L^2(\Omega))^n\}$, $L^2(0, T; X) = \{u(x, t); \int_0^T \|u(x, t)\|_X dt < \infty\}$, where $X \in \{L^\infty(\Omega), L^2(\Omega), H^1(\Omega)\}$, $H^2(0, T; L^\infty(\Omega)) = \{u(x, t); u(x, t), u_t(x, t), u_{tt}(x, t) \in L^\infty(\Omega) \text{ for } t \in (0, T)\}$.

One can remark that the previously stated uniqueness Theorem 1 requires that the Neumann observation (3.6) is over the complete boundary $\Gamma = \partial\Omega$. In the incomplete case that $\Gamma \subset \partial\Omega$ is only a part of $\partial\Omega$ then, the uniqueness Theorem 1 holds under the assumption that h is independent of \underline{x} , (Yamamoto, 1995), as follows.

Theorem 2. Assume that $\Omega \subset \mathbb{R}^n$ is a bounded star-shaped domain with smooth boundary such that $T > \text{diam}(\Omega)$. Let $h \in C^1[0, T]$ be independent of \underline{x} such that equation (3.8) becomes

$$u_{tt}(\underline{x}, t) = \nabla^2 u(\underline{x}, t) + f(\underline{x})h(t), \quad (\underline{x}, t) \in \Omega \times (0, T), \quad (3.11)$$

and assume further that $h(0) \neq 0$. Then the inverse problem (3.3)-(3.6) and (3.11) has at most one solution in the class of functions

$$u \in C^1([0, T]; H^1(\Omega)) \cap C^2([0, T]; L^2(\Omega)), \quad f \in L^2(\Omega). \quad (3.12)$$

In (3.12), $C^m([0, T]; X)$, where $m \in \{1, 2\}$ and $X \in \{H^1(\Omega), L^2(\Omega)\}$, denotes the space of m -times continuously differentiable functions defined on $[0, T]$ with values in X .

In Section 3.4, we shall consider the numerical determination of the space-dependent forcing function $f(\underline{x})$. But before we do that, in the next section we explain the FDM adopted for the numerical discretisation of the direct problem.

3.3 Numerical solution of the direct problem

In this section, we consider the direct initial Dirichlet boundary value problem (3.1), (3.3)-(3.5) for simplicity, in one-dimension, i.e. $n = 1$ and $\Omega = (0, L)$ with $L > 0$, when the force $F(x, t)$ is known and the displacement $u(x, t)$ is to be determined, namely,

$$u_{tt}(x, t) = c^2 u_{xx}(x, t) + F(x, t), \quad (x, t) \in (0, L) \times (0, T], \quad (3.13)$$

$$u(x, 0) = \varphi(x), \quad u_t(x, 0) = \psi(x), \quad x \in [0, L], \quad (3.14)$$

$$u(0, t) = P(0, t) =: P_0(t), \quad t \in (0, T], \quad (3.15)$$

$$u(L, t) = P(L, t) =: P_L(t), \quad t \in (0, T]. \quad (3.16)$$

The discrete form of this problem is as follows. We divide the solution domain $(0, L) \times (0, T)$ into M and N subintervals of equal space length Δx and time step Δt , where $\Delta x = L/M$ and $\Delta t = T/N$. We denote by $u_{i,j} := u(x_i, t_j)$, where $x_i = i\Delta x$, $t_j = j\Delta t$, and $F_{i,j} := F(x_i, t_j)$ for $i = \overline{0, M}$, $j = \overline{0, N}$. Then, a central-difference approximation to equations (3.13)-(3.16) at the mesh points $(x_i, t_j) = (i\Delta x, j\Delta t)$ of the rectangular mesh covering the solution domain $(0, L) \times (0, T)$ is, see (Smith, 1985) and Appendix A,

$$u_{i,j+1} = r^2 u_{i+1,j} + 2(1 - r^2) u_{i,j} + r^2 u_{i-1,j} - u_{i,j-1} + (\Delta t)^2 F_{i,j}, \quad (3.17)$$

$$i = \overline{1, (M-1)}, \quad j = \overline{1, (N-1)},$$

$$u_{i,0} = \varphi(x_i), \quad i = \overline{0, M}, \quad \frac{u_{i,1} - u_{i,-1}}{2\Delta t} = \psi(x_i), \quad i = \overline{1, (M-1)}, \quad (3.18)$$

$$u_{0,j} = P_0(t_j), \quad u_{M,j} = P_L(t_j), \quad j = \overline{0, N}, \quad (3.19)$$

where the Courant number $r = c\Delta t/\Delta x$. Equation (3.17) represents an explicit FDM which is second-order accurate in both space and time, and stable if $r \leq 1$, giving approximate values for the solution at mesh points along $t = 2\Delta t, 3\Delta t, \dots$,

3.4 Numerical solution of the inverse problem

as soon as the solution at the mesh points along $t = \Delta t$ has been determined by allowing $j = 0$ in equation (3.17) and using (3.18), to obtain

$$\begin{aligned} u_{i,1} &= \frac{1}{2}r^2\varphi(x_{i+1}) + (1-r^2)\varphi(x_i) + \frac{1}{2}r^2\varphi(x_{i-1}) + (\Delta t)\psi(x_i) \\ &+ \frac{1}{2}(\Delta t)^2 F_{i,0}, \quad i = \overline{1, (M-1)}. \end{aligned} \quad (3.20)$$

The normal derivatives $\frac{\partial u}{\partial \nu}(0, t)$ and $\frac{\partial u}{\partial \nu}(L, t)$ are calculated using the finite-difference approximations, see Appendix A,

$$\begin{aligned} -\frac{\partial u}{\partial x}(0, t_j) &= -\frac{4u_{1,j} - u_{2,j} - 3u_{0,j}}{2\Delta x}, \\ \frac{\partial u}{\partial x}(L, t_j) &= \frac{3u_{M,j} - 4u_{M-1,j} + u_{M-2,j}}{2\Delta x}, \quad j = \overline{1, N}. \end{aligned} \quad (3.21)$$

3.4 Numerical solution of the inverse problem

We now consider the inverse initial boundary value problem (3.3)-(3.6) and (3.8) in one-dimension, i.e. $n = 1$ and $\Omega = (0, L)$, when both the force $f(x)$ and the displacement $u(x, t)$ are to be determined, from the governing equation (take $c = 1$ for simplicity)

$$u_{tt}(x, t) = u_{xx}(x, t) + f(x)h(x, t), \quad (x, t) \in (0, L) \times (0, T], \quad (3.22)$$

subject to the initial and boundary conditions (3.14)-(3.16) and the overspecified flux tension condition (3.6) at one end of the string, say at $x = 0$, namely

$$-\frac{\partial u}{\partial x}(0, t) = q(0, t) =: q_0(t), \quad t \in (0, T]. \quad (3.23)$$

In the case that h is independent of x , according to Theorem 2, the inverse source problem (3.14)-(3.16), (3.22) and (3.23) has at most one solution in the class of functions (3.12) provided that $h \in C^1[0, T]$, $h(0) \neq 0$ and $T > L$.

In discretised finite-difference form equations (3.14)-(3.16) and (3.22) recast as equations (3.18), (3.19),

$$\begin{aligned} u_{i,j+1} - (\Delta t)^2 f_i h_{i,j} &= r^2 u_{i+1,j} + 2(1-r^2)u_{i,j} + r^2 u_{i-1,j} - u_{i,j-1}, \\ & \quad i = \overline{1, (M-1)}, \quad j = \overline{1, (N-1)}, \end{aligned} \quad (3.24)$$

3.4 Numerical solution of the inverse problem

and

$$\begin{aligned} u_{i,1} - \frac{1}{2}(\Delta t)^2 f_i h_{i,0} &= \frac{1}{2}r^2\varphi(x_{i+1}) + (1-r^2)\varphi(x_i) + \frac{1}{2}r^2\varphi(x_{i-1}) \\ &+ (\Delta t)\psi(x_i), \quad i = \overline{1, (M-1)}, \end{aligned} \quad (3.25)$$

where $f_i := f(x_i)$ and $h_{i,j} := h(x_i, t_j)$.

Discretizing (3.23) using (3.21) we also have

$$q_0(t_j) = -\frac{\partial u}{\partial x}(0, t_j) = -\frac{4u_{1,j} - u_{2,j} - 3u_{0,j}}{2\Delta x}, \quad j = \overline{1, N}. \quad (3.26)$$

In practice, the additional observation (3.26) comes from measurement which is inherently contaminated with errors. We therefore model this by replacing the exact data $q_0(t)$ by the noisy data

$$q_0^\epsilon(t_j) = q_0(t_j) + \epsilon_j, \quad j = \overline{1, N}, \quad (3.27)$$

where $(\epsilon_j)_{j=\overline{1, N}}$ are N random noisy variables generated using the MATLAB routine 'normrnd' from a Gaussian normal distribution with mean zero and standard deviation $\sigma = p \times \max_{t \in [0, T]} |q_0(t)|$, where p represents the percentage of noise.

Assembling (3.24)-(3.26) and using (3.18) and (3.19), the discretised inverse problem reduces to solving a global linear system of $(M-1) \times N + N$ equations with $(M-1) \times N + (M-1)$ unknowns. Since this system is linear we can eliminate the unknowns $u_{i,j}$ for $i = \overline{1, (M-1)}$, $j = \overline{1, N}$, to reduce the problem to solving an ill-conditioned system of N equations with $(M-1)$ unknowns of the generic form

$$A\underline{f} = \underline{b}^\epsilon, \quad (3.28)$$

where the right-hand side vector \underline{b}^ϵ incorporates the noisy measurement (3.27). For a unique solution we require $N \geq M-1$. The method of least squares can be used to find an approximate solution to overdetermined systems. For the system of equations (3.28), the least squares solution is given by $\underline{f} = (A^T A)^{-1} A^T \underline{b}^\epsilon$, where the superscript T denotes the transpose.

For the Examples 1-4 that will be considered in the next section, the condition numbers of the matrix A in (3.28) given in Table 3.1 are between $O(10^4)$ to $O(10^8)$ for $M = N = 80$. These large condition numbers indicate that the

3.4 Numerical solution of the inverse problem

system of equations (3.28) is ill-conditioned. The ill-conditioning nature of the matrix A can also be revealed by plotting its normalised singular values σ_k/σ_1 for $k = \overline{1, (M - 1)}$, in Figure 3.1.

Table 3.1: Condition number of matrix A for Examples 1-4.

$N = M$	Example 1 $h(x, t) = 1$	Example 2 $h(x, t) = 1 + t$	Example 3 $h(x, t) = 1 + x + t$	Example 4 $h(x, t) = t^2$
10	28.55	39.53	33.73	3394.55
20	110.98	152.38	131.29	53232.36
40	437.93	596.91	518.51	826827.12
80	1740.25	2361.22	2061.53	12956244.4

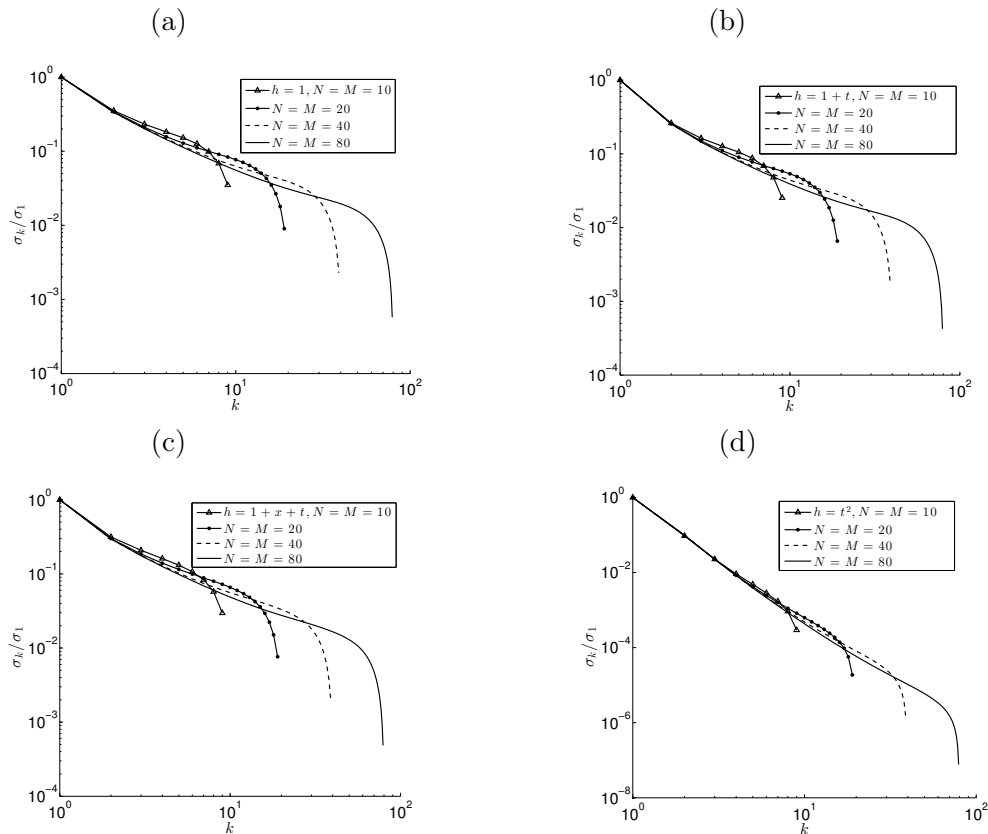


Figure 3.1: Normalised singular values σ_k/σ_1 for $k = \overline{1, (M - 1)}$, for (a) Example 1, (b) Example 2, (c) Example 3, and (d) Example 4.

3.5 Numerical results and discussion

In all examples in this section we take, for simplicity, $c = L = T = 1$. Although the geometrical condition $1 = T > \text{diam}(\Omega) = L = 1$ is slightly violated, it is expected that the uniqueness Theorems 1 and 2 still hold, especially in $n = 1$ -dimension and when the inverse problems are numerically discretised.

3.5.1 Example 1 ($h(x, t) = 1$)

This is an example in which we take $h(x, t) = 1$ a constant function and consider first the direct problem (3.13)-(3.16) with the input data (2.66), (2.67) and

$$F(x, t) = f(x) = 1 + \pi^2 \sin(\pi x), \quad x \in (0, 1). \quad (3.29)$$

The exact solution is given by (2.64).

The numerical and exact solutions for $u(x, t)$ at interior points are shown in Figure 3.2 and one can observe that an excellent agreement is obtained. Table 3.2 also gives the exact and numerical solutions for the flux tension (3.23). From this table it can be seen that the numerical results are convergent, as the mesh size decreases, and they are in very good agreement with the exact solution (3.30). Moreover, the ℓ^2 -error between the exact and the numerical solutions of Table 3.2 are $\{0.1306, 0.0331, 0.0083, 0.0020\}$ for $N = M \in \{10, 20, 40, 80\}$, respectively, showing that, as expected from the theory of central finite differences, the error reduces by a factor of 4 as $N = M$ are doubled. Although not illustrated, it is reported that the same excellent agreement has also been obtained between the exact and numerical solutions for the flux tension at $x = 1$.

3.5 Numerical results and discussion

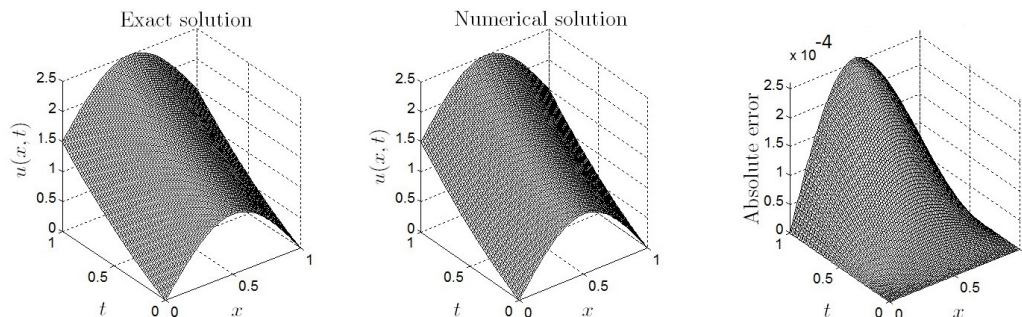


Figure 3.2: Exact and numerical solutions for the displacement $u(x, t)$ and the absolute error between them for the direct problem, obtained with $N = M = 80$, for Example 1.

Table 3.2: Exact and numerical solutions for the flux tension at $x = 0$, for the direct problem of Example 1.

t	0.1	0.2	...	0.8	0.9	1
$N = M = 10$	-3.2427	-3.2465	...	-3.2899	-3.2937	-3.295
$N = M = 20$	-3.1675	-3.1685	...	-3.1790	-3.1799	-3.1802
$N = M = 40$	-3.1481	-3.1483	...	-3.1510	-3.1512	-3.1513
$N = M = 80$	-3.1432	-3.1433	...	-3.1439	-3.1440	-3.1440
<i>exact</i>	-3.1416	-3.1416	...	-3.1416	-3.1416	-3.1416

The inverse problem given by equations (3.22) with $h(x, t) = 1$, (2.66), (2.67) and

$$-\frac{\partial u}{\partial x}(0, t) = q_0(t) = -\pi, \quad t \in (0, 1], \quad (3.30)$$

is considered next. Since $h(0) = 1 \neq 0$, Theorem 2 ensures the uniqueness of the solution in the class of functions (3.12).

In fact, the exact solution $(f(x), u(x, t))$ of this inverse problem is given by equations (2.65) and (2.64), respectively. Numerically, we employ the FDM for discretising the inverse problem, as described in Section 3.4. Note that this is exactly the same example problem as the one solved in Section 2.5 using a different

3.5 Numerical results and discussion

technique. So, where appropriate, we shall compare and discuss the performance of the techniques of Chapters 2 and 3 in terms of their accuracy and stability.

3.5.1.1 Exact data

We first consider the case of exact data, i.e. $p = 0$ and hence $\underline{\epsilon} = \underline{0}$ in (3.27). The numerical results corresponding to $f(x)$ and $u(x, t)$ are plotted in Figures 3.3 and 3.4, respectively. From these figures it can be seen that convergent and accurate numerical solutions are obtained.

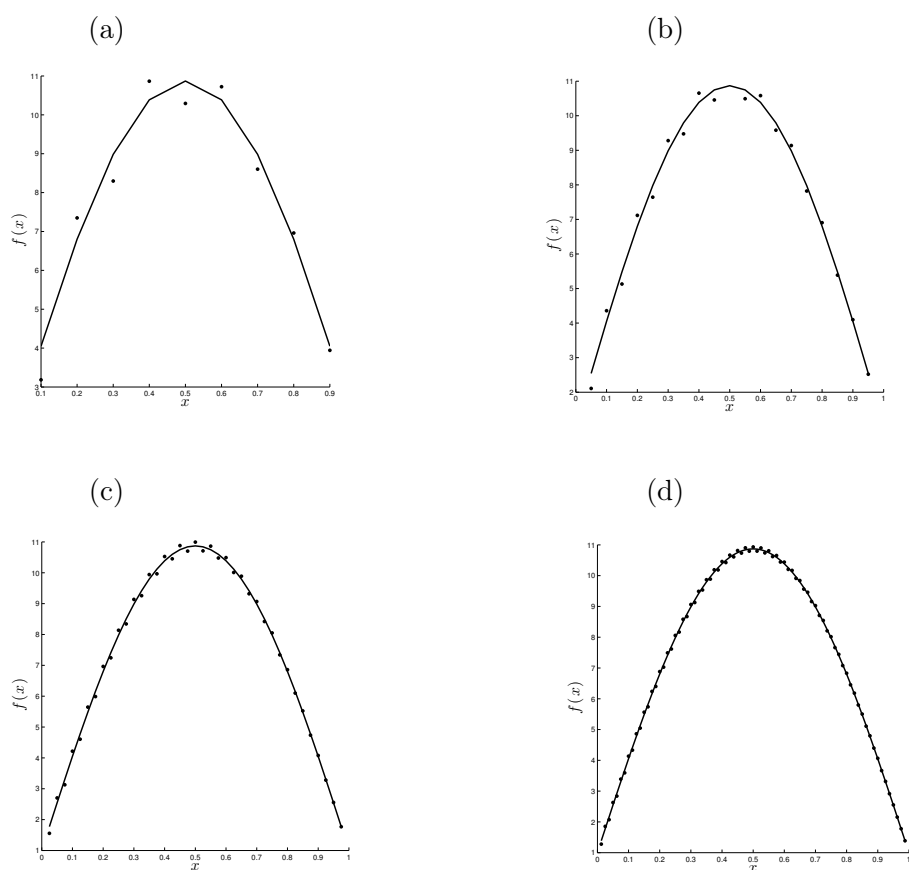


Figure 3.3: The exact (—) solution (2.65) for the force $f(x)$ in comparison with the numerical solution ($\cdot \cdot \cdot$) for various $N = M =$ (a) 10, (b) 20, (c) 40, and (d) 80, and no regularization, for exact data, for the inverse problem of Example 1.

By comparing Figures 2.4 and 3.3 it can be seen that both the BEM of Chapter

3.5 Numerical results and discussion

2 and the FDM of Chapter 3 provide very accurate numerical solutions for the source function (2.65) for exact data.

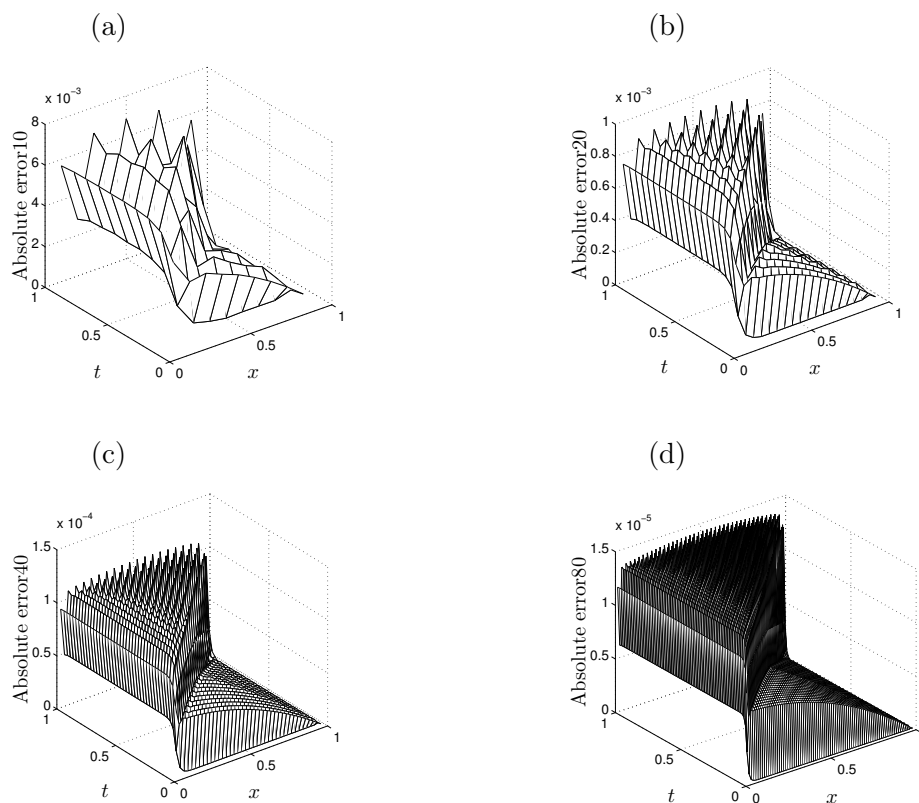


Figure 3.4: The absolute errors between the exact and numerical displacement $u(x, t)$ obtained with $N = M \in \{10, 20, 40, 80\}$ and no regularization, for exact data, for the inverse problem of Example 1.

3.5.1.2 Noisy data

In order to investigate the stability of the numerical solution we include some ($p = 1\%$) noise into the input data (3.26), as given by equation (3.27). The numerical solution for $f(x)$ obtained with $N = M = 80$ and no regularization is plotted in Figure 3.5. It can be clearly seen that very high oscillations appear. This clearly shows that the inverse force problem (3.14)-(3.16), (3.22) and (3.23) is ill-posed. In the previous chapter, we have dealt with this instability by truncating the infinite series (2.54) at a finite threshold K , see Figure 2.6 where for low values

3.5 Numerical results and discussion

of $K \leq 10$ stable reconstructions can be obtained. In this chapter, in order to deal with this instability we employ the (zeroth-order) Tikhonov regularization which yields the solution

$$\underline{f}_\lambda = (A^T A + \lambda I)^{-1} A^T \underline{b}^\epsilon, \quad (3.31)$$

where I is the identity matrix and $\lambda > 0$ is a regularization parameter to be prescribed. Including regularization we obtain the numerical solution (3.31) whose accuracy error, as a function of λ , is plotted in Figure 3.6. From this figure it can be seen that the minimum of the error occurs around $\lambda = 10^{-6}$. Clearly, this argument cannot be used as a suitable choice for the regularization parameter λ in the absence of an analytical (exact) solution (2.65) being available. However, one possible criterion for choosing λ is given by the L-curve method, (Hansen, 2001), which plots the residual norm $\|A\underline{f}_\lambda - \underline{b}^\epsilon\|$ versus the solution norm $\|\underline{f}_\lambda\|$ for various values of λ . This is shown in Figure 3.7 for various values of $\lambda \in \{10^{-9}, 5 \times 10^{-9}, 10^{-8}, \dots, 10^{-2}\}$. The portion to the right of the curve corresponds to large values of λ which make the solution oversmooth, whilst the portion to the left of the curve corresponds to small values of λ which make the solution undersmooth. The compromise is then achieved around the corner region of the L-curve where the aforementioned portions meet. Figure 3.7 shows that this corner region includes the values around $\lambda = 10^{-6}$, which is a good prediction of the optimal value demonstrated in Figure 3.6.

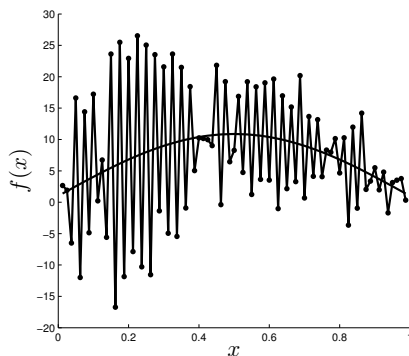


Figure 3.5: The exact solution (2.65) for the force $f(x)$ in comparison with the numerical solution ($-\bullet-$) for $N = M = 80$, with no regularization, for $p = 1\%$ noisy data, for the inverse problem of Example 1.

3.5 Numerical results and discussion

Finally, Figure 3.8 shows the regularized numerical solution for $f(x)$ obtained with various values of the regularization parameter $\lambda \in \{10^{-7}, 10^{-6}, 10^{-5}\}$ for $p = 1\%$ noisy data. From this figure it can be seen that the value of the regularization parameter λ can also be chosen by trial and error. By plotting the numerical solution for various values of λ we can infer when the instability starts to kick off. For example, in Figure 3.8, the value of $\lambda = 10^{-5}$ is too large and the solution is oversmooth, whilst the value of $\lambda = 10^{-7}$ is too small and the solution becomes unstable. We could therefore inspect the value of $\lambda = 10^{-6}$ and conclude that this is a reasonable choice of the regularization parameter which balances the smoothness with the instability of the solution.

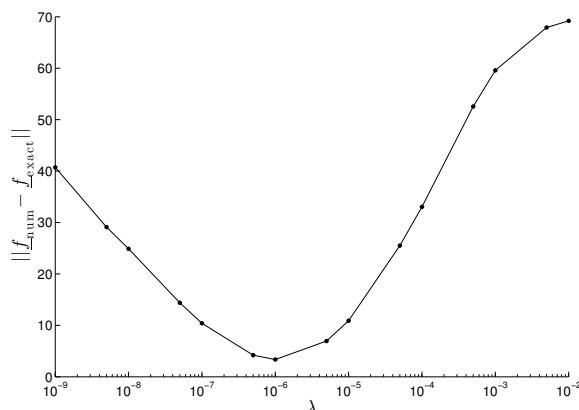


Figure 3.6: The accuracy error $\|f_{\text{num}} - f_{\text{exact}}\|$, as a function of λ , for $N = M = 80$ and $p = 1\%$ noise, for the inverse problem of Example 1.

Finally, similar features for the errors, L-curves and force reconstructions are revealed when comparing Figures 2.8 - 2.10 with Figures 3.6 - 3.8, respectively.

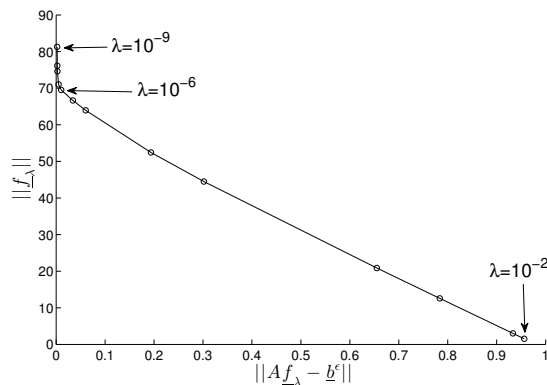


Figure 3.7: The L-curve for the Tikhonov regularization, for $N = M = 80$ and $p = 1\%$ noise, for the inverse problem of Example 1.

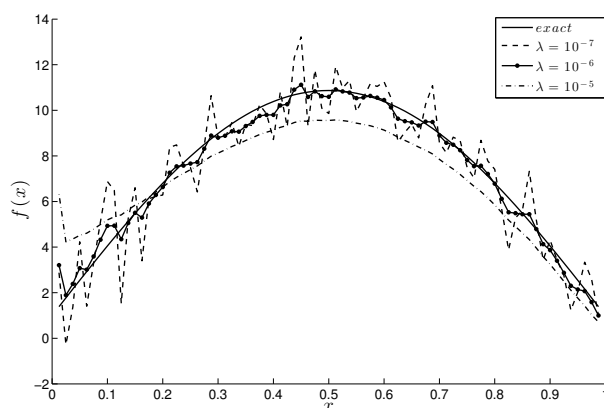


Figure 3.8: The exact solution (2.65) for the force $f(x)$ in comparison with the numerical solution (3.31), for $N = M = 80$, $p = 1\%$ noise, and regularization parameters $\lambda \in \{10^{-7}, 10^{-6}, 10^{-5}\}$, for the inverse problem of Example 1.

3.5.2 Example 2 ($h(x, t) = 1 + t$)

This is an example in which we take $h(x, t) = 1 + t$ a linear function of t and independent of x and consider first the direct problem (3.14)-(3.16) and (3.22) with the input data

$$u(x, 0) = \varphi(x) = 0, \quad u_t(x, 0) = \psi(x) = 0, \quad x \in [0, 1], \quad (3.32)$$

3.5 Numerical results and discussion

$$u(0, t) = P_0(t) = 0, \quad u(1, t) = P_L(t) = 0, \quad t \in (0, 1], \quad (3.33)$$

$$f(x) = \begin{cases} x & \text{if } 0 \leq x \leq \frac{1}{2}, \\ 1 - x & \text{if } \frac{1}{2} < x \leq 1. \end{cases} \quad (3.34)$$

As in Example 1, since $h(0) = 1 \neq 0$, Theorem 2 ensures the uniqueness of the solution in the class of the functions (3.12). Also, remark that in this example, the force (3.34) has a triangular shape, being continuous but non-differentiable at the peak $x = 1/2$. This example also does not possess an explicit analytical solution readily available for the displacement $u(x, t)$.

The numerical solutions for the displacement $u(x, t)$ at interior points are shown in Figure 3.9. The flux tension (3.23) is presented in Table 3.3 and Figure 3.10. From these figures and table it can be seen that convergent numerical solutions for both $u(x, t)$ and $q_0(t)$ are obtained, as $N = M$ increases.

3.5 Numerical results and discussion

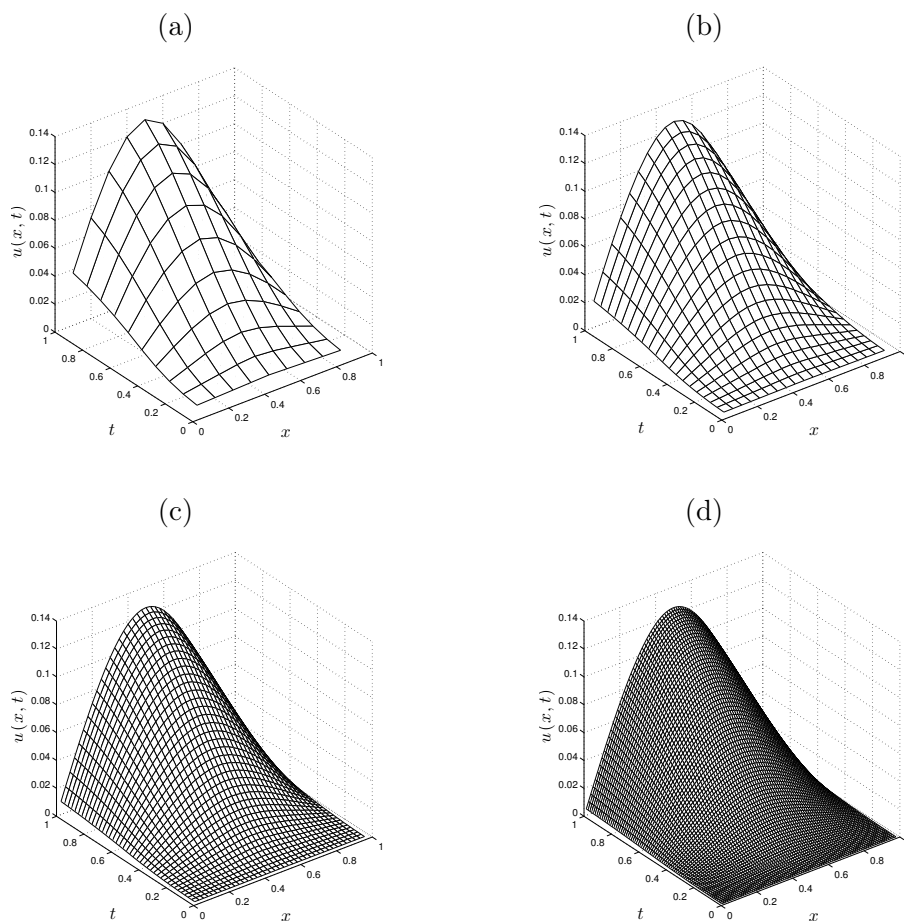


Figure 3.9: Numerical solutions for the displacement $u(x, t)$ obtained using the direct problem with various $N = M \in \{10, 20, 40, 80\}$ in (a)-(d), respectively, for Example 2.

Table 3.3: The numerical solutions for the flux tension at $x = 0$, for the direct problem of Example 2.

t	0.1	0.2	...	0.8	0.9	1
$N = M = 10$	-0.00500	-0.02100	...	-0.31900	-0.35900	-0.39000
$N = M = 20$	-0.00512	-0.02125	...	-0.3095	-0.34862	-0.37875
$N = M = 40$	-0.00515	-0.02131	...	-0.30712	-0.34603	-0.37593
$N = M = 80$	-0.00516	-0.02132	...	-0.30653	-0.34538	-0.37523

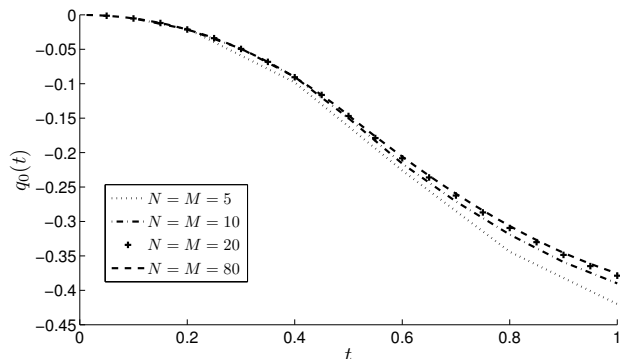


Figure 3.10: Numerical solution for the flux tension at $x = 0$, for various $N = M \in \{5, 10, 20, 80\}$, for the direct problem of Example 2.

Consider now the inverse problem given by equations (3.22) with $h(x, t) = 1 + t$, (3.32), (3.33) and (3.23) with $q_0(t)$ numerically simulated and given in Figure 3.10 for $N = M = 80$. We perturb further this flux by adding to it some $p \in \{1, 3, 5\}\%$ noise, as given by equation (3.27). The numerical solution for $f(x)$ obtained with $N = M = 80$ and no regularization has been found highly oscillatory and unstable similar to that obtained in Figure 3.5 and therefore is not presented. In order to deal with this instability we employ and test the Tikhonov regularization of various orders such as zero, first and second, which yields the solution, (Twomey, 1963),

$$\underline{f}_{\lambda} = (A^T A + \lambda D_k^T D_k)^{-1} A^T \underline{b}^{\epsilon}, \quad (3.35)$$

where D_k is the regularization derivative operator of order $k \in \{0, 1, 2\}$, defined in (1.3). Observe that for $k = 0$, equation (3.35) becomes the zeroth-order regularized solution (3.31) which was previously employed in Example 1 in order to obtain a stable solution.

Including regularization we obtain the solution (3.35) whose accuracy error, as a function of λ , is plotted in Figure 3.11 for various orders of regularization $k \in \{0, 1, 2\}$. From this figure it can be seen that there are wide ranges for choosing the regularization parameters in the valleys of minima of the plotted error curves. The minimum points λ_{opt} and the corresponding accuracy errors are listed in Table 3.4. The L-curve criterion for choosing λ in the zeroth-order regularization is shown in Figure 3.12 for various values of $\lambda \in \{10^{-9}, 10^{-8}, \dots, 10^{-2}\}$ and for

3.5 Numerical results and discussion

$p \in \{1, 3, 5\}\%$ noisy data. This figure shows that the L-corner region includes indeed values around the optimal ones of $\lambda = 10^{-6}$ for $p = 1\%$, $\lambda = 10^{-5}$ for $p = 3\%$, and $\lambda = 10^{-5}$ for $p = 5\%$ derived previously from Figure 3.11 and included in Table 3.4. Similar L-curves, which plot the penalised solution norm $\|D_k \underline{f}_\lambda\|$ versus the residual norm $\|A \underline{f}_\lambda - \underline{b}^\epsilon\|$, have been obtained for the first and second-order regularizations and therefore, they are not illustrated.

Figure 3.13 shows the regularized numerical solutions (3.35) for $f(x)$ obtained for various orders of regularization methods $k \in \{0, 1, 2\}$, with the values of the regularization parameter λ_{opt} given in Table 3.4 for $p \in \{1, 3, 5\}\%$ noisy data. First, from this figure it can be seen how the order of regularization acts on the regularity of solution, e.g. $k = 0$ -order allows wiggles, $k = 1$ -order penalises gradient and $k = 2$ -order penalises curvature. Second, it can be seen that the numerical results are stable and they become more accurate as the amount of noise p decreases.

3.5 Numerical results and discussion

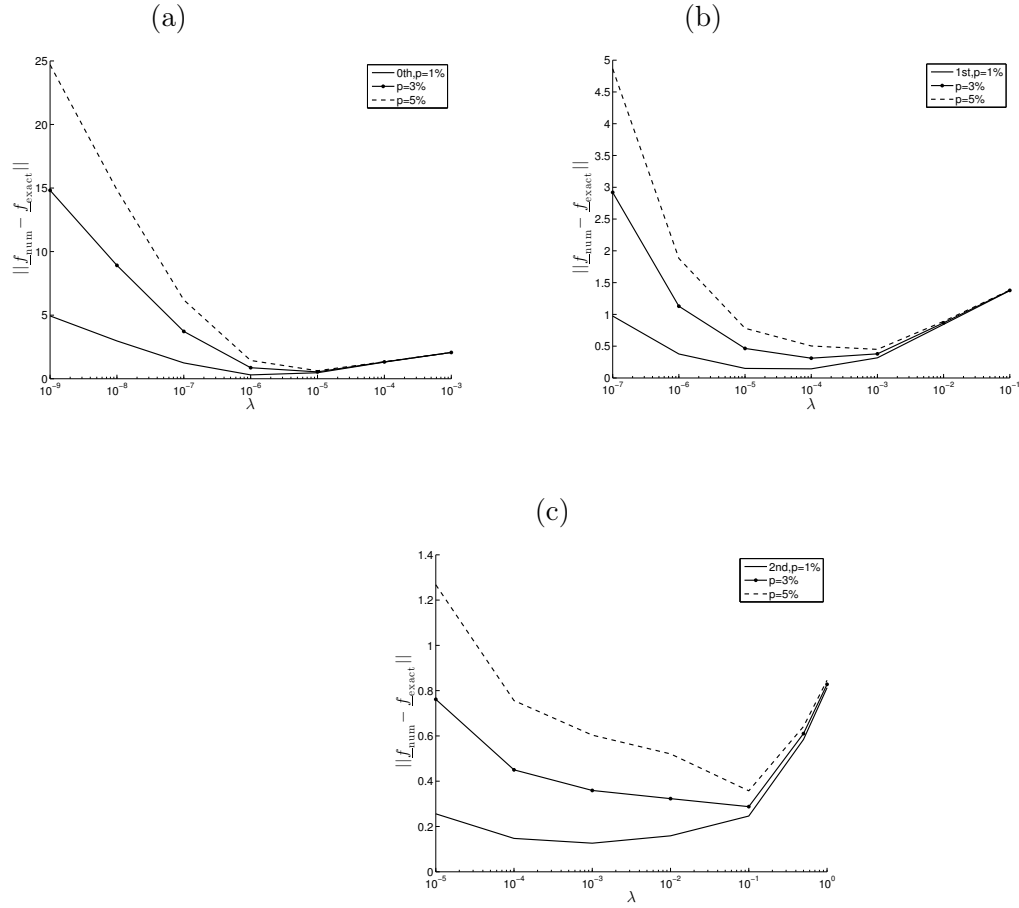


Figure 3.11: The accuracy error $\|f_{\text{num}} - f_{\text{exact}}\|$, as a function of λ , for $M = N = 80$, $p \in \{1, 3, 5\}\%$ noise, obtained using (a) zeroth, (b) first, and (c) second-order regularization, for the inverse problem of Example 2.

3.5 Numerical results and discussion

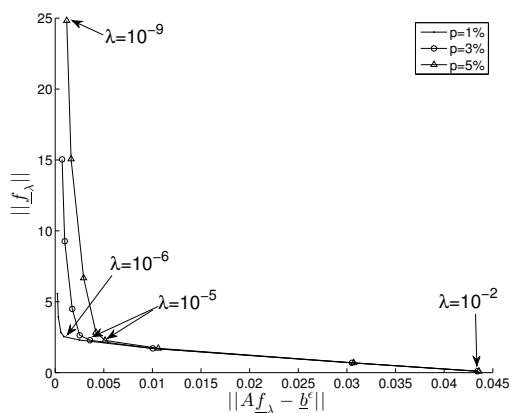


Figure 3.12: The L-curve for the zeroth-order Tikhonov regularization, for $N = M = 80$ and $p \in \{1, 3, 5\}\%$ noise, for the inverse problem of Example 2.

Table 3.4: The accuracy error $\|f_{\text{num}} - f_{\text{exact}}\|$ for various order regularization methods and percentages of noise p , for the inverse problem of Example 2. The values of λ_{opt} are also included.

Regularization	$p = 1\%$	$p = 3\%$	$p = 5\%$
zeroth	$\lambda_{\text{opt}} = 10^{-6}$ 0.2987	$\lambda_{\text{opt}} = 10^{-5}$ 0.5389	$\lambda_{\text{opt}} = 10^{-5}$ 0.6259
first	$\lambda_{\text{opt}} = 10^{-4}$ 0.1433	$\lambda_{\text{opt}} = 10^{-4}$ 0.3112	$\lambda_{\text{opt}} = 10^{-3}$ 0.4494
second	$\lambda_{\text{opt}} = 10^{-3}$ 0.1264	$\lambda_{\text{opt}} = 10^{-1}$ 0.2876	$\lambda_{\text{opt}} = 10^{-1}$ 0.3576

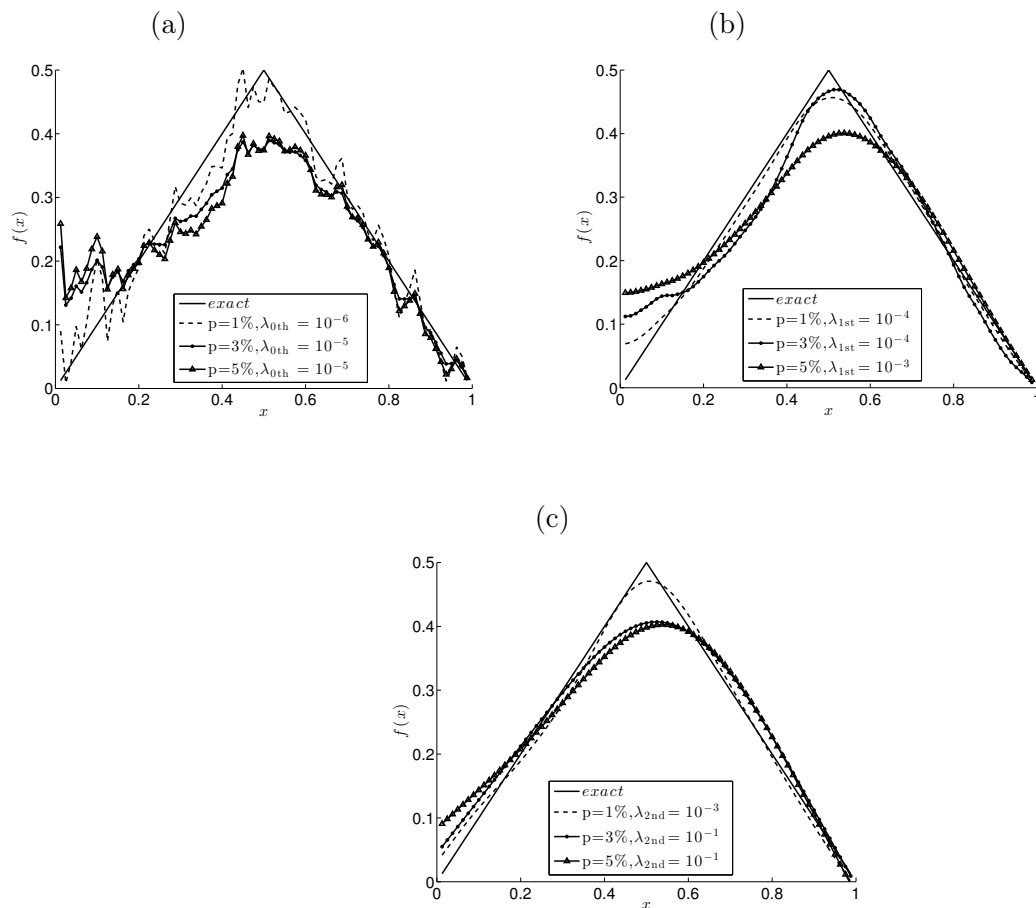


Figure 3.13: The exact solution (3.34) for the force $f(x)$ in comparison with the numerical regularized solution (3.35), for $N = M = 80$, $p \in \{1, 3, 5\}\%$ noise, and various order regularization methods, for the inverse problem of Example 2.

3.5.3 Example 3 ($h(x, t) = 1 + x + t$)

All the data and details of the numerical implementation are the same as those for Example 2, except that in the present example $h(x, t) = 1 + x + t$ in equation (3.22). Since in this case h depends also on x we cannot apply Theorem 2, but we can apply instead Theorem 1, because $H = 0$ in (3.9) is sufficiently small. This then ensures the uniqueness of the solution in the class of functions (3.10).

Figure 3.14 shows the regularized numerical solution for $f(x)$ obtained with various values of the regularization parameters listed in Table 3.5 for $p \in \{1, 3, 5\}\%$

3.5 Numerical results and discussion

noisy data. From this figure it can be seen that stable numerical solutions are obtained and that similar conclusions maintain as those obtained for Example 2.

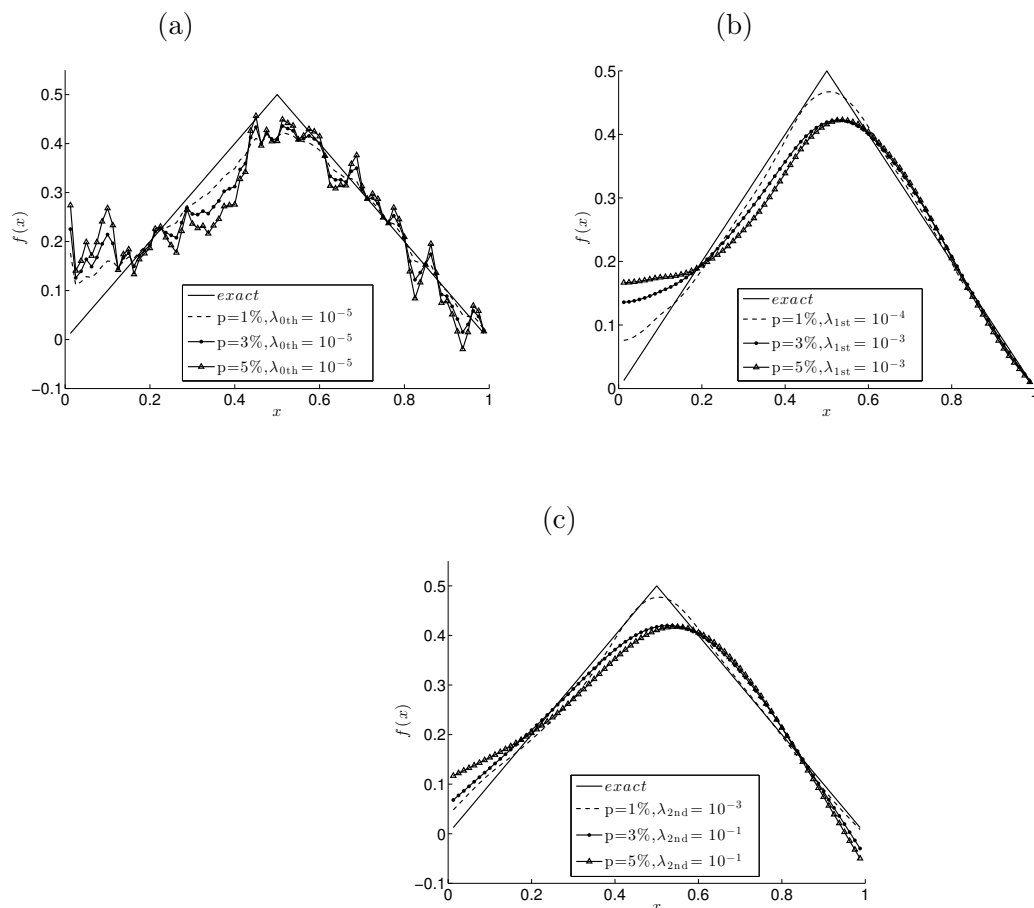


Figure 3.14: The exact solution (3.34) for the force $f(x)$ in comparison with the regularized numerical solution (3.35), for $N = M = 80$, $p \in \{1, 3, 5\}\%$ noise, and various order regularization methods, for the inverse problem of Example 3.

3.5 Numerical results and discussion

Table 3.5: The accuracy error $\|f_{\text{num}} - f_{\text{exact}}\|$ for various order regularization methods and percentages of noise p , for the inverse problem of Example 3. The values of λ_{opt} are also included.

Regularization	$p = 1\%$	$p = 3\%$	$p = 5\%$
zeroth	$\lambda_{\text{opt}} = 10^{-5}$ 0.35490	$\lambda_{\text{opt}} = 10^{-5}$ 0.49093	$\lambda_{\text{opt}} = 10^{-5}$ 0.65283
first	$\lambda_{\text{opt}} = 10^{-4}$ 0.14821	$\lambda_{\text{opt}} = 10^{-3}$ 0.35679	$\lambda_{\text{opt}} = 10^{-3}$ 0.45932
second	$\lambda_{\text{opt}} = 10^{-3}$ 0.13326	$\lambda_{\text{opt}} = 10^{-1}$ 0.27424	$\lambda_{\text{opt}} = 10^{-1}$ 0.39021

3.5.4 Example 4 ($h(x, t) = t^2$)

All the details are the same as those of Example 2, except that in the present example $h(x, t) = t^2$ in equation (3.22) is independent of x , but is a nonlinear function of t . Furthermore, one can see that $h(0) = 0$ and also, condition (3.9) is violated. Hence, we cannot apply the uniqueness Theorems 1 or 2 and, in this case, we expect a more severe situation than in the previous examples to occur. This is reflected in the very large condition numbers of the matrix A reported in Table 3.1 for Example 4 in comparison with the milder condition numbers for Examples 1-3.

The numerical solution for the flux tension (3.23) obtained by solving the direct problem given by equation (3.22) with $h(x, t) = t^2$ and equations (3.32)-(3.34) is illustrated in Figure 3.15 for various mesh sizes. From this figure it can be seen that a rapidly convergent numerical solution is achieved. As in Example 2, we add noise to the numerical flux $q_0(t)$ obtained with the finer mesh $N = M = 80$.

3.5 Numerical results and discussion

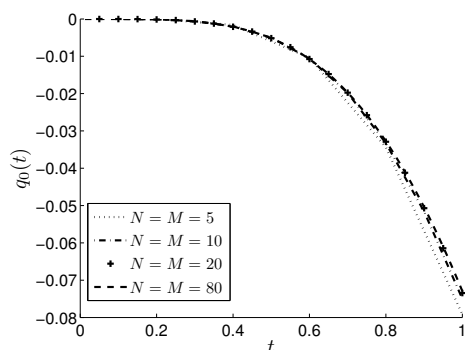


Figure 3.15: Numerical solution for the flux tension at $x = 0$, for various $N = M \in \{5, 10, 20, 80\}$, for the direct problem of Example 4.

Figure 3.16 shows the regularized numerical solution for $f(x)$ obtained with various regularization parameters listed in Table 3.6 for $p \in \{1, 3, 5\}\%$ noisy data. As in all the previous examples, stable numerical solutions are obtained. However, in contrast to Examples 2 and 3, the first-order regularization seems to perform better than the second-order regularization, with the latter one also presenting some unexpected behaviour of increase in accuracy when p increases from 1% to 3%. These conclusions may be attributed to the severe ill-posedness of the Example 4 which, as discussed above, in addition to ill-conditioning it fails to satisfy the conditions for uniqueness of solution of Theorems 1 or 2.

3.5 Numerical results and discussion

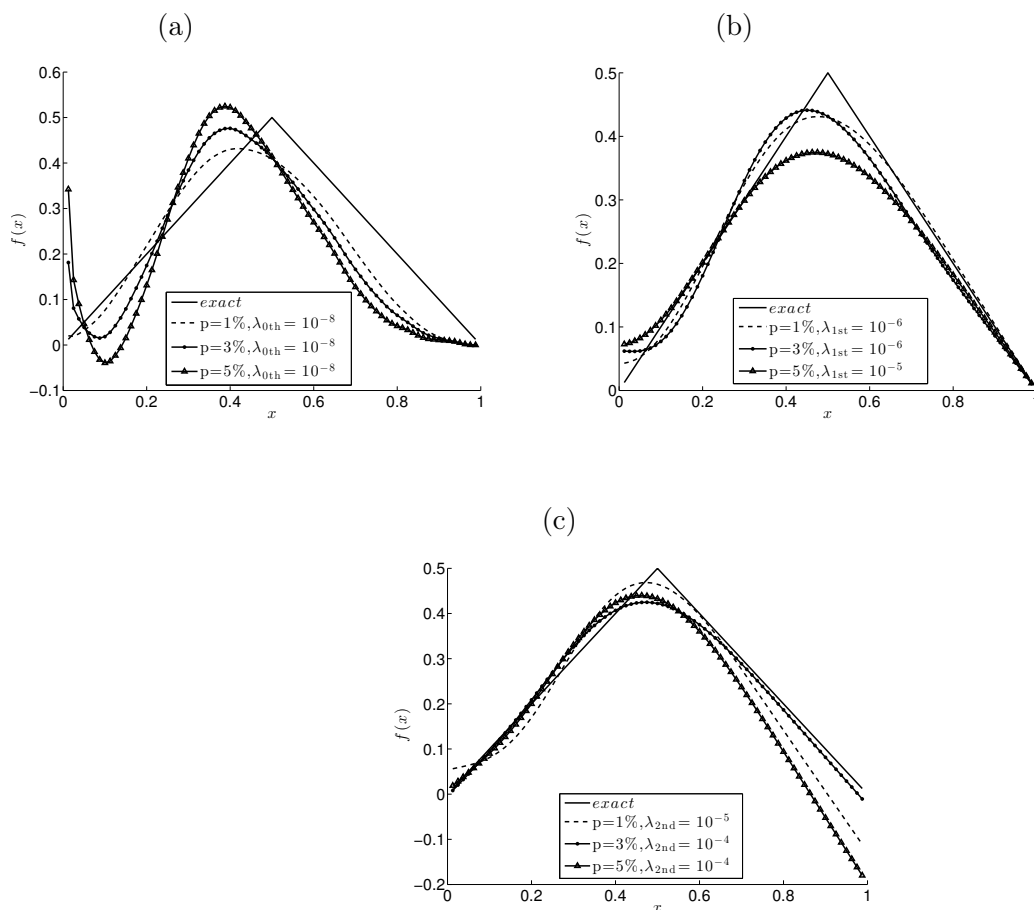


Figure 3.16: The exact solution (3.34) for the force $f(x)$ in comparison with the regularized numerical solution (3.35), for $N = M = 80$ and $p \in \{1, 3, 5\}\%$ noise, and various order regularization methods, for the inverse problem of Example 4.

Table 3.6: The accuracy error $\|f_{\text{num}} - f_{\text{exact}}\|$ for various order regularization methods and percentages of noise p , for the inverse problem of Example 4. The values of λ_{opt} are also included.

Regularization	$p = 1\%$	$p = 3\%$	$p = 5\%$
zeroth	$\lambda_{\text{opt}} = 10^{-8}$ 0.5947	$\lambda_{\text{opt}} = 10^{-8}$ 0.8082	$\lambda_{\text{opt}} = 10^{-8}$ 1.0863
first	$\lambda_{\text{opt}} = 10^{-6}$ 0.1826	$\lambda_{\text{opt}} = 10^{-6}$ 0.2668	$\lambda_{\text{opt}} = 10^{-5}$ 0.4053
second	$\lambda_{\text{opt}} = 10^{-5}$ 0.4313	$\lambda_{\text{opt}} = 10^{-4}$ 0.2178	$\lambda_{\text{opt}} = 10^{-4}$ 0.6912

3.6 Extension to multiple sources

In this section, we consider an extension of the inverse space-dependent problem, in the situation when

$$F(\underline{x}, t) = f(\underline{x})h(\underline{x}, t) + g(\underline{x})\theta(\underline{x}, t), \quad (\underline{x}, t) \in \Omega \times (0, T]. \quad (3.36)$$

where $h(\underline{x}, t)$ and $\theta(\underline{x}, t)$ are given functions and $f(\underline{x})$ and $g(\underline{x})$ are space-dependent unknown force components to be determined. Under the assumption (3.36), equation (3.1) (take $c = 1$ for simplicity) in one-dimension, i.e. $n = 1$ and $\Omega = (0, L)$, becomes

$$u_{tt}(x, t) = u_{xx}(x, t) + f(x)h(x, t) + g(x)\theta(x, t), \quad (x, t) \in (0, L) \times (0, T]. \quad (3.37)$$

This has to be solved subject to the initial and boundary conditions (3.14)-(3.16) and the overspecified flux tensions at both ends of the string, namely, (3.23) and

$$\frac{\partial u}{\partial x}(L, t) = q(L, t) =: q_L(t), \quad t \in (0, T]. \quad (3.38)$$

The uniqueness of solution still holds in the case $h(x, t) = 1$, $\theta(x, t) = t$, see Theorem 8 of (Engl, Scherzer and Yamamoto, 1994), but for more general cases, e.g. $h(x, t) = 1$, $\theta(x, t) = t^2$, the solution $(f(x), g(x), u(x, t))$ is not unique, see the counterexample to uniqueness given in (Engl, Scherzer and Yamamoto, 1994).

3.6 Extension to multiple sources

In discretised finite-difference form equations (3.14)-(3.16) and (3.37) recast as equations (3.18), (3.19),

$$u_{i,j+1} - (\Delta t)^2 f_i h_{i,j} - (\Delta t)^2 g_i \theta_{i,j} = r^2 u_{i+1,j} + 2(1-r^2)u_{i,j} + r^2 u_{i-1,j} - u_{i,j-1}, \quad i = \overline{1, (M-1)}, \quad j = \overline{1, (N-1)}, \quad (3.39)$$

and

$$u_{i,1} - \frac{1}{2}(\Delta t)^2 f_i h_{i,0} - \frac{1}{2}(\Delta t)^2 g_i \theta_{i,0} = \frac{1}{2}r^2 \varphi(x_{i+1}) + (1-r^2)\varphi(x_i) + \frac{1}{2}r^2 \varphi(x_{i-1}) + (\Delta t)\psi(x_i), \quad i = \overline{1, (M-1)}. \quad (3.40)$$

where $g_i := g(x_i)$ and $\theta_{i,j} := \theta(x_i, t_j)$.

Discretizing (3.23) and (3.38), using (3.21), we also have (3.26) and

$$q_L(t_j) = \frac{\partial u}{\partial x}(L, t_j) = \frac{3u_{M,j} - 4u_{M-1,j} + u_{M-2,j}}{2\Delta x}, \quad j = \overline{1, N}. \quad (3.41)$$

In practice, the additional observations (3.26) and (3.41) come from measurement which is inherently contaminated with errors. We therefore model this by replacing the exact data $q_0(t)$ and $q_L(t)$ by the noisy data (3.27) and

$$q_L^\epsilon(t_j) = q_L(t_j) + \tilde{\epsilon}_j, \quad j = \overline{1, N}, \quad (3.42)$$

where $(\tilde{\epsilon}_j)_{j=\overline{1, N}}$ and N random noisy variables generated from a Gaussian normal distribution with mean zero and standard deviation $\tilde{\sigma} = p \times \max_{t \in [0, T]} |q_L(t)|$.

Assembling (3.26), (3.39)-(3.41), and using (3.18) and (3.19), the discretised inverse problem reduces to solving a global linear system of $(M-1) \times N + (N+N)$ equations with $(M-1) \times N + ((M-1) + (M-1))$ unknowns. Since this system is linear we can eliminate the unknowns $u_{i,j}$ for $i = \overline{1, (M-1)}, j = \overline{1, N}$, to reduce the problem to solving an ill-conditioned system of $2N$ equations with $2(M-1)$ unknowns of the form

$$A(\underline{f}, \underline{g}) = \underline{b}^\epsilon. \quad (3.43)$$

This system is solved using the Tikonov regularization method, as described in the previous section.

3.6.1 Example 5

This is an example in which we take $c = L = T = 1$, $h(x, t) = 1$ and $\theta(x, t) = t$ and the input data

$$u(x, 0) = \varphi(x) = \sin(\pi x), \quad u_t(x, 0) = \psi(x) = x^2 + 1, \quad x \in [0, 1], \quad (3.44)$$

$$u(0, t) = P_0(t) = t + \frac{t^2}{2}, \quad u(1, t) = P_L(t) = 2t + \frac{t^2}{2}, \quad t \in (0, 1], \quad (3.45)$$

$$-\frac{\partial u}{\partial x}(0, t) = q_0(t) = -\pi, \quad \frac{\partial u}{\partial x}(1, t) = q_L(t) = 2t - \pi, \quad t \in (0, 1]. \quad (3.46)$$

The exact solution is given by

$$f(x) = 1 + \pi^2 \sin(\pi x), \quad g(x) = -2, \quad u(x, t) = x^2 t + \sin(\pi x) + t + \frac{t^2}{2}, \\ (x, t) \in [0, 1] \times [0, 1]. \quad (3.47)$$

We first consider the case of exact data, i.e. $p = 0$ and hence $\underline{\epsilon} = \underline{\tilde{\epsilon}} = \underline{0}$ in (3.27) and (3.42). The numerical results corresponding to $f(x)$ and $g(x)$ are plotted in Figure 3.17. From this figure it can be seen that convergent and accurate numerical solutions are obtained especially, for $f(x)$, although for $g(x)$ there are some inaccuracies manifested near the end points $x \in \{0, 1\}$.

We include some ($p = 1\%$) noise into the input data (3.26) and (3.41), as given by equations (3.27) and (3.42). Figure 3.18 shows the regularized numerical solutions for $f(x)$ and $g(x)$ obtained with various regularizations and one can observe that reasonably stable numerical solutions are obtained, especially by the first- and second-order regularizations.

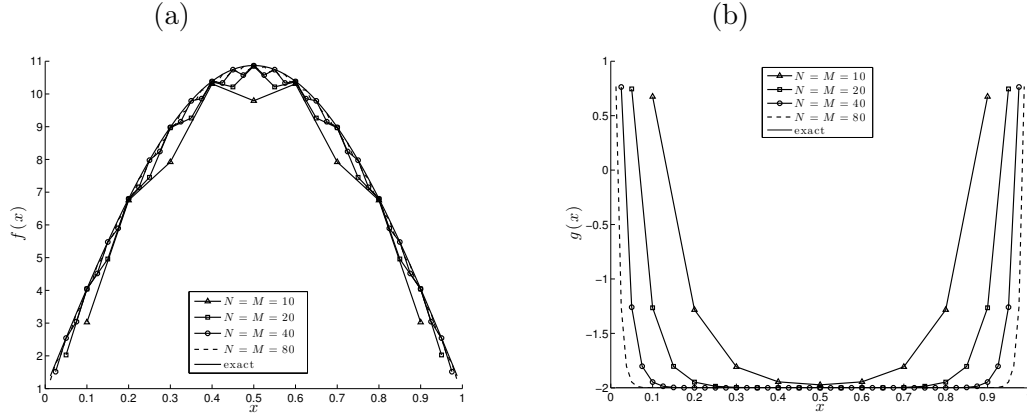


Figure 3.17: The exact (—) solutions (3.47) for the force components $f(x)$ and $g(x)$ in comparison with the numerical solutions for various $N = M \in \{10, 20, 40, 80\}$, and no regularization, for exact data, for the inverse problem of Example 5.

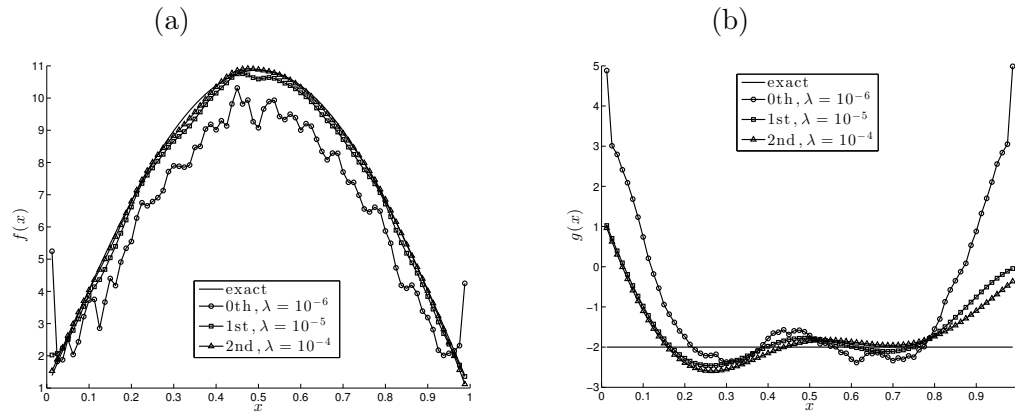


Figure 3.18: The exact (—) solutions (3.47) for the force components $f(x)$ and $g(x)$ in comparison with the numerical solutions, for $N = M = 80$, $p = 1\%$ noise and various order regularization methods, for the inverse problem of Example 5.

3.7 Conclusions

In this chapter, the determination of space-dependent forces from boundary Cauchy data in the wave equation has been investigated. The solution of this linear inverse problem is unique, but is still ill-posed since small errors in the

input measured flux tension cause large errors in the output force. The same problem has been considered in Chapter 2 using the BEM, the separation of variables and a truncation or a regularization method. However, in this chapter the problem is discretised numerically using the FDM, and in order to stabilise the solution, the Tikhonov regularization method has been employed. This approach is more general as it is applicable to non-homogeneous materials which are not feasible to be approached by the methods of Chapter 2. The choice of the regularization parameter was based on the L-curve criterion. Numerical examples indicate that the method can accurately and stably recover the unknown space-dependent force.

As previously discussed in subsection 2.7 of the previous chapter, there is much more literature on the corresponding inverse space-dependent heat source identification from Cauchy data for the parabolic heat equation, see (Cannon, 1968; Coles and Murio, 2001; Engl, Scherzer and Yamamoto, 1994; Hasanov, 2011; Yamamoto, 1995). In addition to these, one can also mention the case of retrieving point sources for the heat equation, see e.g. (El Badia, Ha-Duong and Hamdi, 2005), and it would be interesting in the future to address the identification of point forces for the wave equation, see (El Badia and Ha-Duong, 2001) or even for the Euler-Bernoulli beam equation, see (Hasanov and Kawano, 2016).

The corresponding time-dependent force identification for the wave equation will be investigated in the next chapter.

Chapter 4

Determination of forcing functions in the wave equation. Part II: the time-dependent case

4.1 Introduction

In the previous two chapters the unknown force function in the wave equation was sought as a function of the space variable. In this chapter, it is assumed to depend on the time variable only. The theoretical basis for our numerical investigation is given in (Prilepko, Orlovsky and Vasin, 2000, Sect. 9.2), where the existence and uniqueness of solution of the inverse time-dependent force function for the wave equation have been established. However, no numerical results were presented and it is the main purpose of this chapter to develop an efficient numerical solution for this linear, but ill-posed inverse problem.

The mathematical formulation of the inverse problem under investigation is given in Section 4.2. No *a priori* information is assumed available on the functional form of the unknown external force. The numerical discretisation of both the direct and inverse problems based on the FDM are described in one-dimension in Sections 4.3 and 4.4, respectively. Both these problems are linear, but the direct problem is well-posed, whilst the inverse problem is ill-posed. Consequently, upon the numerical FDM discretisation the resulting systems of linear algebraic equations are well-, respectively, ill-conditioned. The ill-conditioning is dealt with

by employing the Tikhonov regularization method, (Philips, 1962). The choice of the regularization parameter introduced by this technique is important for the stability of the numerical solution and in this chapter this is based on the L-curve criterion, (Hansen, 2001). The accuracy and stability of the inverse problem solution is analysed by using exact and numerically simulated noisy measurements. Numerical results are illustrated and discussed in Sections 4.5, and conclusions are provided in Section 4.6.

4.2 Mathematical formulation

The governing equation for a vibrating bounded structure $\Omega \subset \mathbb{R}^n$, $n = 1, 2, 3$, acted upon by a force $F(\underline{x}, t)$ is given by the wave equation (3.1). For simplicity, we assume that c is a constant, but we can also let c be a positive smooth function depending on the space variable \underline{x} . Equation (3.1) has to be solved subject to the initial conditions (3.3) and (3.4).

On the boundary of the structure $\partial\Omega$ we can prescribe Dirichlet, Neumann or Robin boundary conditions. Due to the linearity of equation (3.1) and of the direct and inverse force problems which are investigated we can assume, for simplicity, that these boundary conditions are homogeneous. We can therefore take

$$u(\underline{x}, t) = 0, \quad (\underline{x}, t) \in \partial\Omega \times [0, T], \quad (4.1)$$

or,

$$\frac{\partial u}{\partial \nu} + \sigma(\underline{x})u = 0, \quad (\underline{x}, t) \in \partial\Omega \times [0, T], \quad (4.2)$$

where σ is a sufficiently smooth function. Equation (4.2) includes the Neumann boundary condition which is obtained for $\sigma \equiv 0$.

If the force $F(\underline{x}, t)$ is given, then the equations above form a direct well-posed problem for the displacement $u(\underline{x}, t)$. However, if the force function $F(\underline{x}, t)$ cannot be directly observed it hence becomes unknown and then clearly, the above set of equations is not sufficient to determine the pair solution $(u(\underline{x}, t), F(\underline{x}, t))$. Then, we can consider the additional integral measurement

$$\int_{\Omega} \omega(\underline{x})u(\underline{x}, t)d\underline{x} = \Lambda(t), \quad t \in [0, T], \quad (4.3)$$

where ω is a given weight function, and further assume that

$$F(\underline{x}, t) = f_1(\underline{x}, t)h(t) + f_2(\underline{x}, t), \quad (\underline{x}, t) \in \Omega \times [0, T], \quad (4.4)$$

where $f_1(\underline{x}, t)$ and $f_2(\underline{x}, t)$ represent known forcing function components and $h(t)$ is an unknown time-dependent coefficient that is sought. Physically, the expression (4.3) represents a space average measurement of the displacement. Also, if one takes the weight function ω to mimic an approximation to the Dirac delta distribution $\delta(\underline{x} - \underline{x}_0)$, where $\underline{x}_0 \in \Omega$ is fixed, then (4.3) becomes a pointwise measurement of the displacement, namely, $u(\underline{x}_0, t) = \Lambda(t)$ for $t \in [0, T]$. Also, physically, (4.4) expresses that any unknown feature of the force F acting on the structure is confined to the time variation only while any space dependency is assumed known. The assumption (4.4) is also needed in order to ensure the unique solvability of the inverse force problem under investigation, see Chapter 9 of the book by (Prilepko, Orlovsky and Vasin, 2000). In that book theorems that establish the existence and uniqueness of solution of the inverse force problems (3.1), (3.3), (3.4), (4.1), (4.3), (4.4) and (3.1), (3.3), (3.4), (4.2)-(4.4), respectively, are provided. Although these theorems ensure that a unique solution exists, the following example shows that this solution does not depend continuously upon the input data.

Example of instability. Consider the one-dimensional case, i.e. $n = 1$ and $\Omega = (0, \pi)$, and the inverse problem given by equations (3.1), (3.3), (3.4), (4.1), (4.3) and (4.4) in the form

$$u_{tt}(x, t) = u_{xx}(x, t) + f_1(x, t)h(t) + f_2(x, t), \quad (x, t) \in (0, \pi) \times (0, T), \quad (4.5)$$

$$u(x, 0) = \varphi(x) = 0, \quad u_t(x, 0) = \psi(x) = \frac{x(x - \pi)}{n^{1/2}}, \quad x \in (0, \pi), \quad (4.6)$$

$$u(0, t) = u(\pi, t) = 0, \quad t \in [0, T], \quad (4.7)$$

$$\Lambda(t) = \int_0^\pi \omega(x)u(x, t)dx = \frac{\pi^5 \sin(nt)}{30n^{3/2}}, \quad t \in [0, T], \quad (4.8)$$

4.3 Numerical solution of the direct problem

where $n \in \mathbb{N}^*$ and

$$\omega(x) = x(x - \pi), \quad f_1(x, t) = -x(x - \pi), \quad f_2(x, t) = -\frac{2 \sin(nt)}{n^{3/2}}.$$

One can observe that the analytical solution of the inverse problem (4.5)-(4.8) is given by

$$u(x, t) = \frac{\sin(nt)x(x - \pi)}{n^{3/2}}, \quad (4.9)$$

$$h(t) = n^{1/2} \sin(nt). \quad (4.10)$$

Then, one can easily see that, as $n \rightarrow \infty$ all the input data (4.6)-(4.8) tend to zero, but the output time-dependent component (4.10) becomes unbounded and oscillatory. This shows that the inverse problem under investigation is ill-posed by violating the stability condition with respect to errors in the data (4.8).

The next Sections 4.3 and 4.4 describe the actual numerical reconstruction of the solution of the direct and inverse problems, respectively.

4.3 Numerical solution of the direct problem

In this section, we consider the direct initial boundary value problem (3.1), (3.3), (3.4) and (4.1), for simplicity, in one-dimension, i.e. $n = 1$ and $\Omega = (0, L)$ with $L > 0$, when the force $F(x, t)$ is known and the displacement $u(x, t)$ is to be determined. That is, we have to solve the wave equation (3.13) subject to the initial conditions (3.14) and the homogeneous Dirichlet boundary conditions.

$$u(0, t) = u(L, t) = 0, \quad t \in [0, T]. \quad (4.11)$$

The discrete form of this problem is as in subsection 3.3 given by equations (3.17), (3.18), (3.20) and

$$u_{0,j} = 0, \quad u_{M,j} = 0, \quad j = \overline{0, N}. \quad (4.12)$$

The desired output (4.3) is calculated using the trapezium rule

$$\Lambda(t_j) = \frac{\Delta x}{2} \left(\omega_0 u_{0,j} + 2 \sum_{i=1}^{M-1} \omega_i u_{i,j} + \omega_M u_{M,j} \right) = \Delta x \sum_{i=1}^{M-1} \omega_i u_{i,j}, \quad j = \overline{1, N}, \quad (4.13)$$

4.4 Numerical solution of the inverse problem

where $\omega_i = \omega(x_i)$ for $i = \overline{0, M}$, and use has been made of (4.12).

The normal derivative at the boundary is calculated using the second-order finite-difference approximations (3.21), namely,

$$\begin{aligned} -\frac{\partial u}{\partial x}(0, t_j) &= -\frac{4u_{1,j} - u_{2,j} - 3u_{0,j}}{2\Delta x} = \frac{u_{2,j} - 4u_{1,j}}{2\Delta x}, \\ \frac{\partial u}{\partial x}(L, t_j) &= \frac{3u_{M,j} - 4u_{M-1,j} + u_{M-2,j}}{2\Delta x} = \frac{u_{M-2,j} - 4u_{M-1,j}}{2\Delta x}, \quad j = \overline{1, N}, \end{aligned} \quad (4.14)$$

where again use has been made of (4.12). This is also consistent with the general second-order finite-difference scheme used.

4.4 Numerical solution of the inverse problem

We now consider the inverse initial boundary value problem (3.3), (3.4), (4.1), (4.3) and (4.4), in one-dimension, i.e. $n = 1$ and $\Omega = (0, L)$, when both the force $h(t)$ and the displacement $u(x, t)$ are to be determined, from the governing equation

$$u_{tt}(x, t) = c^2 u_{xx}(x, t) + f_1(x, t)h(t) + f_2(x, t), \quad (x, t) \in (0, L) \times [0, T], \quad (4.15)$$

subject to the initial and boundary conditions (3.14) and (4.11), and the measurement (4.3).

In discretised finite-difference form equations (3.14), (4.11) and (4.15) recast as equations (3.18), (4.12), and

$$\begin{aligned} u_{i,j+1} - (\Delta t)^2 f_{1i,j} h_j &= r^2 u_{i+1,j} + 2(1 - r^2)u_{i,j} + r^2 u_{i-1,j} - u_{i,j-1} \\ &+ (\Delta t)^2 f_{2i,j}, \quad i = \overline{1, (M-1)}, \quad j = \overline{1, (N-1)}, \end{aligned} \quad (4.16)$$

where $f_{1i,j} := f_1(x_i, t_j)$, $h_j := h(t_j)$ and $f_{2i,j} := f_2(x_i, t_j)$. Putting $j = 0$ in equation (4.16) and using (3.18), we obtain

$$\begin{aligned} u_{i,1} - \frac{1}{2}(\Delta t)^2 f_{1i,0} h_0 &= \frac{1}{2}r^2 \varphi(x_{i+1}) + (1 - r^2)\varphi(x_i) + \frac{1}{2}r^2 \varphi(x_{i-1}) \\ &+ (\Delta t)\psi(x_i) + \frac{1}{2}(\Delta t)^2 f_{2i,0}, \quad i = \overline{1, (M-1)}. \end{aligned} \quad (4.17)$$

4.4 Numerical solution of the inverse problem

In practice, the additional observation (4.13) comes from measurement which is inherently contaminated with errors. We therefore model this by replacing the exact data $\Lambda(t_j)$ with the noisy data

$$\Lambda^\epsilon(t_j) = \Lambda(t_j) + \epsilon_j, \quad j = \overline{1, N}, \quad (4.18)$$

where $(\epsilon_j)_{j=\overline{1, N}}$ are N random noisy variables generated (using the MATLAB routine 'normrnd') from a Gaussian normal distribution with mean zero and standard deviation $\tilde{\sigma}$ given by

$$\tilde{\sigma} = p \times \max_{t \in [0, T]} |\Lambda(t)|, \quad (4.19)$$

where p represents the percentage of noise.

Assembling equations (4.13), (4.16) and (4.17), and using (3.18) and (4.12), the discretised inverse problem reduces to solving a global linear, but ill-conditioned system of $(M-1) \times N + N$ equations with $(M-1) \times N + N$ unknowns. Since this system is linear we can eliminate the unknowns $u_{i,j}$ for $i = \overline{1, (M-1)}, j = \overline{1, N}$, to reduce the problem to solving an ill-conditioned system of N equations with N unknowns of the generic form

$$A\underline{h} = \underline{b}^\epsilon, \quad (4.20)$$

where the right-hand side \underline{b}^ϵ includes the noisy data (4.18).

For the examples that will be considered in the next section, the condition numbers of the matrix A in (4.20) given in Table 4.1 are of $O(10^2)$ to $O(10^4)$ for $M = N \in \{10, 20, 40, 80\}$, respectively. These large condition numbers indicate that the system of equations (4.20) is ill-conditioned. One can finally remark that the condition number $\text{cond}(A)$ increases like $O(N^2)$ for Examples 1 and 3.

The ill-conditioning nature of the matrix A can also be revealed by plotting its normalised singular values σ_k/σ_1 for $k = \overline{1, M}$, in Figure 4.1.

Table 4.1: Condition number of the matrix A .

$N = M$	Example 1	Example 2	Example 3
10	57.8	73.9	78.3
20	234.5	309.9	313.8
40	939.5	1273.7	1251.7
80	3755.7	5172.4	4993.9

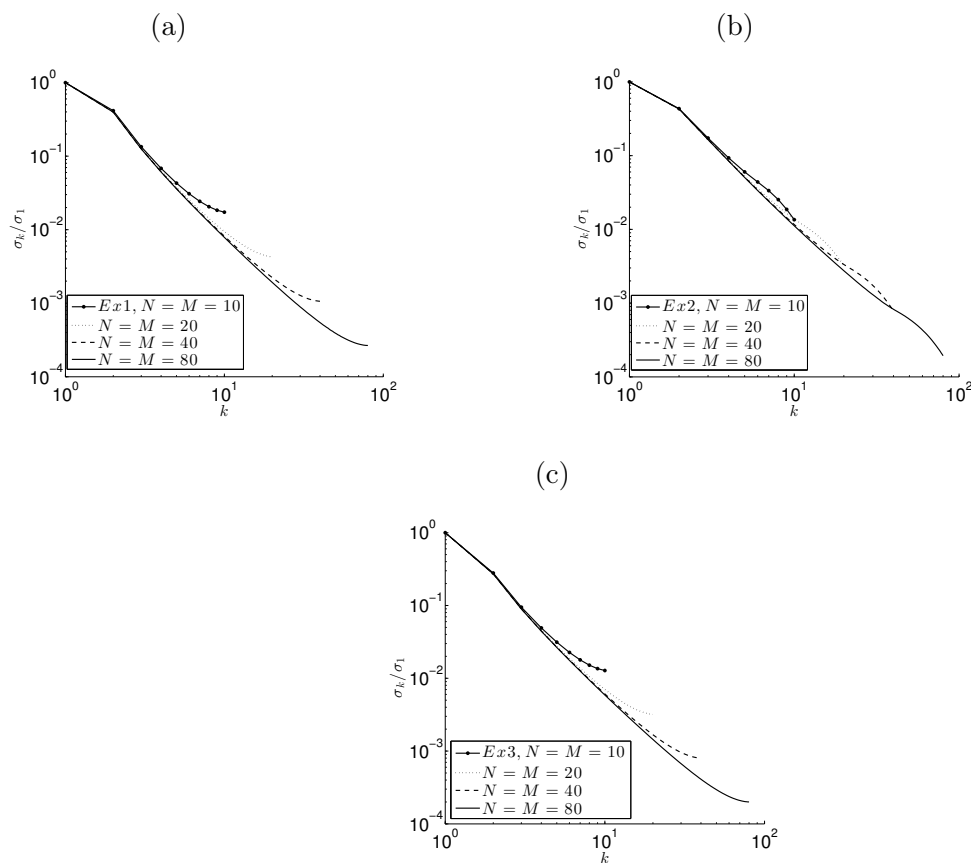


Figure 4.1: Normalised singular values σ_k/σ_1 for $k = \overline{1, M}$, for Examples 1-3.

4.5 Numerical results and discussion

In all examples we take, for simplicity, $c = L = T = 1$.

4.5.1 Example 1

As a typical test example, consider first the direct problem (3.13), (3.14) and (4.11) with the input data

$$u(x, 0) = \varphi(x) = x(x - 1), \quad u_t(x, 0) = \psi(x) = 0, \quad x \in [0, 1], \quad (4.21)$$

$$u(0, t) = 0, \quad u(1, t) = 0, \quad t \in [0, 1], \quad (4.22)$$

4.5 Numerical results and discussion

$$F(x, t) = 6tx(x - 1) - 2(t^3 + 1), \quad (x, t) \in (0, 1) \times [0, 1]. \quad (4.23)$$

The exact solution of this direct problem is given by

$$u(x, t) = x(x - 1)(t^3 + 1), \quad (x, t) \in [0, 1] \times [0, 1]. \quad (4.24)$$

For the weight function

$$\omega(x) = x(x - 1), \quad x \in (0, 1), \quad (4.25)$$

the desired output (4.3) is given by

$$\Lambda(t) = \int_0^1 \omega(x)u(x, t)dx = \frac{1}{30}(t^3 + 1), \quad t \in [0, 1]. \quad (4.26)$$

The absolute errors between the numerical and exact solutions for $u(x, t)$ at interior points are shown in Figure 4.2 and one can observe that an excellent agreement is obtained. From this figure it can also be observed that the errors are reduced by a factor of 4(= 2^2), when N is doubled, which confirms that the numerical results are correct, and accurate up to second-order, due to the second-order FDM used. Figure 4.3 also gives the corresponding absolute errors for $\Lambda(t)$. From this figure it can be seen that the numerical results are in very good agreement with the exact solution (4.26), and that convergence is rapidly achieved as $N = M$ increases.

The inverse problem given by equations (4.15) with $f_1(x, t) = 6x(x - 1)$ and $f_2(x, t) = -2(t^3 + 1)$, (4.21), (4.22) and (4.26) is considered next. One can easily check that conditions in (Prilepko, Orlovsky and Vasin, 2000) are satisfied and hence the existence of a unique solution is ensured. In fact, the exact solution $(u(x, t), h(t))$ of the inverse problem is given by equation (4.24) for $u(x, t)$ and $h(t) = t$.

4.5 Numerical results and discussion

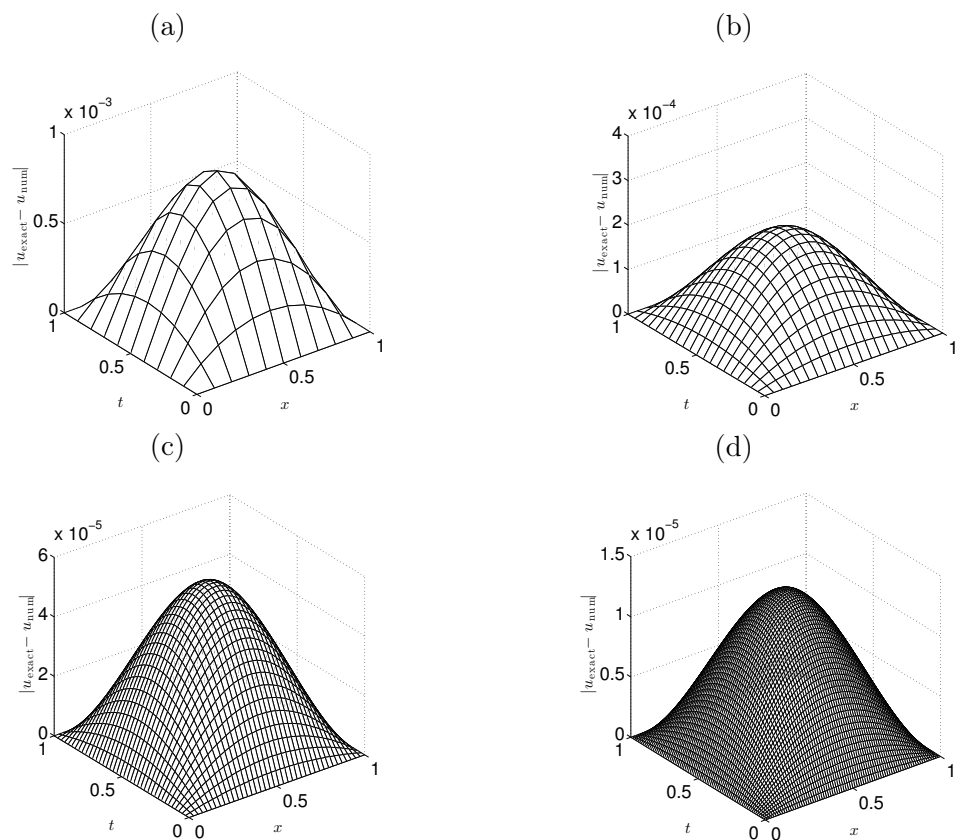


Figure 4.2: The absolute errors between the exact (4.24) and numerical displacement $u(x, t)$ obtained by solving the direct problem with $N = M =$ (a) 10, (b) 20, (c) 40, and (d) 80, for Example 1.

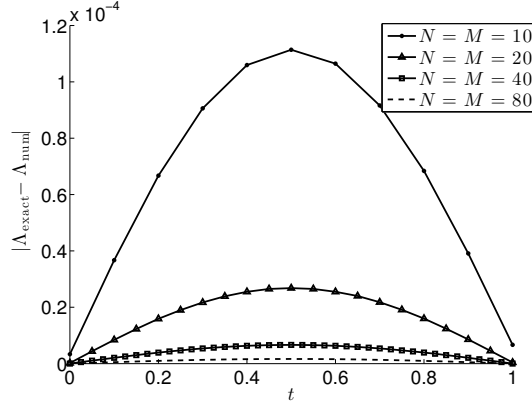


Figure 4.3: The absolute error between the exact (4.26) and numerical $\Lambda(t)$ obtained by solving the direct problem with $N = M \in \{10, 20, 40, 80\}$, for Example 1.

4.5.1.1 Exact data

We first consider the case of exact data, i.e. $p = 0$ and hence $\underline{\epsilon} = \underline{0}$ in (4.18). The numerical results corresponding to $h(t)$ and $u(x, t)$ are plotted in Figures 4.4 and 4.6, respectively. From these figures it can be seen that convergent and accurate numerical solutions are obtained and the accuracy in obtaining the internal displacement $u(x, t)$ is higher than that in the time-dependent coefficient $h(t)$ of the force. In fact, as previously illustrated at the end of section 4.2, expressions (4.9) and (4.10) show that the inverse force problem is ill-posed in the component $h(t)$ but not in the component $u(x, t)$ of the pair solution $(h(t), u(x, t))$.

The ℓ^2 -errors between the analytical and numerical h , plotted in Figure 4.4, as functions of N , have been obtained to be $E = 0.0116, 0.0039, 0.0013$ and 0.0004 for $(M =)N = 10, 20, 40$ and 80 , respectively. These values of the error show that the numerical solution is indeed convergent to the exact solution for $h(t)$, as $M = N$ increases, with the order of convergence being approximately 1.6, see Figure 4.5(a).

4.5 Numerical results and discussion

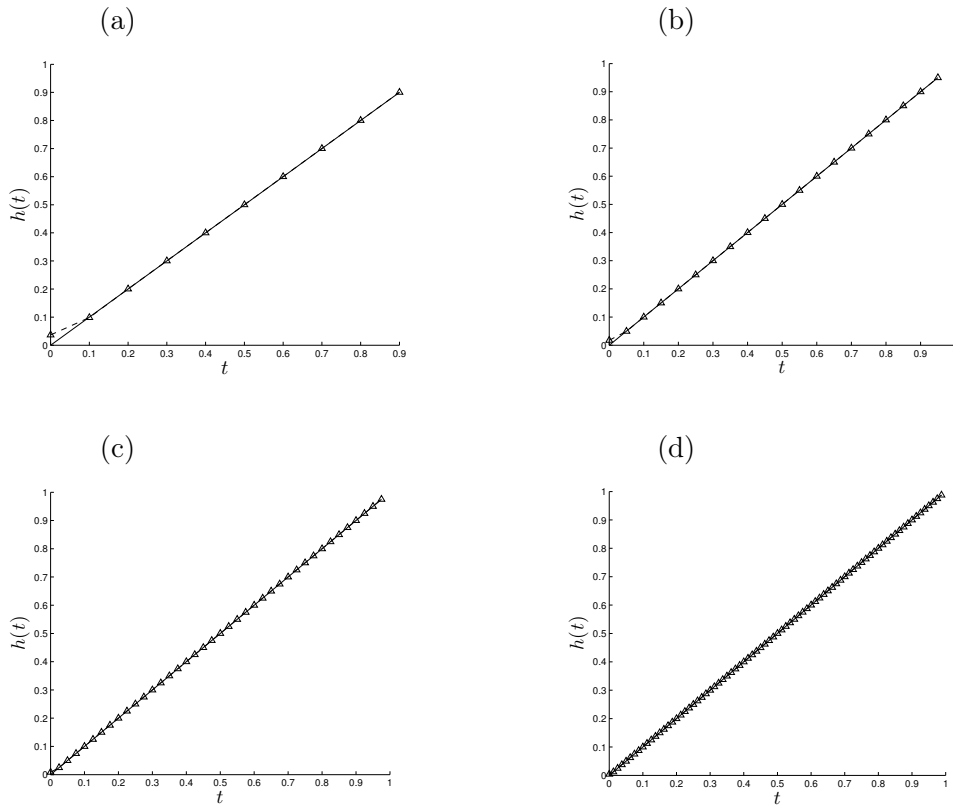


Figure 4.4: The exact (—) solution for $h(t)$ in comparison with the numerical solution (— Δ —) for various $N = M =$ (a) 10, (b) 20, (c) 40, and (d) 80, and no regularization, for exact data, for the inverse problem of Example 1.

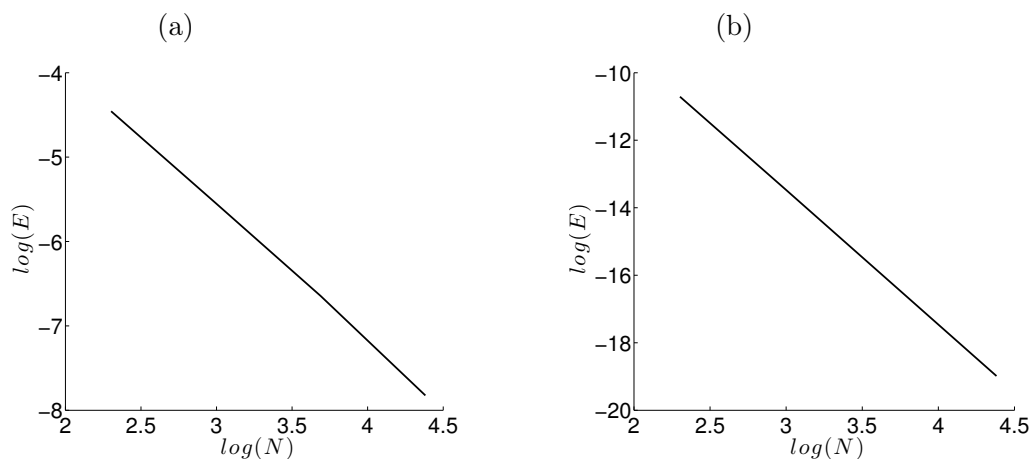


Figure 4.5: The log-log plot of the ℓ^2 -errors between the analytical and numerical (a) $h(t)$ and (b) $u(x, t)$, as functions of N , for Example 1.

On the other hand, the ℓ^2 -errors between the analytical and numerical $u(x, t)$, plotted in Figure 4.6, as functions of N , have been obtained to be $E = 2.2E - 5$, $1.4E - 6$, $9.0E - 8$ and $5.6E - 9$ for $(M =)N = 10, 20, 40$ and 80 , respectively. These values of the error show that the numerical solution is indeed convergent to the exact solution $u(x, t)$ as $M = N$ increases, with the order of convergence being approximately 4, see Figures 4.5(b). This order is greater than the order 2 of convergence obtained in Figure 4.2 when solving the direct problem probably because in the inverse problem more information on u contained in the condition (4.13) is in addition imposed. Nevertheless, more research on predicting the order of convergence of FDM schemes for solving inverse and ill-posed problems should be undertaken in a future work.

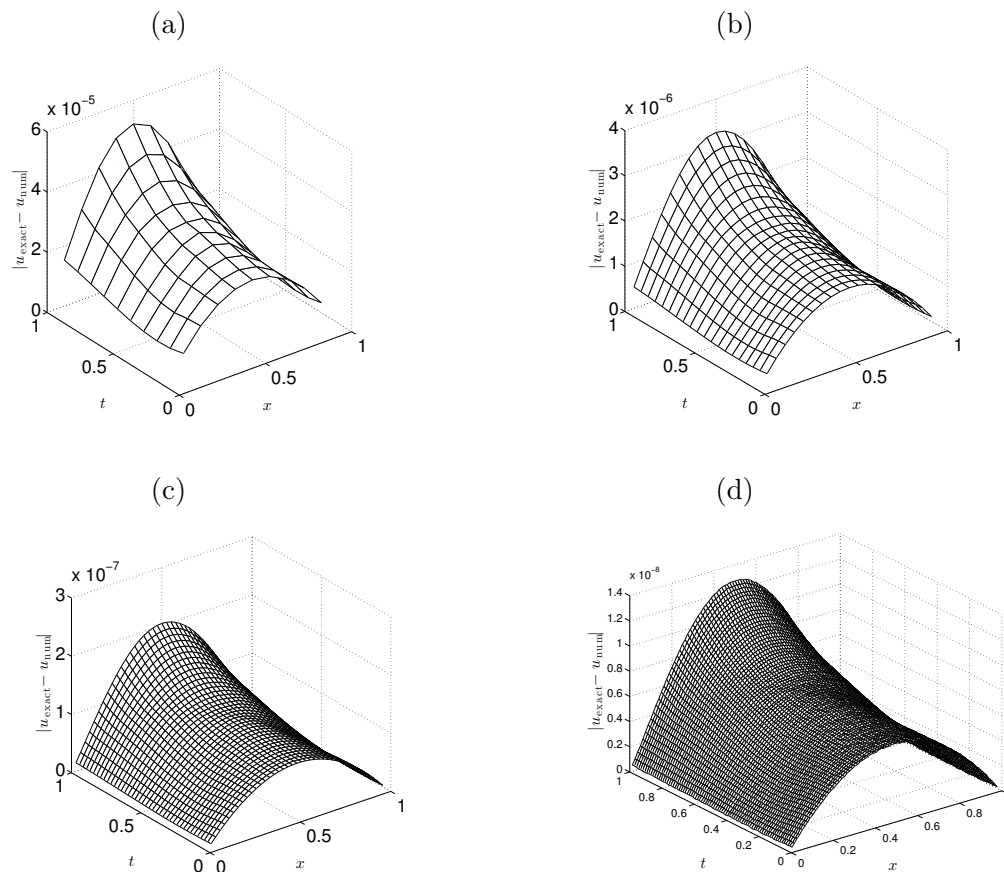


Figure 4.6: The absolute errors between the exact (4.24) and numerical displacement $u(x, t)$ obtained with $N = M =$ (a) 10, (b) 20, (c) 40, and (d) 80, and no regularization, for exact data, for the inverse problem of Example 1.

4.5.1.2 Noisy data

In order to investigate the stability of the numerical solution we include some $p \in \{1, 3, 5\}\%$ noise into the input data (4.13), as given by equation (4.18). The numerical solution for $h(t)$ obtained with $N = M = 80$ and no regularization has been found highly oscillatory and unstable, as shown in Figure 4.7. In order to deal with this instability we employ the Tikhonov regularization which gives the regularized solution, (Philips, 1962),

$$\underline{h}_\lambda = (A^T A + \lambda D_k^T D_k)^{-1} A^T \underline{b}^\epsilon. \quad (4.27)$$

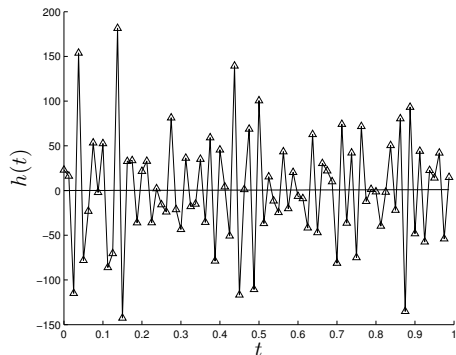


Figure 4.7: The exact (—) solution for $h(t)$ in comparison with the numerical solution (— Δ —) for $N = M = 80$, $p = 1\%$ noise, and no regularization, for the inverse problem of Example 1.

Including regularization we obtain the solution (4.27) whose accuracy error, as a function of λ , is plotted in Figure 4.8. The minimum points λ_{opt} and the minimal errors are listed in Table 4.2. From Figure 4.8 and Table 4.2 it can be seen that the error decreases as the amount of noise p decrease and that the 2nd-order regularization produces much smaller errors than the zeroth and 1st-order regularizations. However, these arguments and conclusions cannot be used for choosing the regularization parameter λ in the absence of an analytical (exact) solution being available. Then, one possible criterion for choosing λ is given by the L-curve method, (Hansen, 2001), which plots the residual norm $\|Ah_\lambda - \underline{b}^\epsilon\|$ versus the solution norm $\|D_k \underline{h}_\lambda\|$ for various values of λ . This is shown in Figure 4.9 for various values of $\lambda \in \{10^{-8}, 10^{-7}, \dots, 10^3\}$ and for $p \in \{1, 3, 5\}\%$ noisy data. The portion to the right of the curve corresponds to large values of λ which make the solution oversmooth, whilst the portion to the left of the curve corresponds to small values of λ which make the solution undersmooth. The compromise is then achieved around the corner region of the L-curve where the aforementioned portions meet. Figure 4.9 shows that this corner region includes the values around $\{\lambda_{0\text{th}} = 10^{-6}, \lambda_{1\text{st}} = 10^{-5}, \lambda_{2\text{nd}} = 2.5\}$ for $p = 1\%$, $\{\lambda_{0\text{th}} = 10^{-5}, \lambda_{1\text{st}} = 10^{-3}, \lambda_{2\text{nd}} = 2.5\}$ for $p = 3\%$, and $\{\lambda_{0\text{th}} = 10^{-5}, \lambda_{1\text{st}} = 10^{-3}, \lambda_{2\text{nd}} = 2.5\}$ for $p = 5\%$, which were previously obtained from Figure 4.8.

Figure 4.10 shows the regularized numerical solution for $h(t)$ obtained with

4.5 Numerical results and discussion

λ_{opt} given in Table 4.2 for $p \in \{1, 3, 5\}\%$ noise and zeroth, first and second-order Tikhonov regularizations. From this figure it can be seen that the 2nd-order regularization produces the most stable and accurate numerical solution. This is expected since the desired solution $h(t) = t$ for Example 1 is very smooth and hence stronger regularization will produce smoother solutions.

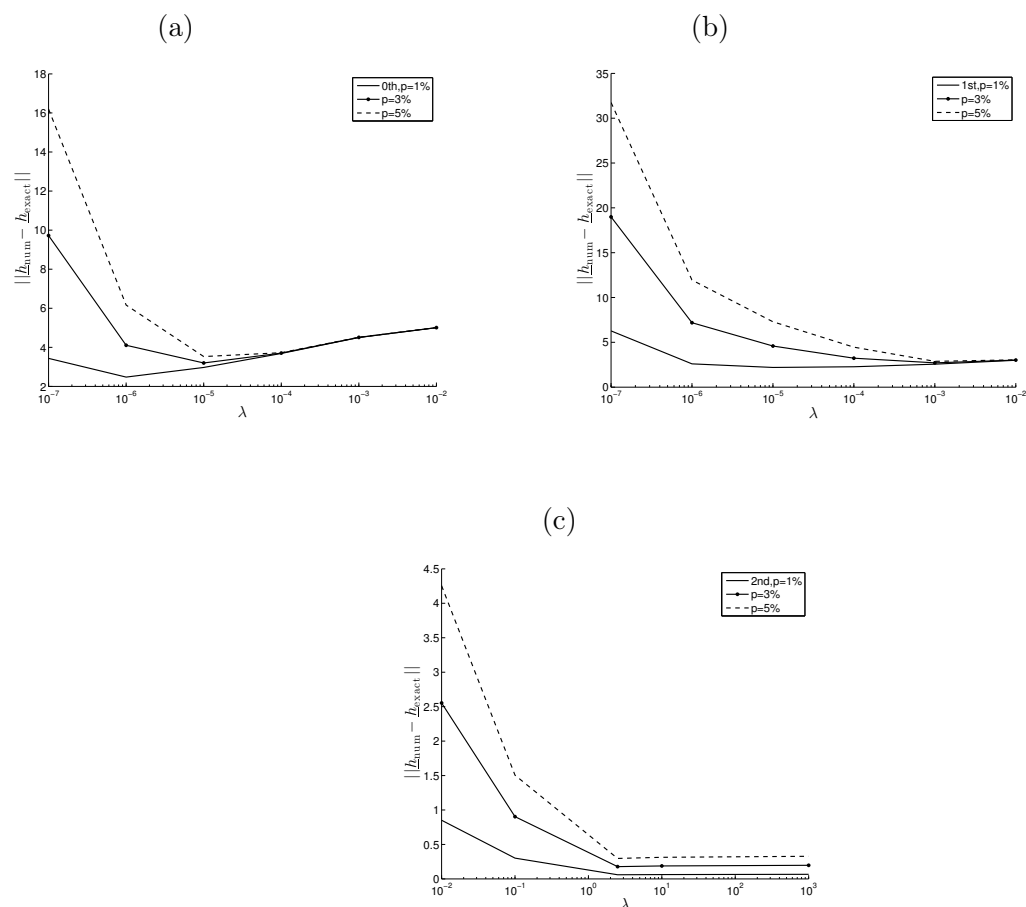


Figure 4.8: The accuracy error $\|h_{\text{num}} - h_{\text{exact}}\|$, as a function of λ , for $M = N = 80$, $p \in \{1, 3, 5\}\%$ noise, obtained using (a) zeroth, (b) first, and (c) second-order regularization, for the inverse problem of Example 1.

4.5 Numerical results and discussion

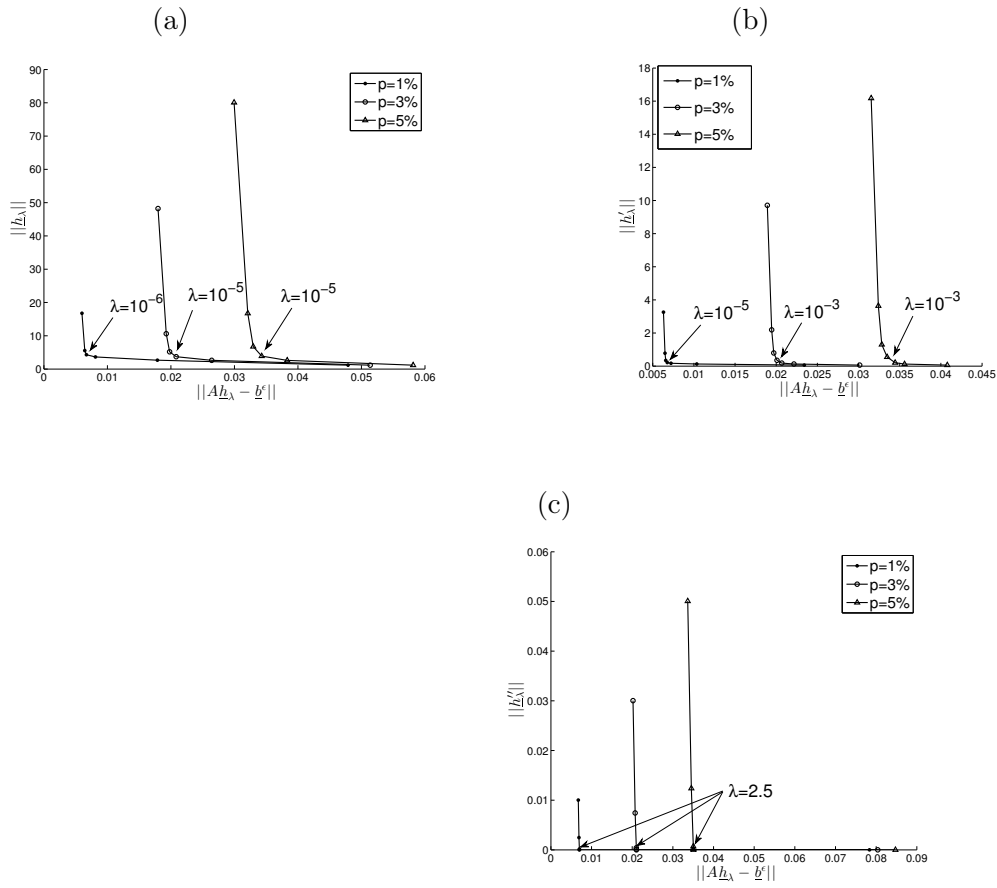


Figure 4.9: The L-curves for $N = M = 80$, $p \in \{1, 3, 5\}\%$ noise, and (a) zeroth, (b) first and (c) second-order regularizations, for the inverse problem of Example 1.

4.5 Numerical results and discussion

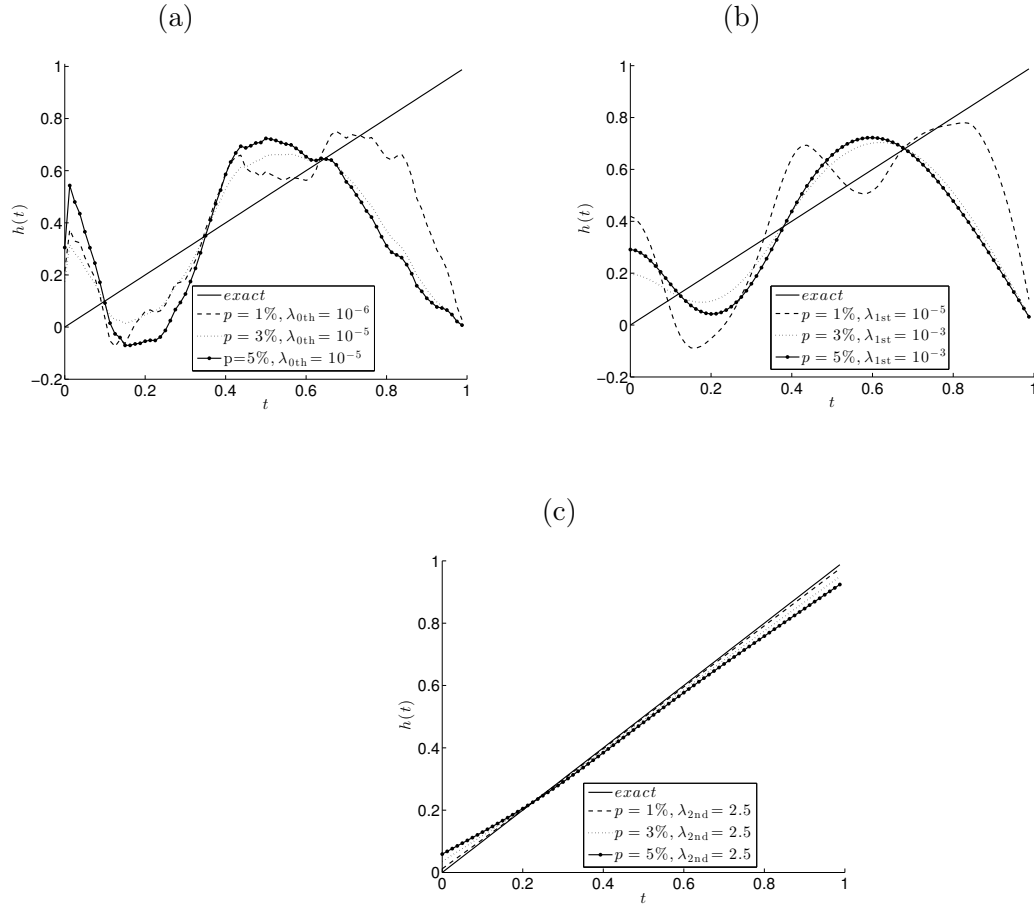


Figure 4.10: The exact (—) solution for $h(t)$ in comparison with the regularized numerical solution (4.27), for $N = M = 80$, $p \in \{1, 3, 5\}\%$ noise, for the inverse problem of Example 1.

4.5 Numerical results and discussion

Table 4.2: The error norms $\|h_{\text{num}} - h_{\text{exact}}\|$ for various order regularization methods and percentages of noise p , for the inverse problem of Example 1.

Regularization	$p = 1\%$	$p = 3\%$	$p = 5\%$
zeroth	$\lambda_{\text{opt}} = 10^{-6}$ 2.4756	$\lambda_{\text{opt}} = 10^{-5}$ 3.1978	$\lambda_{\text{opt}} = 10^{-5}$ 3.5291
first	$\lambda_{\text{opt}} = 10^{-5}$ 2.19566	$\lambda_{\text{opt}} = 10^{-3}$ 2.70695	$\lambda_{\text{opt}} = 10^{-3}$ 2.8813
second	$\lambda_{\text{opt}} = 2.5$ 0.0597	$\lambda_{\text{opt}} = 2.5$ 0.1781	$\lambda_{\text{opt}} = 2.5$ 0.2965

4.5.2 Example 2

As another example, consider first the direct problem (3.14), (4.11) and (4.15) with the input data (4.22),

$$u(x, 0) = \varphi(x) = 0, \quad u_t(x, 0) = \psi(x) = 0, \quad x \in [0, 1], \quad (4.28)$$

$$f_1(x, t) = x^2 + t^2, \quad f_2(x, t) = 0, \quad x \in [0, 1], \quad t \in [0, 1], \quad (4.29)$$

and

$$h(t) = \begin{cases} t & \text{if } 0 \leq t \leq \frac{1}{2}, \\ 1 - t & \text{if } \frac{1}{2} < t \leq 1. \end{cases} \quad (4.30)$$

Remark that in this example, the expression (4.30) has a triangular shape, being continuous but non-differentiable at the peak $t = 1/2$. Furthermore, an explicit analytical solution for the displacement $u(x, t)$ does not seem readily available.

The numerical FDM solutions for the displacement $u(x, t)$ at interior points are shown in Figure 4.11, whilst the desired output (4.3) for ω given by (4.25) is presented in Figure 4.12.

4.5 Numerical results and discussion

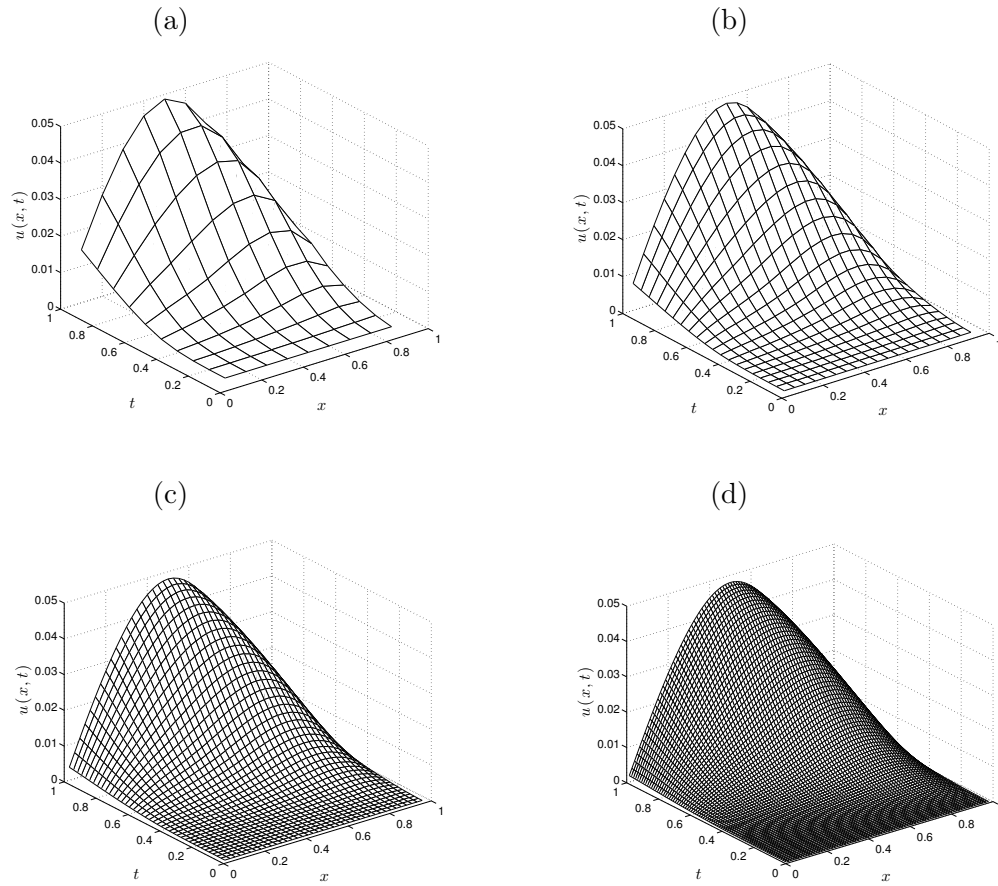


Figure 4.11: Numerical solutions for the displacement $u(x, t)$ obtained by solving the direct problem with various $N = M =$ (a) 10, (b) 20, (c) 40, and (d) 80, for Example 2.

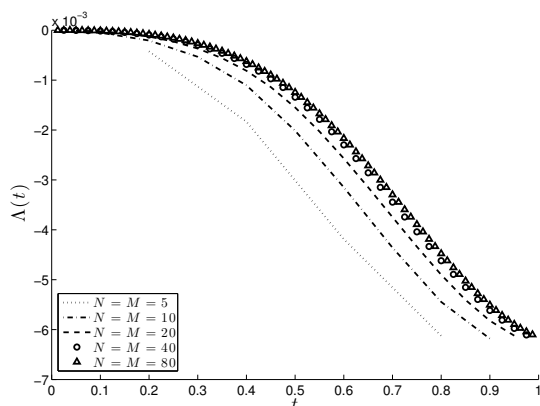


Figure 4.12: Numerical solution for the integral (4.3), obtained by solving the direct problem with various $N = M \in \{5, 10, 20, 40, 80\}$, for Example 2.

The inverse problem given by equations (4.15), (4.22), (4.28), (4.29) and (4.3) with Λ numerically simulated by solving the direct problem using the FDM with $N = M = 160$ is considered next. Remark that from (4.25) and (4.29) it follows that the identifiability condition is satisfied. The solution of the inverse problem is given exactly for $h(t)$ by equation (4.30) and numerically for $u(x, t)$ illustrated for sufficiently large $N = M$ such as 80, in Figure 4.11(d).

4.5.2.1 Exact data

We first consider the case of exact data, i.e. $p = 0$ and hence $\underline{c} = \underline{0}$ in (4.18). The numerical results for $h(t)$ are shown in Figure 4.13 and very good agreement with the exact solution (4.30) can be observed. The numerical solution is convergent as $N = M$ increase from 20 to 40, but some slight instabilities start to manifest as $N = M$ further increases to 80, see Figure 4.13(d) and the condition number of the matrix A given in Table 4.1 for Example 2.

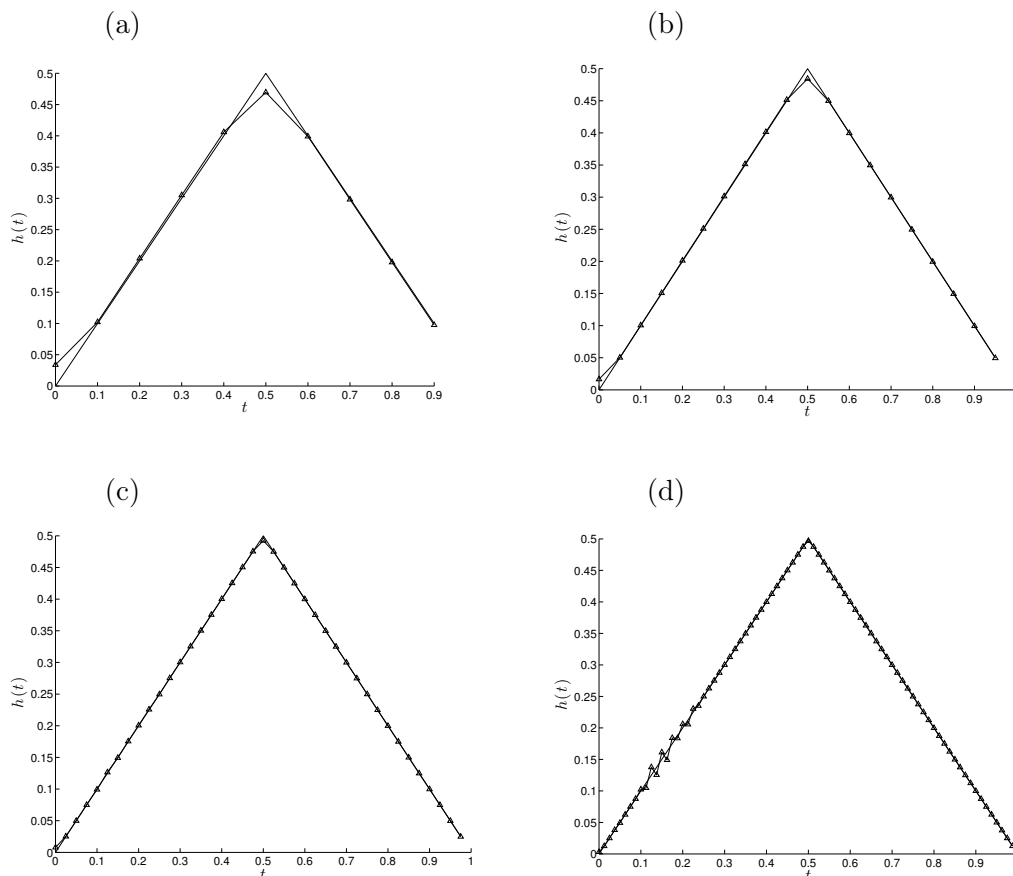


Figure 4.13: The exact (—) solution (4.30) for $h(t)$ in comparison with the numerical solution (— Δ —) for various $N = M =$ (a) 10, (b) 20, (c) 40, and (d) 80, and no regularization, for exact data, for the inverse problem of Example 2.

4.5.2.2 Noisy data

In order to investigate the stability of the numerical solution we include some $p \in \{1, 3, 5\}\%$ noise into the input data (4.13), as given by equation (4.18). The numerical solution for $h(t)$ obtained with $N = M = 80$ and no regularization has been found highly oscillatory and unstable similar to that obtained in Figure 4.7 and therefore is not presented. In order to deal with this instability we employ the Tikhonov regularization which gives the stable solution (4.27) provided that an appropriate regularization parameter λ is chosen. The accuracy error of this regularized solution, as a function of λ , is plotted in Figure 4.14. The minimum

points λ_{opt} and the minimal errors are listed in Table 4.3. The L-curve criterion for choosing λ produces an L-corner, as it also happened in Example 1. This is shown in Figure 4.15 for various values of $\lambda \in \{10^{-9}, 10^{-8}, \dots, 10\}$ and for $p \in \{1, 3, 5\}\%$ noisy data. Figure 4.15 shows that this corner region includes the values around $\{\lambda_{0\text{th}} = 10^{-6}, \lambda_{1\text{st}} = 10^{-6}, \lambda_{2\text{nd}} = 10^{-5}\}$ for $p = 1\%$, $\lambda_{0\text{th},1\text{st},2\text{nd}} = 10^{-4}$ for $p = 3\%$, and $\lambda_{0\text{th},1\text{st},2\text{nd}} = 10^{-2}$ for $p = 5\%$, which were previously obtained from Figure 4.14.

Figure 4.16 shows the regularized numerical solution for $h(t)$ obtained λ_{opt} given in Table 4.3 for $p \in \{1, 3, 5\}\%$ noisy data, in the zeroth, first and second-order Tikhonov regularization. As in this example the desired solution (4.30) is less smooth than the solution $h(t) = t$ of Example 1, from Figure 4.16 it can be seen that the zeroth and first-order regularizations produce more accurate results than the second-order regularization which imposes additional but unwanted smoothness on the sought solution.

4.5 Numerical results and discussion

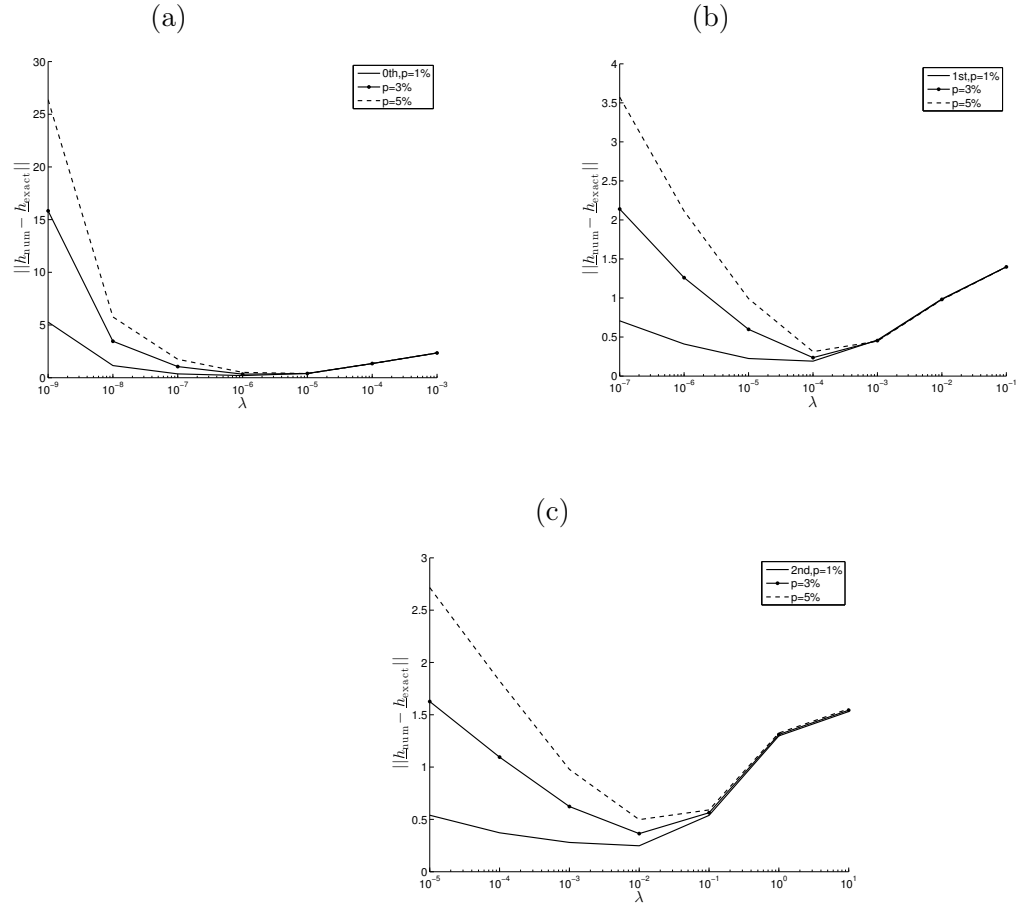


Figure 4.14: The accuracy error $\|h_{\text{num}} - h_{\text{exact}}\|$, as a function of λ , for $M = N = 80$, $p \in \{1, 3, 5\}\%$ noise, obtained using (a) zeroth, (b) first, and (c) second-order regularization, for the inverse problem of Example 2.

4.5 Numerical results and discussion

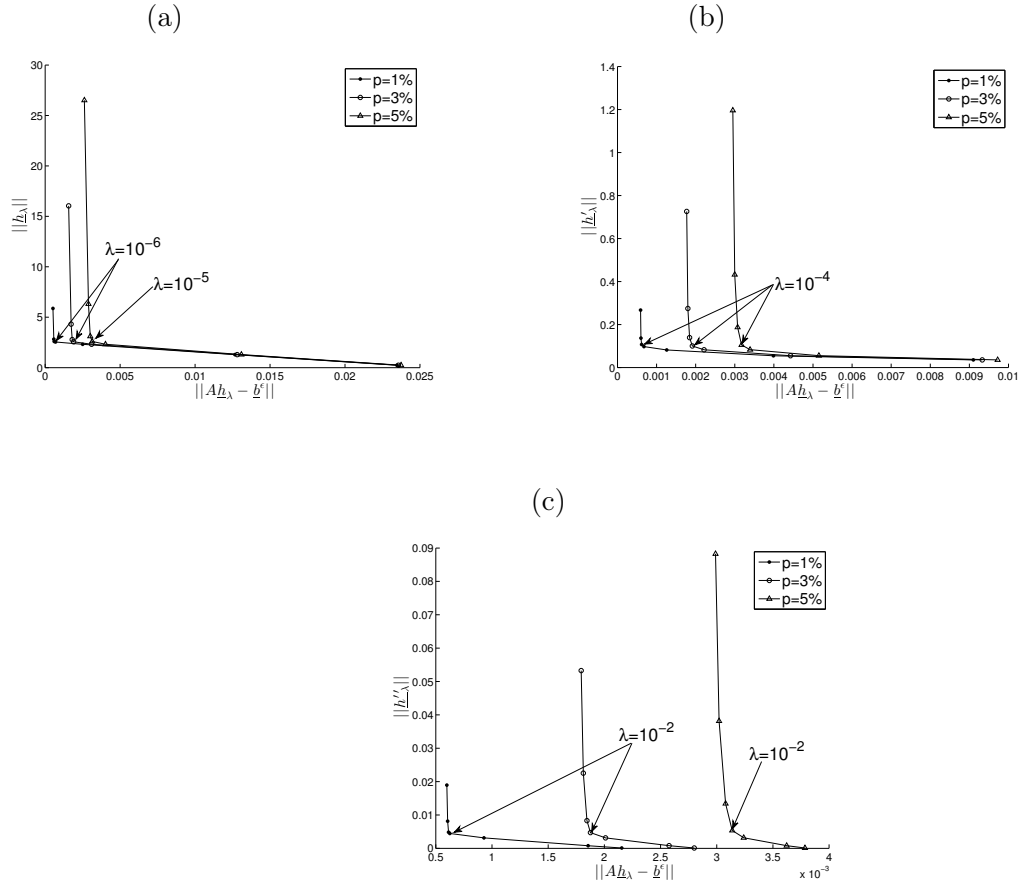


Figure 4.15: The L-curves for $N = M = 80$, $p \in \{1, 3, 5\}\%$ noise, and (a) zeroth, (b) first and (c) second-order regularization, for the inverse problem of Example 2.

4.5 Numerical results and discussion

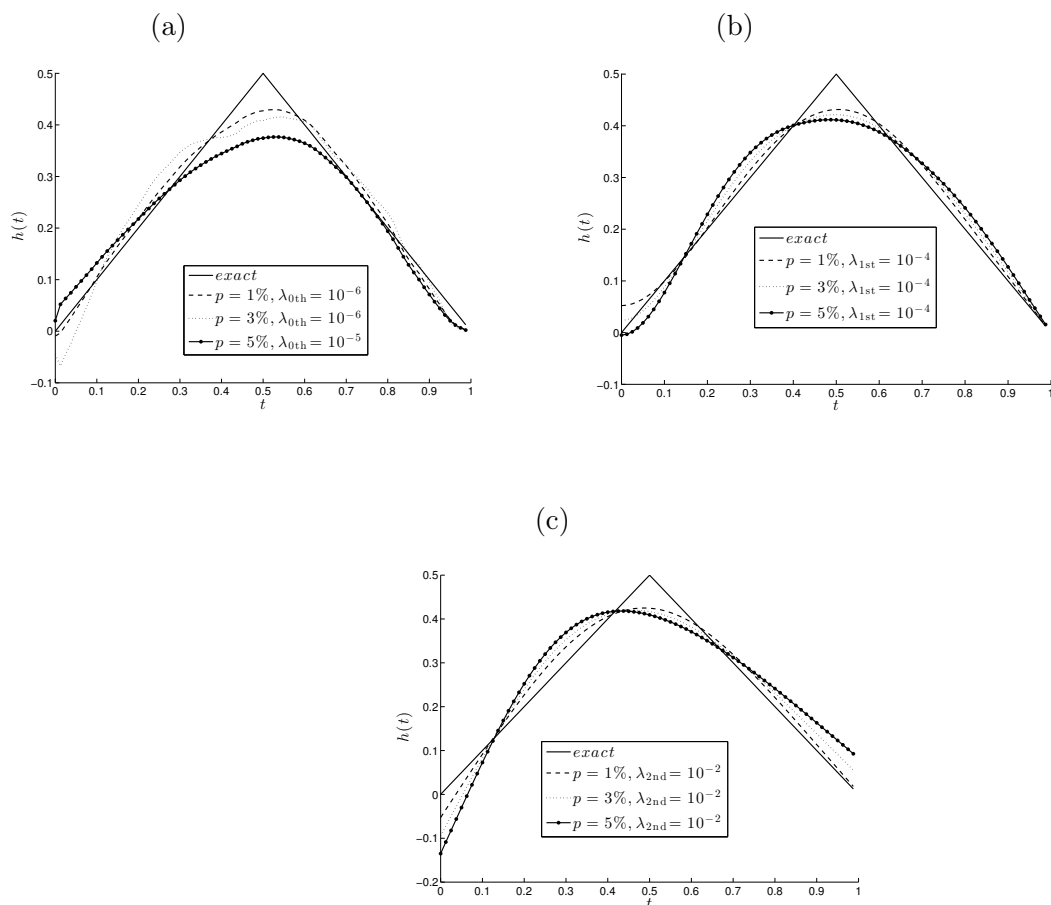


Figure 4.16: The exact solution (4.30) for $h(t)$ in comparison with the regularized numerical solution (4.27), for $N = M = 80$, $p \in \{1, 3, 5\}\%$ noise, for the inverse problem of Example 2.

4.5 Numerical results and discussion

Table 4.3: The error norms $\|h_{\text{num}} - h_{\text{exact}}\|$ for various order regularization methods and percentages of noise p , for the inverse problem of Example 2.

Regularization	$p = 1\%$	$p = 3\%$	$p = 5\%$
zeroth	$\lambda_{\text{opt}} = 10^{-6}$ 0.2008	$\lambda_{\text{opt}} = 10^{-6}$ 0.3388	$\lambda_{\text{opt}} = 10^{-5}$ 0.3925
first	$\lambda_{\text{opt}} = 10^{-4}$ 0.1909	$\lambda_{\text{opt}} = 10^{-4}$ 0.2365	$\lambda_{\text{opt}} = 10^{-4}$ 0.3125
second	$\lambda_{\text{opt}} = 10^{-2}$ 0.2475	$\lambda_{\text{opt}} = 10^{-2}$ 0.3641	$\lambda_{\text{opt}} = 10^{-2}$ 0.4980

4.5.3 Example 3

We finally consider the Robin boundary condition (4.2). Let the initial conditions (3.14) be given by

$$u(x, 0) = \varphi(x) = \sin\left(\frac{3\pi}{4}x + \frac{\pi}{8}\right), \quad u_t(x, 0) = \psi(x) = 0, \quad x \in [0, 1], \quad (4.31)$$

and the Robin boundary conditions (4.2) be given by

$$-\frac{\partial u}{\partial x}(0, t) + \frac{3\pi}{4} \cot\left(\frac{\pi}{8}\right) u(0, t) = 0, \quad \frac{\partial u}{\partial x}(1, t) - \frac{3\pi}{4} \cot\left(\frac{7\pi}{8}\right) u(1, t) = 0, \\ t \in [0, 1]. \quad (4.32)$$

We also take in (4.15),

$$f_1(x, t) = \sin\left(\frac{3\pi}{4}x + \frac{\pi}{8}\right), \quad f_2(x, t) = \frac{9\pi^2}{16} \sin\left(\frac{3\pi}{4}x + \frac{\pi}{8}\right), \\ x \in (0, 1), \quad (4.33)$$

$$h(t) = 6t + \frac{9\pi^2}{16}t^3, \quad t \in [0, 1]. \quad (4.34)$$

Then, the exact solution of the direct problem (4.15), (4.31) and (4.32) is given by

$$u(x, t) = (t^3 + 1) \sin\left(\frac{3\pi}{4}x + \frac{\pi}{8}\right), \quad (x, t) \in [0, 1] \times [0, 1]. \quad (4.35)$$

4.5 Numerical results and discussion

For the weight function (4.25), the desired output (4.3) is given by

$$\Lambda(t) = \int_0^1 \omega(x)u(x,t)dx = \frac{32}{27\pi^3} \left(3\pi \sin\left(\frac{\pi}{8}\right) - 8 \cos\left(\frac{\pi}{8}\right) \right) (t^3 + 1),$$

$t \in [0, 1]. \quad (4.36)$

The FDM requires slight modifications from the Dirichlet boundary condition (4.22) when implementing the Robin boundary conditions (4.32), but this poses no difficulty, (Smith, 1985). We simply approximate the x -derivatives at $x = 0$ and 1 using central finite differences by introducing fictitious points outside the space domain $[0, 1]$ and apply the general FDM scheme (3.17) for $j = 0$ and N , as well.

The absolute errors between the numerical and exact solutions for $u(x, t)$ at interior points are shown in Figure 4.17 and one can observe that an excellent agreement is obtained. Figure 4.18 also gives the absolute error between the exact (4.36) and numerical desired output integral (4.3). From this figure it can be seen that the numerical results converge to the exact solution (4.36), as $N = M$ increases.

4.5 Numerical results and discussion

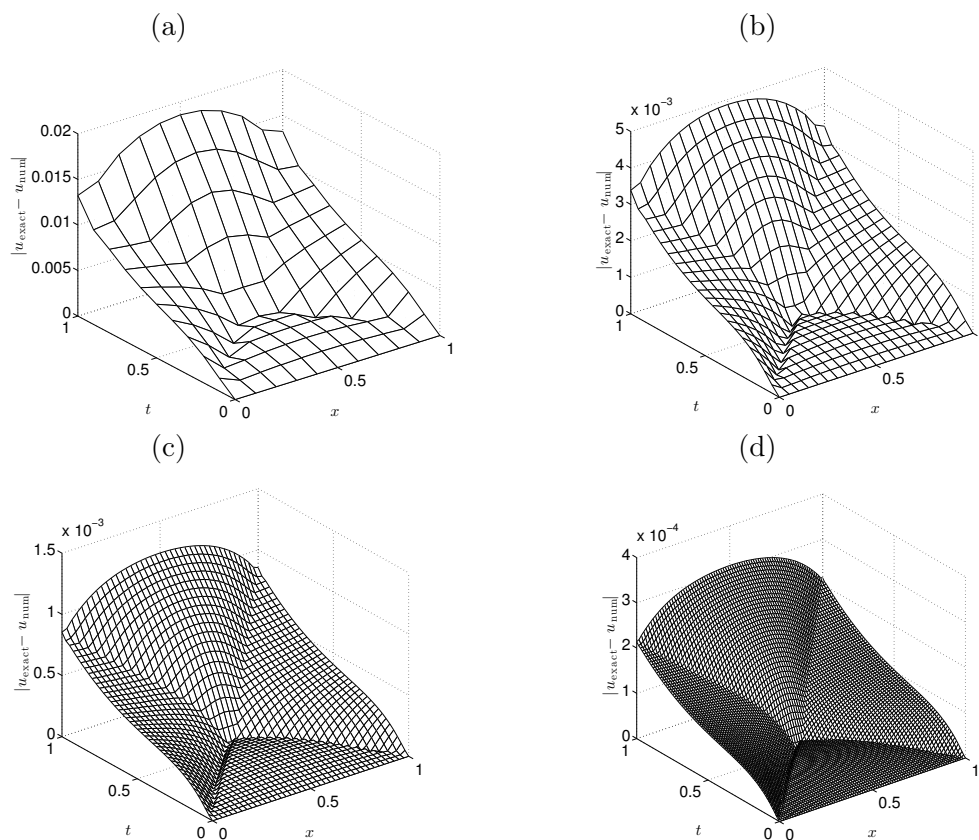


Figure 4.17: The absolute errors between the exact (4.35) and numerical displacement $u(x, t)$ obtained by solving the direct problem with $N = M =$ (a) 10, (b) 20, (c) 40, and (d) 80, for Example 3.

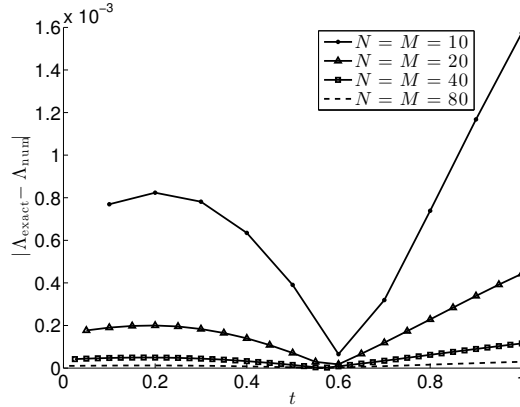


Figure 4.18: The absolute error between the exact (4.36) and numerical $\Lambda(t)$ obtained by solving the direct problem with $N = M \in \{10, 20, 40, 80\}$, for Example 3.

The inverse problem given by equations (4.15), (4.31), (4.32) and (4.36) is considered next. The exact solution is given by equations (4.34) and (4.35).

The discretised inverse problem reduces to solving a global linear, but ill-conditioned system of $(M+1) \times N + N$ equations with $(M+1) \times N + N$ unknowns. Since this system is linear we can eliminate the unknowns $u_{i,j}$ for $i = \overline{0, M}$, $j = \overline{1, N}$, as in (4.20), to reduce the problem to solving an ill-conditioned system of N equations with N unknowns.

4.5.3.1 Exact data

We first consider the case of exact data, i.e. $p = 0$ and hence $\underline{\epsilon} = \underline{0}$ in (4.18). The numerical results corresponding to $h(t)$ and $u(x, t)$ are plotted in Figures 4.19 and 4.21, respectively. From these figures it can be seen that convergent and accurate numerical solutions are obtained. The same comments to those made in subsection 4.5.1.1 for Example 1 apply to Example 3 with the mention that the ℓ^2 -errors between the analytical and numerical h , plotted in Figure 4.19, as functions of N , have been obtained to be $E = 0.3703, 0.2406, 0.1629$ and 0.1127 for $(M =)N = 10, 20, 40$ and 80 , respectively. Also, the order of convergence in $h(t)$ is approximatively 0.5 , see Figure 4.20(a), which is lower than 1.6 previously obtained for Example 1 in Figure 4.5(a). This shows that the Robin inverse

4.5 Numerical results and discussion

problem considered in Example 3 is more severe than the Dirichlet inverse problem of Example 1, see also Table 4.1 for the comparison of the condition numbers of the matrices of Examples 1 and 3.

As for as Figure 4.21 is concerned, the errors decrease as N increases, the ℓ^2 -errors between the analytical and numerical $u(x, t)$ are $E = 5.4E - 3$, $1.3E - 3$, $3.3E - 4$ and $8.3E - 5$ for $(M =)N = 10, 20, 40$, and 80 , respectively, and the order of convergence is approximatively 2, see Figure 4.20(b). The errors in $u(x, t)$ in Figure 4.21 are lower than those of Figure 4.17 for the direct problem but this difference is not as prominent as that observed previously by comparing Figures 4.6 and 4.2 of Example 1.

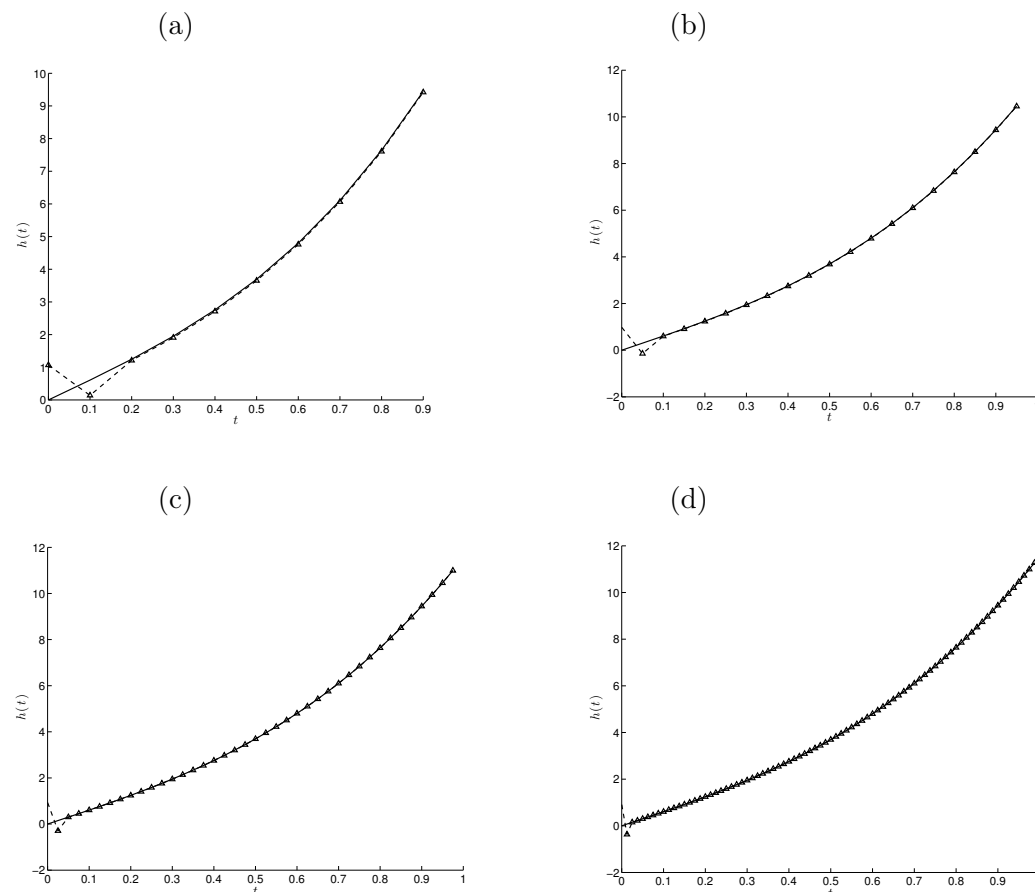


Figure 4.19: The exact (—) solution (4.34) for $h(t)$ in comparison with the numerical solution (— Δ —) for various $N = M =$ (a) 10, (b) 20, (c) 40, and (d) 80, no regularization, for exact data, for the inverse problem of Example 3.

4.5 Numerical results and discussion

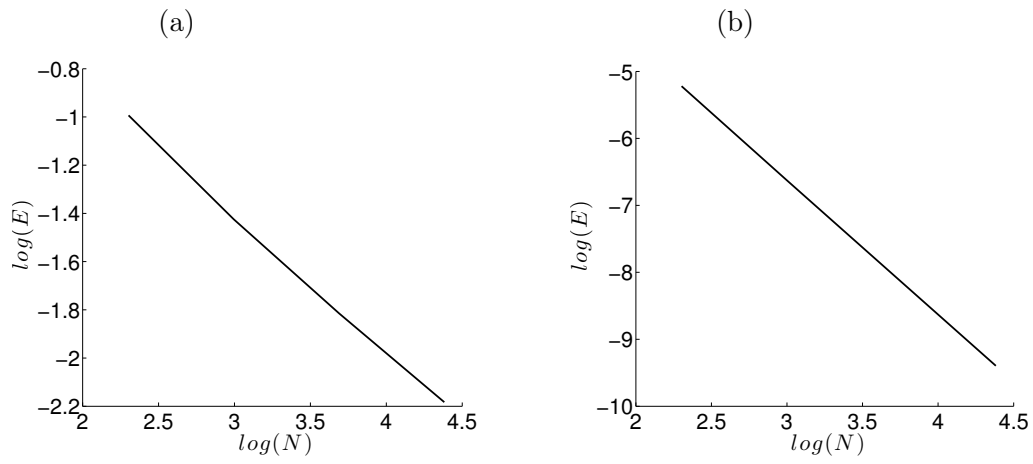


Figure 4.20: The log-log plot of the ℓ^2 -errors between the analytical and numerical (a) $h(t)$ and (b) $u(x,t)$, as functions of N , for Example 3.

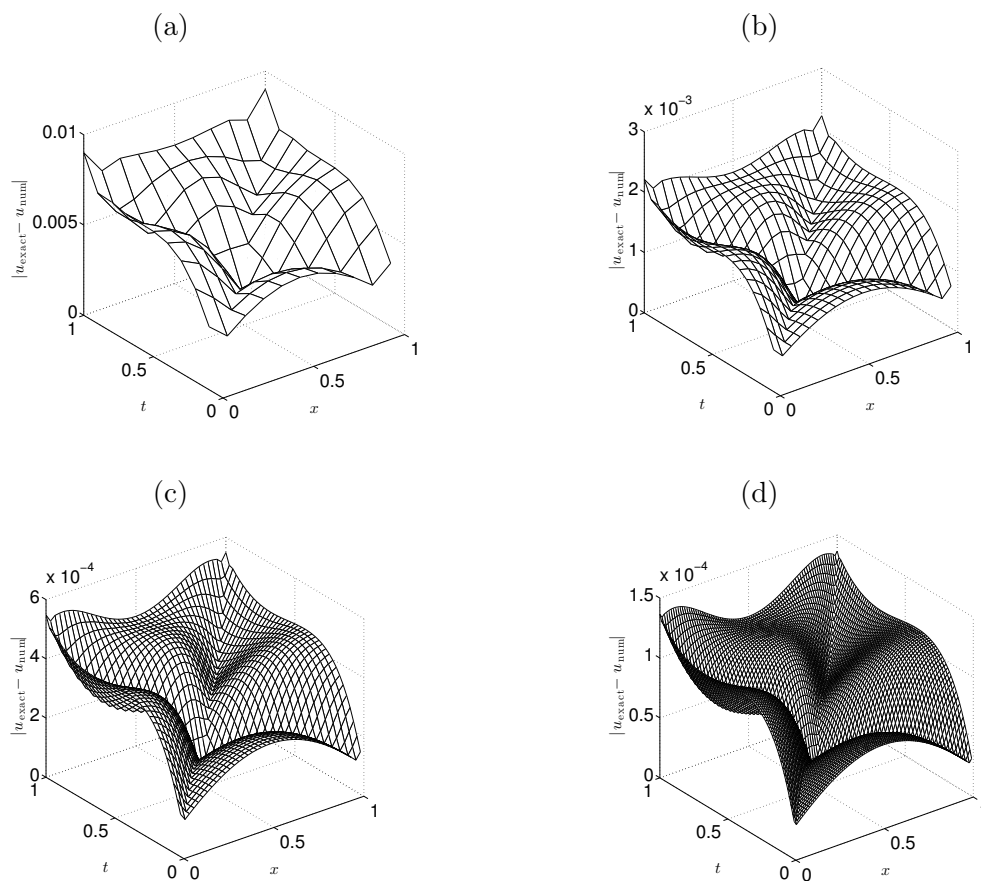


Figure 4.21: The absolute errors between the exact (4.35) and numerical displacement $u(x, t)$ obtained with $N = M =$ (a) 10, (b) 20, (c) 40, and (d) 80, and no regularization, for exact data, for the inverse problem of Example 3.

4.5.3.2 Noisy data

In order to investigate the stability of the numerical solution we include some $p \in \{1, 3, 5\}\%$ noise into the input data (4.13), as given by equation (4.18). The numerical solution for $h(t)$ obtained with $N = M = 80$ and no regularization has been found highly oscillatory and unstable similar to that obtained in Figure 4.7 and therefore is not presented. In order to deal with this instability we employ the zeroth order, first-order and second-order Tikhonov regularization, similar to Section 4.5.1.2 for Example 1. The accuracy error of the regularized solution (4.27), as a function of λ , is plotted in Figure 4.22. The minimum points λ_{opt}

4.5 Numerical results and discussion

and the minimal errors are listed in Table 4.4. The L-curve criterion for choosing λ produces an L-corner, as it also happened in Example 1. This is shown in Figure 4.23 for various values of $\lambda \in \{10^{-8}, 10^{-7}, \dots, 10\}$ and for $p \in \{1, 3, 5\}\%$ noisy data. Figure 4.23 shows that this corner region includes the values around $\{\lambda_{0\text{th}} = 10^{-7}, \lambda_{1\text{st}} = 5 \times 10^{-5}, \lambda_{2\text{nd}} = 5 \times 10^{-2}\}$ for $p = 1\%$, $\{\lambda_{0\text{th}} = 10^{-6}, \lambda_{1\text{st}} = 10^{-4}, \lambda_{2\text{nd}} = 10^{-1}\}$ for $p = 3\%$, and $\{\lambda_{0\text{th}} = 10^{-5}, \lambda_{1\text{st}} = 10^{-4}, \lambda_{2\text{nd}} = 10^{-1}\}$ for $p = 5\%$, as previously predicted from Figure 4.22.

Figure 4.24 shows the regularized numerical solution for $h(t)$ obtained with λ_{opt} given in Table 4.4 for $p \in \{1, 3, 5\}\%$ noisy data, in the zeroth, first and second-order Tikhonov regularization. As in Example 1, one can see that the second-order regularization method produces the most stable and accurate numerical results. As in Example 1, this is expected since the desired solution (4.34) for Example 3 is very smooth and hence stronger regularization will produce smoother solutions.

4.5 Numerical results and discussion

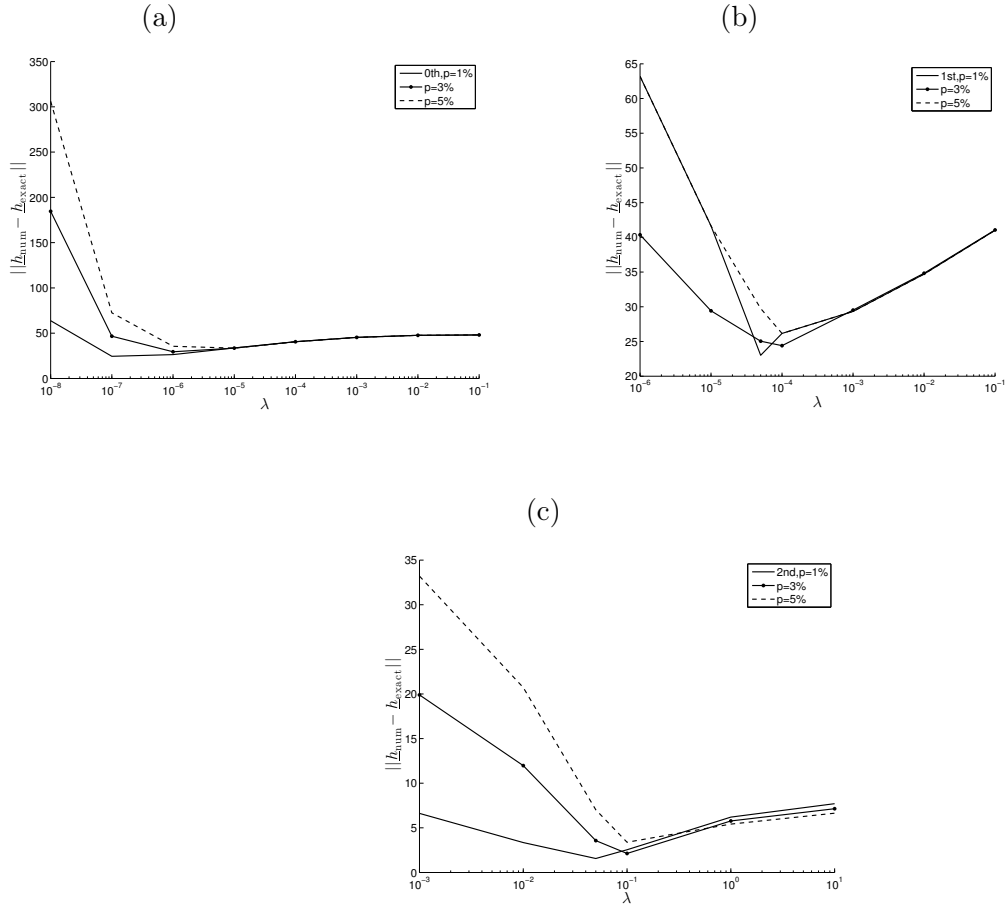


Figure 4.22: The accuracy error $\|h_{\text{num}} - h_{\text{exact}}\|$, as a function of λ , for $M = N = 80$, $p \in \{1, 3, 5\}\%$ noise, obtained using (a) zeroth, (b) first, and (c) second-order regularization, for the inverse problem of Example 3.

4.5 Numerical results and discussion

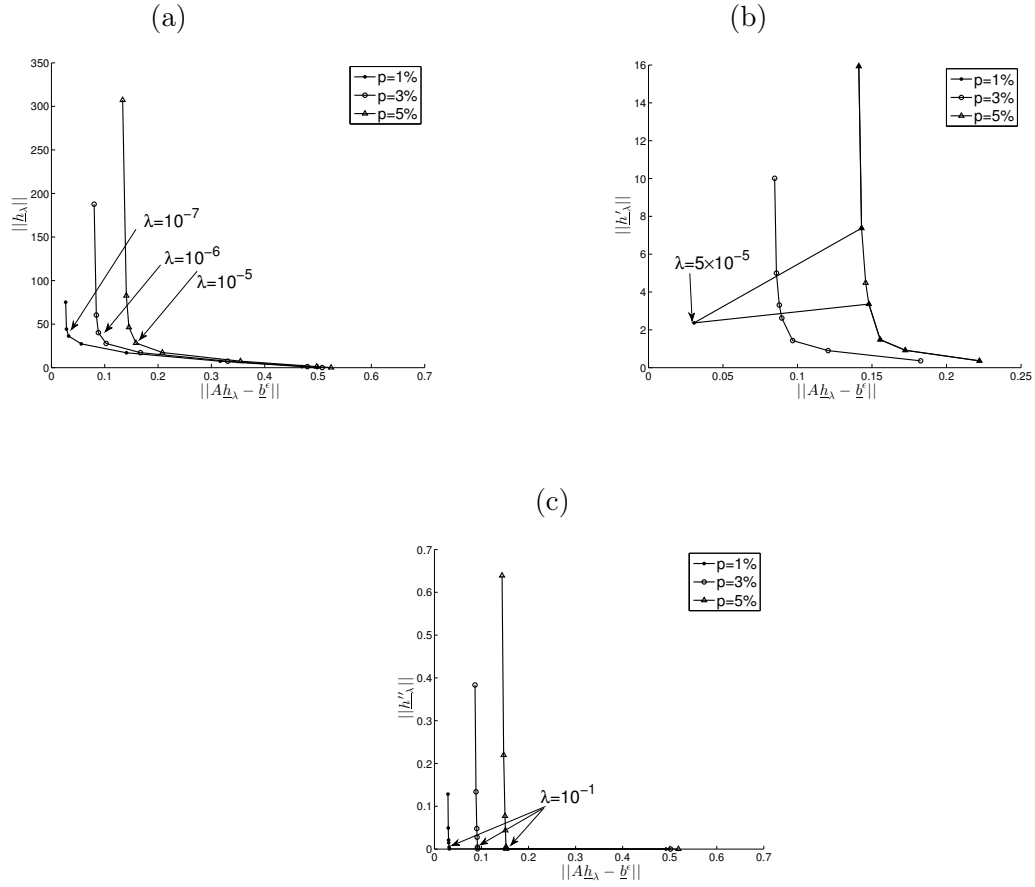


Figure 4.23: The L-curves for $N = M = 80$, $p \in \{1, 3, 5\}\%$ noise, and (a) zeroth, (b) first and (c) second-order regularizations, for the inverse problem of Example 3.

4.5 Numerical results and discussion

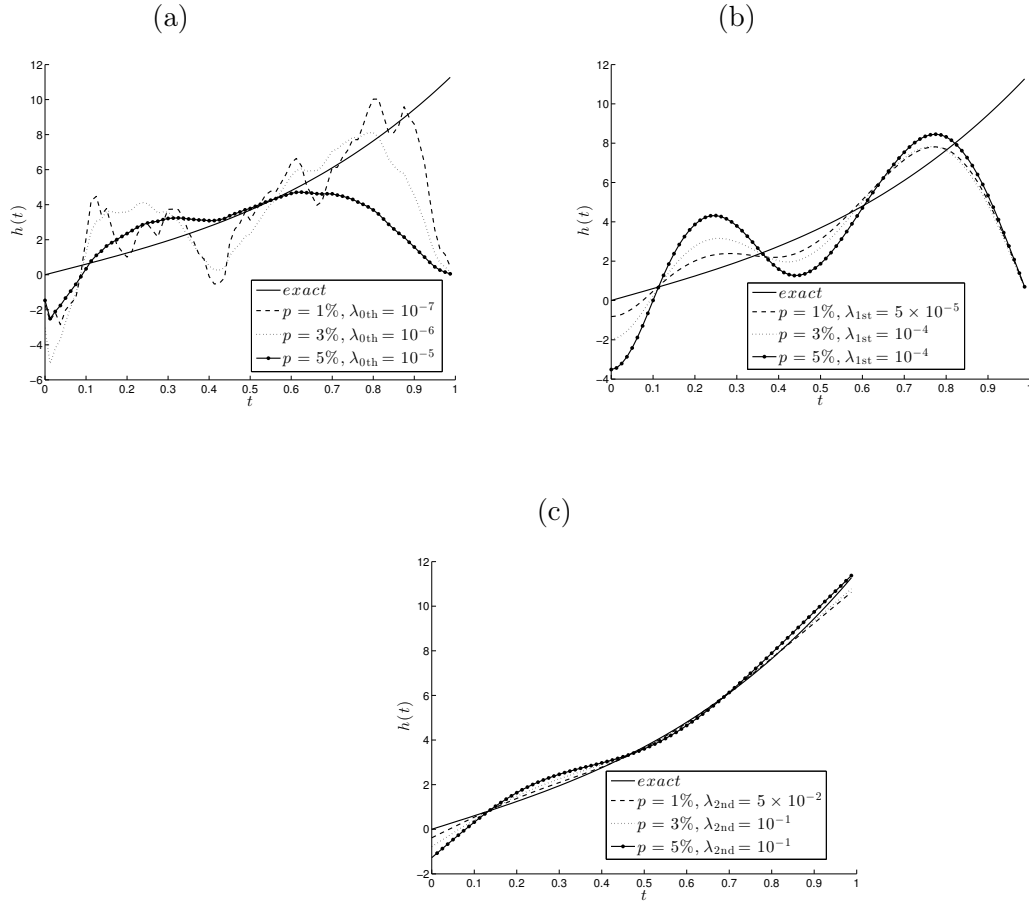


Figure 4.24: The exact solution (4.34) for $h(t)$ in comparison with the numerical regularized solution (4.27), for $N = M = 80$, $p \in \{1, 3, 5\}\%$ noise, for the inverse problem of Example 3.

Table 4.4: The error norms $\|h_{\text{num}} - h_{\text{exact}}\|$ for various order regularization methods and percentages of noise p , for the inverse problem of Example 3.

Regularization	$p = 1\%$	$p = 3\%$	$p = 5\%$
zeroth	$\lambda_{\text{opt}} = 10^{-7}$ 24.4962	$\lambda_{\text{opt}} = 10^{-6}$ 29.5028	$\lambda_{\text{opt}} = 10^{-5}$ 33.5244
first	$\lambda_{\text{opt}} = 5 \times 10^{-5}$ 23.0137	$\lambda_{\text{opt}} = 10^{-4}$ 24.4016	$\lambda_{\text{opt}} = 10^{-4}$ 26.1625
second	$\lambda_{\text{opt}} = 5 \times 10^{-2}$ 1.5648	$\lambda_{\text{opt}} = 10^{-1}$ 2.1300	$\lambda_{\text{opt}} = 10^{-1}$ 3.3874

4.6 Conclusions

In this chapter, the determination of a time-dependent force from the space average integral of the displacement in the wave equation has been investigated. This linear inverse problem is uniquely solvable, but is still ill-posed since small errors in the input data cause large errors in the output force. The problem was discretised numerically using the FDM, and in order to stabilise the solution, the Tikhonov regularization method of various orders has been employed. The choice of the regularization parameter was based on the L-curve criterion. Numerical simulations for a wide range of external forces have been performed in order to test the validity of the present investigation. The obtained results indicate that the method can accurately and stably recover the unknown force. Although the numerical method and results have been presented for the one-dimensional time-dependent wave equation a similar FDM can easily be extended to higher dimensions.

In closure, we note that a similar time-dependent heat source problem but for the parabolic heat equation has recently been investigated in (Hazanee Ismailov Lesnic and Kerimov, 2013) using the same technique based on the Tikhonov regularization method of various orders, (though discretised with the BEM instead of FDM) and similar conclusions have been obtained. In the absence of an *a priori* knowledge of the regularity class of the coefficient $h(t)$ it would be difficult to state which order one should choose and one may pick the zeroth-order as it is

the largest class. One way to deal with this situation is to employ the methods of iterative regularization, as is described in the next chapter.

Chapter 5

Inverse space-dependent force problem for the wave equation

5.1 Introduction

As mentioned at the end of Chapter 2, in this chapter we investigate the retrieval of a space-dependent force function from internal displacement measurements at a fixed time. Prior to this study, the reconstruction of a space-dependent force in the wave equation from Cauchy data measurements of both displacement and its normal derivative on the boundary has been attempted in several studies, e.g. (Cannon and Dunninger, 1970; Hussein and Lesnic, 2014, 2016). Although the uniqueness of solution still holds, (Engl, Scherzer and Yamamoto, 1994; Klibanov, 1992; Yamamoto, 1995), this inverse formulation is, as expected, improperly posed because the unknown output force $f(x)$ depends on x in the domain Ω , whilst the known input data, say u and $\partial_n u$, depend on (x, t) on the boundary $\partial\Omega \times (0, T)$. Therefore, it seems more natural to measure instead information about the displacement $u(x, t)$ for $x \in \Omega$ and time $t = T$, or the time-averaged displacement $\int_0^T u(x, t) dt$ for $x \in \Omega$. This way, the output-input mapping satisfies the meta-theorem that the overposed data and the unknown force function lie in the same direction, (Pilant and Rundell, 1990). This spacewise-dependent force $f(x)$ identification from the upper-base spacewise dependent displacement measurement $u(x, T)$ has been investigated theoretically in Section 8.2 of (Prilepko, Orlovsky and Vasin, 2000), where the uniqueness of a solution was proved. For other wave

related force identification studies which use the final time displacement data we refer to (Hasanov, 2008) which employs a weak solution approach for a relatively general inverse problem with a highly non-unique solution, and to (Slodicka, 2014) which nicely introduces a quasi-nonlinearity in the governing wave equation to resolve the non-uniqueness of solution. The other inverse problem generated by the measurement of the time-averaged displacement $\int_0^T u(x, t)dt$ which we investigate in our study is new. Essentially, the same inverse problem with unknown space-wise dependent right-hand side source in the governing equation arises also for the parabolic heat equation in the thermal field, see (Erdem, Lesnic and Hasanov, 2013; Johansson and Lesnic, 2007b).

The plan of the chapter is as follows. Section 5.2 introduces the inverse problem formulations, whilst Section 5.2.1 highlights several issues related to the existence, uniqueness and stability of a solution to the direct and inverse problems, respectively. Section 5.3 presents the variational formulations of the inverse problems under investigation and derives explicitly the expressions for the gradients of the least-squares functionals which are minimized. Section 5.4 describes the iterative Landweber method accommodated and applied in order to obtain regularized stable solutions, whilst Section 5.5 illustrates and discusses extensive numerical results in one dimension, for the recovery of smooth as well as non-smooth force functions. Furthermore, the conjugate gradient method (CGM) is also described and employed in one of the examples. A numerical extension to two-dimensions is presented in Section 5.6 and finally, conclusions are presented in Section 5.7.

5.2 Problem formulation

Assume that we have a medium, denoted by Ω , occupying a bounded sufficiently smooth domain in \mathbb{R}^n , where $n \geq 1$. The boundary of Ω is denoted by $\partial\Omega$, and we define the space-time cylinder $Q_T = \Omega \times (0, T)$, where $T > 0$. We wish to find the displacement $u(\underline{x}, t)$ and the force $f(\underline{x})$ in the hyperbolic wave equation

$$u_{tt} - \nabla^2 u = f(\underline{x})g(\underline{x}, t) + \chi(\underline{x}, t) \quad \text{in } Q_T, \quad (5.1)$$

where g and χ are given functions. For inhomogeneous media, we can have $\mathcal{L}u = c(\underline{x})\nabla^2 u$, or $\nabla \cdot (K(\underline{x})\nabla u)$, where c and K are given positive material

properties, (Chow and Zou, 2015), replacing the Laplace operator in (5.1)

Equation (5.1) has to be solved subject to prescribed initial conditions (3.3) and (3.4), prescribed homogeneous Dirichlet boundary conditions (4.1), and the additional final displacement measurement

$$u(\underline{x}, T) = u_T(\underline{x}), \quad \underline{x} \in \Omega, \quad (5.2)$$

or, the time-average displacement measurement

$$\int_0^T u(\underline{x}, t) dt = U_T(\underline{x}), \quad \underline{x} \in \Omega. \quad (5.3)$$

5.2.1 Inverse problem

Consider first, for simplicity, the one-dimensional case, i.e. $n = 1$, and take $\Omega = (0, L)$. Let us also take $\chi(x, t) = 0$, and $g(x, t) = 1$. Then, in (Cannon and Dunninger, 1970) it was remarked that the inverse force problem (5.1)-(5.2) has a unique solution if and only if $T/L \notin \mathbb{Q}$, i.e. T/L is an irrational number. This follows immediately from separation of variables, whereas for $\varphi = \psi = 0$ and $g = 1$ the solution of the inverse problem

$$u_{tt} - u_{xx} = f(x), \quad (x, t) \in (0, L) \times (0, T), \quad (5.4)$$

$$u(x, 0) = u_t(x, 0) = 0, \quad x \in (0, L), \quad (5.5)$$

$$u(0, t) = u(L, t) = 0, \quad t \in (0, T), \quad (5.6)$$

$$u(x, T) = 0, \quad x \in (0, L), \quad (5.7)$$

is given by

$$u(x, t) = \frac{\sqrt{2}}{\pi^2} \sum_{k=1}^{\infty} \frac{c_k}{k^2} \left(1 - \cos\left(\frac{k\pi t}{L}\right) \right) \sin\left(\frac{k\pi x}{L}\right), \quad (5.8)$$

$$f(x) = \sum_{k=1}^{\infty} c_k \sin\left(\frac{k\pi x}{L}\right), \quad (5.9)$$

where

$$c_k = \frac{\sqrt{2}}{L} \int_0^L f(x) \sin\left(\frac{k\pi x}{L}\right) dx, \quad k \geq 1. \quad (5.10)$$

Now, in order to impose (5.7) we apply (5.8) at $t = T$ to obtain

$$0 = \frac{\sqrt{2}}{\pi^2} \sum_{k=1}^{\infty} \frac{c_k}{k^2} \left(1 - \cos\left(\frac{k\pi T}{L}\right)\right) \sin\left(\frac{k\pi x}{L}\right), \quad x \in (0, L). \quad (5.11)$$

One can easily observe that $c_k = 0$ for all $k \geq 1$, and hence from (5.8) and (5.9), $u = f = 0$, if and only if $T/L \notin \mathbb{Q}$. Moreover, this condition cannot be removed even if one additionally prescribe $u_t(x, T)$, as can be easily seen by differentiating (5.8) with respect to t .

However, if we consider the additional time-average displacement measurement (5.3) instead of (5.2), by integrating (5.8) with respect to t and make it zero, we obtain

$$0 = \frac{\sqrt{2}}{\pi^2} \sum_{k=1}^{\infty} \frac{c_k}{k^2} \left(T - \frac{L}{k\pi} \sin\left(\frac{k\pi T}{L}\right)\right) \sin\left(\frac{k\pi x}{L}\right), \quad x \in (0, L). \quad (5.12)$$

Since $\frac{k\pi T}{L} > \sin\left(\frac{k\pi T}{L}\right)$ for all $k \in \mathbb{N}^*$, we then obtain that $c_k = 0$ for every $k \in \mathbb{N}^*$ and hence, from (5.8) and (5.9), that $u = f = 0$. Thus, the inverse problem (5.4)-(5.6) together with the integral condition

$$\int_0^T u(x, t) dt = 0, \quad x \in (0, L), \quad (5.13)$$

has only the trivial solution, which in turn implies that the solution of the inverse problem given by equations (5.4)-(5.6) and the time-average displacement measurement

$$\int_0^T u(x, t) dt = U_T(x), \quad x \in (0, L), \quad (5.14)$$

is unique, with no restriction on the ratio T/L being irrational number or not.

Even if one has proved that the solution exists and is unique, both inverse problems (5.1)-(5.2) and (5.1), (3.3), (3.4), (4.1), (5.3) are still ill-posed since the continuous dependence upon the input data (5.2) or (5.3) is violated. This can

5.3 Variational formulation of the inverse problems

easily be seen from the following example of instability.

Example of instability

Let $\Omega = (0, L = \pi)$ and, for $n \in \mathbb{N}^*$ take

$$u_n(x, t) = \frac{(1 - \cos(nt)) \sin(nx)}{n^{3/2}}, \quad (x, t) \in (0, \pi) \times (0, T),$$

which satisfies the wave equation $(u_n)_{tt} = (u_n)_{xx} + f_n(x)$ with homogeneous initial and Dirichlet boundary conditions, and

$$u_{nT}(x) = u_n(x, T) = \frac{(1 - \cos(nT)) \sin(nx)}{n^{3/2}}, \quad x \in (0, \pi),$$

$$U_{nT}(x) = \int_0^T u_n(x, t) dt = \frac{\sin(nx)}{n^{3/2}} \left(T - \frac{\sin(nT)}{n} \right), \quad x \in (0, \pi),$$

with the force

$$f_n(x) = n^{1/2} \sin(nx), \quad x \in (0, \pi).$$

One can observe that whilst all the input data tends to zero, the force $f_n(x)$ becomes oscillatory and unbounded, as $n \rightarrow \infty$.

5.3 Variational formulation of the inverse problems

For the solution of the inverse problem (5.1)-(5.2), define the operator $A : L^2(\Omega) \rightarrow L^2(\Omega)$ by

$$Af = u_f(\cdot, T), \tag{5.15}$$

where $u_f(x, t)$ is the unique solution of the direct problem (5.1), (3.3), (3.4) and (4.1) corresponding to the given force f (the other term g in the force is known and fixed and we also take $\chi = 0$). By A_0 we denote the similar linear operator defined for $\varphi = \psi = 0$. The inverse problem (5.1)-(5.2) recasts as

$$Af = u_T. \tag{5.16}$$

5.3 Variational formulation of the inverse problems

Since in practice u_T is contaminated with random noisy errors it is convenient to minimize the least-squares cost functional $J : L^2(\Omega) \rightarrow \mathbb{R}_+$ defined by

$$J(f) = \frac{1}{2} \|Af - u_T\|_{L^2(\Omega)}^2. \quad (5.17)$$

In (Lesnic, Hussein and Johansson, accepted), we have shown that the gradient of this functional is given by

$$J'(f) = - \int_0^T g(\underline{x}, t) v_1(\underline{x}, t) dt, \quad (5.18)$$

where v_1 solves the adjoint problem

$$(v_1)_{tt} - \nabla^2 v_1 = 0, \quad \text{in } Q_T, \quad (5.19)$$

$$v_1(\underline{x}, T) = 0, \quad (v_1)_t(\underline{x}, T) = u_f(\underline{x}, T) - u_T(\underline{x}), \quad \underline{x} \in \Omega, \quad (5.20)$$

$$v_1(\underline{x}, t) = 0, \quad (\underline{x}, t) \in \partial\Omega \times (0, T). \quad (5.21)$$

Similarly, for the solution of the inverse problem (5.1), (3.3), (3.4), (4.1), (5.3), we define the operator $\tilde{A} : L^2(\Omega) \rightarrow L^2(\Omega)$ by

$$\tilde{A}f = \int_0^T u_f(\cdot, t) dt, \quad (5.22)$$

and \tilde{A}_0 denotes its linear part. Then the inverse problem (5.1), (3.3), (3.4), (4.1), (5.3) recasts as

$$\tilde{A}f = U_T. \quad (5.23)$$

As in the previous case, since the right-hand side is in general contaminated with noise, we seek a quasi-solution to (5.23) in the form of minimizing the cost functional $\tilde{J} : L^2(\Omega) \rightarrow \mathbb{R}_+$ defined by

$$\tilde{J}(f) := \frac{1}{2} \|\tilde{A}f - U_T\|_{L^2(\Omega)}^2. \quad (5.24)$$

Its gradient is given by, see (Lesnic, Hussein and Johansson, accepted),

$$\tilde{J}'(f) = - \int_0^T \left(\int_0^t g(\underline{x}, s) ds \right) \tilde{v}_1(\underline{x}, t) dt, \quad (5.25)$$

5.4 An iterative procedure for the inverse problem

where \tilde{v}_1 solves the adjoint problem

$$(\tilde{v}_1)_{tt} - \nabla^2 \tilde{v}_1 = 0, \quad \text{in } Q_T, \quad (5.26)$$

$$\tilde{v}_1(\underline{x}, T) = 0, \quad (\tilde{v}_1)_t(\underline{x}, T) = \int_0^T u_f(\underline{x}, t) dt - U_T(\underline{x}), \quad \underline{x} \in \Omega, \quad (5.27)$$

$$\tilde{v}_1(\underline{x}, t) = 0, \quad (\underline{x}, t) \in \partial\Omega \times (0, T). \quad (5.28)$$

5.4 An iterative procedure for the inverse problem

In much of the previous chapters where the non-iterative Tikhonov regularization method was used there could be some difficulty in choosing the order of the regularization if no *a priori* knowledge on the smoothness of solution is available. In such a situation, one could resort to iterative methods of regularization which do not involve choosing any order of regularization. One such popular method is the Landweber method, which is commonly used for solving ill-posed problems, see (Landweber, 1951), and has been previously employed by (Johansson and Lesnic, 2007b) for solving the inverse related source problem for the heat equation.

Once the gradient of the functional J (or \tilde{J}) has been explicitly derived, as described in the previous section, we apply the iterative Landweber method for minimising the functionals (5.17) (or (5.24)) using the recurrence (5.31) below. This has a regularization character producing a stable solution if the iteration process is stopped according to (5.34) below, see for more details (Engl, Hanke and Neubauer, 2000), as follows:

- (i) Choose an arbitrary function $f_0 \in L^2(\Omega)$. Let u_0 be the solution of the direct problem (5.1), (3.3), (3.4), (4.1) with $f = f_0$.
- (ii) Assume that f_k and u_k have been constructed. For the inverse problem (5.1) and (5.2), let v_k solve the adjoint problem (5.18)-(5.21) and calculate the gradient (5.18) given by

$$z_k(\underline{x}) = - \int_0^T g(\underline{x}, t) v_k(\underline{x}, t) dt, \quad \underline{x} \in \Omega. \quad (5.29)$$

5.5 Numerical results and discussion

For the inverse problem (5.1), (3.3), (3.4), (4.1) and (5.3) let \tilde{v}_k solve the adjoint problem (5.25)-(5.28) and calculate the gradient (5.25) given by

$$z_k(\underline{x}) = - \int_0^T \left(\int_0^t g(\underline{x}, s) ds \right) \tilde{v}_k(\underline{x}, t) dt, \quad \underline{x} \in \Omega. \quad (5.30)$$

(iii) Construct the new iterate for the force given by

$$f_{k+1}(\underline{x}) = f_k(\underline{x}) - \gamma z_k(\underline{x}), \quad \underline{x} \in \Omega, \quad (5.31)$$

where $0 < \gamma$ is sufficiently small.

Let u_{k+1} be the solution of the direct problem (5.1), (3.3), (3.4), (4.1) with $f = f_{k+1}$.

(iv) Repeat steps (ii) and (iii) until convergence is achieved in the case of exact data u_T (or U_T). In the case of noisy data

$$\|u_T - u_T^\epsilon\|_{L^2(\Omega)} \leq \epsilon, \quad \text{or} \quad \|U_T - U_T^\epsilon\|_{L^2(\Omega)} \leq \epsilon \quad (5.32)$$

we can use the Morozov discrepancy principle, see e.g. (Elfving and Nikazad, 2007; Engl, Hanke and Neubauer, 2000), to terminate the iterations. This suggests choosing the stopping index $k = k(\epsilon)$ as the smallest k for which

$$\|u_k^\epsilon(\cdot, T) - u_T^\epsilon\|_{L^2(\Omega)} \leq \tau\epsilon, \quad \text{or} \quad \left\| \int_0^T u_k^\epsilon(\cdot, t) dt - U_T^\epsilon \right\|_{L^2(\Omega)} \leq \tau\epsilon, \quad (5.33)$$

where $\tau > 1$ is some constant to be prescribed. According to (5.17) and (5.24), criterion (5.33) can be rewritten as

$$J(f_k) \leq \tau^2 \frac{\epsilon^2}{2}, \quad \text{or} \quad \tilde{J}(f_k) \leq \tau^2 \frac{\epsilon^2}{2}. \quad (5.34)$$

5.5 Numerical results and discussion

In all examples in this section we take, for simplicity, $T = 1$ and $\chi = 0$. The examples are one-dimensional, i.e. $n = 1$ and $\Omega = (0, L)$ with $L = 1$ for simplicity. The extension of the analysis to higher dimensions, e.g. $n = 2$ -dimensions, is illustrated separately in Section 5.6. We take the initial guess arbitrary such as $f_0 \equiv 0$. Also, except for Example 5, where we investigate the influence of the relaxation parameter γ on the speed of convergence, in all other examples we take $\gamma = 1$.

5.5.1 Example 1

Consider first the direct problem (5.1), (3.3), (3.4) and (4.1) given by wave equation

$$u_{tt} - u_{xx} = f(x)g(x, t), \quad (x, t) \in (0, 1) \times (0, 1), \quad (5.35)$$

and the input data

$$u(x, 0) = \varphi(x) = 2 \sin(\pi x), \quad u_t(x, 0) = \psi(x) = 0, \quad x \in [0, 1], \quad (5.36)$$

$$u(0, t) = u(1, t) = 0, \quad t \in (0, 1], \quad (5.37)$$

$$g(x, t) = 1, \quad (x, t) \in (0, 1) \times (0, 1). \quad (5.38)$$

$$f(x) = \pi^2 \sin(\pi x), \quad x \in (0, 1). \quad (5.39)$$

The exact solution of this problem is given by

$$u(x, t) = \sin(\pi x)(\cos(\pi t) + 1), \quad (x, t) \in [0, 1] \times [0, 1]. \quad (5.40)$$

We will illustrate the numerical results for obtaining the final displacement

$$u(x, T) = u(x, 1) = u_T(x) = 0, \quad x \in [0, 1], \quad (5.41)$$

and the time-average displacement

$$\int_0^T u(x, t) dt = \int_0^1 u(x, t) dt = U_T(x) = \sin(\pi x), \quad x \in [0, 1], \quad (5.42)$$

as this will become the input data in the inverse problem later on.

The discrete finite-difference form of the problem (5.35)-(5.37) is as follows. We divide the solution domain $(0, L) \times (0, T)$ into M and N subintervals of equal space length Δx and time-step Δt , where $\Delta x = L/M$ and $\Delta t = T/N$. We put $u_{i,j} := u(x_i, t_j)$, where $x_i = i\Delta x$, $t_j = j\Delta t$, $f_i := f(x_i)$ and $g_{i,j} := g(x_i, t_j)$ for

5.5 Numerical results and discussion

$i = \overline{0, M}, j = \overline{0, N}$. Then, a central-difference approximation to equations (5.35)-(5.37) at the mesh points $(x_i, t_j) = (i\Delta x, j\Delta t)$ of the rectangular mesh covering the solution domain $(0, L) \times (0, T)$ is,

$$u_{i,j+1} = r^2 u_{i+1,j} + 2(1-r^2)u_{i,j} + r^2 u_{i-1,j} - u_{i,j-1} + (\Delta t)^2 f_i g_{i,j}, \quad (5.43)$$

$$i = \overline{1, (M-1)}, \quad j = \overline{1, (N-1)},$$

$$u_{i,0} = \varphi(x_i), \quad i = \overline{0, M}, \quad \frac{u_{i,1} - u_{i,-1}}{2\Delta t} = \psi(x_i), \quad i = \overline{1, (M-1)}, \quad (5.44)$$

$$u_{0,j} = 0, \quad u_{M,j} = 0, \quad j = \overline{1, N}, \quad (5.45)$$

where $r = \Delta t / \Delta x$. Remark that (5.44) is the same as (3.18) but it has been rewritten here again in order to stress that (5.43) initiates from these initial values. Equation (5.43) represents an explicit FDM which is stable if $r \leq 1$, giving approximate values for the solution at mesh points along $t = 2\Delta t, 3\Delta t, \dots$, as soon as the solution at the mesh points along $t = \Delta t$ has been determined by allowing $j = 0$ in equation (5.43) and using (5.44), to obtain

$$u_{i,1} = \frac{1}{2}r^2\varphi(x_{i+1}) + (1-r^2)\varphi(x_i) + \frac{1}{2}r^2\varphi(x_{i-1}) + (\Delta t)\psi(x_i) + \frac{1}{2}(\Delta t)^2 f_i g_{i,0},$$

$$i = \overline{1, (M-1)}. \quad (5.46)$$

For finding the numerical solution to (5.41), we put $j = N - 1$ in (5.43). And for (5.42) we use the trapezoidal rule approximation

$$\int_0^T u(x_i, t) dt = \frac{\Delta t}{2} \left(\varphi(x_i) + 2 \sum_{j=1}^{N-1} u(x_i, t_j) + u(x_i, t_N) \right), \quad i = \overline{1, M-1}. \quad (5.47)$$

The absolute errors between the exact solution (5.41) and the numerical solution for u_T , and also between (5.42) and (5.47) for U_T , are shown in Figure 5.1 and Table 5.1. From this figure and table, it can be seen that the numerical solutions for u_T and U_T converge to the exact solutions (5.41) and (5.42), respectively, as the FDM mesh size decreases, and this convergence is of second order.

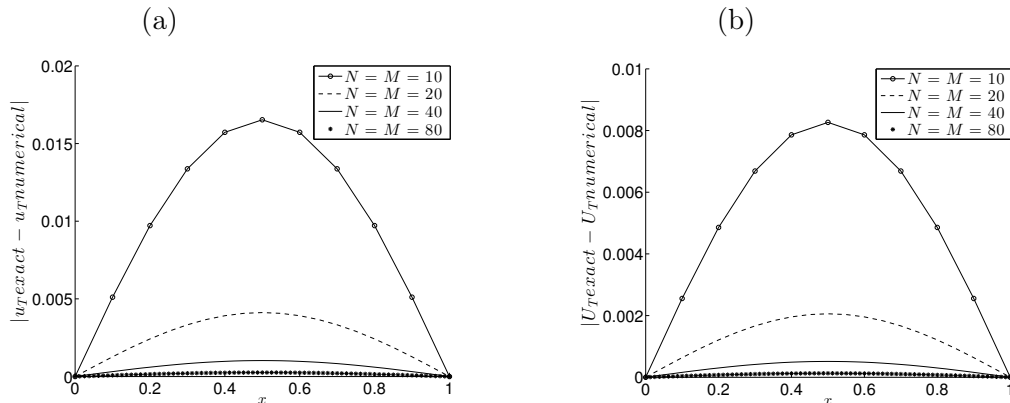


Figure 5.1: The absolute errors between exact and numerical solutions for (a) $u_T(x)$ and (b) $U_T(x)$, for $N = M \in \{10, 20, 40, 80\}$ for the direct problem of Example 1.

Table 5.1: The ℓ^2 -errors between exact and numerical solutions for $u_T(x)$ and $U_T(x)$, for $N = M \in \{10, 20, 40, 80\}$ for the direct problem of Example 1.

$M = N$	10	20	40	80
ℓ^2 - error in u_T	0.0123	0.0029	0.0007	0.0001
ℓ^2 - error in U_T	0.0062	0.0015	0.0004	$9.1E - 5$

In all inverse numerical simulations in Section 5.5 we fix $N = M = 80$.

5.5.1.1 Inverse problem

Since from (5.38) we have $g \equiv 1$, and also since $T/L = 1 \in \mathbb{Q}$ we do not have the uniqueness of a solution of the inverse problem (5.35)-(5.37) when measuring the final displacement (5.41). Therefore, for Example 1 we only consider the inverse problem (5.35)-(5.37) with the time-average displacement measurement (5.42) which, according to the discussion in Section 5.2.1, has a unique solution given by equations (5.39) and (5.40).

The objective function (5.24) discretised and given by

$$\tilde{J}(f_k) = \frac{1}{2} \|\xi_k\|^2 = \frac{1}{2} \sum_{i=1}^{M-1} \xi_k^2(x_i), \quad (5.48)$$

5.5 Numerical results and discussion

where

$$\xi_k = \int_0^T u_k(x, t) dt - U_T(x), \quad x \in \Omega, \quad (5.49)$$

is plotted in Figure 5.2(a), as a function of the number of iterations k . From this figure it can be seen that convergence of \tilde{J} is achieved after about 3000 iterations. Figure 5.2(b) shows the error between the exact solution f and numerical solution f_k , defined by

$$E(f_k) = \|f_{exact} - f_k\| = \sqrt{\sum_{i=1}^{M-1} (f(x_i) - f_k(x_i))^2}, \quad (5.50)$$

as a function of the number of iterations. From this figure it can be seen a monotonic decreasing convergence to zero of the error (5.50). In fact, we obtain that $E(f_{500}) = 0.366$ which is small compared to the maximum value of f which, from (5.39), is about 10.

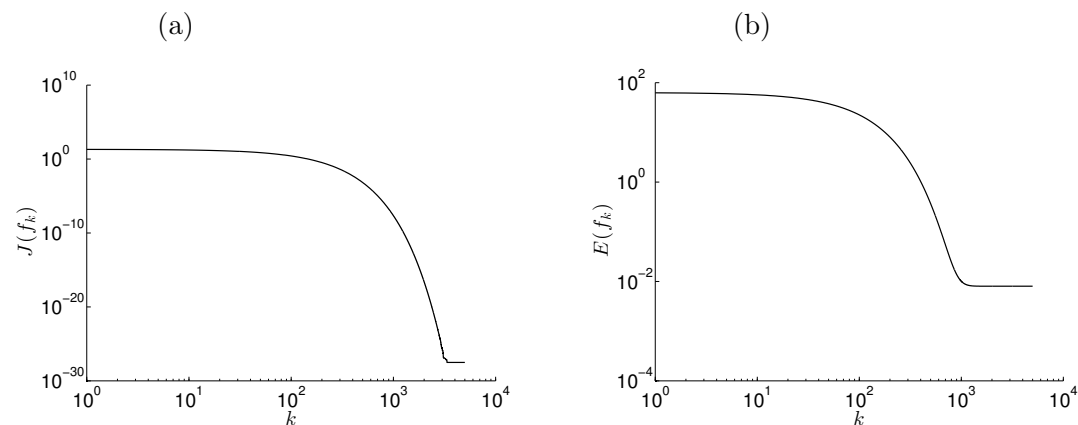


Figure 5.2: (a) The objective function $\tilde{J}(f_k)$ and (b) the accuracy error $E(f_k)$, versus the number of iterations $k = \overline{1, 5000}$, no noise for the inverse problem of Example 1.

Figure 5.3 shows the numerical solution f_k at various iteration numbers k . From this figure a monotonic increasing convergence of the numerical solution f_k towards the exact solution (5.39) can be clearly observed.

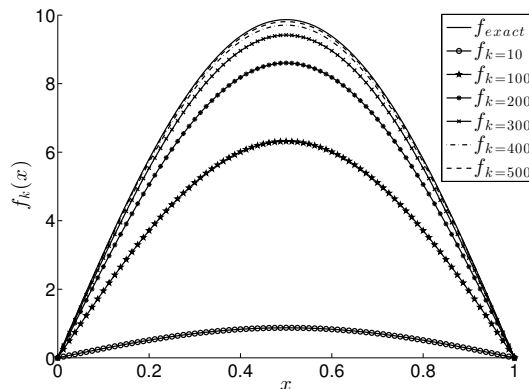


Figure 5.3: The numerical solution f_k at various iteration numbers k , in comparison with the exact solution (5.39), no noise for the inverse problem of Example 1.

In practice, the additional observation (5.3) comes from measurement which is inherently contaminated with errors. We therefore model this by replacing the exact data U_T by the noisy data

$$U_T^\epsilon(x_i) = U_T(x_i) + \epsilon_i, \quad i = \overline{1, (M-1)}, \quad (5.51)$$

where $(\epsilon_i)_{i=\overline{1, M-1}}$ are random variables generated (using the MATLAB routine 'normrnd') from a Gaussian normal distribution with mean zero and standard deviation $\sigma = p \times \max_{x \in [0, L]} |U_T(x)|$, where p represents the percentage of noise. The total amount of noise introduced in the objective functional (5.24) is then given by

$$\frac{1}{2} \epsilon^2 = \frac{1}{2} \sum_{i=1}^{M-1} \epsilon_i^2. \quad (5.52)$$

In order to investigate the stability of the numerical solution we include some $p \in \{10, 30, 50\}\%$ noise into the input data (5.42), as given by equation (5.51). The objective functional $\tilde{J}(f_k)$ and the errors $E(f_k)$ are shown in Figure 5.4 for $k = \overline{1, 500}$ iterations. In Figure 5.4(a) the threshold $\tau^2 \frac{\epsilon^2}{2}$ (with $\tau = 1.15$) in the stopping criterion (5.34) is included and indicated by a horizontal line. Intersecting the horizontal line $y = \tau^2 \frac{\epsilon^2}{2}$ with the graph of the objective functional $\tilde{J}(f_k)$ yields the stopping iteration number k_{discr} given by the discrepancy principle criterion (5.34). On the other hand, the minimum of the curve $E(f_k)$ in Figure

5.5 Numerical results and discussion

5.4(b) yields the optimal iteration number k_{opt} . For various percentages of noise p , the values of k_{discr} and k_{opt} together with the corresponding accuracy errors (5.50) are given in Table 5.2 for better illustrative purposes. From Figures 5.4(a), 5.4(b) and Table 5.2 it can be seen that there is not much difference between k_{opt} and k_{discr} for all percentages of noise p considered and this adds to the robustness of the numerical iterative method employed.

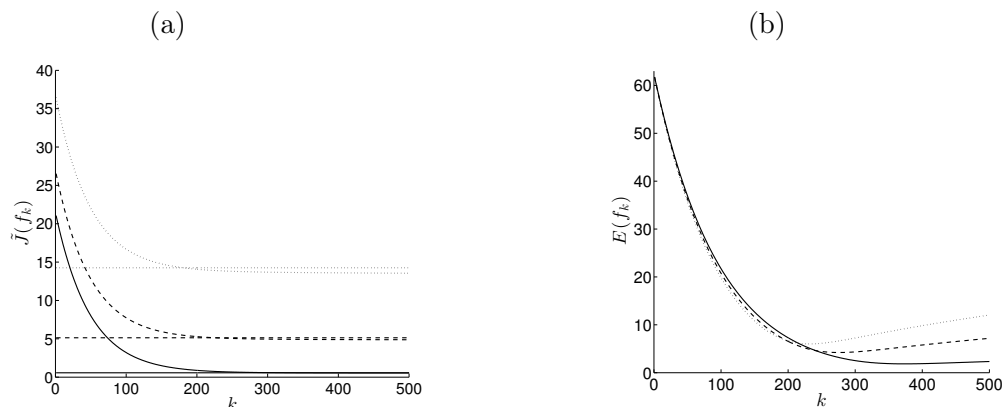


Figure 5.4: (a) The objective function $\tilde{J}(f_k)$ and (b) the accuracy error $E(f_k)$, versus the number of iterations $k = \overline{1, 500}$, for $p = 10\%$ (—), $p = 30\%$ (- - -) and $p = 50\%$ ($\cdot \cdot \cdot$) noise for the inverse problem of Example 1. The horizontal lines in (a) represent the threshold $\tau^2 \epsilon^2 / 2$ with $\tau = 1.15$.

Table 5.2: The stopping iteration number k_{discr} chosen according to the discrepancy principle criterion (5.34) (with $\tau = 1.15$), as illustrated in Figure 5.4(a), and the optimal iteration number k_{opt} chosen according to the minimum of the accuracy error function (5.50) in Figure 5.4(b) for various percentages of noise $p \in \{10, 30, 50\}\%$ for Example 1. The corresponding accuracy errors $E(f_{k_{discr}})$ and $E(f_{k_{opt}})$ are also included.

p	10%	30%	50%
k_{opt}	373	276	232
$E(f_{k_{opt}})$	1.8471	4.2181	6.0124
k_{discr}	300	245	205
$E(f_{k_{discr}})$	2.5213	4.5269	6.4347

5.5 Numerical results and discussion

Figures 5.5(a) and 5.5(b) show the regularized numerical solution for $f(x)$ obtained with various values of the iteration numbers listed in Table 5.2, namely, $k_{opt} \in \{373, 276, 232\}$ and $k_{discr} \in \{240, 225, 220\}$, respectively, for $p \in \{10, 30, 50\}\%$ noisy data. From these figures it can be seen that there is not much difference obtained between the corresponding curves in Figures 5.5(a) and 5.5(b), except perhaps slightly for $p = 10\%$. Moreover, the numerical results illustrated in Figure 5.5(b) reveal that stable numerical solutions are obtained if one stops the iteration process according to the discrepancy principle (5.34). Stability is further maintained even for large percentages of noise such as $p = 50\%$. Furthermore, as expected, numerical results in Figure 5.5(b) become more accurate as the percentage of noise p decreases.

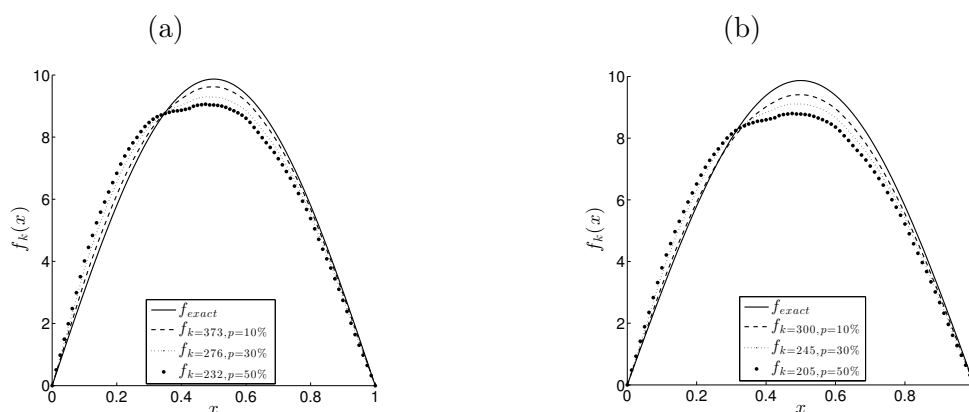


Figure 5.5: The exact solution f in comparison with the numerical solution f_k for (a) $k_{opt} \in \{373, 276, 232\}$ and (b) $k_{discr} \in \{300, 245, 205\}$, for $p \in \{10, 30, 50\}\%$ noise, for the inverse problem of Example 1.

5.5.2 Example 2

Consider the inverse problem given by the wave equation (5.35) with the input data (5.37),

$$u(x, 0) = \varphi(x) = \sin(\pi x), \quad u_t(x, 0) = \psi(x) = \sin(\pi x), \quad x \in [0, 1], \quad (5.53)$$

$$g(x, t) = e^t(\pi^2 + 1), \quad (x, t) \in (0, 1) \times (0, 1), \quad (5.54)$$

5.5 Numerical results and discussion

and the displacement measurement at the final time $t = T = 1$

$$u(x, t) = u(x, 1) = u_T(x) = \sin(\pi x)e, \quad x \in [0, 1], \quad (5.55)$$

or the time-average displacement

$$\int_0^T u(x, t)dt = \int_0^1 u(x, t)dt = U_T(x) = \sin(\pi x)(e - 1), \quad x \in [0, 1]. \quad (5.56)$$

One can easily observe that the function (5.54) satisfies $g(x, t) \geq 0$, $g_t(x, t) > 0$, for every $(x, t) \in \overline{Q}_T$ and hence, according to (Lesnic, Hussein and Johansson, accepted), both the inverse problems (5.35), (5.37), (5.53), (5.55), and (5.35), (5.37), (5.53), (5.56) have unique solutions. In fact, it can readily be checked by direct substitution that the analytical solution of both problems is given by

$$u(x, t) = \sin(\pi x)e^t, \quad (x, t) \in [0, 1] \times [0, 1], \quad (5.57)$$

$$f(x) = \sin(\pi x), \quad x \in (0, 1). \quad (5.58)$$

5.5 Numerical results and discussion

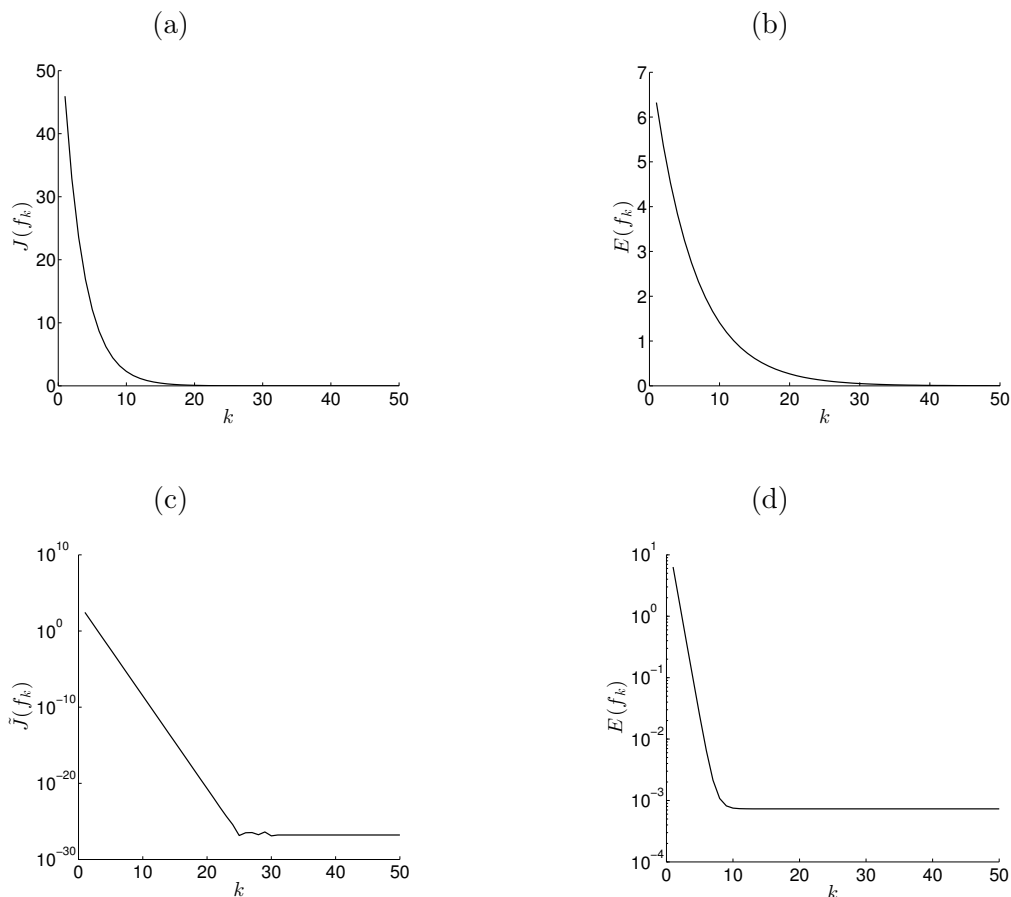


Figure 5.6: (a) The objective function $J(f_k)$ and (b) the corresponding accuracy error $E(f_k)$ for the inverse problem of Example 2 with the displacement measurement (5.55), and (c) the objective function $\tilde{J}(f_k)$ and (d) the corresponding accuracy error $\tilde{E}(f_k)$ for the inverse problem of Example 2 with the time-average displace measurement (5.56). All curves are as functions of the number of iterations $k = \overline{1, 50}$, for no noise.

For exact data, i.e. no noise in (5.55) and (5.56), Figures 5.6 and 5.7 are analogous to Figures 5.2 and 5.3 of Example 1 and similar conclusions can be drawn. Remark that the errors in Figure 5.6(b) are ten times smaller than in Figure 5.2(b) because the force function (5.58) is about $\pi^2 \approx 10$ time smaller than the force function (5.39). Furthermore, by inspecting Figures 5.6 and 5.7 it can be seen that for Example 2 the convergence is much faster when using the

5.5 Numerical results and discussion

displacement measurement (5.55) than when using the time-average displacement measurement (5.56). This illustrates the fact that the pointwise measurement (5.55) contains stronger information than the local average measurement (5.56).

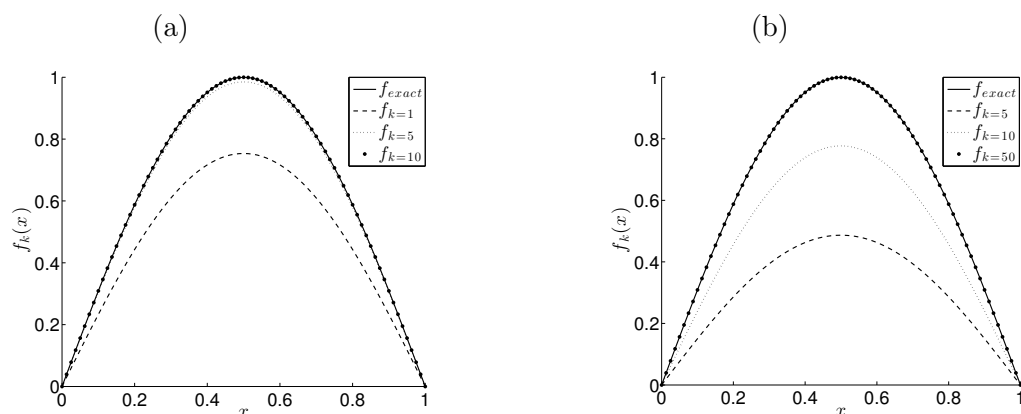


Figure 5.7: The numerical solution f_k at various iteration numbers k , in comparison with the exact solution (5.58), no noise for the inverse problem of Example 2 with (a) the displacement measurement (5.55), and (b) the time-average displacement measurement (5.56).

In order to investigate the stability of the numerical solutions we include some $p \in \{1, 3, 5\}\%$ noise into the input data (5.55) (or (5.56)), as given by a similar expression to (5.51). For this noisy data, Figures 5.8, 5.9 and Table 5.3 are analogous to Figures 5.4, 5.5 and Table 5.2 of Example 1 and similar conclusions can be drawn. Stability is achieved if the iterations are stopped at the index k_{discr} which is much closer to k_{opt} for Example 2 than for Example 1 because the amount of noise is much smaller (10 times) in the former case. For the same reason, the agreement between the numerical and analytical solutions is much better in Figure 5.9 than in Figure 5.5. The final thing to remark is that from Figures 5.8(b) and 5.8(d) (and also previously from Figure 5.4(b)) one can observe the semi-convergence phenomenon which is commonly encountered with iterative regularization techniques for solving ill-posed problems, see for more detail (Elfving, Nikazad and Hansen, 2010).

5.5 Numerical results and discussion

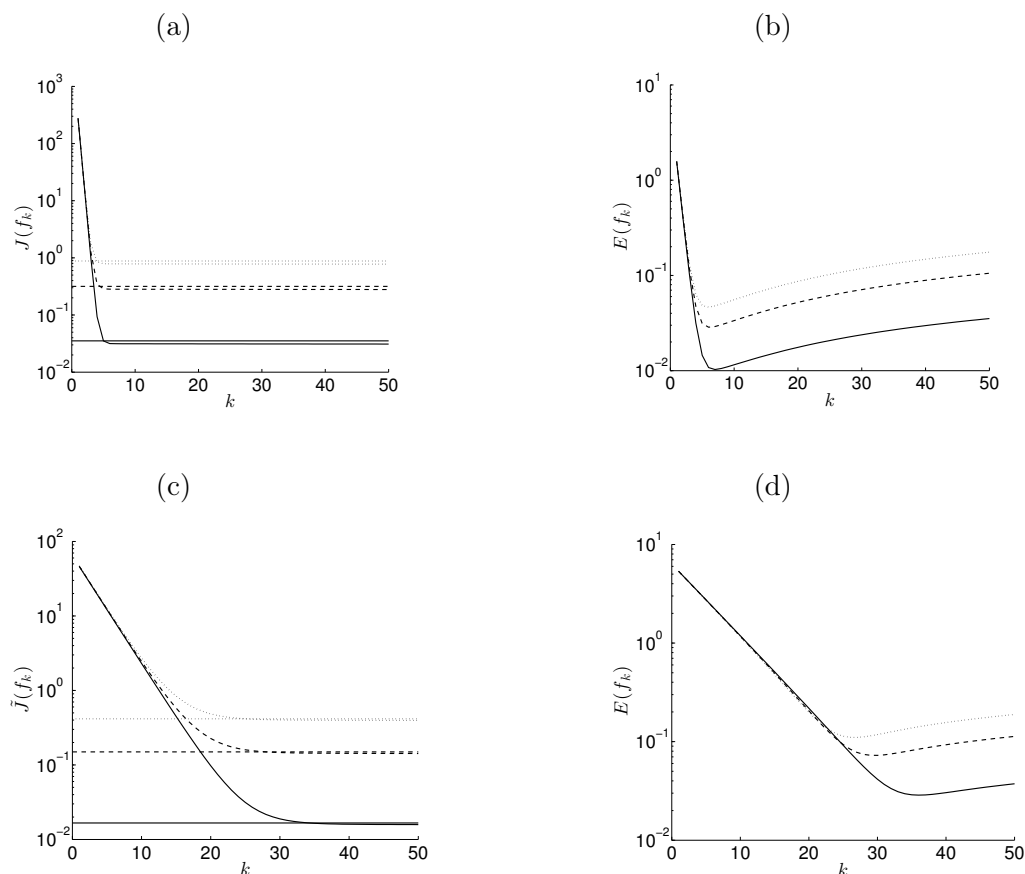


Figure 5.8: (a) The objective function $J(f_k)$ and (b) the corresponding accuracy error $E(f_k)$ for the inverse problem of Example 2 with the displacement measurement (5.55), and (c) the objective function $\tilde{J}(f_k)$ and (d) the corresponding accuracy error $E(f_k)$ for the inverse problem of Example 2 with the time-average displace measurement (5.56). All curves are as functions of the number of iterations $k = \overline{1, 50}$, for $p = 1\%$ (—), $p = 3\%$ (- - -) and $p = 5\%$ ($\cdot\cdot\cdot$) noise. The horizontal lines in (a) and (c) represent the threshold $\tau^2\epsilon^2/2$ with $\tau = 1.15$ and $\tau = 1.25$, respectively.

5.5 Numerical results and discussion

Table 5.3: The stopping iteration number k_{discr} chosen according to the discrepancy principle criterion (5.34), as illustrated in Figures 5.8(a) and 5.8(c), and the optimal iteration number k_{opt} chosen according to the minimum of the accuracy error function (5.50) in Figures 5.8(b) and 5.8(d), for various percentages of noise $p \in \{1, 3, 5\}\%$ for Example 2 with the displacement measurement (5.55) and $\tau = 1.15$ (upper part of the table) and with the time-average displacement measurement (5.56) and $\tau = 1.25$ (lower part of the table). The corresponding accuracy errors $E(f_{k_{discr}})$ and $E(f_{k_{opt}})$ are also included.

p	1%	3%	5%
k_{opt}	7	6	6
$E(f_{k_{opt}})$	0.0102	0.0286	0.0464
k_{discr}	6	5	4
$E(f_{k_{discr}})$	0.0107	0.0313	0.0632
k_{opt}	36	30	27
$E(f_{k_{opt}})$	0.0286	0.0725	0.1102
k_{discr}	33	27	24
$E(f_{k_{discr}})$	0.0310	0.0778	0.1200

So far, we have tested successfully examples for which analytical solutions for the displacement and force are available, as given by equations (5.39) and (5.40) for Example 1, and (5.57) and (5.58) for Example 2. The next three examples that we test concern relatively arbitrary input data for which an analytical solution for the displacement $u(x, t)$ is not readily available.

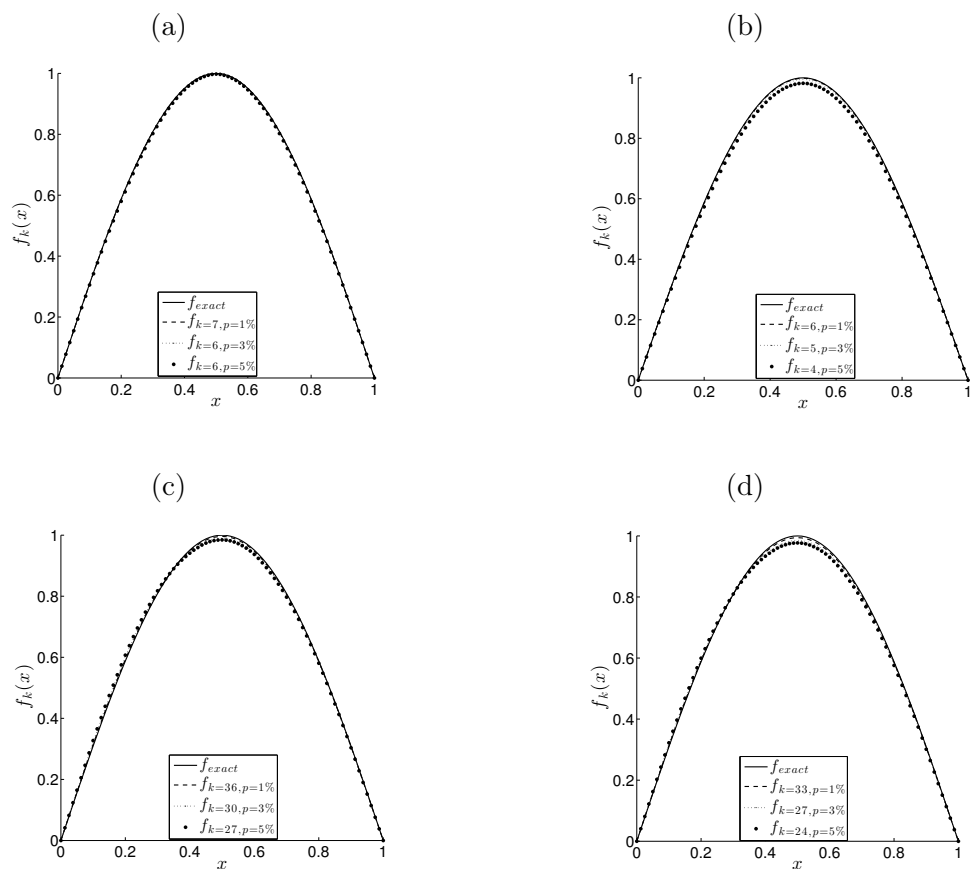


Figure 5.9: The numerical solution f_k at various iteration numbers k , in comparison with the exact solution (5.58), for $p \in \{1, 3, 5\}\%$ noise for the inverse problem of Example 2 with the displacement measurement (5.55) for (a) $k_{opt} \in \{7, 6, 6\}$, (b) $k_{discr} \in \{6, 5, 4\}$, and with the time-average displacement measurement (5.56) for (c) $k_{opt} \in \{36, 30, 27\}$, (d) $k_{discr} \in \{33, 27, 24\}$.

5.5.3 Example 3

Consider first the direct problem given by the wave equation (5.35) with the input data (5.37),

$$u(x, 0) = \varphi(x) = \sin(\pi x), \quad u_t(x, 0) = \psi(x) = 0, \quad x \in [0, 1], \quad (5.59)$$

$$g(x, t) = 1 + t, \quad t \in [0, 1], \quad (5.60)$$

5.5 Numerical results and discussion

$$f(x) = \frac{1}{\tilde{\sigma}\sqrt{2\pi}} \exp\left(-\frac{(x-\mu)^2}{2\tilde{\sigma}^2}\right), \quad (5.61)$$

where $\tilde{\sigma} = 0.1$ and $\mu = 0.5$. Note that for this example, the force (5.61) is a Gaussian normal function with mean μ and standard deviation $\tilde{\sigma}$. As $\tilde{\sigma} \rightarrow 0$, expression (5.61) mimics the Dirac delta distribution $\Delta(x - \mu)$.

Unlike in the previous two examples, for the above direct problem an explicit analytical solution for the displacement $u(x, t)$ is not readily available and therefore, the values (5.2) and (5.3) of $u(x, 1)$ and $\int_0^1 u(x, t) dt$, illustrated in Figures 5.10(a) and 5.10(b), respectively, have been obtained numerically using the FDM, as described in subsection 5.5.1. From these figures, a rapid convergence of the numerical results can be observed.

We next solve the inverse problems using the numerically simulated data with $N = M = 80$ from Figure 5.10. In the numerical solutions of the direct and adjoint problems of the iterative procedure described in Section 5.4 we also take $N = M = 80$ and $\gamma = 1$. We deliberately use the same mesh discretisation $N = M = 80$ in order to check for exact data the numerical convergence of the Landweber method proposed in the absence of any numerical discretisation error, the only noise present being of the $O(10^{-16})$ double precision computer round-off errors. Note that we do not commit an inverse crime since the initial guess is arbitrary, we also add random noise to the input data and the inverse iterative procedure is different than the direct problem solver.

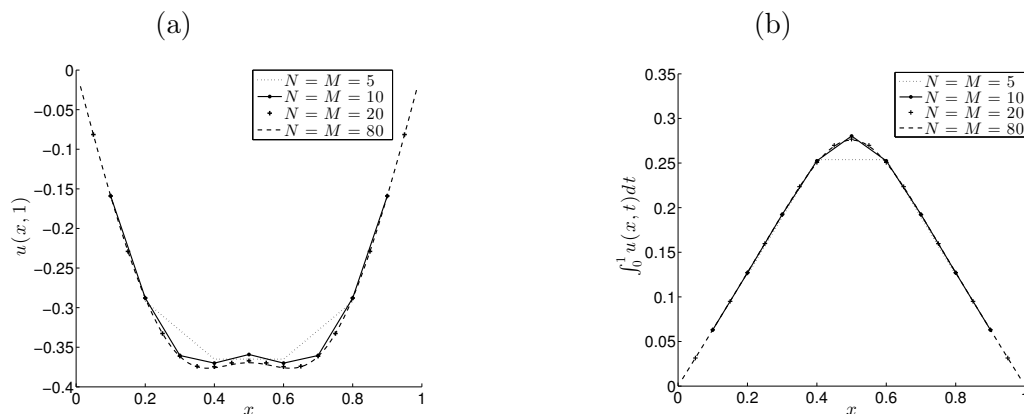


Figure 5.10: Numerical solution for (a) $u(x, 1)$ and (b) $\int_0^1 u(x, t) dt$, for various $N = M \in \{5, 10, 20, 80\}$, for the direct problem of Example 3.

5.5.3.1 Inverse problems

As in Example 2, the function (5.60) satisfies $g(x, t) \geq 0, g_t(x, t) > 0$, for every $(x, t) \in \overline{Q}_T$ and hence, see (Lesnic, Hussein and Johansson, accepted), both the inverse problems (5.35), (5.37), (5.59) with the input (5.2) or (5.3) represented in Figure 5.10(a) or 5.10(b), respectively, have unique solutions.

First consider the case without noise, i.e. $p = 0$. Figure 5.11 shows the objective functions (5.17) and (5.24), and the corresponding accuracy error (5.50), versus the number of iterations. Also, Figure 5.12 shows the convergence of the corresponding numerical solutions, as the number of iterations increases. From both figures it can be seen that the number of iterations needed to achieve a high level of accuracy is large of $O(10^5)$. It is much larger than in the previous Examples 1 and 2 because the force function (5.61) to be retrieved has a small standard deviation $\tilde{\sigma}$ and therefore a sharper peak centred at the mean value $\mu = 0.5$ than the trigonometric functions (5.39) and (5.58). By comparing the results in Figures 5.11 and 5.12 one can also observe that the convergence for the inverse problem with the displacement measurement (5.2) is much faster (and for most number of iterations more accurate) than that with time-average displacement measurement (5.14).

5.5 Numerical results and discussion

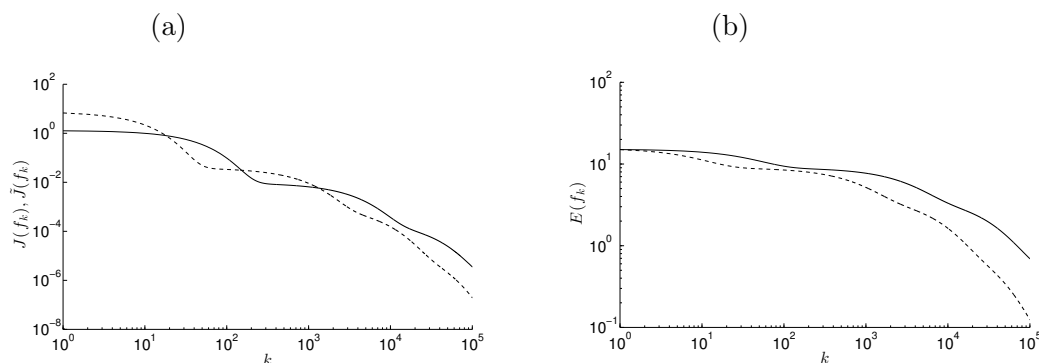


Figure 5.11: (a) The objective functions $J(f_k)$, $\tilde{J}(f_k)$ and (b) the accuracy error $E(f_k)$, versus the number of iterations $k = \overline{1, 10^5}$, no noise for the inverse problem of Example 3 with the displacement measurement (5.2) (---) and with the time-average displacement measurement (5.14) (—).

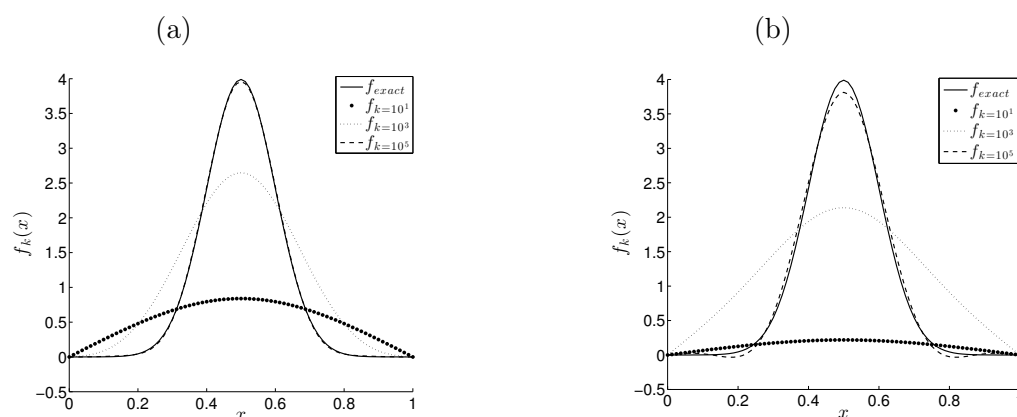


Figure 5.12: The numerical solution f_k at various iteration numbers k , in comparison with the exact solution (5.61), no noise for the inverse problem of Example 3 with (a) the displacement measurement (5.2), and (b) the time-average displacement measurement (5.14).

Next we add some $p \in \{1, 3, 5\}\%$ noise in the input data with $N = M = 80$ of Figure 5.10. Figures 5.13, 5.14 and Table 5.4 are analogous to Figures 5.8, 5.9 and Table 5.3 of Example 2 and similar quantitative conclusions can be drawn

5.5 Numerical results and discussion

in terms of comparing the inverse problems with either the displacement measurement (5.2) numerically simulated in Figure 5.10(a) or with the time-average measurement (5.14) numerically simulated in Figure 5.10(b). Of course, since more iterations are required for Example 3 than for Example 2, the thresholds k_{discr} and k_{opt} are much higher (and also more different between themselves) in Table 5.4 than in Table 5.3. Furthermore, the accuracy of the numerical results in Figure 5.9 for Example 2 is much higher than that in Figure 5.14 for Example 3, as expected since the trigonometric source (5.58) is less complicated than the Gaussian normal bell-shaped function (5.61).

5.5 Numerical results and discussion

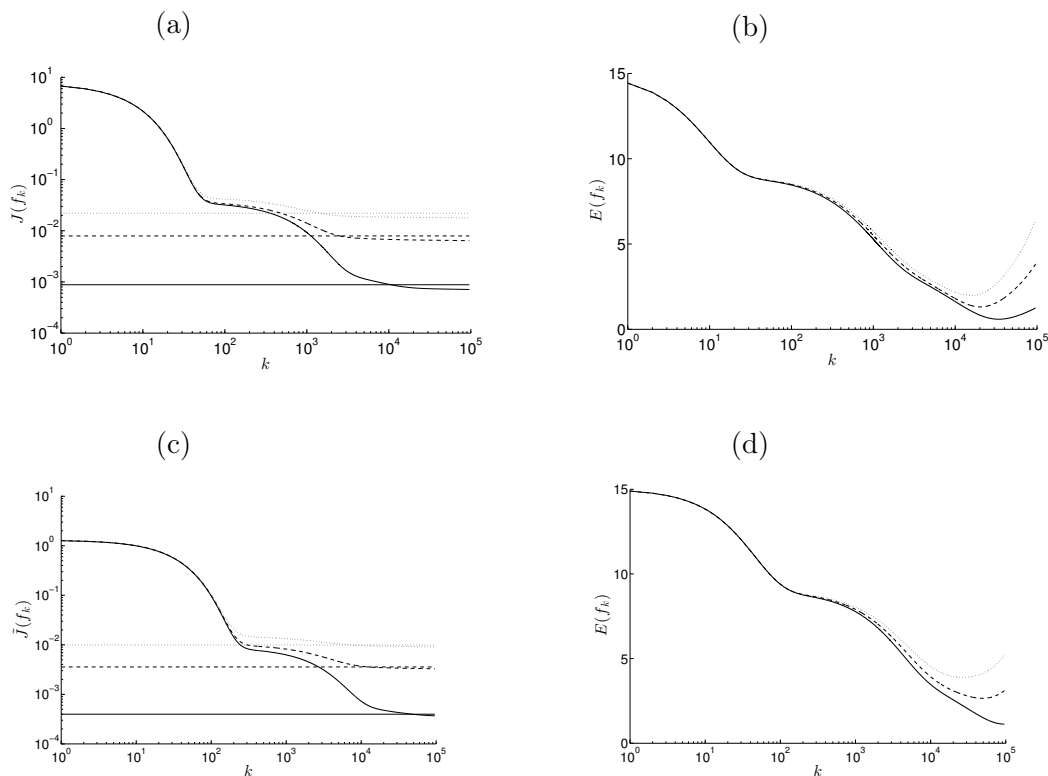


Figure 5.13: (a) The objective function $J(f_k)$ and (b) the corresponding accuracy error $E(f_k)$ for the inverse problem of Example 3 with the displacement measurement from Figure 5.10(a) with $N = M = 80$, and (c) the objective function $\tilde{J}(f_k)$ and (d) the corresponding accuracy error $E(f_k)$ for the inverse problem of Example 3 with the time-average displace measurement of Figure 5.10(b) with $N = M = 80$. All curves are functions of the number of iterations $k = \overline{1, 10^5}$, for $p = 1\%$ (—), $p = 3\%$ (- - -) and $p = 5\%$ (\cdots) noise. The horizontal lines in (a) and (c) represent the threshold $\tau^2 \epsilon^2 / 2$ with $\tau = 1.2$ and $\tau = 1.1$, respectively.

5.5 Numerical results and discussion

Table 5.4: The stopping iteration number k_{discr} chosen according to the discrepancy principle criterion (5.34), as illustrated in Figures 5.13(a), 5.13(c), and the optimal iteration number k_{opt} chosen according to the minimum of the accuracy error function (5.50) in Figures 5.13(b), 5.13(d), for various percentages of noise $p \in \{1, 3, 5\}\%$ for Example 3 with the displacement measurement from Figure 5.10(a) with $N = M = 80$ and $\tau = 1.2$ (upper part of the table) and with the time-average displacement measurement from Figure 5.10(b) with $N = M = 80$ and $\tau = 1.1$ (lower part of the table). The corresponding accuracy errors $E(f_{k_{discr}})$ and $E(f_{k_{opt}})$ are also included.

p	1%	3%	5%
k_{opt}	34080	20363	15577
$E(f_{k_{opt}})$	0.5899	1.3122	1.9840
k_{discr}	17712	7949	7012
$E(f_{k_{discr}})$	0.9448	2.0762	2.5206
k_{opt}	95908	49208	26760
$E(f_{k_{opt}})$	1.1314	2.6532	3.8913
k_{discr}	64996	35905	14998
$E(f_{k_{discr}})$	1.2761	2.7219	4.1004

5.5 Numerical results and discussion

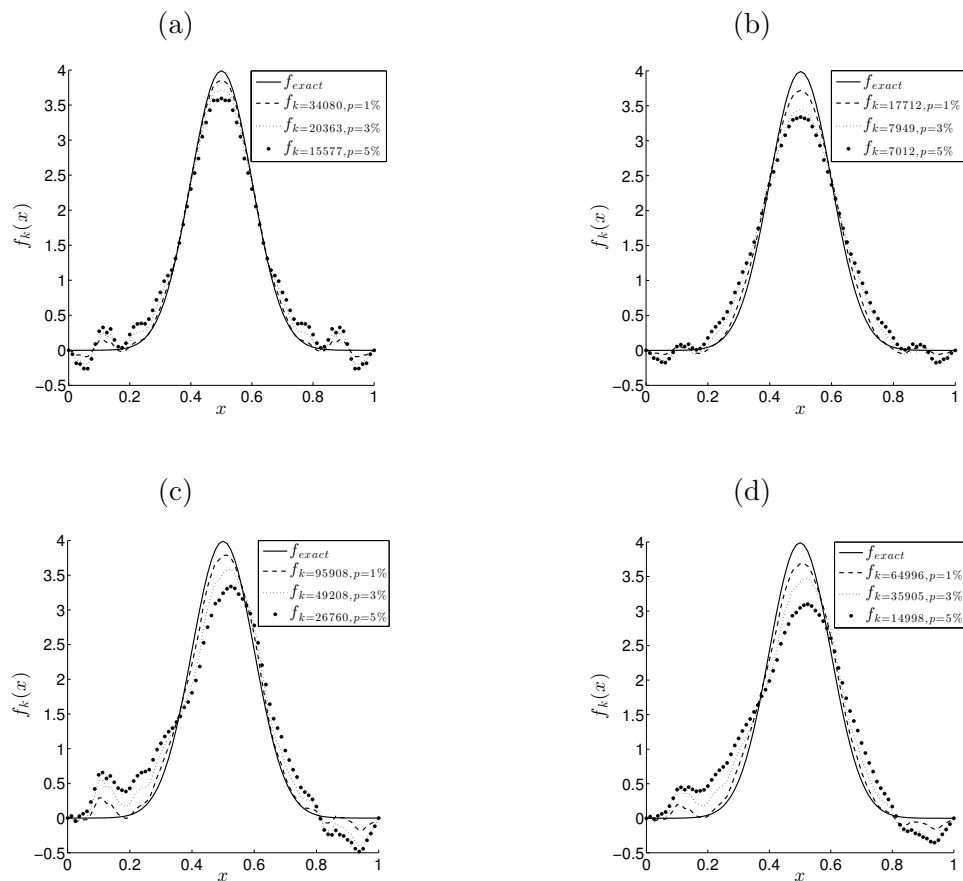


Figure 5.14: The numerical solution f_k at various iteration numbers k , in comparison with the exact solution (5.61), for $p \in \{1, 3, 5\}\%$ noise for the inverse problem of Example 3 with the displacement measurement from Figure 5.10(a) with $N = M = 80$ for (a) $k_{opt} \in \{34080, 20363, 15577\}$, (b) $k_{discr} \in \{17712, 7949, 7012\}$, and with the time-average displacement measurement from Figure 5.10(b) with $N = M = 80$ for (c) $k_{opt} \in \{95908, 49208, 26760\}$, (d) $k_{discr} \in \{64996, 35905, 14998\}$.

5.5.4 Example 4

Consider first the direct problem given by the wave equation (5.35) with the input data (5.37),

$$u(x, 0) = \varphi(x) = 0, \quad u_t(x, 0) = \psi(x) = 0, \quad x \in [0, 1], \quad (5.62)$$

5.5 Numerical results and discussion

$$g(x, t) = 1 + t, \quad t \in [0, 1], \quad (5.63)$$

$$f(x) = \begin{cases} x & \text{if } 0 \leq x \leq \frac{1}{2}, \\ 1 - x & \text{if } \frac{1}{2} < x \leq 1. \end{cases} \quad (5.64)$$

Note that for this example, the force (5.64) has a triangular shape, being continuous but non-differentiable at the peak $x = 1/2$. This example also does not possess an explicit analytical solution for the displacement $u(x, t)$ being readily available.

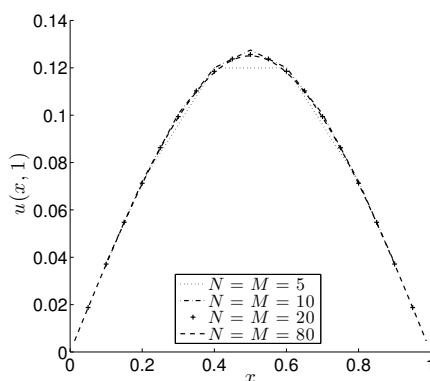


Figure 5.15: Numerical solution for $u(x, 1)$, for various $N = M \in \{5, 10, 20, 80\}$, for the direct problem of Example 4.

Figure 5.15 shows the rapid convergence of the FDM numerical solution $u(x, 1)$ of the direct problem (5.35), (5.37) and (5.62), as $N = M$ increases. The numerically simulated $u(x, 1)$ with $N = M = 80$ is used as input data (5.2) in the inverse problem (5.35), (5.37), (5.62).

It was observed in Example 3 and elsewhere that the convergence of the Landweber iterative method described in Section 5.4 can become prohibitively slow. One way to increase the rate of convergence is to increase the value of the relaxation parameter γ in (5.31) and we shall investigate this effect in the next Example 5. Alternatively, one can speed up the convergence of the minimization of the least-squares functional (5.17) or (5.24) by employing the convergent and regularizing conjugate gradient method (CGM), see (Engl, Hanke and Neubauer, 2000), based on the recurrence (5.68) below. In addition, the CGM does not

5.5 Numerical results and discussion

require any choice of a relaxation parameter γ , as the Landweber method does in order to iterate in formula (5.31). Similarly, as described in (Erdem, Lesnic and Hasanov, 2013; Johansson and Lesnic, 2007a) for the heat equation, this algorithm runs as follows:

Let steps (i) and (ii) be the same as in the algorithm of Section 5.4. The next steps are as follows:

(iii) Calculate

$$d_k(x) = -z_k(x) + \beta_{k-1}d_{k-1}(x), \quad (5.65)$$

with the convention that $\beta_{-1} = 0$ and

$$\beta_{k-1} = \frac{\|z_k\|_{L^2(\Omega)}^2}{\|z_{k-1}\|_{L^2(\Omega)}^2}, \quad k \geq 1. \quad (5.66)$$

(iv) Solve the direct problem (5.1), (3.3), (3.4), (4.1) with $\varphi = \psi = 0$ and $f = d_k$ to determine A_0d_k or \tilde{A}_0d_k , where the operators A_0 and \tilde{A}_0 have been defined in Section 5.3. Set the direction search

$$\alpha_k = \frac{\|z_k\|_{L^2(\Omega)}^2}{\|A_0d_k\|_{L^2(\Omega)}^2}, \quad \text{or} \quad \alpha_k = \frac{\|z_k\|_{L^2(\Omega)}^2}{\|\tilde{A}_0d_k\|_{L^2(\Omega)}^2}, \quad k \geq 0, \quad (5.67)$$

and pass to the new iteration by letting

$$f_{k+1}(x) = f_k(x) + \alpha_k d_k(x). \quad (5.68)$$

(v) Let u_{k+1} solve the direct problem (5.1), (3.3), (3.4), (4.1) with $f = f_{k+1}$ and go back (repeat) steps (ii)-(iv) until the discrepancy principle stopping criterion (5.34) is satisfied.

Note that for $\Omega = (0, L)$ the $L^2(0, L)$ integrals in (5.66) and (5.67) are calculated using the trapezoidal rule which, for the homogeneous Dirichlet boundary data (5.37), is given by

$$\|z_k\|_{L^2(0,L)}^2 = (\Delta x) \sum_{i=1}^{M-1} z_k^2(x_i), \quad (5.69)$$

5.5 Numerical results and discussion

and a similar expression exists for $\|A_0 d_k\|_{L^2(0,L)}^2$.

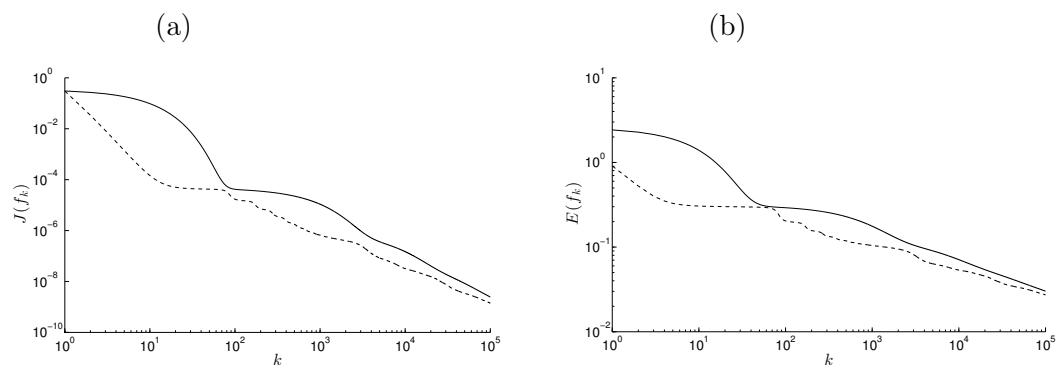


Figure 5.16: (a) The objective function $J(f_k)$ and (b) the accuracy error $E(f_k)$, versus the number of iterations $k = \overline{1, 10^5}$, obtained using the Landweber method (—) and the CGM (- - -), no noise for the inverse problem of Example 4.

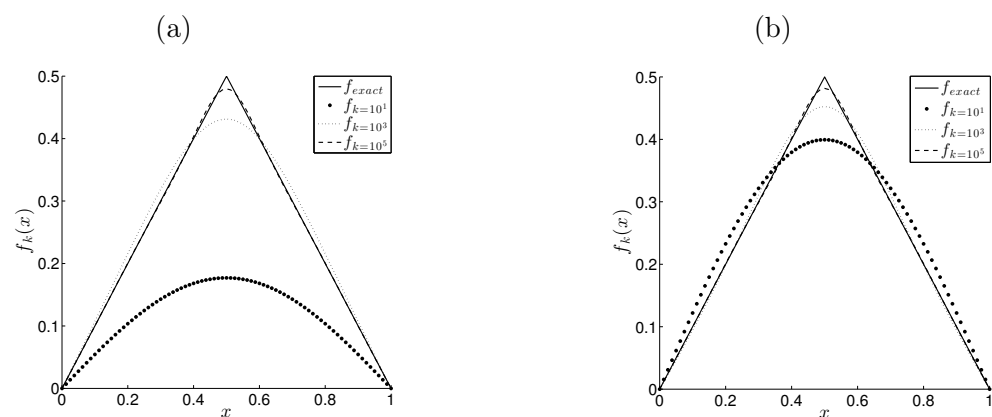


Figure 5.17: Numerical solution f_k for various iteration numbers $k \in \{10^1, 10^3, 10^5\}$, in comparison with the exact solution (5.64), obtained using (a) the Landweber method and (b) the CGM, no noise for the inverse problem of Example 4.

The objective function (5.17), the accuracy error (5.50) and the numerical solution for the force at various iteration numbers obtained using the Landweber method and the CGM are plotted in Figures 5.16(a), 5.16(b) and 5.17, respectively. From these figures it can be seen that it takes a large number of iterations

5.5 Numerical results and discussion

of $O(10^5)$ to converge with a good accuracy to the exact solution (5.64), similarly to what happened for Example 3, when the Landweber method is employed. In comparison to the previous Examples 1 and 2 this is to be expected because the force function (5.64) to be retrieved is non-smooth possessing a sharp corner at the peak $x = 1/2$. Moreover, the behaviour of the convergence is similar to that of Example 3 for which the Gaussian normal force function (5.61) to be retrieved, although smooth, it possesses also a sharp peak at $x = 1/2$. On the other hand, the convergence is much faster when the CGM is employed.

When we add some $p \in \{1, 3, 5\}\%$ noise in the input data (5.2), the conclusions are similar to those drawn from Example 3 if one compares Figures 5.18, 5.19 and Table 5.5 with Figures 5.13, 5.14 and the upper part of Table 5.4. Furthermore, the numerical details included in Table 5.5 show that the CGM is much faster than the Landweber method in obtaining the thresholds k_{opt} and k_{discr} .

5.5 Numerical results and discussion

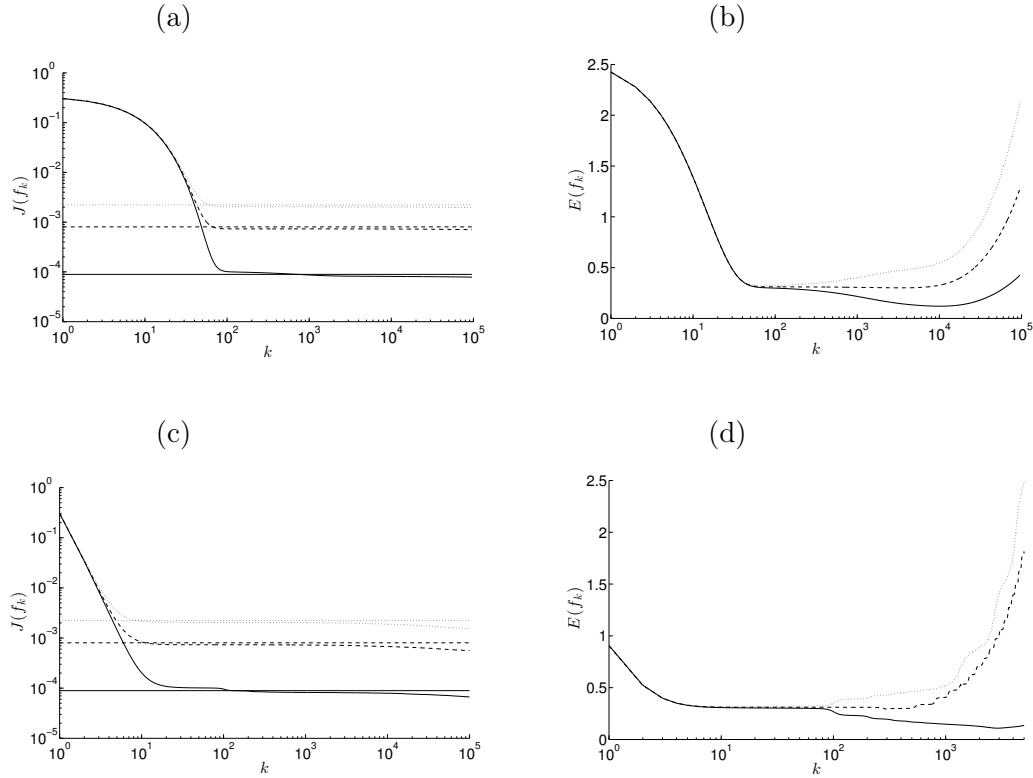


Figure 5.18: (a) and (c) The objective function $J(f_k)$, and (b) and (d) the accuracy error $E(f_k)$, versus the number of iterations $k = \overline{1, 10^5}$, obtained using the Landweber method and the CGM, respectively, for $p = 1\%$ (—), $p = 3\%$ (- - -) and $p = 5\%$ (· · ·) noise for the inverse problem of Example 4. The horizontal lines represents the threshold $\tau^2 \frac{\epsilon^2}{2}$ with $\tau = 1.15$.

5.5 Numerical results and discussion

Table 5.5: The stopping iteration numbers k_{discr} chosen according to the discrepancy principle criterion (5.34) (with $\tau = 1.15$), as illustrated in Figures 5.18(a) and 5.18(c), and the optimal iteration numbers k_{opt} chosen according to the minimum of the accuracy error function (5.50) in Figures 5.18(b) and 5.18(d), for various percentages of noise $p \in \{1, 3, 5\}\%$ for Example 4. The corresponding accuracy errors $E(f_{k_{discr}})$ and $E(f_{k_{opt}})$ are also included. The CGM results are included in brackets.

p	1%	3%	5%
k_{opt}	10171 (2908)	3429 (295)	68 (12)
$E(f_{k_{opt}})$	0.1202 (0.1090)	0.3009 (0.2943)	0.3198 (0.3167)
k_{discr}	2995 (130)	95 (21)	70 (11)
$E(f_{k_{discr}})$	0.1507 (0.2341)	0.3105 (0.3108)	0.3199 (0.3168)

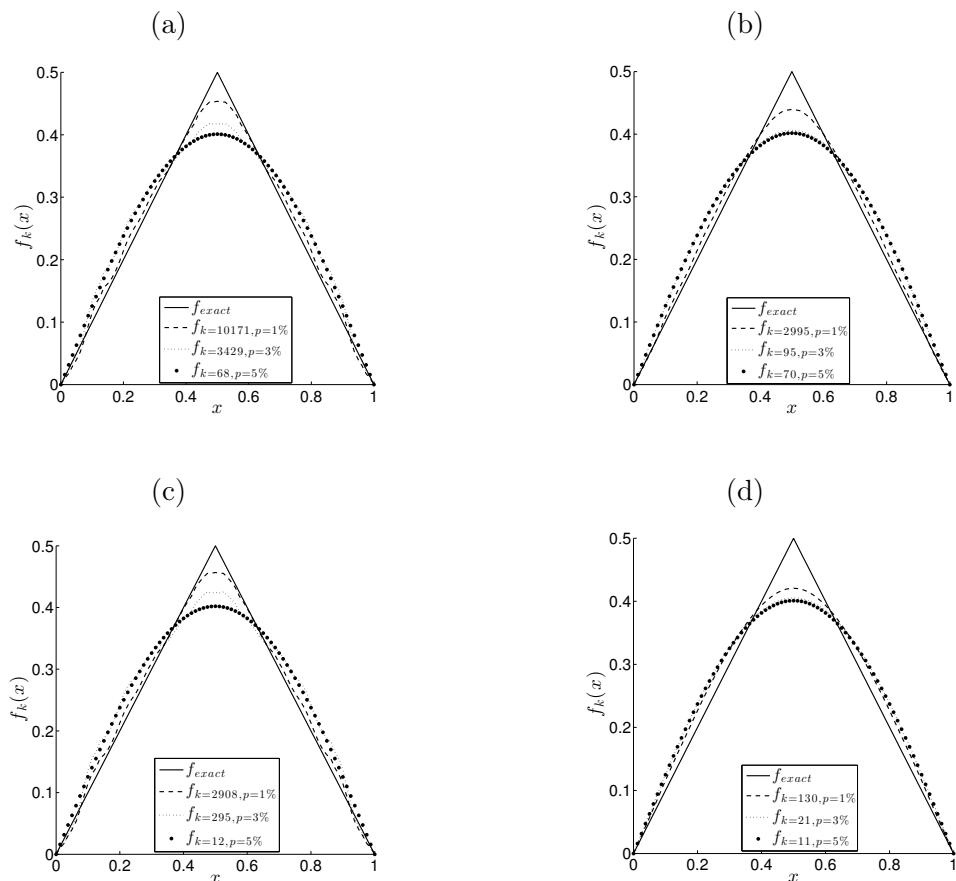


Figure 5.19: The exact solution f in comparison with numerical solution f_k for (a) and (c) $k_{opt} \in \{10171, 3429, 68\}$ and $k_{opt} \in \{2908, 295, 12\}$, and (b) and (d) $k_{discr} \in \{2995, 95, 70\}$ and $k_{discr} \in \{130, 21, 11\}$, obtained using the Landweber method and the CGM, respectively, for $p \in \{1, 3, 5\}\%$ noise for the inverse problem of Example 4.

We finally note that similar results have been obtained for the inverse problem given by equations (5.35), (5.37), (5.62) with the integral measurement (5.14) and therefore, they are not presented.

5.5.5 Example 5

The previous example investigated a severe test given by the non-smooth triangular shape force function (5.64). In this subsection, we consider an even more

severe test example given by the discontinuous force

$$f(x) = \begin{cases} 0 & \text{if } 0 \leq x < \frac{1}{3}, \\ 1 & \text{if } \frac{1}{3} \leq x \leq \frac{2}{3}, \\ 0 & \text{if } \frac{2}{3} < x \leq 1. \end{cases} \quad (5.70)$$

We take the same input data (5.62) and (5.63), as in Example 4. Then, on solving the direct problem given by equations (5.35), (5.37), (5.62) with the forcing term given by the product of the functions in (5.63) and (5.70), we obtain the numerical results for the time-average displacement $\int_0^1 u(x, t) dt$ illustrated in Figure 5.20. From this figure it can be seen that a convergent FDM numerical solution is achieved.

For brevity, in what follows we only illustrate the numerical results obtained for the inverse problem (5.1), (3.3), (3.4), (4.1), (5.14), noting that similar results have been obtained for the inverse problem (5.1)-(5.2).

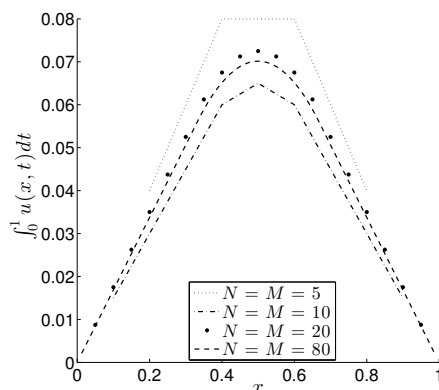


Figure 5.20: Numerical solution for $\int_0^1 u(x, t) dt$, for various $N=M \in \{5, 10, 20, 80\}$, for the direct problem of Example 5.

The numerically simulated data for $\int_0^1 u(x, t) dt$ obtained with $N = M = 80$ is used as input (5.3) in the inverse problem given by equations (5.35), (5.37) and (5.62).

As expected, for exact data a very slow convergence of the objective function (5.24) is encountered by the Landweber iteration method because the force function (5.70) to be retrieved is discontinuous at the points $x \in \{1/3, 2/3\}$. In

5.5 Numerical results and discussion

fact, we had to increase the value of the relaxation factor γ in order to achieve convergence in a reasonable number of iterations.

Figure 5.21 shows the objective function (5.24) and the accuracy error (5.50), versus the number of iterations $k = \overline{1, 10^5}$, for various values of the relaxation parameter $\gamma \in \{1, 5, 15\}$. From this figure it can be seen that the rate of convergence increases as we increase γ from 1 to 5 and then to 15. The corresponding numerical solutions for the force $f_k(x)$ are shown in Figure 5.22 for various numbers of iterations $k \in \{10^1, 10^3, 10^5\}$, and again more accurate results are obtained as we increase k and/or γ .

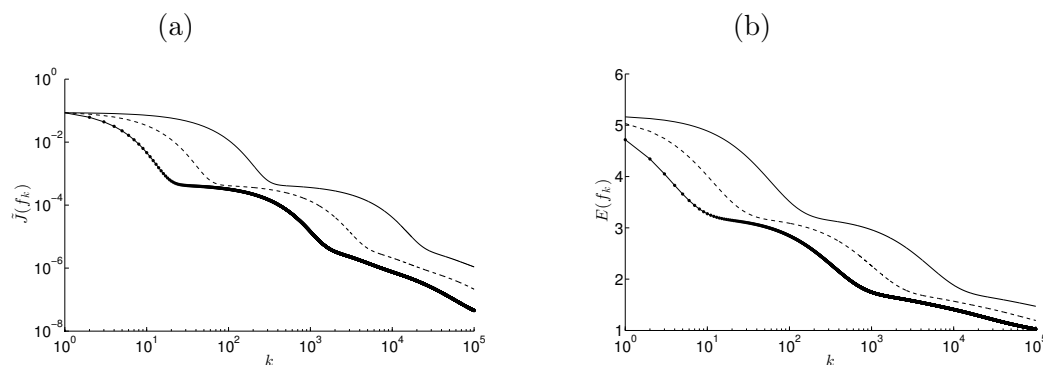


Figure 5.21: (a) The objective function $\tilde{J}(f_k)$ and (b) the accuracy error $E(f_k)$, versus the number of iterations $k = \overline{1, 10^5}$, for various $\gamma = 1$ (—), $\gamma = 5$ (- - -) and $\gamma = 15$ (- • -), no noise for the inverse problem of Example 5.

5.5 Numerical results and discussion

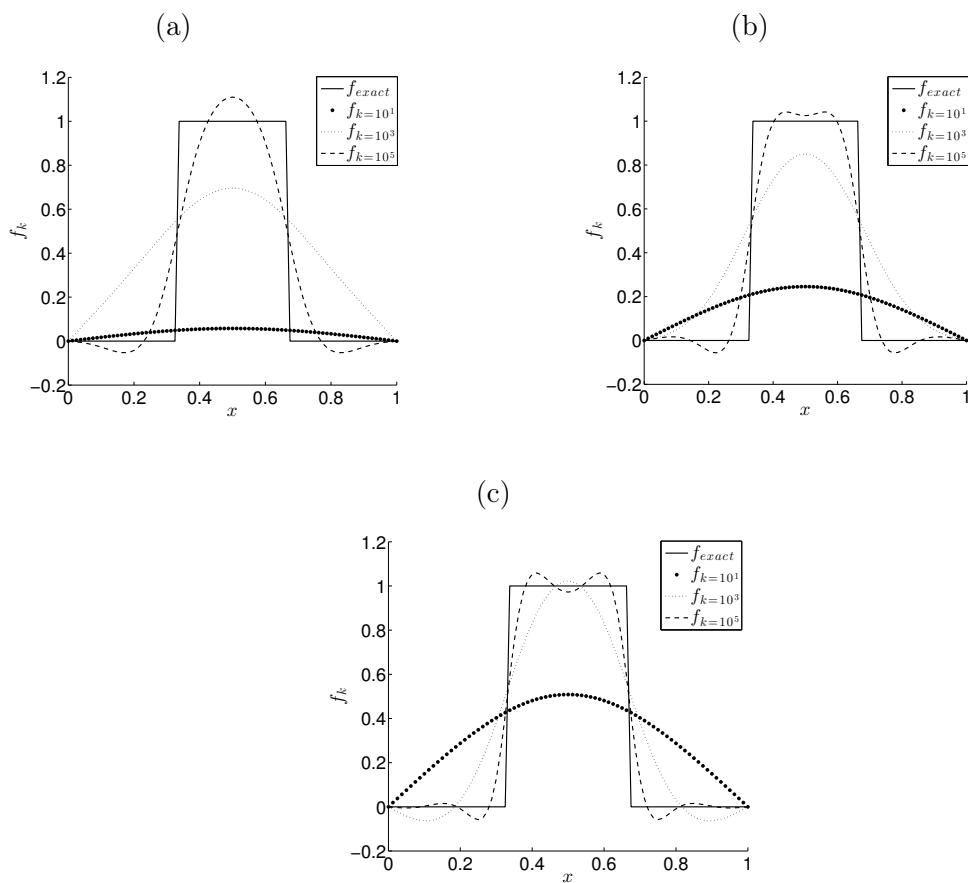


Figure 5.22: Numerical solution f_k for various iteration numbers $k \in \{10^1, 10^3, 10^5\}$, in comparison with the exact solution (5.70), for (a) $\gamma=1$, (b) $\gamma=5$ and (c) $\gamma=15$, no noise for the inverse problem of Example 5.

In order to investigate the stability of the numerical solution we include some $p \in \{1, 3, 5\}\%$ noise into the input data, as given by equation (5.51), and the numerical results obtained with $\gamma = 15$ are presented in Figures 5.23, 5.24 and Table 5.6. As in the previous examples, Figure 5.23 and Table 5.6 justify the choice of the stopping iteration number k_{discr} and furthermore, the numerical solutions illustrated in Figure 5.24 show that stable and reasonably accurate results are obtained for recovering the severely discontinuous force function (5.70).

5.5 Numerical results and discussion

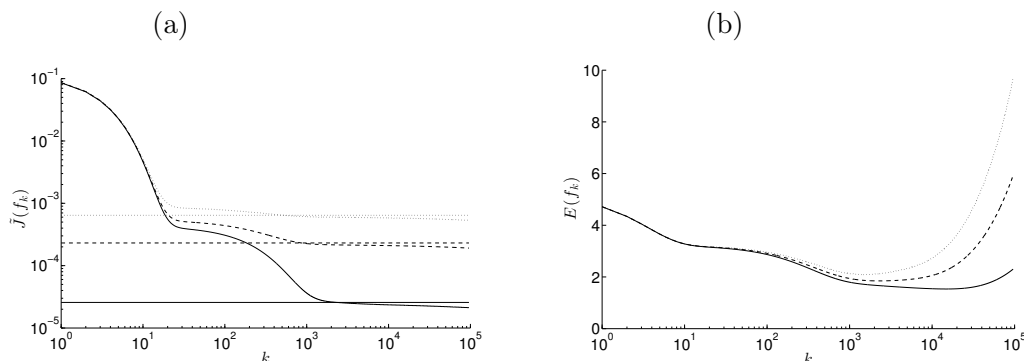


Figure 5.23: (a) The objective function $\tilde{J}(f_k)$ and (b) the accuracy error $E(f_k)$, versus the number of iterations $k = \overline{1, 10^5}$, for $p = 1\%$ (—), $p = 3\%$ (- - -) and $p = 5\%$ (· · ·) noise for the inverse problem of Example 5 obtained with $\gamma = 15$. The horizontal lines represents the threshold $\tau^2 \frac{\epsilon^2}{2}$ with $\tau = 1.1$.

Table 5.6: The stopping iteration number k_{discr} chosen according to the discrepancy principle criterion (5.34) (with $\tau = 1.1$), as illustrated in Figure 5.23(a), and the optimal iteration number k_{opt} chosen according to the minimum of the accuracy error function (5.50) in Figure 5.23(b), for various percentages of noise $p \in \{1, 3, 5\}\%$ for Example 5 obtained with $\gamma = 15$. The corresponding accuracy errors $E(f_{k_{discr}})$ and $E(f_{k_{opt}})$ are also included.

p	1%	3%	5%
k_{opt}	14823	2275	1523
$E(f_{k_{opt}})$	1.5342	1.8471	2.0906
k_{discr}	9599	2000	1000
$E(f_{k_{discr}})$	1.5466	1.8488	2.1319

In the next section we present a numerical extension to two-dimensions.

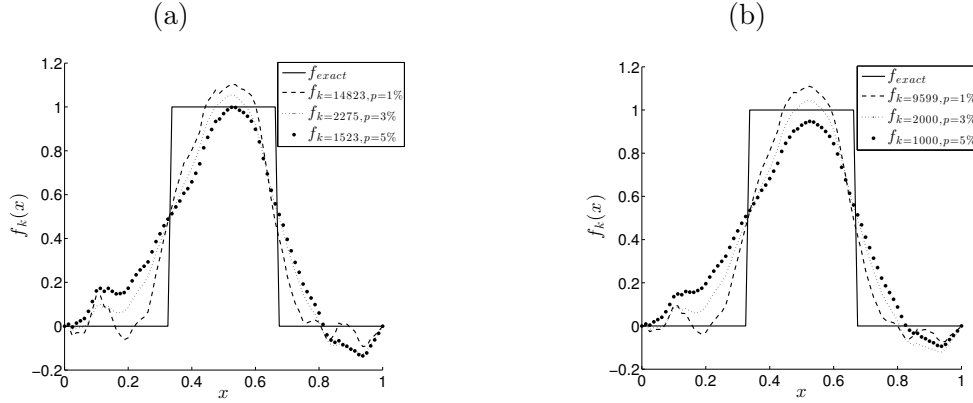


Figure 5.24: The exact solution (5.70) for f in comparison with the numerical solution f_k for (a) $k_{opt} \in \{14823, 2275, 1523\}$ and (b) $k_{discr} \in \{9599, 2000, 1000\}$, for $p \in \{1, 3, 5\}\%$ noise for the inverse problem of Example 5 obtained with $\gamma = 15$.

5.6 Two-dimensions

The theoretical results obtained for the inverse problems together with the regularizing methods are not limited to one spatial dimension. In principle, the numerical examples and observations can be carried forward to two and three-dimensional solution domains and similar results and conclusion are expected. However, recovering sources with complicated behaviour in higher dimensions would require delicate numerical considerations that would expand the present work too much. To at least show that the proposed methods are practical also in higher dimensions, we therefore consider a two-dimensional example being analogous to Example 1 in terms of level of complication of the source to be retrieved.

We consider the initial boundary value problem (5.1), (3.3), (3.4), (4.1) in two-dimensions, i.e. $n = 2$ and $\Omega = (0, L) \times (0, L)$ with $L > 0$, given by

$$u_{tt}(x, y, t) = u_{xx}(x, y, t) + u_{yy}(x, y, t) + f(x, y)g(x, y, t),$$

$$(x, y, t) \in (0, L) \times (0, L) \times (0, T], \quad (5.71)$$

$$u(x, y, 0) = \varphi(x, y), \quad u_t(x, y, 0) = \psi(x, y), \quad (x, y) \in (0, L) \times (0, L), \quad (5.72)$$

$$u(x, y, t) = 0, \quad (x, y) \in \partial\Omega \times (0, T). \quad (5.73)$$

The discrete form of this direct problem is as follows. We divide the solution domain $(0, L) \times (0, L) \times (0, T)$ into M , N and K subintervals of equal space lengths Δx , Δy and time step Δt , where $\Delta x = L/M$, $\Delta y = L/N$ and $\Delta t = T/K$. We denote $u_{i,j,k} = u(x_i, y_j, t_k)$, where $x_i = i\Delta x$, $y_j = j\Delta y$, $t_k = k\Delta t$, $f_{i,j} := f(x_i, y_j)$ and $g_{i,j,k} := g(x_i, y_j, t_k)$ for $i = \overline{0, M}$, $j = \overline{0, N}$, $k = \overline{0, K}$. Then, a central-difference approximation to equations (5.71)-(5.73) at the mesh points $(x_i, y_j, t_k) = (i\Delta x, j\Delta y, k\Delta t)$ is

$$\begin{aligned} u_{i,j,k+1} &= r_x(u_{i+1,j,k} + u_{i-1,j,k}) + r_y(u_{i,j+1,k} + u_{i,j-1,k}) + 2r_{xy}u_{i,j,k} - u_{i,j,k-1} \\ &+ (\Delta t)^2 f_{i,j} g_{i,j,k}, \quad i = \overline{1, (M-1)}, \quad j = \overline{1, (N-1)}, \quad k = \overline{1, (K-1)}, \end{aligned} \quad (5.74)$$

$$\begin{aligned} u_{i,j,0} &= \varphi(x_i, y_j), \quad i = \overline{0, M}, \quad j = \overline{0, N}, \\ \frac{u_{i,j,1} - u_{i,j,-1}}{2\Delta t} &= \psi(x_i, y_j), \quad i = \overline{1, (M-1)}, \quad j = \overline{1, N-1}, \end{aligned} \quad (5.75)$$

$$\begin{aligned} u_{0,j,k} &= u_{M,j,k} = u_{i,0,k} = u_{i,N,k} = 0, \\ i &= \overline{1, (M-1)}, \quad j = \overline{1, (N-1)}, \quad k = \overline{1, K}, \end{aligned} \quad (5.76)$$

where $r_x = \frac{(\Delta t)^2}{(\Delta x)^2}$, $r_y = \frac{(\Delta t)^2}{(\Delta y)^2}$, and $r_{xy} = 1 - r_x - r_y$. This is an explicit formula which is stable if $\frac{4(\Delta t)^2}{(\Delta x)^2 + (\Delta y)^2} \leq 1$, giving approximation values for the solution at mesh points along $t = 2\Delta t, 3\Delta t, \dots$, as soon as the mesh values along $t = \Delta t$ have been determined by allowing $j = 0$ in equation (5.74) and using (5.75), to obtain

$$\begin{aligned} u_{i,j,1} &= \frac{r_x}{2}(\varphi(x_{i+1}, y_j) + \varphi(x_{i-1}, y_j)) + \frac{r_y}{2}(\varphi(x_i, y_{j+1}) + \varphi(x_i, y_{j-1})) \\ &+ r_{xy}\varphi(x_i, y_j) + (\Delta t)\psi(x_i, y_j) + \frac{1}{2}(\Delta t)^2 f_{i,j} g_{i,j,0}, \\ i &= \overline{1, (M-1)}, \quad j = \overline{1, N-1}. \end{aligned} \quad (5.77)$$

5.6.1 Example 6

Consider first the direct problem given by the two-dimensional wave equation (5.71) with $L = T = 1$, the initial conditions (5.72) given by

$$\begin{aligned} u(x, y, 0) &= \varphi(x, y) = 2 \sin(\pi x) \sin(\pi y), \quad u_t(x, y, 0) = \psi(x, y) = 0, \\ x &\in [0, 1], \quad y \in [0, 1], \end{aligned} \quad (5.78)$$

and the homogeneous Dirichlet boundary conditions (5.73) given by

$$u(0, y, t) = u(1, y, t) = u(x, 0, t) = u(x, 1, t) = 0, \quad x \in (0, 1), \quad y \in (0, 1), \\ t \in (0, 1), \quad (5.79)$$

when

$$g(x, y, t) = 2 + \cos(\pi t), \quad (x, y, t) \in (0, 1) \times (0, 1) \times (0, 1), \quad (5.80)$$

and

$$f(x, y) = \pi^2 \sin(\pi x) \sin(\pi y), \quad (x, y) \in (0, 1) \times (0, 1). \quad (5.81)$$

The exact solution is given by

$$u(x, y, t) = \sin(\pi x) \sin(\pi y) (1 + \cos(\pi t)), \quad (x, y, t) \in [0, 1] \times [0, 1] \times [0, 1]. \quad (5.82)$$

We consider the time-average displacement given by

$$U_T(x, y) = \int_0^1 u(x, y, t) dt = \sin(\pi x) \sin(\pi y), \quad (x, y) \in (0, 1) \times (0, 1), \quad (5.83)$$

which will be used as additional measurement information in the inverse problem of the next subsection.

This example is similar in behaviour to the one-dimensional Example 1. The absolute errors between (5.83) and the numerical values obtained using the trapezoidal rule approximation

$$\int_0^1 u(x_i, y_j, t) dt = \frac{\Delta t}{2} \left(\varphi(x_i, y_j) + 2 \sum_{k=1}^{K-1} u(x_i, y_j, t_k) + u(x_i, y_j, t_K) \right), \\ i = \overline{1, M-1}, j = \overline{1, N-1} \quad (5.84)$$

are shown in Figure 5.25, and one can observe that an excellent agreement and convergence are obtained.

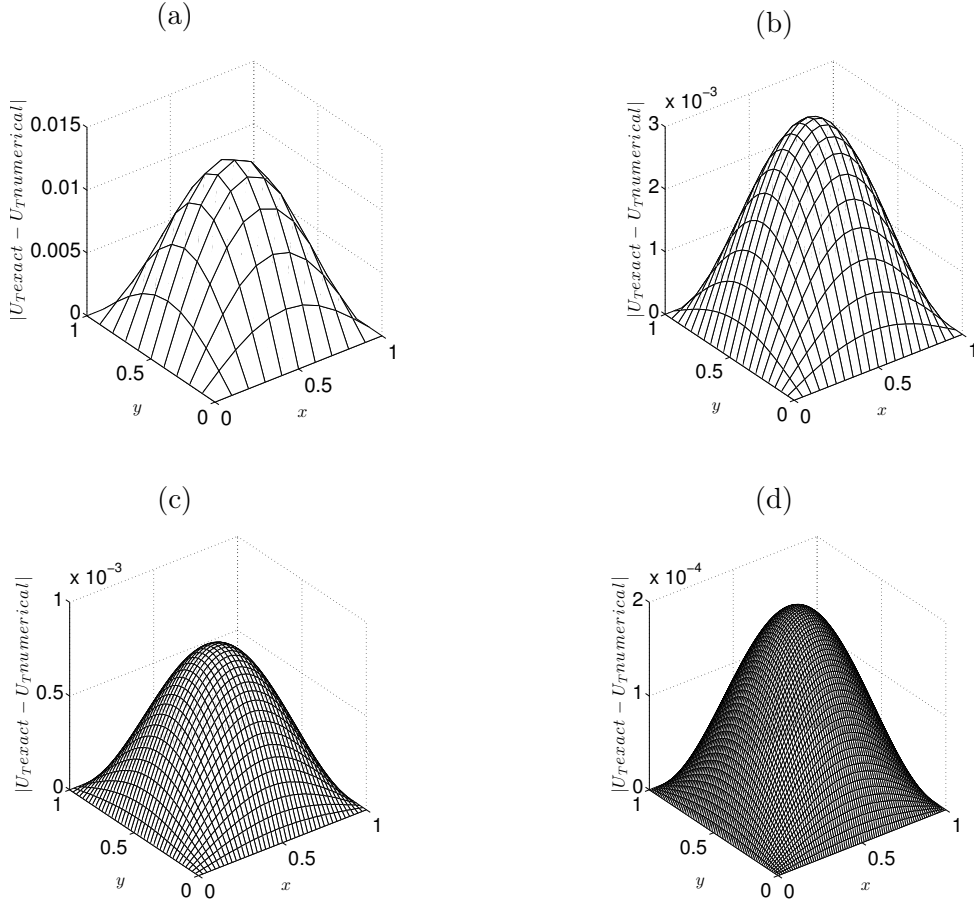


Figure 5.25: The absolute errors between the exact (5.83) and numerical solutions (5.84) for $\int_0^1 u(x, y, t) dt$ for various $N = M \in \{10, 20, 40, 80\}$ and $K = 2N \in \{20, 40, 80, 160\}$ in (a)-(d), respectively, for the direct problem of Example 6.

5.6.1.1 Inverse problem

In this subsection, we consider solving the inverse problem given by the wave equation (5.71) with g given by (5.80), subject to the initial conditions (5.78), the homogeneous Dirichlet boundary conditions (5.79) and the additional time-average displacement measurement (5.83) using the FDM with $N = M = 80$, $K = 160$ and the iterative Landweber method described in Section 5.4 with the relaxation parameter $\gamma = 1$ and the initial guess $f_0 \equiv 0$. The analytical solution of the above inverse problem of Example 6 is given by equations (5.81) and (5.82).

The objective function (5.24)

$$\tilde{J}(f_k) = \frac{1}{2} \|\xi_k\|^2 = \frac{1}{2} \sum_{i=1}^{M-1} \sum_{j=1}^{N-1} \xi_k^2(x_i, y_j), \quad (5.85)$$

where ξ_k is given by (5.49), is plotted in Figure 5.26(a), as a function of the number of iterations k . Whilst Figure 5.26(b) shows the accuracy error

$$E(f_k) = \|f_{exact} - f_k\| = \sqrt{\sum_{i=1}^{M-1} \sum_{j=1}^{N-1} (f(x_i, y_j) - f_k(x_i, y_j))^2}. \quad (5.86)$$

From these figures it can be seen that convergence of both functions (5.85) and (5.86) is achieved in about 300 to 500 iterations.

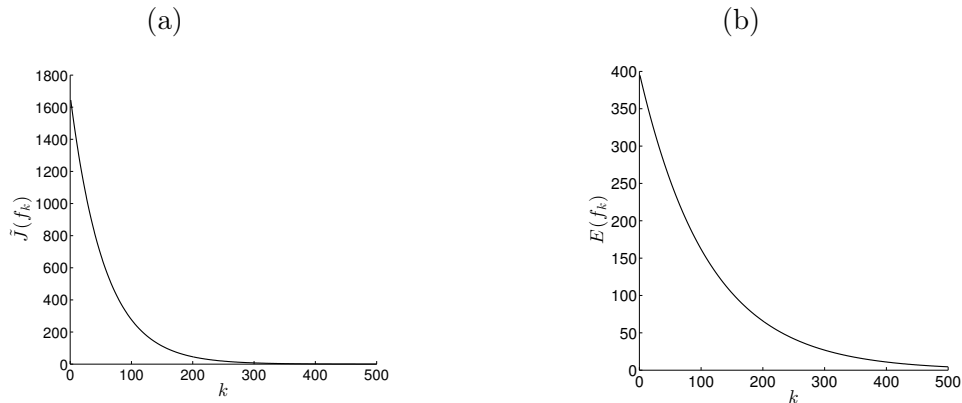


Figure 5.26: (a) The objective function (5.85) and (b) the accuracy error (5.86), versus the number of iterations $k = \overline{1, 500}$, no noise for the inverse problem of Example 6.

Figure 5.27 shows the numerical force solution f_k at various iteration numbers k and a monotonic increasing convergence to the exact solution (5.81) can be clearly observed.

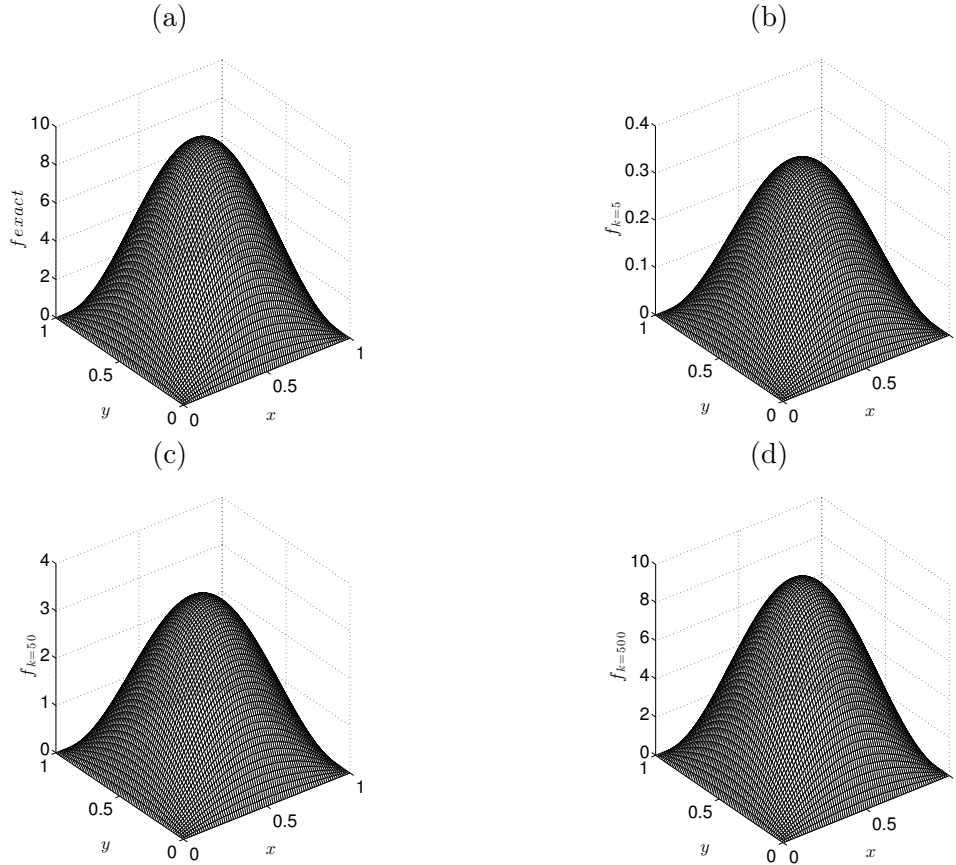


Figure 5.27: The numerical solution f_k for $k \in \{5, 50, 500\}$, in comparison with the exact solution (5.81), no noise for the inverse problem of Example 6.

In practice, the additional observation (5.83) comes from measurement which is inherently contaminated with errors. We therefore model this by replacing the exact data U_T by the noisy data

$$U_T^\epsilon(x_i, y_j) = U_T(x_i, y_j) + \epsilon_{i,j}, \quad i = \overline{1, (M-1)}, \quad j = \overline{1, (N-1)}, \quad (5.87)$$

where $(\epsilon_{i,j})_{i=\overline{1, M-1}, j=\overline{1, N-1}}$ are random noisy variables generated (using the MATLAB routine 'normrd') from a Gaussian normal distribution with mean zero and standard deviation $\sigma = p \times \max_{x,y \in [0,L]} |U_T(x, y)|$, where p represents the percentage of noise. The total amount of noise introduced in the cost functional (5.24)

is then given by

$$\frac{1}{2}\epsilon^2 = \frac{1}{2} \sum_{i=1}^{M-1} \sum_{j=1}^{N-1} \epsilon_{i,j}^2. \quad (5.88)$$

In order to investigate the stability of the numerical solution we include some $p \in \{1, 3, 5\}\%$ noise into the input data (5.83), as given by equation (5.87). The objective function (5.85) and the accuracy error (5.86) are shown in Figures 5.28(a) and 5.28(b), respectively, for $k = \overline{1, 1000}$ and $p \in \{1, 3, 5\}\%$ noisy data. These figures yield the values of the stopping iteration numbers k_{discr} and k_{opt} , as given in Table 5.7.

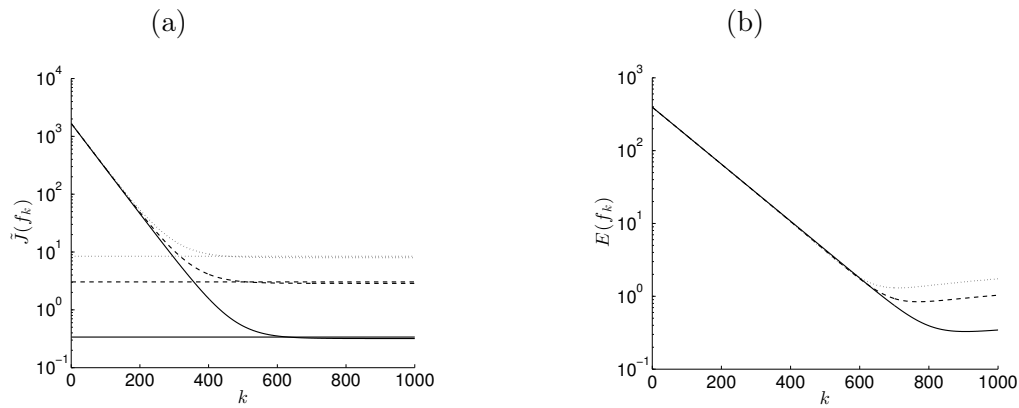


Figure 5.28: (a) The objective function (5.85) and (b) the accuracy error (5.86), versus the number of iterations $k = \overline{1, 1000}$, for $p = 1\%$ (—), $p = 3\%$ (- - -) and $p = 5\%$ (· · ·) noise for the inverse problem of Example 6. The horizontal lines represents the threshold $\tau^2 \frac{\epsilon^2}{2}$ with $\tau = 1.05$.

Table 5.7: The stopping iteration number k_{discr} chosen according to the discrepancy principle criterion (5.34) (with $\tau = 1.05$), as illustrated in Figure 5.28(a), and the optimal iteration number k_{opt} chosen according to the minimum of the accuracy error function (5.86) in Figure 5.28(b), for various percentages of noise $p \in \{1, 3, 5\}\%$ for Example 6. The corresponding accuracy errors $E(f_{k_{discr}})$ and $E(f_{k_{opt}})$ are also included.

p	1%	3%	5%
k_{opt}	906	769	711
$E(f_{k_{opt}})$	0.3285	0.8425	1.3057
k_{discr}	796	599	597
$E(f_{k_{discr}})$	0.4013	1.7573	1.8598

Finally, Figure 5.29 shows the analytical solution (5.81) for the force $f(x, y)$ in comparison with the numerical force $f_{k_{discr}}(x, y)$ for various percentages of noise $p \in \{1, 3, 5\}\%$. From this figure accurate and stable numerical predictions of the force can be observed.

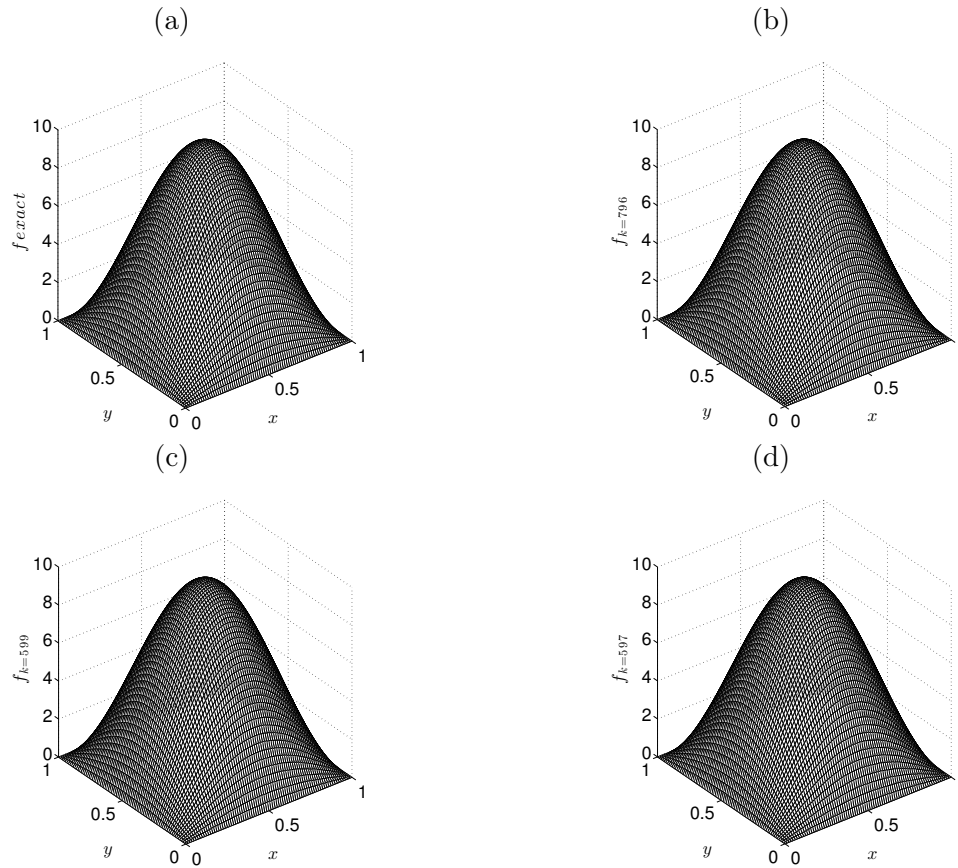


Figure 5.29: The exact solution (5.81) for f in comparison with the numerical solution f_k for $k_{discr} \in \{796, 599, 597\}$ for $p \in \{1, 3, 5\}\%$ noise, respectively, for the inverse problem of Example 6.

5.7 Conclusions

In this chapter, the determination of the displacement and the space-dependent force acting on a vibrating structure from measured final or time-average displacement in the wave equation has been investigated. These linear inverse problems are uniquely solvable, but they are still ill-posed since small errors in the input data cause large errors in the output force. The problems have been discretised numerically using the FDM, and the Landweber method and CGM have been presented and discussed illustrating the convergence of the iterative procedures for exact input data and their stability for noisy data. These iterative methods for

minimizing the least-squares functionals (5.17) or (5.24) have a regularizing character (providing they are stopped according to the discrepancy principle (5.33)). Moreover, unlike the classical non-iterative Tikhonov regularization method, employed in previous chapters and elsewhere for the heat equation, see (Yang and Fu, 2010), these iterative methods do not require employing or choosing a smoothing regularization matrix D_k in (1.1).

The Landweber method is simple to implement but it can be slowly convergent because a uniform search magnitude γ is adopted at each iteration in (5.31). On the other hand, the CGM is more sophisticated but it is more rapidly convergent than the Landweber method because a variable search magnitude α_k is adopted at various iterations in (5.68).

For the similar inverse source analyses for the parabolic heat equation using the Landweber and CGM methods we refer to (Johansson and Lesnic, 2007a,b), respectively, where similar conclusions were derived.

Numerical results have been presented for both smooth and non-smooth examples. As expected, smoother examples require less numbers of iterations to achieve convergence for exact data. Furthermore, an extension to a two-dimensional example has also been illustrated and qualitatively the results obtained possessed the same features in terms of good accuracy and stability as in the one-dimensional case, but for the increase in computational time.

Future work will consist in investigating the nonlinear inverse problem in which the unknown force depends on the displacement.

Chapter 6

Reconstruction of space-dependent potential and/or damping coefficients in the wave equation

6.1 Introduction

So far, all problems investigated in Chapters 2-5 have been linear and therefore, the minimization of the Tikhonov functional (1.1) was possible to have been performed exactly yielding the explicit solution (1.2). In this chapter, we investigate nonlinear inverse force problems which lend themselves to more difficult nonlinear minimizations. In particular, nonlinear identifications of the space-dependent potential and/or damping coefficients in the wave equation from Cauchy data boundary measurements of the deflection and the flux tension are investigated. Physically, this would correspond to the case when the unknown force function depends on the displacement u and velocity u_t in the form $f(\underline{x}, u, u_t) = Q_0(\underline{x})u + Q_1(\underline{x})u_t$, where $Q_0(\underline{x})$ and $Q_1(\underline{x})$ are the potential and damping coefficients, respectively.

Previous theoretical studies, (Baudouin and Ervedoza, 2013; Bukhgeim, Cheng, Isakov and Yamamoto, 2001; Imanuvilov and Yamamoto, 2001) have established the uniqueness of solution, but no numerical reconstruction has been performed. Therefore, it is the purpose of this chapter to attempt such as a numerical realization.

Although uniqueness of solution holds, the inverse coefficient identification problems under investigation are still ill-posed since small random errors in the input data cause large errors in the output solution. In order to stabilise the solution we employ the nonlinear Tikhonov regularization method. Numerical results are presented and discussed.

6.2 Mathematical formulation

Assume that we have a medium, denoted by Ω , occupying a bounded domain in \mathbb{R}^n , $n \geq 1$, with a sufficiently smooth boundary $\partial\Omega$, e.g. of class C^2 . The boundary of Ω is denoted by $\partial\Omega$, and we define the space-time cylinder $Q_T = \Omega \times (0, T)$, where $T > 0$. We wish to find the displacement $u(\underline{x}, t)$ and the spacewise dependent coefficients $Q_0(\underline{x})$ and/or $Q_1(\underline{x})$ of the lower-order terms in the hyperbolic wave equation

$$u_{tt} = \nabla^2 u + Q_0(\underline{x})u + Q_1(\underline{x})u_t \quad \text{in } Q_T. \quad (6.1)$$

The initial conditions are given by (3.3) and (3.4). On the boundary we can prescribe Dirichlet, Neumann, Robin or mixed boundary conditions.

Let us consider, Neumann boundary conditions being prescribed, namely,

$$\frac{\partial u}{\partial \nu}(\underline{x}, t) = q(\underline{x}, t), \quad (\underline{x}, t) \in \partial\Omega \times (0, T), \quad (6.2)$$

where q is a given function.

If the functions Q_0 and Q_1 are given, then equations (6.1)-(6.2) form a direct well-posed problem. However, if some of the functions Q_0 and/or Q_1 cannot be directly observed they hence become unknown and then clearly, the above set of equations is not sufficient to determine uniquely the solution of the so-generated inverse coefficient identification problem (ICIP). In order to compensate for this non-uniqueness, we consider the additional measurement given by the Dirichlet boundary data,

$$u(\underline{x}, t) = P(\underline{x}, t), \quad (\underline{x}, t) \in \partial\Omega \times (0, T), \quad (6.3)$$

6.3 Numerical solutions of the direct and inverse problems

where P is a prescribed boundary displacement. We can also consider the case when the boundary displacement Dirichlet data (6.3) is being prescribed and it is the flux tension Neumann data (6.2) which is being measured.

Note that the unknowns $Q_0(\underline{x})$ and $Q_1(\underline{x})$ are interior quantities depending on the space variable $\underline{x} \in \Omega \subset \mathbb{R}^n$, whilst the additional measurement (6.3) is a boundary quantity depending on $(\underline{x}, t) \in \partial\Omega \times (0, T)$. It is also worth noting that a corresponding inverse spacewise-dependent coefficient identification problem given by equations (3.3), (6.2), (6.3) also arises for the bio-heat equation $u_t = \nabla^2 u + Q_0(\underline{x})u$, see (Ramm, 2001; Trucu, Ingham and Lesnic, 2010).

The uniqueness of solution of the ICIPs associated to equations (6.1)-(6.3) has been established elsewhere in various forms, see (Baudouin and Ervedoza, 2013; Bukhgeim, Cheng, Isakov and Yamamoto, 2001; Imanuvilov and Yamamoto, 2001).

6.3 Numerical solutions of the direct and inverse problems

6.3.1 Direct problem

In this section, we consider the direct initial Neumann boundary value problem (6.1)-(6.2) for simplicity, in one-dimension, i.e. $n = 1$ and $\Omega = (0, L)$ with $L > 0$, when the coefficients $Q_0(x)$, $Q_1(x)$ and $Q_2(x)$ are known and the displacement $u(x, t)$ is to be determined, namely,

$$u_{tt}(x, t) = u_{xx}(x, t) + Q_0(x)u + Q_1(x)u_t + Q_2(x)u_x, \quad (x, t) \in (0, L) \times (0, T], \quad (6.4)$$

$$u(x, 0) = \varphi(x), \quad u_t(x, 0) = \psi(x), \quad x \in [0, L], \quad (6.5)$$

$$-\frac{\partial u}{\partial x}(0, t) = q(0, t) =: q_0(t), \quad \frac{\partial u}{\partial x}(L, t) = q(L, t) =: q_L(t), \quad t \in (0, T]. \quad (6.6)$$

In the direct problem (6.4)-(6.6) of interest is to determine the Dirichlet boundary data (6.3) at $x = 0$ and $x = L$, namely

$$u(0, t) = P(0, t) =: P_0(t), \quad u(L, t) = P(L, t) =: P_L(t), \quad t \in (0, T]. \quad (6.7)$$

6.3 Numerical solutions of the direct and inverse problems

The discrete form of the problem (6.1)-(6.2) is as follows. We divide the solution domain $(0, L) \times (0, T)$ into M and N subintervals of equal space length Δx and time step Δt , where $\Delta x = L/M$ and $\Delta t = T/N$. We denote $u_{i,j} := u(x_i, t_j)$, where $x_i = i\Delta x$, $t_j = j\Delta t$, $Q_{0i} := Q_0(x_i)$, $Q_{1i} := Q_1(x_i)$ and $Q_{i2} := Q_2(x_i)$ for $i = \overline{0, M}$, $j = \overline{0, N}$. Then, a central-difference approximation to equations (6.4)-(6.6) at the mesh points $(x_i, t_j) = (i\Delta x, j\Delta t)$ of the rectangular mesh covering the solution domain $(0, L) \times (0, T)$ is, see e.g. (Smith, 1985),

$$u_{i,j+1} = \frac{r + r_0 Q_{2i}}{1 - r_1 Q_{1i}} u_{i+1,j} + \frac{2 - 2r + (\Delta t)^2 Q_{0i}}{1 - r_1 Q_{1i}} u_{i,j} + \frac{r - r_0 Q_{2i}}{1 - r_1 Q_{1i}} u_{i-1,j} - \frac{1 + r_1 Q_{1i}}{1 - r_1 Q_{1i}} u_{i,j-1}, \quad i = \overline{1, (M-1)}, \quad j = \overline{1, (N-1)}, \quad (6.8)$$

$$u_{i,0} = \varphi(x_i), \quad i = \overline{0, M}, \quad \frac{u_{i,1} - u_{i,-1}}{2\Delta t} = \psi(x_i), \quad i = \overline{1, (M-1)}, \quad (6.9)$$

$$-\frac{\partial u}{\partial x}(0, t_j) = -\frac{4u_{1,j} - u_{2,j} - 3u_{0,j}}{2\Delta x} = q_0(t_j),$$

$$\frac{\partial u}{\partial x}(L, t_j) = \frac{3u_{M,j} - 4u_{M-1,j} + u_{M-2,j}}{2\Delta x} = q_L(t_j), \quad j = \overline{1, N}, \quad (6.10)$$

where $r = (\Delta t)^2/(\Delta x)^2$, $r_0 = (\Delta t)^2/(2\Delta x)$ and $r_1 = \Delta t/2$. Equation (6.8) represents an explicit finite-difference method (FDM) which is stable if $r \leq 1$, giving approximate values for the solution at mesh points along $t = 2\Delta t, 3\Delta t, \dots$, as soon as the solution at the mesh points along $t = \Delta t$ has been determined by allowing $j = 0$ in equation (6.8) and using (6.9), to obtain

$$u_{i,1} = \frac{r + r_0 Q_{2i}}{2} \varphi(x_{i+1}) + \frac{2 - 2r + (\Delta t)^2 Q_{0i}}{2} \varphi(x_i) + \frac{r - r_0 Q_{2i}}{2} \varphi(x_{i-1}) + \Delta t(1 + r_1 Q_{1i}) \psi(x_i) \quad i = \overline{1, (M-1)}. \quad (6.11)$$

The time-marching FDM procedure described above provides the displacement u throughout the solution domain and in particular the Dirichlet data (6.7) given by

$$u_{0,j} = P_0(t_j), \quad u_{M,j} = P_L(t_j), \quad j = \overline{1, N}. \quad (6.12)$$

6.3.2 Inverse problems

In the inverse problems stated in Section 6.2, we wish to determine the solution of unknown $(u(x, t), Q_0(x), Q_1(x))$ by minimizing the nonlinear objective function

$$\mathcal{F}(Q_0, Q_1) = \|u(x, t; Q_0, Q_1) - P(x, t)\|_{L^2(\partial\Omega \times (0, T))}^2. \quad (6.13)$$

This minimisation is accomplished using the MATLAB optimisation toolbox routine *lsqnonlin* which attempts to find a minimum of a sum of squares, starting from an arbitrary initial guess, subject to constraints. In MATLAB, this routine allows to choose the trust-region-reflective algorithm based on the interior-reflective Newton method described in (Coleman and Li, 1994).

In practice, the additional observation (6.3) comes from measurement which is inherently contaminated with errors,

$$P^\epsilon(x, t) = P(x, t) + \epsilon, \quad (x, t) \in \partial\Omega \times (0, T), \quad (6.14)$$

where ϵ stands for the amount of noise. In this case, we replace in the objective functional (6.13) the exact data $P(x, t)$ by the noisy data $P^\epsilon(x, t)$.

6.4 Numerical results and discussion

In this section, the discussion is divided into three subsections 6.4.1-6.4.3 with respect to the three inverse problems generated when $Q_0(x)$, or $Q_1(x)$, or $Q_0(x)$ and $Q_1(x)$ is/are unknown, respectively. In all examples in this section we take, for simplicity, $L = T = 1$.

6.4.1 Example 1 (determination of $Q_0(x)$ when $Q_1(x)$ is known)

Consider the inverse initial boundary value problem (3.3), (3.4), (6.2), (6.3) and (6.4) in one-dimension, i.e. $n = 1$ and $\Omega = (0, L)$, when both the potential $Q_0(x)$ and the displacement $u(x, t)$ are to be determined (assuming that $Q_1(x)$ is known and taken for simplicity to be zero), from the governing equation

$$u_{tt} = u_{xx} + Q_0(x)u, \quad (x, t) \in (0, 1) \times (0, 1), \quad (6.15)$$

with the input data

$$u(x, 0) = \varphi(x) = 2 + \cos(\pi x), \quad u_t(x, 0) = \psi(x) = 2 + \cos(\pi x), \quad x \in [0, 1], \quad (6.16)$$

$$-\frac{\partial u}{\partial x}(0, t) = q_0(t) = 0, \quad \frac{\partial u}{\partial x}(1, t) = q_L(t) = 0, \quad t \in (0, 1], \quad (6.17)$$

$$u(0, t) = P_0(t) = 3e^t, \quad u(1, t) = P_1(t) = e^t, \quad t \in [0, 1]. \quad (6.18)$$

The inverse problem (6.15)-(6.18) is uniquely solvable and, in fact, it can easily be checked that its exact solution is given by

$$u(x, t) = e^t(\cos(\pi x) + 2), \quad (x, t) \in [0, 1] \times [0, 1]. \quad (6.19)$$

$$Q_0(x) = \frac{2 + (1 + \pi^2) \cos(\pi x)}{2 + \cos(\pi x)}, \quad x \in [0, 1]. \quad (6.20)$$

First, before we attempt the inversion, it is worth to assess the convergence and accuracy of the FDM direct solver described in Section 6.3. Therefore, solving the direct problem (6.15)-(6.17) when Q_0 is assumed known and given by (6.20) we obtain the numerical results for the boundary Dirichlet data presented in Figures 6.1 for various $N = M \in \{5, 10, 20\}$ in comparison with the exact solutions (6.18). From this figure a rapid monotonically increasing convergence of the numerical solutions to their exact targets (6.18) and excellent accuracy can be observed (in fact the numerical results obtained with $N = M = 10$ and 20 are undistinguishable) In fact, the ℓ^2 -errors between the analytical and numerical solutions in Figures 6.1(a) and 6.1(b) were obtained to be 0.1429, 0.0107 and 0.0005, and 0.0974, 0.0047 and 0.0009, for $M = N \in \{5, 10, 20\}$, respectively.

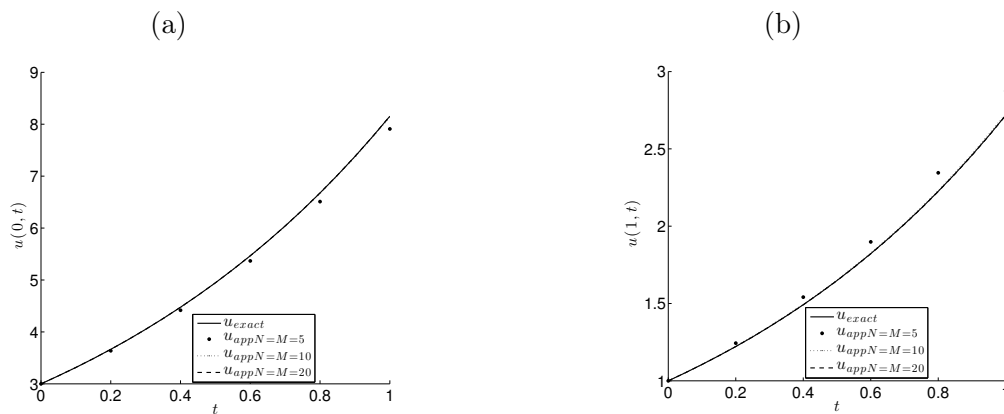


Figure 6.1: The exact solutions (a) $u(0,t) = 3e^t$, (b) $u(1,t) = e^t$ in comparison with the numerical solutions for various $N = M \in \{5, 10, 20\}$, for the direct problem of Example 1.

Next, we attempt solving numerically the inverse problem (6.15)-(6.18) by minimizing the least-squares objective function

$$\mathcal{F}(\underline{Q}_0) := \sum_{j=1}^N (u(0, t_j; \underline{Q}_0) - P_0(t_j))^2 + \sum_{j=1}^N (u(1, t_j; \underline{Q}_0) - P_1(t_j))^2, \quad (6.21)$$

using the routine *lsqnonlin* described in Section 6.3.2 starting with the initial guess zero. Remark that when both Dirichlet data in (6.18) are measured this corresponds to the full data measurement (6.3) and minimizing (6.21) imposes $2N$ constraints in M unknowns. In this subsection, we also investigate the case when we only measure partially the data in (6.18) in which case we minimize the partial least-squares objective function

$$\mathcal{F}_{\text{partial}}(\underline{Q}_0) := \sum_{j=1}^N (u(0, t_j; \underline{Q}_0) - P_0(t_j))^2. \quad (6.22)$$

In this case, minimizing (6.22) imposes N constraints in M unknowns.

For exact data, the results are depicted in Figure 6.2. From this figure it can be seen that the numerical solution for $Q_0(x)$ converges to the exact solution (6.20), as the FDM mesh size decreases, and there is not much difference in the excellently obtained accuracy when using both data in (6.18) or, when using the

partial data in (6.18) alone. This is true for exact data, but for noisy data which we consider next the accuracy of the solution changes significantly, as described below.

We consider therefore solving the inverse problem with fixed $N = M = 20$ but with noise included in the Dirichlet boundary measured data (6.18), as described in (6.14). This is numerically simulated by

$$P_i^\epsilon(t_j) = P_i(t_j) + \epsilon_j^i, \quad j = \overline{1, N}, \quad i = 0, 1, \quad (6.23)$$

where $(\epsilon_j^i)_{j=\overline{1, N}}$ are N random noisy variables generated using the MATLAB command 'normrnd' from a Gaussian normal distribution with mean zero and standard deviation $\sigma_i = p \times \max_{t \in [0, T]} |P_i(t)|$ for $i = 0, 1$, where p represents the percentage of noise.

6.4 Numerical results and discussion

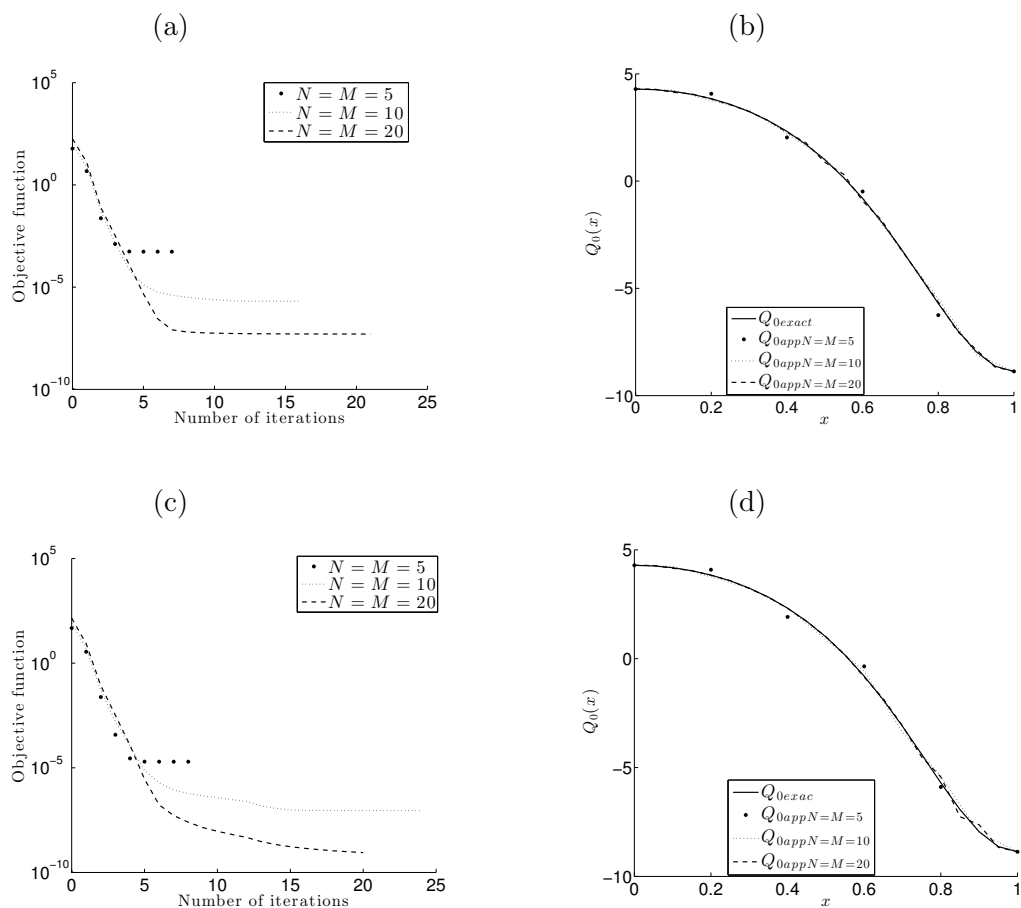


Figure 6.2: (a) The objective function (6.21), as a function of the number of iterations, and (b) the exact solution (6.20) for the coefficient $Q_0(x)$ in comparison with the numerical solutions, for various $N = M \in \{5, 10, 20\}$, no noise for the inverse problem of Example 1. Figures (c) and (d) represent the same quantities as (a) and (b), but obtained by minimizing the partial objective function (6.22) instead of (6.21).

In order to investigate the stability of the numerical solution we include $p \in \{1, 3, 5\}\%$ noise into the input data (6.18), as described in (6.14). In this case the perturbed noisy data (6.14) replaces the exact data in (6.21). The numerical solutions for $Q_0(x)$ obtained by minimizing (6.21) or (6.22) with no regularization are plotted in Figure 6.3. It can be clearly seen that very high and unbounded oscillations appear. This clearly shows that the ICIPS under investigation are

ill-posed. In order to deal with this instability we employ the Tikhonov regularization which minimizes the penalised least-squares functional

$$\mathcal{F}_\lambda(\underline{Q}_0) := \mathcal{F}(\underline{Q}_0) + \lambda \sum_{i=1}^M Q_{0i}^2, \quad (6.24)$$

or, its partial version

$$\mathcal{F}_{\text{partial},\lambda}(\underline{Q}_0) := \mathcal{F}_{\text{partial}}(\underline{Q}_0) + \lambda \sum_{i=1}^M Q_{0i}^2, \quad (6.25)$$

where $\lambda > 0$ is a regularization parameter to be prescribed. Including regularization we obtain the numerical solutions presented in Figure 6.5, whose accuracy errors

$$E_0 := \sqrt{\frac{1}{M} \sum_{i=1}^M (Q_{0\text{exact}}(x_i) - Q_{0\text{app}}(x_i))^2}, \quad (6.26)$$

as functions of λ , are plotted in Figure 6.4. From Figure 6.4 it can be seen that the minimum of the error occurs around $\lambda = 0.05$ for $p = 1\%$ and $\lambda = 0.1$ for $p \in \{3, 5\}\%$. The value of the regularization parameter λ can be chosen by trial and error. By plotting the numerical solution for various values of λ we can infer when the instability starts to kick off.

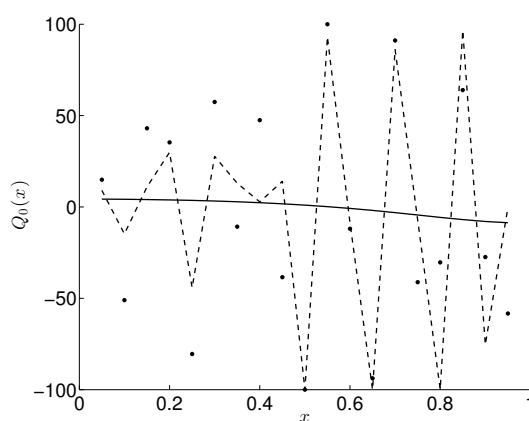


Figure 6.3: The exact solution (6.20) for the coefficient $Q_0(x)$ in comparison with the numerical solutions obtained by minimizing (6.21) (- - -) or (6.22) (· · ·), with no regularization, for $p = 1\%$ noisy data for the inverse problem of Example 1.

6.4 Numerical results and discussion

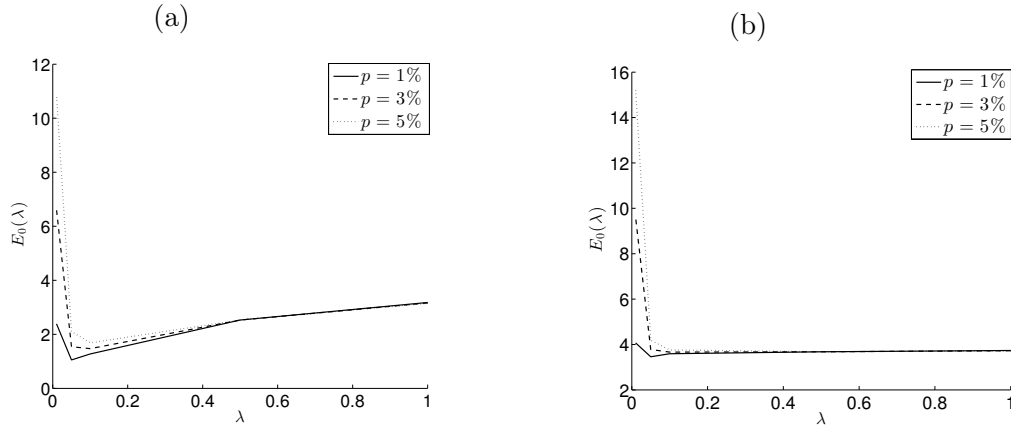


Figure 6.4: The accuracy error E_0 , as a function of λ , for $p \in \{1, 3, 5\}\%$ noise, for the inverse problem of Example 1, obtained by minimizing: (a) the functional (6.24) and (b) the partial functional (6.25).

Figure 6.5 shows the regularized numerical solution for $Q_0(x)$ obtained with various values of the regularization parameter $\lambda \in \{0.05, 0.1\}$ for $p \in \{1, 3, 5\}\%$ noisy data. From this figure it can be seen that the numerical results are stable and they become more accurate as the amount of noise p decreases.

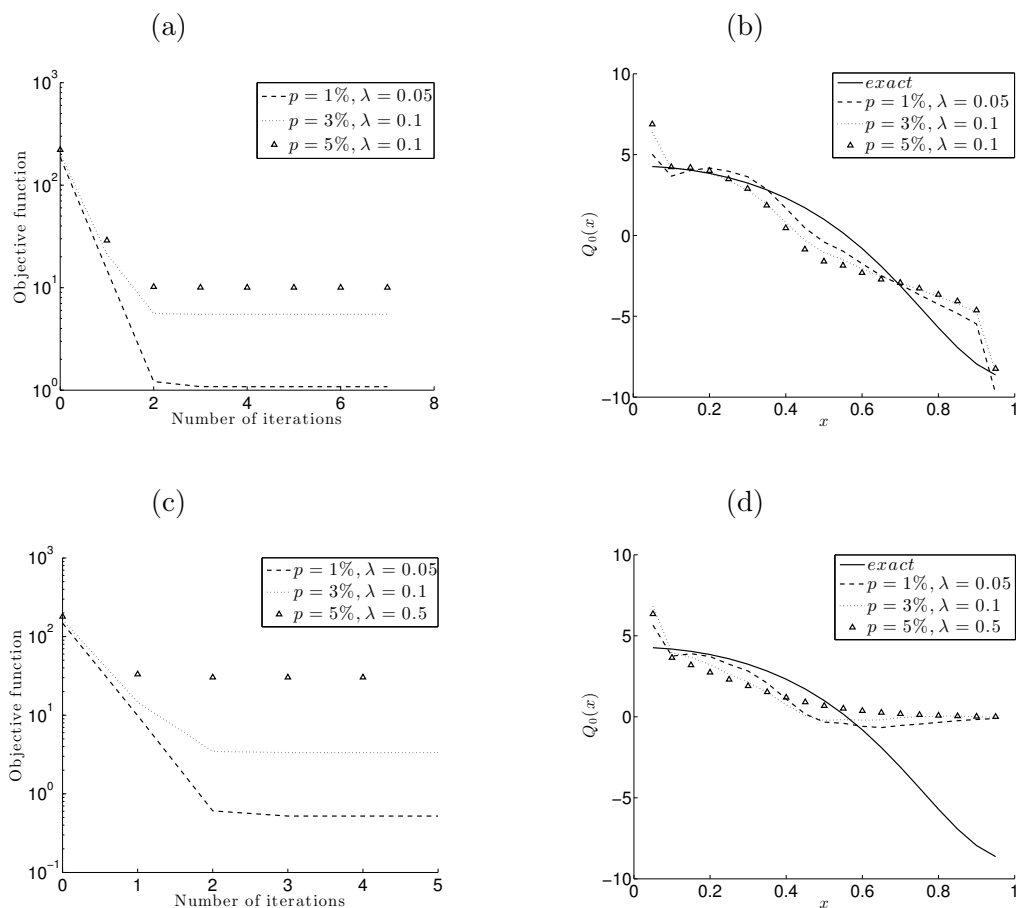


Figure 6.5: (a) The regularized objective function (6.24), as a function of the number of iterations, and (b) the exact solution (6.20) for the coefficient $Q_0(x)$ in comparison with the numerical solutions, for $p \in \{1, 3, 5\}\%$ noise and regularization parameters $\lambda \in \{0.05, 0.1\}$, for the inverse problem of Example 1. Figures (c) and (d) represent the same quantities as (a) and (b), but obtained by minimizing the partial regularized objective function (6.25) instead of (6.24).

6.4.2 Example 2 (determination of $Q_1(x)$ when $Q_0(x)$ is known)

Consider the inverse initial boundary value problem (3.3), (3.4), (6.2), (6.3) and (6.4) in one-dimension, i.e. $n = 1$ and $\Omega = (0, L)$, when both the damping term

$Q_1(x)$ and the displacement $u(x, t)$ are to be determined (assuming that $Q_0(x)$ is known and taken for simplicity to be zero), from the governing equation

$$u_{tt} = u_{xx} + Q_1(x)u_t, \quad (x, t) \in (0, 1) \times (0, 1), \quad (6.27)$$

with the same input data (6.16)-(6.18). One can easily check that the solution $(u(x, t), Q_1(x))$ is given by equation (6.19) for $u(x, t)$, whilst for $Q_1(x)$ has the same expression as that of equation (6.20), namely,

$$Q_1(x) = \frac{2 + (1 + \pi^2) \cos(\pi x)}{2 + \cos(\pi x)}, \quad x \in [0, 1]. \quad (6.28)$$

As for Example 1, the convergence and accuracy of the FDM direct solver described in Section 6.3 have first been assessed by solving the direct problem (6.16), (6.17) and (6.27) when Q_1 is assumed known and given by (6.28). Similar graphs to those presented in Figure 6.1 have been obtained and therefore they are not further illustrated herein.

Next, we attempt solving numerically the inverse problem (6.16)-(6.18) and (6.27) by minimizing the least-squares objective function

$$\mathcal{F}(\underline{Q}_1) := \sum_{j=1}^N (u(0, t_j; \underline{Q}_1) - P_0(t_j))^2 + \sum_{j=1}^N (u(1, t_j; \underline{Q}_1) - P_1(t_j))^2, \quad (6.29)$$

using the routine *lsqnonlin* described in Section 6.3.2 starting with the initial guess zero.

For exact data, the results are depicted in Figure 6.6 and similar convergent results as those obtained in Figure 6.2 for Example 1 can be observed.

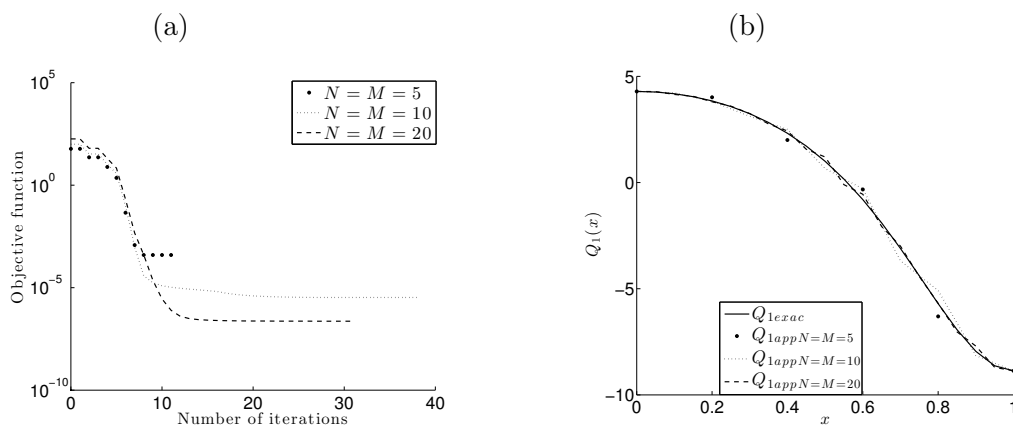


Figure 6.6: (a) The objective function (6.29), as a function of the number of iterations, and (b) the exact solution (6.28) for the coefficient $Q_1(x)$ in comparison with the numerical solutions, for various $N = M \in \{5, 10, 20\}$, no noise for the inverse problem of Example 2.

Next, we fix $M = N = 20$ and add $p = 1\%$ noise in the Dirichlet boundary data (6.23). As shown in Figure 6.7, the unregularized numerical solution obtained by minimizing (6.29) is seen to be highly unstable. This is similar to the unstable behaviour of the numerical results shown with dashed line (---) in Figure 6.3 for Example 1, though the amplitude of the oscillations in Figure 6.7 for Example 2 is about 3 times lower than that for Example 1.

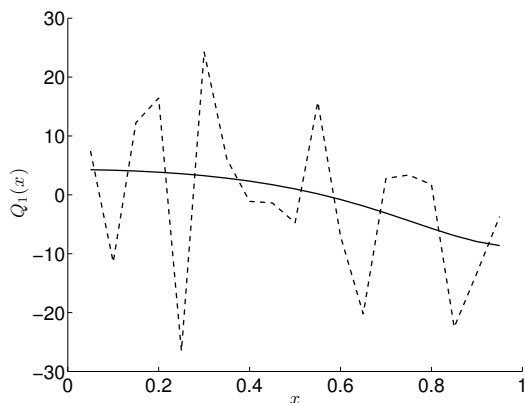


Figure 6.7: The exact solution (6.28) for the coefficient $Q_1(x)$ in comparison with the numerical solution (- - -), with no regularization, for $p = 1\%$ noisy data for the inverse problem of Example 2.

As for Example 1, in order to stabilise the solution the functional (6.29) is regularized and this recasts into minimizing the penalised least-squares functional

$$\mathcal{F}_\lambda(\underline{Q}_1) := \mathcal{F}(\underline{Q}_1) + \lambda \sum_{i=1}^M Q_{1i}^2. \quad (6.30)$$

The accuracy error defined as

$$E_1 := \sqrt{\frac{1}{M} \sum_{i=1}^M (Q_{1exact}(x_i) - Q_{1app}(x_i))^2}, \quad (6.31)$$

as a function of λ , is plotted in Figure 6.8 for $p \in \{1, 3, 5\}\%$ noise and similar behaviour to that illustrated in Figure 6.4 for Example 1 can be observed.

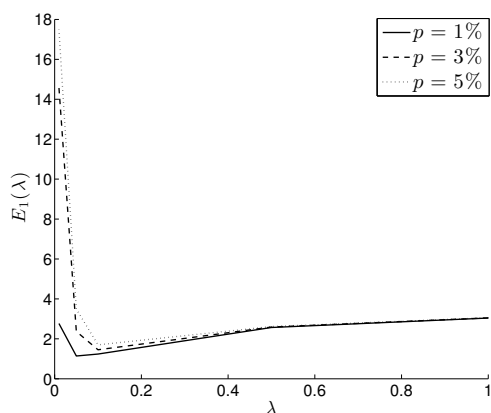


Figure 6.8: The accuracy error E_1 , as a function of λ , for $p \in \{1, 3, 5\}\%$ noise, for the inverse problem of Example 2.

Stable numerical results are obtained as illustrated in Figure 6.9.

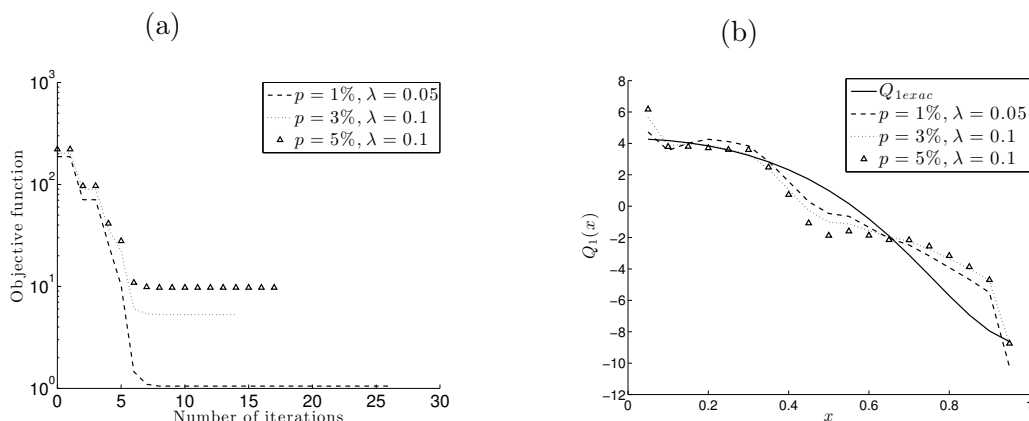


Figure 6.9: (a) The regularized objective function (6.30), as a function of the number of iterations, and (b) the exact solution (6.28) for the coefficient $Q_1(x)$ in comparison with the numerical solutions, for $p \in \{1, 3, 5\}\%$ noise and regularization parameters $\lambda \in \{0.05, 0.1\}$, for the inverse problem of Example 2.

6.4.3 Example 3 (determination of $Q_0(x)$ and $Q_1(x)$)

We consider the inverse initial boundary value problem (3.3), (3.4) and (6.1)-(6.3) in one-dimension, i.e. $n = 1$ and $\Omega = (0, L)$, when the potential $Q_0(x)$, the

damping term $Q_1(x)$ and the displacement $u(x, t)$ are to be determined from the governing equation

$$u_{tt} = u_{xx} + Q_0(x)u + Q_1(x)u_t, \quad (x, t) \in (0, 1) \times (0, 1), \quad (6.32)$$

with the homogeneous flux data (6.17) and

$$u(x, 0) = \varphi(x) = 0, \quad u_t(x, 0) = \psi(x) = 2 + \cos(\pi x), \quad x \in [0, 1], \quad (6.33)$$

$$u(0, t) = P_0(t) = 3(e^t - 1), \quad u(1, t) = P_1(t) = e^t - 1, \quad t \in [0, 1]. \quad (6.34)$$

One can easily check that the triplet solution $(u(x, t), Q_0(x), Q_1(x))$ is given by

$$u(x, t) = (e^t - 1)(\cos(\pi x) + 2), \quad (x, t) \in [0, 1] \times [0, 1]. \quad (6.35)$$

$$Q_0(x) = \frac{\pi^2 \cos(\pi x)}{2 + \cos(\pi x)}, \quad x \in [0, 1]. \quad (6.36)$$

$$Q_1(x) = 1, \quad x \in [0, 1]. \quad (6.37)$$

As for Examples 1 and 2, the convergence and accuracy of the FDM direct solver described in Section 6.3 have first been assessed by solving the direct problem (6.33), (6.17) and (6.32) when Q_0 and Q_1 are assumed known and given by (6.36) and (6.37). Although not illustrated, it is reported that an excellent accuracy has been obtained.

We attempt solving numerically the inverse problem (6.17), (6.32)-(6.34), by minimizing the least-squares objective function

$$\mathcal{F}(\underline{Q}_0; \underline{Q}_1) := \sum_{j=1}^N (u(0, t_j; \underline{Q}_0; \underline{Q}_1) - P_0(t_j))^2 + \sum_{j=1}^N (u(1, t_j; \underline{Q}_1; \underline{Q}_1) - P_1(t_j))^2, \quad (6.38)$$

using the routine *lsqnonlin* described in Section 6.3.2 starting with the initial guess zero.

For exact data, the results are depicted in Figure 6.10. From this figure it can be seen that the numerical solution for $Q_0(x)$ and $Q_1(x)$ converges to the exact solution (6.36) and (6.37), respectively, as the FDM mesh size decreases.

6.4 Numerical results and discussion

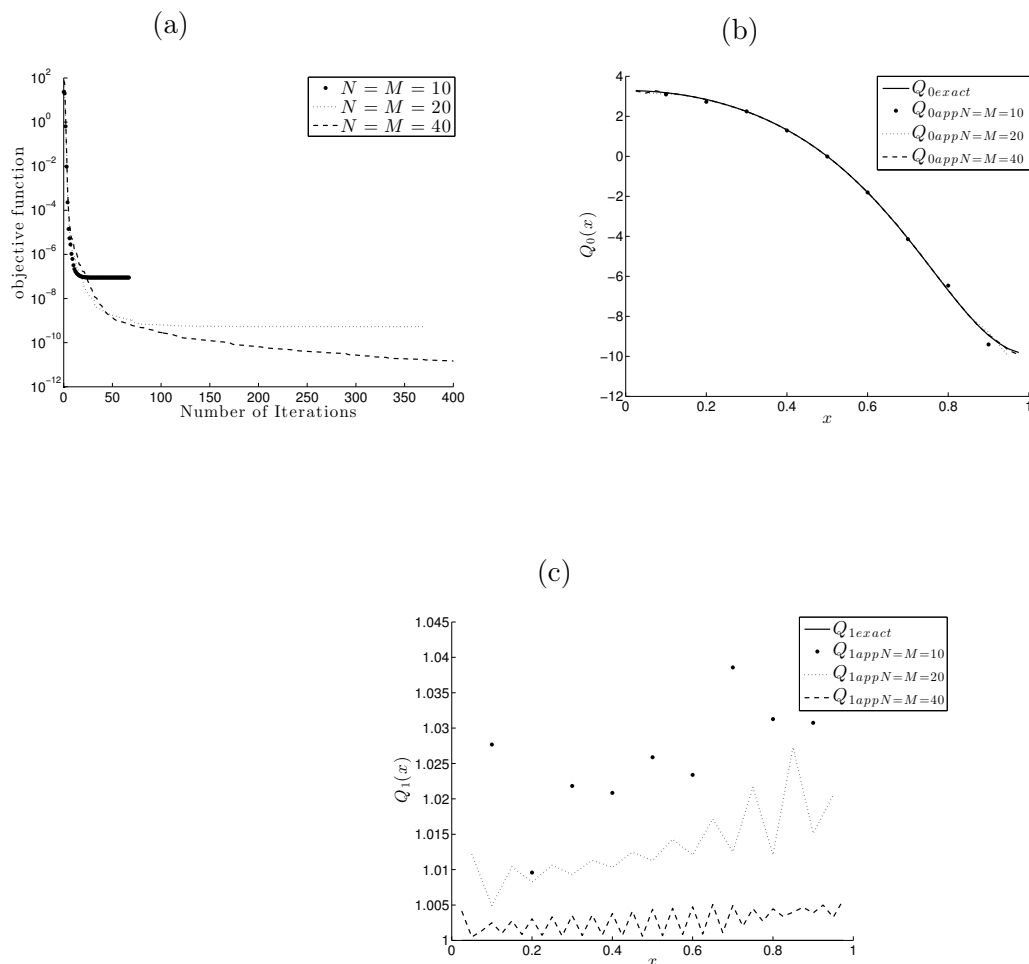


Figure 6.10: (a) The objective function (6.38), as a function of the number of iterations, (b) the exact solution (6.36) for $Q_0(x)$ and (c) the exact solution (6.37) for $Q_1(x)$ in comparison with the numerical solutions, for various $N = M \in \{10, 20, 40\}$, no noise for the inverse problem of Example 3.

Next we consider solving the inverse problem with fixed $N = M = 40$ but with $p = 1\%$ noise included in the Dirichlet boundary measured data, as described in (6.23). As shown in Figure 6.11, the unregularized numerical solutions for both $Q_0(x)$ and $Q_1(x)$ obtained by minimizing (6.38) is seen to be highly unstable.

6.4 Numerical results and discussion

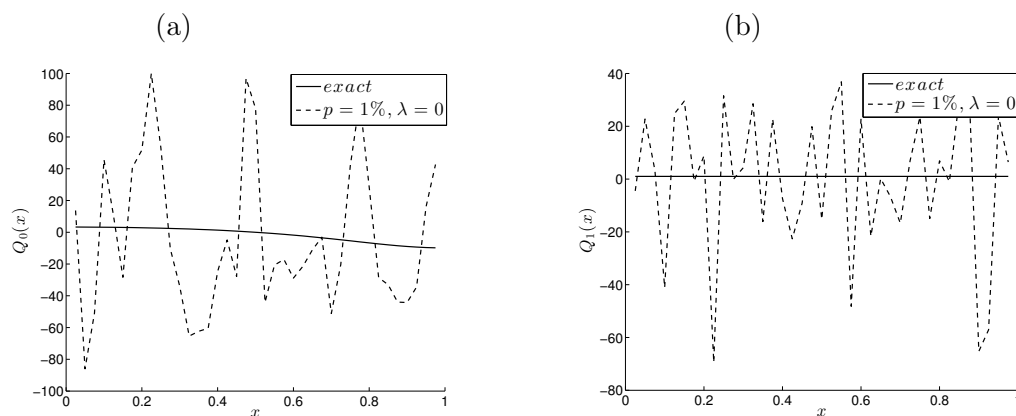


Figure 6.11: The exact solutions given by (a) equation (6.36) and (b) equation (6.37) for the coefficients $Q_0(x)$ and $Q_1(x)$, respectively, in comparison with the numerical solutions, with no regularization, for $p = 1\%$ noisy data for the inverse problem of Example 3.

In order to stabilise the solution, the functional (6.38) is regularized and this recasts into minimizing the penalised least-squares functional

$$\mathcal{F}_\lambda(\underline{Q}_0; \underline{Q}_1) := \mathcal{F}(\underline{Q}_0; \underline{Q}_1) + \lambda \sum_{i=1}^M Q_{0i}^2 + \lambda \sum_{i=1}^M Q_{1i}^2. \quad (6.39)$$

The numerically obtained results for $p = 1\%$ noise and $\lambda = 0.01$ are illustrated in Figure 6.12. By comparing Figures 6.11 and 6.12 the benefit of regularization can be clearly observed.

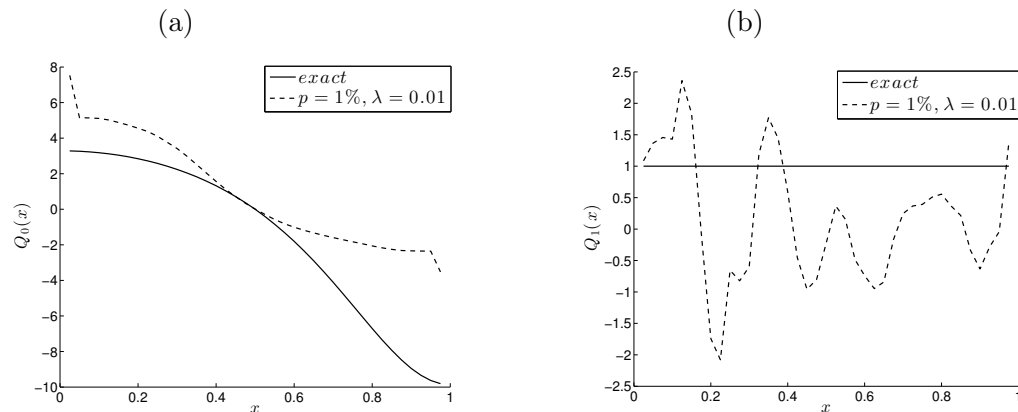


Figure 6.12: The exact solutions given by (a) equation (6.36) and (b) equation (6.37) for the coefficients $Q_0(x)$ and $Q_1(x)$, respectively, in comparison with the numerical solutions, with regularization, for $p = 1\%$ noisy data for the inverse problem of Example 3.

6.5 Conclusions

In this chapter, nonlinear identifications of the space-dependent potential and/or damping coefficients in the wave equation have been investigated.

As illustrated in Figures 6.3, 6.7 and 6.11, these inverse coefficient identification problems are ill-posed since small random errors in the input data cause large errors in the output solution. In order to stabilise the solution, the nonlinear Tikhonov regularization method has been employed. The minimization has been performed numerically using the MATLAB toolbox optimization routine *lsqnonlin*. Numerical results presented and discussed for various examples concerned with the inverse reconstruction of the coefficient $Q_0(x)$, or $Q_1(x)$, or both $Q_0(x)$ and $Q_1(x)$.

We mention that the techniques of this chapter (FDM plus *lsqnonlin* minimization of the Tikhonov functional) have recently been applied successfully in (Hussein and Lesnic, 2016), for solving a similar coefficient identification problem for the heat equation.

The case of partial Cauchy data has also been considered in subsection 6.4.1

for the inverse problem of retrieving the potential $Q_0(x)$. By comparing Figures 6.2(b) and 6.2(d) one has observed that in the case of exact data accurate numerical solutions have been obtained in both cases of full or partial Cauchy data being considered. However, for noisy data by comparing Figures 6.5(b) and 6.5(d) one has observed that, as expected, the full Cauchy data provide more (significant) information than the partial Cauchy data.

Another comparison was made by observing Figures 6.5(b) and 6.9(b) corresponding to the identification of the potential $Q_0(x)$ and the damping coefficient $Q_1(x)$, respectively. From these figures it has been seen that there was no major difference between the two regularized solutions in terms of stability and accuracy.

A final inverse problem consisted in simultaneously identifying both $Q_0(x)$ and $Q_1(x)$, as performed in subsection 6.4.3. As expected, this is a more difficult problem than the separate single identification of the coefficient $Q_0(x)$ or $Q_1(x)$, as performed in subsections 6.4.1 and 6.4.2, respectively. For exact data, Figures 6.10(b) and 6.10(c) have showed that both coefficients can be retrieved accurately, but for noisy data, Figures 6.12(a) and 6.12(b) have showed that the accuracy and stability deteriorate. On the other hand, comparison of Figures 6.11 and 6.12 have showed that the use of regularization significantly alleviates the highly unbounded and oscillatory numerical reconstructions obtained when no regularization was employed.

Nevertheless, one could try to improve on the numerical results of Figure 6.12 by employing more sophisticated iterative regularization methods such as the CGM, but this is deferred to a future work. Future work will also be concerned with the reconstruction of the vectorial function $\underline{Q}_2(\underline{x})$ in the wave equation $u_{tt} = \nabla^2 u + Q_0(\underline{x})u + Q_1(\underline{x})u_t + \underline{Q}_2(\underline{x}) \cdot \nabla u$.

Chapter 7

General conclusions and future work

7.1 Conclusions

Prior to this study, much work has been performed for solving both theoretically and numerically inverse source problems for the parabolic heat equation, but the literature is much scarcer on inverse force problems for the hyperbolic wave equation. Therefore, the objective of this thesis was to investigate, develop and apply numerical methods for solving several inverse force problems for the wave equation which have important applications in various fields ranging from acoustics and geophysics to medicine.

Throughout the thesis numerical results have been compared with their analytical solutions, where available, or with the numerical solution of the corresponding direct problem otherwise. In all the inverse force problems considered in this thesis, the convergence and the stability of the combined BEM/FDM plus regularization was thoroughly investigated for various orders of regularization and various levels of noise added into the input data.

As opposed to the direct problem formulation (in which the force is known and the displacement is to be determined), the main difficulty with inverse force problems is the fact that they are ill-posed, i.e. either the existence, uniqueness or continuous dependence upon the input data are violated.

In this thesis, the uniqueness issue has been resolved by assuming that the force depends only on a single variable, i.e. either of space (Chapters 2, 3 and 5) or time (Chapter 4). Moreover, it is clear that the lack of knowledge of the force requires some extra information being prescribed and with respect to what additional information we supply we have distinguished various inverse formulations in Chapters 2 and 5 for example. Various forms of the unknown force function have been sought to be retrieved from various types of additional information/measurement. This may involve non-destructive, i.e. only boundary data are over prescribed, as in Chapter 2, 3 and 6, or intrusive pointwise displacement or average displacement measurements, as in Chapters 4 and 5.

Chapters 2 and 3 have considered solving the inverse space-dependent force identification problem using completely different methods. In Chapter 2, we have employed a split into a direct and an inverse problem, and BEM has been used. Whereas in Chapter 3 the same problem was solved without split and discretised numerically using the FDM. The results obtained by these two different approaches have been compared in terms of accuracy and stability for one typical example in Section 3.5.1. Both methods produced similar good results but although the former approach is faster in terms of computational time it is more restrictive in terms of the generality of application than the latter approach.

The numerical work presented in this thesis extends the range of applications of the BEM (Chapter 2) and the FDM (Chapters 3-6) for discretising inverse force problems for the wave equation. Whilst obviously the BEM has many advantages over domain discretisation methods such as the FDM or the FEM, it is restricted to partial differential operators which possess an explicit fundamental solution being available. This was the case of the inverse force problem investigated in Chapter 2, but as in subsequent chapters the aim was to allow for solving wave propagation problems in inhomogeneous materials, the FDM was the preferred numerical discretisation method in the subsequent chapters. Moreover, even for homogeneous media the BEM loses some of its 'boundary only' character when force terms are present and generate volume integrals to deal with.

In practice, the additional information supplied in inverse problems has to come from measurements and therefore it is usually contaminated with random noise. Due to the ill-posed nature of the inverse problems, this random noise is

drastically magnified if standard solution procedures are used, as in direct problems, hence highly oscillatory and unbounded behaviour occurs in the solution. As a consequence, classical numerical methods are not capable of handling such inverse problems without being augmented by some stabilising techniques. This means that special corrective techniques, such as the Tikhonov regularization method or iterative regularization employed throughout the thesis, are required to achieve an accurate and stable solution.

In Chapter 2, the BEM and in Chapters 3-6, the FDM have been applied to solve inverse force problems for the wave equation. The inverse force problems then have been reduced to ill-conditioned systems of linear/nonlinear equations which have been solved, except for Chapter 5, by the Tikhonov regularization method. This method modifies the least-squares approach by adding smoothing factors which are dependent upon regularization parameters in order to reduce the influence of the measurement errors on the numerical results. Meanwhile, in Chapters 3 and 4 we have employed and tested the Tikhonov regularization of various orders such as zero, first and second. The choice of the order of regularization depends on the smoothness of the desired solution. One possible selection of the regularization parameter is based on the L-curve method. The L-curve is one of the simplest and most popular methods for selecting a single regularization parameter. This method plots the size of the solution (measured in appropriate norm) against the corresponding residual for many positive regularization parameters and picks the regularization parameter at the corner of the resulting L-curve. We have shown that, when plotted in a log-log scale, L-curves indeed have a characteristic L-shaped appearance and that the corner corresponds to a good choice of the regularization parameter. Numerically obtained results clearly illustrate the usefulness of the L-curve criterion for choosing the regularization parameter.

Although popular and simple to implement the Tikhonov regularization method has the drawback that it involves a delicate choice of the regularization parameter, as well as of the order of the regularization matrix. For example, the latter choice is often based on the a priori knowledge of the smoothness of solution and this information may not be available in certain applications. As a possible alternative and remedy to this, iteration regularization methods such as the Landweber

and the conjugate gradient methods have been developed in Chapter 5 in order to solve an inverse space-dependent force problem. The regularization is still needed and is represented by the number of iterations at which the process should be ceased in order to prevent the instability setting in. The numerical results presented in Section 5.5 show that stability was restored by stopping the iterations according to the discrepancy principle criterion once the residual becomes smaller than the amount of noise which which the input data has been contaminated.

All problems investigated in Chapters 2-5 were linear problems and the purpose of the final computational Chapter 6 was to investigate the more difficult nonlinear inverse force problems. This resulted in the need to minimize and regularize nonlinear least squares problems which may have multiple local minima and the numerical results may depend on the initial guess. Of course, one is recommended to use the most of the available information expected from the solution, but in the absence of any such physical insight for the initial guess one can rely on the estimates provided by other less rigorous methods of search minimization, e.g. genetic algorithms, simulated annealing, swarm optimization, etc.

In the remaining of this section we summarize in more detail the conclusions that we have drawn from the inverse force problems analysed in each chapter.

In Chapter 1, a general introduction to direct and inverse problems has been presented, with the difficulties associated with the latter ones highlighted and a review of the previous work on this subject summarised. Upon a suitable numerical method, e.g. BEM or FDM in our thesis, for discretising the governing partial differential equation, a well-conditioned system of linear algebraic equations can be solved using the Gaussian elimination method, whilst a highly ill-conditioned system of equations can be solved using a regularised least-squares method in order to achieve a stable and accurate solution. In this thesis, mainly the Tikhonov regularization method has been considered which is the most known stabilising technique. In this method, the influence of the measurement errors on the stability of results is reduced by adding smoothing terms in the least-squares functional. Also, the Landweber iteration for solving ill-posed linear inverse problems has been employed. In this method, stability is achieved by stopping the iterations at an appropriate threshold.

In Chapter 2, the determination of an unknown spacewise dependent force function acting on a vibrating string from over-specified Cauchy boundary data has been investigated numerically using the BEM combined with a regularized method of separating variables. The problem is split into a direct well-posed problem for the linear wave equation, which is solved numerically using the BEM, and an inverse ill-posed problem whose unstable solution is expressed as a separation of variables truncated series. When the input data was contaminated with noise we have used the Tikhonov regularization method in order to obtain a stable solution. The choice of the regularization parameter was based on the L-curve method. Numerical results showed that accurate and stable solutions have been achieved.

In Chapter 3, the inverse problem for the wave equation which consists of determining an unknown space-dependent force function acting on a vibrating structure from Cauchy boundary data has been investigated. However, in contrast to the problem in Chapter 2 the space-dependent source term is multiplied with a known space and time dependent function. This prevents the previous splitting technique being applicable. Numerically, the FDM was used and the resulting ill-conditioned system of linear equations was solved using the Tikhonov regularization. In a similar way to Chapter 2, the L-curve method has been employed for the choice of the regularization parameter.

In Chapter 4, the determination of an unknown time-dependent force function in the wave equation has been investigated. In other words, the forcing function was assumed to depend only upon the single time variable. This was a natural continuation of Chapter 3, where the space-dependent force identification has been considered. The additional data was given by a space integral average measurement of the displacement. As in Chapter 3, this linear inverse problem has a unique solution, but it is still ill-posed since small errors in the input data cause large errors in the output solution. Therefore, when the input data was contaminated with noise we have used the Tikhonov regularization method in order to obtain a stable solution. The choice of the regularization parameter was based on the L-curve method.

In Chapter 5, the determination of the space-dependent force acting on a vibrating structure from measured final or time-average displacement observation

has been thoroughly investigated. In this chapter, the variational formulations of the inverse problems under investigation have been presented and expressions for the gradients of the least-squares functionals which were minimized have been explicitly provided. The problems have been discretised numerically using the FDM in one- and two dimensions, and the Landweber and the conjugate gradient iterative methods have been applied. For noisy data, the semi-convergence phenomenon appears, as expected, and stability was restored by stopping the iterations according to the discrepancy criterion once the residual becomes close to the amount of noise. Numerical results in one- and two-dimensions, for the recovery of smooth as well as non-smooth force functions have been illustrated and discussed.

In Chapter 6, nonlinear identifications of the space-dependent potential and/or damping coefficients in the wave equation from Cauchy data boundary measurements of the deflection and the flux tension have investigated. The problems have been discretised numerically using the FDM and in order to stabilise the solution the nonlinear Tikhonov regularization method has been employed. Numerically, the nonlinear constrained minimization problem has been solved iteratively using the Matlab toolbox routine *lsqnonlin*. By plotting the numerical solution for various values of regularization parameter we can infer when the instability starts to kick off and then decide on its appropriate selection.

Overall, the results obtained by the methods proposed in this thesis, i.e. BEM or FDM combined with Tikhonov's regularization or Landweber/Conjugate gradient methods, showed that accurate and stable numerical solutions can be obtained for solving inverse force problems for the wave equation. The methods were found to be convergent with respect to increasing the number of boundary elements in the BEM or decreasing the mesh size in the FDM and stable with respect to decreasing the level of noise added into the input data. Of course, much work remains to be done in the future and some possible avenues are proposed in the next section.

7.2 Future work

The work presented in this thesis concerning inverse force problems for the wave equation can be developed as well for inverse boundary value problems, inverse initial value problems or coefficient identification problems. Practical applications can also be envisaged. Some possible future work may consist of:

- Extending and developing the BEM to deal with the inverse force problems for the wave equations of Chapters 3-5. This will involve discretising a time-domain integral, as explained in (Benmansour, 1993).
- A natural extension will concern the numerical implementation in higher dimensions. This is straightforward for the FDM in rectangular, cuboid, annular or spherical geometries, but for the BEM the extensions to two- and three-dimensions require extra skills and care, (Mansur and Brebbia, 1982a,b).
- Identification of a nonlinear force $f(u)$ entering the wave equation $u_{tt} = \nabla^2 u + f(u)$, (Cannon and DuChateau, 1983), will be of interest. In this case, both the direct and inverse problems are nonlinear.
- Extending the work of Chapter 6 to the wave equation $u_{tt} = \nabla^2 u + Q_0(\underline{x})u + Q_1(\underline{x})u_t + \underline{Q}_2(\underline{x}) \cdot \nabla u$ and investigate the reconstruction of the vectorial function $\underline{Q}_2(\underline{x})$, (Liu and Triggiani, 2011).

Chapter 8

Appendix A

In this appendix we first derive the finite-difference formula (3.17) for approximating the wave equation (3.13). In doing this, assume U is a function of the independent variable x , then by using Taylor's series

$$U_{i+1} = U(x_{i+1}) = U(x_i + \Delta x) = U_i + (\Delta x)U'_i + \frac{(\Delta x)^2}{2!}U''_i + \frac{(\Delta x)^3}{3!}U'''_i + O((\Delta x)^4), \quad (8.1)$$

$$U_{i-1} = U(x_{i-1}) = U(x_i - \Delta x) = U_i - (\Delta x)U'_i + \frac{(\Delta x)^2}{2!}U''_i - \frac{(\Delta x)^3}{3!}U'''_i + O((\Delta x)^4), \quad (8.2)$$

where $\Delta x = x_{i+1} - x_i$ and $U'_i = U'(x_i)$, $U''_i = U''(x_i)$ and $U'''_i = U'''(x_i)$.

From (8.1) and (8.2) we obtain the approximations for the derivatives, as follows:

- First order forward difference:

$$[U_{i+1} = U_i + (\Delta x)U'_i + O((\Delta x)^2)] \div \Delta x,$$

$$\frac{U_{i+1} - U_i}{\Delta x} = U'_i + O(\Delta x).$$

- First order backward difference:

$$[U_{i-1} = U_i - (\Delta x)U'_i + O((\Delta x)^2)] \div \Delta x,$$

$$\frac{U_i - U_{i-1}}{\Delta x} = U'_i + O(\Delta x).$$

-
- Second order central difference for first derivative: subtracting (8.2) from (8.1) leads to

$$[U_{i+1} - U_{i-1} = 2(\Delta x)U'_i + O((\Delta x)^3)] \div 2\Delta x,$$

$$\frac{U_{i+1} - U_{i-1}}{2\Delta x} = U'_i + O((\Delta x)^2).$$

- Second order central difference for second derivative: adding (8.1) and (8.2) leads to

$$\left[U_{i+1} + U_{i-1} = 2U_i + 2\frac{(\Delta x)^2}{2!}U''_i + O((\Delta x)^4) \right] \div (\Delta x)^2,$$

$$\frac{U_{i+1} + U_{i-1} - 2U_i}{(\Delta x)^2} = U''_i + O((\Delta x)^2).$$

Then, we use the same idea for $u(x, t)$ (i.e. u is a function of the independent variables x and t). Equations (8.1) and (8.2) for space partial derivatives become

$$u_{i+1,j} = u_{i,j} + \Delta x(u_x)_{i,j} + \frac{(\Delta x)^2}{2!}(u_{xx})_{i,j} + \frac{(\Delta x)^3}{3!}(u_{xxx})_{i,j} + O((\Delta x)^4),$$

$$u_{i-1,j} = u_{i,j} - \Delta x(u_x)_{i,j} + \frac{(\Delta x)^2}{2!}(u_{xx})_{i,j} - \frac{(\Delta x)^3}{3!}(u_{xxx})_{i,j} + O((\Delta x)^4),$$

and for time partial derivatives

$$u_{i,j+1} = u_{i,j} + \Delta t(u_t)_{i,j} + \frac{(\Delta t)^2}{2!}(u_{tt})_{i,j} + \frac{(\Delta t)^3}{3!}(u_{ttt})_{i,j} + O((\Delta t)^4),$$

$$u_{i,j-1} = u_{i,j} - \Delta t(u_t)_{i,j} + \frac{(\Delta t)^2}{2!}(u_{tt})_{i,j} - \frac{(\Delta t)^3}{3!}(u_{ttt})_{i,j} + O((\Delta t)^4).$$

Thus we approximate the time and space second-order derivatives u_{tt} and u_{xx} as

$$u_{tt}(x_i, t_j) = \frac{u_{i,j+1} - 2u_{i,j} + u_{i,j-1}}{(\Delta t)^2} + O((\Delta t)^2),$$

$$u_{xx}(x_i, t_j) = \frac{u_{i+1,j} - 2u_{i,j} + u_{i-1,j}}{(\Delta x)^2} + O((\Delta x)^2),$$

with leading errors of orders $(\Delta t)^2$ and $(\Delta x)^2$, respectively. Similarly, for the time and space first-order derivatives u_t and u_x we have

$$u_t(x_i, t_j) = \frac{u_{i,j+1} - u_{i,j-1}}{2\Delta t} + O((\Delta t)^2),$$

and

$$u_x(x_i, t_j) = \frac{u_{i+1,j} - u_{i-1,j}}{2\Delta x} + O((\Delta x)^2),$$

which are of order $(\Delta t)^2$ and $(\Delta x)^2$, respectively. Introducing these expressions in (3.13) and re-arranging terms we obtain (3.17).

Secondly, we derive the approximation (3.21) for the flux derivative using Taylor's series, as follows:

$$u(\Delta x, t) = u(0, t) + (\Delta x)u_x(0, t) + \frac{(\Delta x)^2}{2}u_{xx}(0, t) + O((\Delta x)^3),$$

$$u(2\Delta x, t) = u(0, t) + 2(\Delta x)u_x(0, t) + \frac{(2\Delta x)^2}{2}u_{xx}(0, t) + O((\Delta x)^3).$$

Multiplying the first equation by 4 and subtracting from the second one we obtain the first approximation for the derivative $u_x(0, t)$ in (3.21) (which is order $(\Delta x)^2$ forward finite difference approximation for $u_x(0, t)$).

Similarly, for approximating the derivative $u_x(L, t)$ in (3.21) (which is order $(\Delta x)^2$ backward finite difference approximation for $u_x(L, t)$) we employ the Taylor's series expansions

$$u(L - \Delta x, t) = u(L, t) - (\Delta x)u_x(L, t) + \frac{(\Delta x)^2}{2}u_{xx}(L, t) + O((\Delta x)^3),$$

$$u(L - 2\Delta x, t) = u(L, t) - 2(\Delta x)u_x(L, t) + \frac{(2\Delta x)^2}{2}u_{xx}(L, t) + O((\Delta x)^3).$$

References

- Aliabadi, M. H. *The Boundary Element Method, Applications in Solids and Structures*, Vol. 2, J. Wiley, New York, 2002.
- Alifanov, O.M., Artyukhin, E.A. and Rummyantsev, S.V. *Extreme Methods for Solving Ill-posed Problems with Applications to Inverse Heat Transfer Problems*, Begell House, New York, 1995.
- Baudouin, M. de Buhan, M. and Ervedoza, S. *Global Carleman estimates for waves and applications*, Communications in Partial Differential Equations, **38**, 823-859, 2013.
- Benmansour, N., Ouazar, D. and Brebbia, C.A. *Boundary element approach to one-dimensional wave equation*, in Computer Methods in Water Resources, (ed. C.A. Brebbia), Computational Mechanics Publications, Southampton, 142-152, 1988.
- Benmansour, N. *Boundary Element Solution to Stratified Shallow Water Wave Equations*, PhD Thesis, Wessex Institute of Technology, University of Portsmouth, 1993.
- Benmansour, N., Ouazar, D. and Wrobel, L.C. *Numerical simulation of shallow water wave propagation using a boundary element wave equation model*, International Journal for Numerical Methods in Fluids, **24**, 1-15, 1997.
- Bukhgeim, A.L., Cheng, J., Isakov, V. and Yamamoto, M. *Uniqueness in determining damping coefficients in hyperbolic equations*, In: Analytic Extension Formulas and Their Applications, (eds. S. Saitoh, N. Hayashi and M. Yamamoto), Kluwer Academic Publishers, Dordrecht, 27-46, 2001.

REFERENCES

- Cannon, J.R. *Determination of an unknown heat source from overspecified boundary data*, SIAM Journal on Numerical Analysis, **5**, 275-286, 1968.
- Cannon, J.R. and Dunninger, D.R. *Determination of an unknown forcing function in a hyperbolic equation from overspecified data*, Annali di Matematica Pura ed Applicata, **1**, 49-62, 1970.
- Cannon, J.R. and DuChateau, P. *An inverse problem for an unknown source term in a wave equation*, SIAM Journal on Applied Mathematics, **43**, 553-564, 1983.
- Chow, Y.T. and Zou, J. *A numerical method for reconstructing the coefficient in a wave equation*, Numerical Methods for Partial Differential Equations, **31**, 289-307, 2015.
- Coleman, T.F. and Li, Y. *On the convergence of interior-reflective Newton methods for nonlinear minimization subject to bounds*, Mathematical Programming, **67**, 189-224, 1994.
- Coles, C. and Murio, D. A. *Simultaneous space diffusivity and source term reconstruction in 2D IHCP*, Computers and Mathematics with Applications, **42**, 1549-1564, 2001.
- Collins, M.D. and Kuperman, W.A. *Inverse problems in ocean acoustics*, Inverse Problems, **10**, 1023-1040, 1994.
- Colton, D. and Kress, R. *Inverse Acoustic and Electromagnetic Scattering Theory*, 3rd edn., Springer-Verlag, New York, 2013.
- Costabel, M. *Time-dependent problems with the boundary integral equation method*, In: Encyclopedia of Computational Mechanics, (eds. E. Stein, R. de Borst and T.J.R. Hughes), J. Wiley, New York, 1-28, 2004.
- Dhatt, G., Touzot, G. and Lefrancois, E. *Finite Element Method*, ISTE Ltd and John Wiley Sons, Great Britain and the United States, 2012.
- El Badia, A., Ha-Duong, T. and Hamdi, A. *Identification of a point source in a linear advection-dispersion-reaction equation: application to a pollution source problem*, Inverse Problems, **21**, 1-17, 2005.

REFERENCES

- El Badia, A. and Ha-Duong, T. *Determination of point wave sources by boundary measurements*, Inverse Problems, **17**, 1127-1139, 2001.
- Elfving, T. and Nikazad, T. *Stopping rules for Landweber-type iteration*, Inverse Problems, **23**, 1417-1432, 2007.
- Elfving, T., Nikazad, T. and Hansen, P.C. *Semi-convergent and relaxation parameter for a class of SIRT algorithms*, Electronic Transactions on Numerical Analysis, **37**, 321-336, 2010.
- Engl, H.W., Scherzer, O. and Yamamoto, M. *Uniqueness and stable determination of forcing terms in linear partial differential equations with overspecified boundary data*, Inverse Problems, **10**, 1253-1276, 1994.
- Engl, H.W., Hanke, M. and Neubauer, A. *Regularization of Inverse Problems*, Kluwer Publ., Dordrecht, 2000.
- Erdem, A., Lesnic, D. and Hasanov, A. *Identification of a spacewise dependent heat source*, Applied Mathematical Modelling, **37**, 10231-10244, 2013.
- Ewing, R. and Lin, T. *A note on source term identification for parabolic equations*, International Series of Numerical Mathematics, **91**, 263-281, 1989.
- French, D.A. *A space-time finite element method for the wave equation*, Computer Methods in Applied Mechanics and Engineering, **107**, 145-157, 1993.
- Golub, G.H., Heath, M. and Wahba, G. *Generalized cross-validation as a method for choosing a good ridge parameter*, Technometrics **21**, 215-223, 1979.
- Hadamard, J. *Lectures on Cauchy's Problem in Linear Partial Differential Equations*, Dover Publications, New York, 1923.
- Ha-Duong, T. *On retarded potential boundary integral equations and their discretisation*, In: Topics in Computational Wave Propagation, (eds. M. Ainsworth, P. Davies, D. Duncan, P. Martin and B. Rynne), Springer, Berlin, 301-336, 2003.
- Hanke, M. *Limitations of the L-curve method in ill-posed problems*, BIT, **36**, 287-301, 1996.

REFERENCES

- Hansen, P.C. and O’Leary, D.P. *The use of the L-curve in the regularization of discrete ill-posed problems*, SIAM J. Sci. Comput., **14**, 1487-1503, 1993.
- Hansen, P.C. *The L-curve and its use in the numerical treatment of inverse problems*, in Computational Inverse Problems in Electrocardiology, (ed. P. Johnston), WIT Press, Southampton, 119-142, 2001.
- Hao, D.N. *Methods for Inverse Heat Conduction Problems*, Peter Lang, Frankfurt am Main, 1998.
- Hasanov, A. *Simultaneous determination of the source terms in a linear hyperbolic problem from the final overdetermination: weak solution approach*, IMA Journal of Applied Mathematics, **74**, 1-19, 2008.
- Hasanov, A. *An inverse source problem with single Dirichlet type measured output data for a linear parabolic equation*, Applied Mathematics Letters, **24**, 1269-1273, 2011.
- Hasanov, A. and Kawano, A. *Identification of unknown spatial load distributions in a vibrating Euler-Bernoulli beam from limited measured data*, Inverse Problems, **32**, 055004 (31pp), 2016.
- Hazanee, A., Ismailov, M.I., Lesnic, D. and Kerimov, N.B. *An inverse time-dependent source problem for the heat equation*, Applied Numerical Mathematics, **69**, 13-33, 2013.
- Huang, C.-H. *An inverse non-linear force vibration problem of estimating the external forces in a damped system with time-dependent system parameters*, Journal of Sound and Vibration, **242**, 749-765, 2001.
- Hussein, S.O. and Lesnic, D. *Determination of a space-dependent source function in the one-dimensional wave equation*, Electronic Journal of Boundary Elements, **12**, 1-26, 2014.
- Hussein, S.O. and Lesnic, D. *Determination of forcing functions in the wave equation. Part I: the space-dependent case*, Journal of Engineering Mathematics, **96**, 115-133, 2016.

REFERENCES

- Hussein, S.O. and Lesnic, D. *Determination of forcing functions in the wave equation. Part II: the time-dependent case*, Journal of Engineering Mathematics, **96**, 135-153, 2016.
- Hussein, S.O., Lesnic, D. and Yamamoto, M. *M. Reconstruction of space-dependent potential and/or damping coefficients in the wave equation*, Nonlinear Analysis: Real World Applications, (submitted).
- Hussein, M.S. and Lesnic, D. *Simulations determination of time and space-dependent coefficients in a parabolic equation*, Communications in Nonlinear Science and Numerical Simulation, **33**, 194-217, 2016.
- Imanuvilov, O.Yu. and Yamamoto, M. *Global uniqueness and stability in determining coefficients of wave equations*, Communications in Partial Differential Equations, **26**, 1409-1425, 2001.
- Isakov, V. *Inverse problems for Partial Differential Equations*, Springer, Berlin, 1998.
- Johansson, B.T. and Lesnic, D. *A variational method for identifying a spacewise-dependent heat source*, IMA Journal of Applied Mathematics, **72**, 748-760, 2007a.
- Johansson, T. and Lesnic, D. *Determination of a spacewise dependent heat source*, Journal of Computational and Applied Mathematics, **209**, 66-80, 2007b.
- Juhl, P. *A note on the convergence of the direct collocation boundary element method*, Journal of Sound and Vibration, **212**, 703-719, 1998.
- Kabanikhin, S.I. *Definitions and examples of inverse and ill-posed problems*, Journal of Inverse and Ill-Posed Problems, **16**, 317-357, 2008.
- Klibanov, M.V. *Inverse problems and Carleman estimates*, Inverse Problems, **8**, 575-596, 1992.
- Landweber, L. *An iteration formula for Fredholm integral equations of the first kind*, American Journal of Mathematics, **73**, 615-624, 1951.

REFERENCES

- Lesnic, D., Hussein, S.O. and Johansson, B.T. *Inverse space-dependent force problem for the wave equation*, Journal of Computational and Applied Mathematics, (accepted).
- Lions, J.L. *Optimal Control of Systems Governed by Partial Differential Equations*, Springer, New York, 1971.
- Liu, S. and Triggiani, R. *Global uniqueness and stability in determining the damping and potential coefficients of an inverse hyperbolic problem*, Nonlinear Analysis: Real World Applications, **12**, 1562-1590, 2011.
- Mansur, W.J and Brebbia, C.A. *Numerical implementation of the boundary element method for two dimensional transient scalar wave propagation problems*, Applied Mathematical Modelling, **6**, 299-306, 1982a.
- Mansur, W.J and Brebbia, C.A. *Formulation of the boundary element method for transient problems governed by the scalar wave equation*, Applied Mathematical Modelling, **6**, 307-311, 1982b.
- Morse, P.M. and Feshbach, H. *Methods of Theoretical Physics*, McGraw-Hill, New York, 1953.
- Niwa, Y., Kobayashi, S., and Kitahura, M. *Determination of eigenvalue by boundary element method*, In: Development in Boundary Element Methods 2, (ed. P.K. Banerjee and R. Shaw), Applied Science, Chapter 7, London, pages 143-176, 1982.
- Philips, D.L. *A technique for the numerical solution of certain integral equations of the first kind*, Journal of the Association for Computer Machinery, **9**, 84-97, 1962.
- Pilant, M.S. and Rundell, W. *Undetermined coefficient problems for quasilinear parabolic equations*, In: Inverse Problems in Partial Differential Equations, (eds. D. Colton, R. Ewing and W. Rundell), SIAM, Philadelphia, 165-185, 1990.
- Prilepko, A. I., Orlovsky, D. G. and Vasin, I. A. *Methods for Solving Inverse Problems in Mathematical Physics*, Marcel Dekker, Inc., New York, 2000.

REFERENCES

- Ramm, A.G. *An inverse problem for the heat equation*, Journal of Mathematical Analysis and Applications, **264**, 691-697, 2001.
- Rauch, J. *On convergence of the finite element method for the wave equation*, SIAM Journal on Numerical Analysis, **22**, 245-249, 1985.
- Schatz, A., Thomee, V. and Wendland, W.L. *Mathematical Theory of Finite and Boundary Element Methods*, Birkhauser, Basel, 1990.
- Sjogreen, B. and Petersson, N.A. *Source estimation by full wave form inversion*, Journal of Scientific Computing, **59**, 247-276, 2014.
- Slodicka, M. *Some uniqueness theorems for inverse spacewise dependent source problems in nonlinear PDEs*, Inverse Problems in Science and Engineering, **22**, 2-9, 2014.
- Smith, G.D. *Numerical Solution of Partial Differential Equations: Finite Difference Methods*, Clarendon Press, Oxford, 3rd edn., 1985.
- Tarantola, A. *Inversion of seismic reflection data in the acoustic approximation*, Geophysics, **49**, 1259-1266, 1984.
- Thomee, V. *From finite differences to finite elements a short history of numerical analysis of partial differential equations*, Journal of Computational and Applied Mathematics, **128**, 1-54, 2001.
- Tikhonov, A.N. and Samarskii, A.A. *Equations of Mathematical Physics*, Pergamon Press, London, 1963.
- Trong, D.D., Quan, P.H. and Dinh Alain, P.N. *Determination of a two-dimensional heat source: Uniqueness, regularization and error estimate*, Journal of Computational and Applied Mathematics, **191**, 50-67, 2006
- Trucu, D., B. Ingham, D. and Lesnic, D. *Space-dependent perfusion coefficient identification in the transient bio-heat equation*, Journal of Engineering Mathematics, **67**, 307-315, 2010.

REFERENCES

- Twomey, S. *On the numerical solution of Fredholm integral equations of first kind by inversion of the linear system produced by quadrature*, Journal of the Association for Computing Machinery, **10**, 97-101, 1963.
- Vogel, C.R. *Non-convergence of the L-curve regularization parameter selection method*, Inverse Problems, **12**, 535-547, 1996.
- Wendland, W.L. *Boundary element methods and their asymptotic convergence*, In: Theoretical Acoustics and Numerical Techniques, (ed. P. Filippi), Springer-Verlag, New York, **277**, 135-216, 1983.
- Wrobel, L. C. *The Boundary Element Method, Application in Thermo-Fluids and Acoustics*, Vol. 1, J. Wiley, New York, 2002.
- Yamamoto, M. *Conditional stability in determination of force terms of heat equations in a rectangle*, Mathematical and Computer Modelling, **18**, 79-88, 1993.
- Yamamoto, M. *Stability, reconstruction formula and regularization for an inverse source hyperbolic problem by a control method*, Inverse Problems, **11**, 481-496, 1995.
- Yang, F. and Fu, C.-L. *A simplified Tikhonov regularization method for determining the heat source*, Applied Mathematical Modelling, **34**, 3286-3299, 2010.
- Zinkiewicz, O.C., Taylor, R.L. and Zhu, J.Z. *The Finite Element Method: Its Basis and Fundamentals*, Butterworth-Heinemann, 2005.